



UNIVERSITY OF
LIVERPOOL

New Approaches to Electrochemical CO₂ Reduction with Molecular Catalysts

Francesca Helen Greenwell

Supervisor Professor Alex Cowan

Thesis submitted to the University of Liverpool in partial fulfilment of the
degree of Doctor in Philosophy

September 2023

Stephenson Institute for Renewable Energy

Abstract

Electrochemical CO₂ reduction holds the potential to replace depleting petroleum reserves, harnessing renewable energy to produce fuels and chemical feedstocks. In this thesis, new approaches towards electrochemical CO₂ reduction with molecular complexes have been investigated, addressing limitations through catalyst modification, electrolysis techniques as well as integrating CO₂ capture and conversion.

Through the environmental drive to use aqueous electrolytes while overcoming the low solubility of CO₂ in water, gas diffusion electrodes (GDE), often made of porous sp² carbon cloth or paper, have become prevalent in the CO₂ reduction community.^{1,2} With this in mind a pyrene modified Ni(cyclam) (cyclam = 1,4,8,11-tetraazacyclotetradecane) catalyst was synthesised and successfully immobilised to a range of carbon substrates, including GDE, where significant CO selectivity in both a flow (CO/H₂ >1.5) and zero-gap cell (CO/H₂ > 1.0), outperforming previously reported N-alkylated Ni(cyclam) catalysts in aqueous electrolytes. While the possibility of this catalyst class in a co-electrolysis device was demonstrated, the stability of these electrodes was limited both by the water solubility and poisoning of the complex.

Ni(cyclam), along with other molecular catalysts, suffer greatly from CO poisoning and overreduction, limiting both their long-term stability and performance at higher current densities.^{3,4} This has been previously mitigated with CO scavengers,³ increased flow rates and long recovery periods,^{5,6} though this often only leads to temporary recovery. Recently, pulsed electrolysis has shown to greatly improve the stability of CO₂ reduction with metal catalysts,⁷ however this is largely unstudied on molecular catalysts. In Chapter 3, ms asymmetric anodic pulses were shown to significantly improve the selectivity and stability of Ni(cyclam) by in situ catalyst regeneration from an intermediate formed from the catalyst's degradation pathway.

Recently, pairing the capture of CO₂ with its reduction has come into focus, with the possibility of streamlining the processes, overcoming energetically demanding thermal regeneration of capture solutions. However, this is challenging, as during the capture process, CO₂ undergoes conversion to carbamate and bicarbonate species, which conventional metal CO₂ reduction catalysts remain largely inert towards.^{8,9} While molecular complexes have been shown, both

spectroscopically and electrochemically to interact with these amine-CO₂ species, this is generally done at low amine concentrations in organic solvents which is not representative of conventional capture solutions.^{10–12} In Chapter 4, a water-soluble Mn complex, is shown spectroscopically to interact with aqueous capture amines at industrially relevant concentrations, with initial electrolysis experiments showing CO/H₂ values of 2.1. While this preliminary selectivity is impressive, it was convoluted with issues with reproducibility which require resolution.

References

- 1 D. Higgins, C. Hahn, C. Xiang, T. F. Jaramillo and A. Z. Weber, *ACS Energy Lett*, 2019, **4**, 317–324.
- 2 T. Burdyny and W. A. Smith, *Energy Environ Sci*, 2019, **12**, 1442–1453.
- 3 J. D. Froehlich and C. P. Kubiak, *J Am Chem Soc*, 2015, **137**, 3565–3573.
- 4 G. B. Balazs and F. C. Anson, *J Electroanal Chem*, 1993, **361**, 149–157.
- 5 B. Siritanaratkul, M. Forster, F. Greenwell, P. K. Sharma, E. H. Yu and A. J. Cowan, *J Am Chem Soc*, 2022, **144**, 7551–7556.
- 6 S. Pugliese, N. T. Huan, A. Solé-Daura, Y. Li, J.-G. Rivera de la Cruz, J. Forte, S. Zanna, A. Krief, B.-L. Su and M. Fontecave, *Inorg Chem*, 2022, **61**, 15841–15852.
- 7 R. Casebolt, K. Levine, J. Suntivich and T. Hanrath, *Joule*, 2021, **5**, 1987–2026.
- 8 K. Shen, D. Cheng, E. Reyes-Lopez, J. Jang, P. Sautet and C. G. Morales-Guio, *Joule*, 2023, **7**, 1260–1276.
- 9 L. Chen, F. Li, Y. Zhang, C. L. Bentley, M. Horne, A. M. Bond and J. Zhang, *ChemSusChem*, 2017, **10**, 4109–4118.
- 10 J. Bi, P. Hou, F. W. Liu and P. Kang, *ChemSusChem*, 2019, **12**, 2195–2201.
- 11 H. Koizumi, H. Chiba, A. Sugihara, M. Iwamura, K. Nozaki and O. Ishitani, *Chem Sci*, 2019, **10**, 3080–3088.
- 12 M. Bhattacharya, S. Sebghati, R. T. VanderLinden and C. T. Saouma, *J Am Chem Soc*, 2020, **142**, 17589–17597.

List of publications

The following papers were published in peer-reviewed journals for this PhD project:

Francesca Greenwell, Gaia Neri, Verity Piercy and Alexander J. Cowan, “*Noncovalent immobilization of a nickel cyclam catalyst on carbon electrodes for CO₂ reduction using aqueous electrolytes*”, *Electrochim Acta*, 2021, **392**, 139015. (**Chapter 2**)

Liam M. Welch, Meera Vijayaraghavan, **Francesca Greenwell**, John Satherley and Alexander J. Cowan, “*Electrochemical carbon dioxide reduction in ionic liquids at high pressure*”, *Faraday Discuss*, 2021, **230**, 331-343.

Bhavin Siritanaratkul, Mark Forster, **Francesca Greenwell**, Preetam K. Sharma, Eileen H. Yu and Alexander J. Cowan, “*Zero-gap bipolar membrane electrolyser for carbon dioxide reduction using acid tolerant molecular electrocatalysts*”, *J Am Chem Soc*, 2022, **144**, 7551-7556.

Francesca Greenwell, Bhavin Siritanaratkul, Preetam K. Sharma, Eileen H. Yu and Alexander J. Cowan, “*Pulsed electrolysis with a nickel molecular catalyst improves selectivity for carbon dioxide reduction*”, *J Am Chem Soc*, 2023, **145**, 15078-15083. (**Chapter 3**)

Acknowledgements

It takes a village to write a thesis, and for my village I am very grateful.

First, I need to thank my supervisor, Professor Alex Cowan. Your support and knowledge have been endless, from fuzzy electrodes to CO₂ capture amines, each time you have managed to fix it when I was determined I was doomed. Thank you for the opportunities to push me out of my comfort zone, to present my research or try the wild card experiments. You have cultured such an incredible group environment that has helped shape me into the researcher I am today and I am certain I would not have made it without your constant reassurance that I am in the right place.

Speaking of an incredible group, I am so grateful I got to be part of The World of Alex Cowan, who's members old and new have become lifelong friends across the globe. Gaia, who drove over an hour to take me out to dinner while I was "in the area". Bhavin, for never laughing at my embarrassingly basic questions. Khezar, who's excellent baked goods I still think of. Cathy, who made a horrendous Gordon conference disco hilarious. Liam, for being an excellent thesis writing partner (complaining by day, chaos causing by night). And Alicia, who's kindness knows no bounds, I will miss our fume hood-side chats very much.

I would like to acknowledge all of the wonderful collaborators who have lent their time, knowledge and expertise towards this thesis. Dr Gaia Neri, for introducing me to the world of molecular electrocatalysts and your endless synthesis knowledge. Dr Bhavin Siritanaratkul for your infinite help with electrochemistry and product analysis. Dr Verity Piercy from the University of Liverpool and Dr Preetam Sharma and Prof Eileen Yu from University of Loughborough for XPS measurements and analysis.

I would like to thank everyone from the Stephenson Institute, who have meant I have never dreaded a Monday in my five years here. The 92° coffee and AJ pints (or G&Ts) were only ever as good as the company.

For all of my friends and family, who have supported and encouraged me on this journey, and were proud of me even when I couldn't be proud of myself.

And to my dearest OB, who gave me all the support, reassurance and comfort in the world and only ever wanted sweet nothing in return.

Abbreviations

The following list contains the commonly abbreviated terms used in this thesis. Each one is fully denoted the first time mentioned in each chapter.

AEM	Anion exchange membrane
AMP	2-amine-2-methyl-1-propanol
BPM	Bi-polar membrane
Bpy	2,2'-bipyridine
bpy-COOH	4,4'-dicarboxy-2,2'-bipyridine
C_D	Diffuse capacitance
C_{dl}	Double layer capacitance
CE	Counter electrode
CEM	Cation exchange membrane
CFT	Crystal field theory
C_H	Helmholtz capacitance
CNT	Carbon nanotube
C_0	Molar concentration of redox active species
CV	Cyclic voltammetry
Cyclam	1,4,8,11-tetraazacyclotetradecane
CycPy	1-(4-(pyren-1-yl)butyl)-1,4,8,11-tetraazacyclotetradecane
DCM	Dichloromethane
DEA	Diethanolamine
DGA	Diglycol amine
DIPA	Diisopropanol amine

DMF	Dimethylformamide
DMSO	Dimethylsulfoxide
D_0	Diffusion coefficient
DPSC	Double potential step chronocoulometry
$E_{1/2}$	Formal redox couple
E_A	Anodic potential
E_C	Cathodic potential
eCO_2R	Electrochemical CO_2 reduction
EDL	Electron donating ligand
EEA	2-ethoxyethylamine
$EE_{full\ cell}$	CO Full cell energetic efficiency
EWL	Electron withdrawing ligand
F	Faraday constant
FE	Faradaic Efficiency
FT-IR	Fourier Transformed Infrared Spectrometry
GC	Gas chromatography
GCE	Glassy carbon electrode
GC-MS	Gas chromatography mass spectrometry
GDE	Gas diffusion electrode
GDL	Gas diffusion layer
HER	Hydrogen evolution reaction
i	Current
i_A	Anodic current
i_c	Cathodic current

IC	Ion chromatography
i_p	Peak current
j	Current density
j_c	Peak current density under catalytic conditions
j_p	Peak current density
MDEA	Methyl diethanolamine
MEA	Monoethanolamine
MLCT	Metal-to-ligand charge transfer
MORPH	Morpholine
MORPH-COO ⁻	Morpholine carbamate
MORPH-COOH	Morpholine carbamic acid
MORPH-H ⁺	Morpholinium cation
n	Number of electrons
NMR	Nuclear magnetic resonance
OCP	Open circuit potential
P	Porphyrin
Pc	Phthalocyanine
PFE	Polytetrafluoroethylene
Q_{ads}	Faradaic charge passed to adsorbed species
Q_{An}	Anodic charge fraction
Q_C	Capacitive charge
Q_{Ca}	Cathodic charge fraction
Q_{total}	Total charge
R	Universal gas constant

RE	Reference electrode
RHE	Reversible hydrogen electrode
R_p	Polarisation resistance
R_U	Uncompensated resistance
SHE	Standard hydrogen electrode
SWV	Square wave voltammetry
T	Temperature
t_A	Time spent applying E_A or i_A
TBA	Tetrabutylammonium
t_C	Time spent applying E_C of i_C
TEA	Triethanolamine
TOF	Turnover frequency
TON	Turnover number
TPP	Tetraphenylporphyrin
UV/Vis	Ultraviolet/Visible region
$VE_{full\ cell}$	Full cell voltage efficiency
WE	Working electrode
XPS	X-ray photoelectron spectroscopy
Z	Impedance
Γ	Surface coverage
Γ_{theo}	Theoretical surface coverage
ν	Scan rate

Contents

Chapter 1 Introduction	13
1.1 Motivation	13
1.2 Electrochemical CO ₂ reduction	14
1.3 Electrocatalysis.....	16
1.3.1 Metallic electrodes.....	16
1.3.2 Molecular electrocatalysts	17
1.4 Homogeneous molecular catalysis	18
1.4.1 Phosphine complexes	18
1.4.2 Phthalocyanines and Porphyrins.....	18
1.4.3 Polypyridyl Tricarbonyls.....	19
1.4.4 Cyclams	22
1.5 Heterogeneous molecular catalysis	25
References	28
Chapter 2 Noncovalent immobilization of a Ni(cyclam) catalyst on carbon electrodes	35
2.1 Scope of the chapter	35
2.2 Synthesis and Characterisation.....	38
2.3 Electrochemistry in solution.....	42
2.4 Ni(CycPy) immobilisation onto carbon electrodes	49
2.4.1 Immobilisation on glassy carbon electrodes (GCE) and carbon nanotubes (CNT)	49
2.4.2 Immobilisation onto a gas diffusion electrode (GDE).....	59
2.5 Conclusions	67
2.6 References	68
Chapter 3 Pulsed electrolysis on Ni(cyclam).....	71
3.1 Scope of the chapter	71
3.2 Ni(cyclam) mechanism and degradation.....	73
3.3 Pulsed electrolysis on Ni(cyclam).....	79

3.3.1 Potential dependence of pulsed electrolysis	87
3.3.2 Time dependence of pulsed electrolysis	94
3.3.3 Testing pulsed electrolysis on zero-gap cell.....	97
3.4 Conclusions and Future Work.....	100
3.5 References	101
Chapter 4 Integrating CO ₂ capture and electrocatalytic conversion	105
4.1 Scope of the chapter	105
4.1.1 Equilibria and speciation involved in amine-based CO ₂ capture solutions.....	105
4.1.2 Types of CO ₂ amine	106
4.1.3 Electrochemical CO ₂ reduction in amine solution	107
4.2 Species breakdown of morpholine-CO ₂	112
4.3 Spectroscopy of Mn(bpy-COOH) in morpholine.....	114
4.3.1 FTIR.....	114
4.3.2 UV/Vis & ¹ H NMR	121
4.4 Electrochemistry of Mn(bpy-COOH) in morpholine.....	127
4.4.1 CV Analysis.....	127
4.4.2 Bulk Electrolysis.....	133
4.5 Electrochemistry in other capture amines: MEA and DEA	144
4.6 Conclusions and future work.....	148
4.7 References	149
Chapter 5 Conclusions and future work.....	153
References	156
Chapter 6 Experimental Methods	157
6.1 Catalyst Synthesis	157
6.1.1 NiCycPy (Chapter 2)	157
6.1.2 NiCyc (Chapter 3)	159
6.1.3 Mn(bpy-COOH) (Chapter 4).....	159

6.2 Catalyst immobilisation/ electrode fabrication	159
6.2.1 Immobilisation to GCE and CNT	159
6.2.2 Immobilisation to GDE in flow cell	160
6.2.3 Immobilisation to GDE in zero-gap cell.....	160
6.3 Electrochemistry.....	160
6.4 Product detection.....	162
6.4.1 GC.....	162
6.4.2 GC-MS.....	163
6.4.3 IC	163
6.4.4 ¹ H NMR.....	163
6.5 Catalyst Analysis.....	164
6.5.1 ¹ H NMR.....	164
6.5.2 UV/Vis.....	164
6.5.3 FT-IR	164
6.5.4 XPS	164
6.6 References	165
Appendix.....	166
Mn(bpy-COOH) in CO ₂ capture amines	166

Chapter 1 Introduction

1.1 Motivation

Almost all of our current infrastructure is based on fuels and chemicals produced from non-renewable sources which are depleting rapidly. Because of this, society is shifting to alternative sources for both energy and chemical demands. While renewable energy has come a remarkably long way, intermittency issues require energy storage technologies such as batteries and fuels. As for chemical feedstocks, focus on developing synthetic routes from waste carbon rather than fossil fuels is necessary.

Unlike fossil fuels, levels of CO₂ are rising vastly (**Figure 1**), as emissions rose 423 million tonnes in 2022 alone.¹ This huge output of CO₂ has led to a large spike of CO₂ in the atmosphere from <320ppm in the 1960s to over 410ppm in the 2020s so far,^{2,3} leading to rising global temperatures and ocean acidification on a significant scale. This environmental driving force has led to a large increase in carbon capture technologies, where CO₂ is captured using, most commonly, aqueous solutions of alkanolamines. To release the CO₂ and regenerate capture solution, significant heating is required, adding to current the energy and cost. Once released, the CO₂ is pressurised and often transported to be stored. The abundance of CO₂ has led to significant research into its conversion to higher value chemicals to close the carbon cycle.

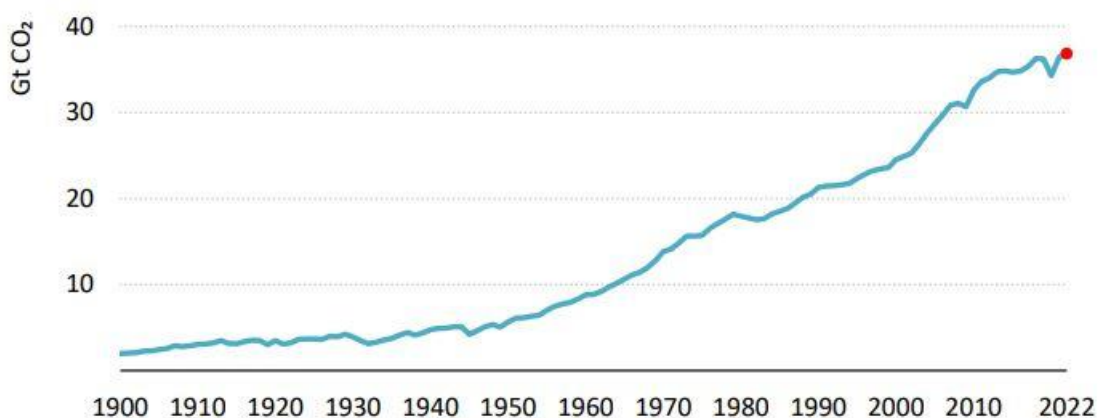
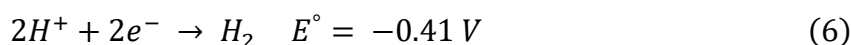
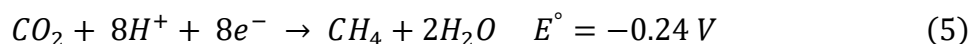
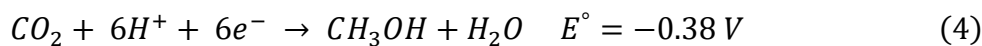
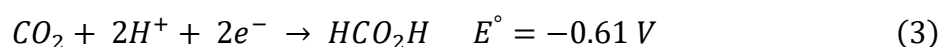
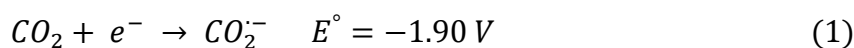


Figure 1 Global CO₂ emissions from energy combustion and industrial processes from 1900 to 2022, reproduced from IEA.¹

1.2 Electrochemical CO₂ reduction

Reduction of CO₂ into various fuels can be driven electrochemically, photochemically and thermally via hydrogenation. The benefit of driving this reaction electro- and photochemically is that renewable sources can be used to drive the energetically uphill reactions and water can be employed as an abundant proton and electron source.^{4,5} For the electrochemical reduction of CO₂, proton coupled, multielectron steps are generally more favourable than the one electron reduction from CO₂ to CO₂^{-•}, which requires a large reduction potential (see Eq. (1)-(5)) introduced by the reorganizational energy associated with changing from the linear molecule and the bent radical anion.⁶

Equations 1-6 Reduction potentials relevant to the reduction of CO₂ saturated water at pH 7 vs. NHE.^{7,8}



While CO₂ reduction to methanol (Eq. (4)) or methane (Eq. (5)) requires a lower reduction potential, the kinetic challenges of these multielectron processes have led to significant research focussing on the electrochemical production of syngas (synthesis gas: CO and H₂ mixtures) from CO₂ and H₂O (Eq (2, 6)). Syngas, currently derived from natural gas and coal, is used to synthesise a wide range of carbon-based products via the well-established Fischer-Tropsch process.^{6,9,10}

The stability of the CO₂ molecule poses a significant challenge to its electrochemical conversion, requiring significant efforts in cell engineering, electrolysis techniques and catalysis.

1.3 Electrocatalysis

To overcome kinetic energy barriers associated with CO₂ reduction, catalysts are required. The electrochemical CO₂ conversion has seen many recent improvements with both molecular and metal catalysts. Molecular catalysts work as a redox relay, where they accept electrons from the working electrode, before transferring them to coordinated CO₂. They can be used either homogeneously, where the complex is freely diffusing in solution or heterogeneously, where the complex is immobilised to the electrode support (**Figure 2**). Metal catalysts act as the working electrode, where CO₂ couples strongly to the metal surface and electron transfer and CO₂ reduction is a concerted process.

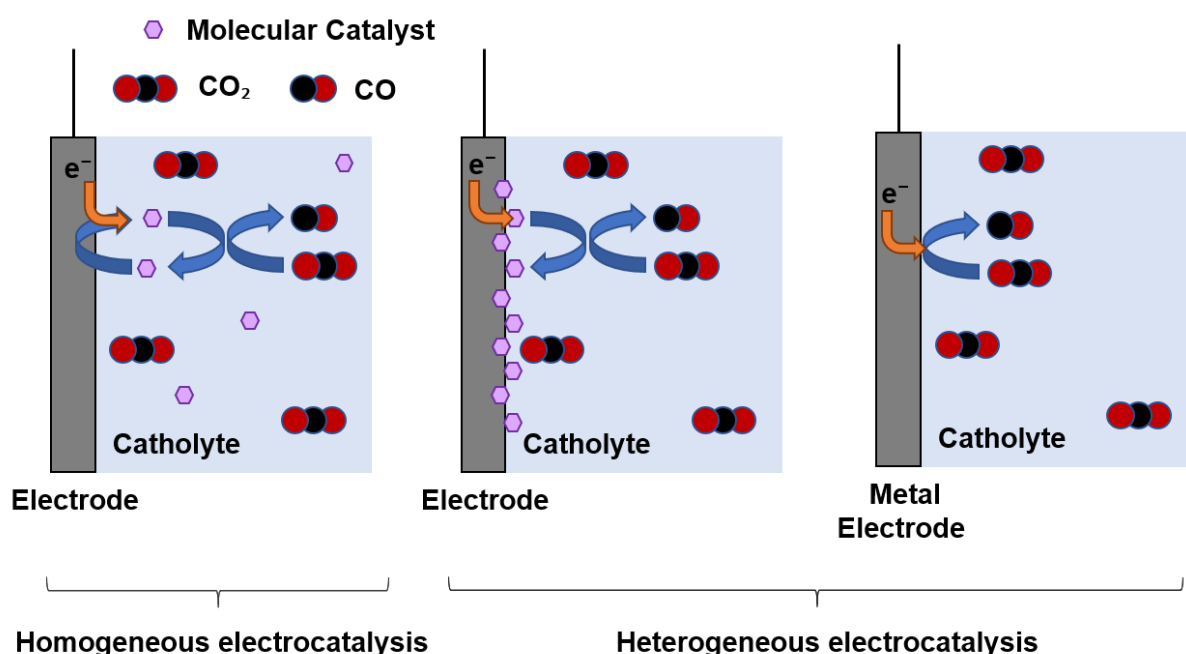


Figure 2 Homogeneous electrocatalysis where molecular catalyst and CO₂ are diffusing in solution (left) heterogeneous electrocatalysis with immobilised molecular catalyst (middle) or metal catalyst (right).

1.3.1 Metallic electrodes

The electrocatalytic activity of heterogeneous metal electrodes is covered extensively in literature.^{11,12} A variety of metal electrodes have been shown to give high product yields at industrially relevant current densities over 200 mAcm⁻².¹³ Products from CO₂ reduction depend on metal type and structure, for example, CO is produced selectively from Au and Ag,¹⁴

formate from Sn,¹⁴ and a variety of products including C₂₊ such as ethene and ethanol are only obtainable through Cu,^{14,15} however selectivity remains low. Other limitations of metal electrodes include their long-term stability as prolonged electrolysis leads to overreduction and surface reconstruction, reducing selectivity overtime.¹⁶

Recently, a different electrolysis technique has been used for CO₂ reduction with metal electrodes. Pulsed electrolysis, introduced in more detail in Chapter 3, incorporates an anodic pulse regularly throughout the course of the reaction. While many studies have reported improvements in both stability and selectivity for a range of metal electrodes, the proposed mechanisms are varied, appearing dependent on the electrochemical system and pulse parameters used.^{17,18}

1.3.2 Molecular electrocatalysts

Molecular catalysts have the advantage of a well-defined structure, with the potential to give greater insight into the CO₂ reduction mechanism and the ability to finetune the complex to maximise selectivity.^{5,19} Electrochemical CO₂ reduction with molecular catalysts most commonly produce CO and/or formate and follow two major reaction pathways (see **Figure 3**). The first is direct electron transfer from the active catalyst to CO₂, usually via coordination of CO₂ to the metal centre. The second is the protonation of the active catalyst, forming a metal hydride complex, followed by CO insertion into the M-H bond, usually resulting in formate as the major product.^{20,21}

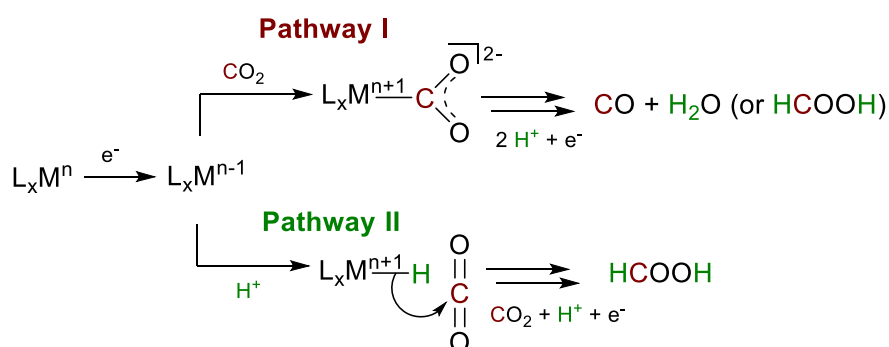


Figure 3 Characterisation of pathways for CO₂R (*M* = metal, *L* = ligand, *x* = stoichiometry of coordinated ligands, *n* = formal oxidation state of metal)

The number of molecular electrocatalysts for CO₂ reduction is substantial and expanding, an overview of the most common is given below, while a more comprehensive list can be found in reviews elsewhere.^{20,21}

1.4 Homogeneous molecular catalysis

1.4.1 Phosphine complexes

Phosphine complexes, while common in thermal catalysis and hydrogenation due to their remarkable thermal stability, are less common in electrochemical CO₂ reduction. With early studies done on a Pd triphosphine complex by DuBois *et al.* who showed significant CO production however suffered from low turnover number (TON) due to degradation.²² Ir pincer complexes are among the most frequent of this catalyst class, generally shown to produce formate as opposed to CO with high selectivity,^{23,24} even in aqueous electrolyte.²⁵ Formate production was also reported with a novel Fe tetraphosphine complex, via the second CO₂ reduction pathway (**Figure 3**), by Bi *et al.* Interestingly, the authors also observe methanol production by the same complex with the addition of diethanolamine (DEA), proposing the direct hydrogenation of the carbamate species which forms upon reaction of CO₂ and DEA (see **Figure 4**).²⁶ This is appealing, both because methanol is a high value product and due to its relevance to combined CO₂ capture and conversion, discussed more in Chapter 4.

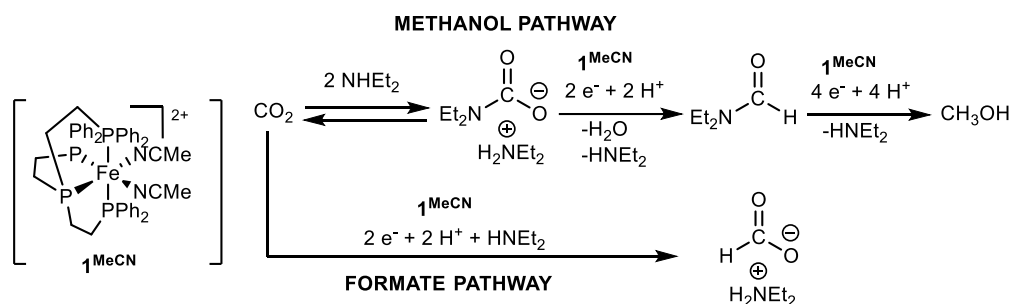


Figure 4 Proposed pathways for electrochemical reduction of CO₂ by Fe tetraphosphine reproduced from Kang *et al.*²⁶

1.4.2 Phthalocyanines and Porphyrins

Porphyrins (P) and Phthalocyanines (Pc) are composed of tetradentate nitrogen ligands with the most common metal centres being Co and Fe (see **Figure 5**). Porphyrins and phthalocyanines were the first molecular electrocatalysts discovered for CO₂ reduction, and mostly lead to the formation of carbon monoxide. First reported by Meshitsuka *et al.*, a wide range of water soluble metal phthalocyanines were synthesised by the group, who identified both NiPc and CoPc as active under CO₂ on a graphite electrodes.²⁷ This was shortly followed by Toshima's group, who synthesised a tetrasulfonated CoPc and later a cobalt porphyrin which were shown to be able to catalyse the reduction of CO₂.^{28,29} While the development of the iron(0) tetraphenylporphyrin (FeTPP) complex was pioneered by Savéant and co-workers. The complex was shown to reduce CO₂ to CO in dimethylformamide (DMF), however suffered from degradation without the addition of Lewis or weak Brønsted acids.^{30,31} The electrocatalysis of FeTPP was further increased by modifying the TPP ligand with phenol groups, which acted as a pre-associated acid source for CO₂ reduction.³² In 2015, FeTPP porphyrin was modified with tetramethyl ammonium group, creating a water soluble form which showed remarkable selectivity FE_{CO} of 90% even in aqueous electrolyte.³³ These electrocatalysts are still prevalent in the CO₂ reduction literature today, particularly CoPc, CoP and FeP, though focus has moved toward using them heterogeneously.^{19,34–37}

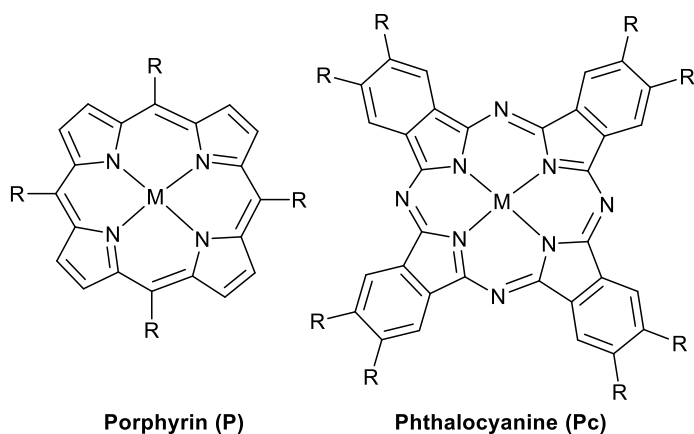


Figure 5 Structures of porphyrin (left) and phthalocyanine (right) ligands.

1.4.3 Polypyridyl Tricarbonyls

Polypyridyl tricarbonyl complexes are prominent in both photo- and electrocatalysis of CO₂. They were first used for electrocatalytic CO₂ reduction with [Re(bpy)(CO)₃Cl] by Lehn *et al.*³⁸ 2,2'-bipyridine (bpy), the most common polypyridyl ligand, and has been modified in various

ways as summarised by Qiao *et al.*⁹ Some of the highest activities were achieved by substituting the bpy ligand with tertiary butyl groups at the 4,4'-position.³⁹ The Re catalyst shows remarkable selectivity for CO₂ binding over H⁺, with an ability to operate in the absence of a proton source, though catalytic rates are significantly increased in the presence of a Brønsted acid.⁴⁰

The more abundant manganese analogue: [Mn^I(bpy)(CO)₃X]ⁿ⁺ (denoted as Mn(bpy)), where X is coordinated anion or solvent and n = 0 or 1, has also shown significant carbon dioxide reduction. However, unlike the corresponding Re catalysts, this is only achieved in the presence of a weak Brønsted acid.⁴¹ This proton dependence originally led to the dismissal of the Mn analogue as an electrocatalyst for CO₂ reduction as initial studies in dry organic solvents had shown the catalyst did not bind to CO₂.⁴²

Insight into the complex catalytic mechanism of Mn(bpy) has since been derived from theoretical studies, modification of the bpy ligand and spectroscopy studies (shown in **Figure 6**).^{43–49} Here the starting complex undergoes initial reduction and dimerization before a second reduction to the primary active complex, [Mn(bpy)(CO)₃]⁻. Sampson *et al.* reported improved eCO₂R using a bulky Mn(bpy) analogue, bypassing the formation of the dimer due to the increased steric hindrance.⁴⁹ The addition of protons then assist CO₂ binding to the active catalyst, forming the more stable [Mn(bpy)(CO)₃(CO₂H)] over the unfavourable [Mn(bpy)(CO)₃(CO₂)]⁻,^{45,50} before reacting via the reduction-first or protonation-first pathways.⁵¹ It has since been shown that Mn(bpy) can also reduce CO₂ through the dimer pathway at lower over-potentials.⁴³ Generally, CO is the primary product of eCO₂R with Mn(bpy) catalysts, with only few reports of formate production.^{52–54}

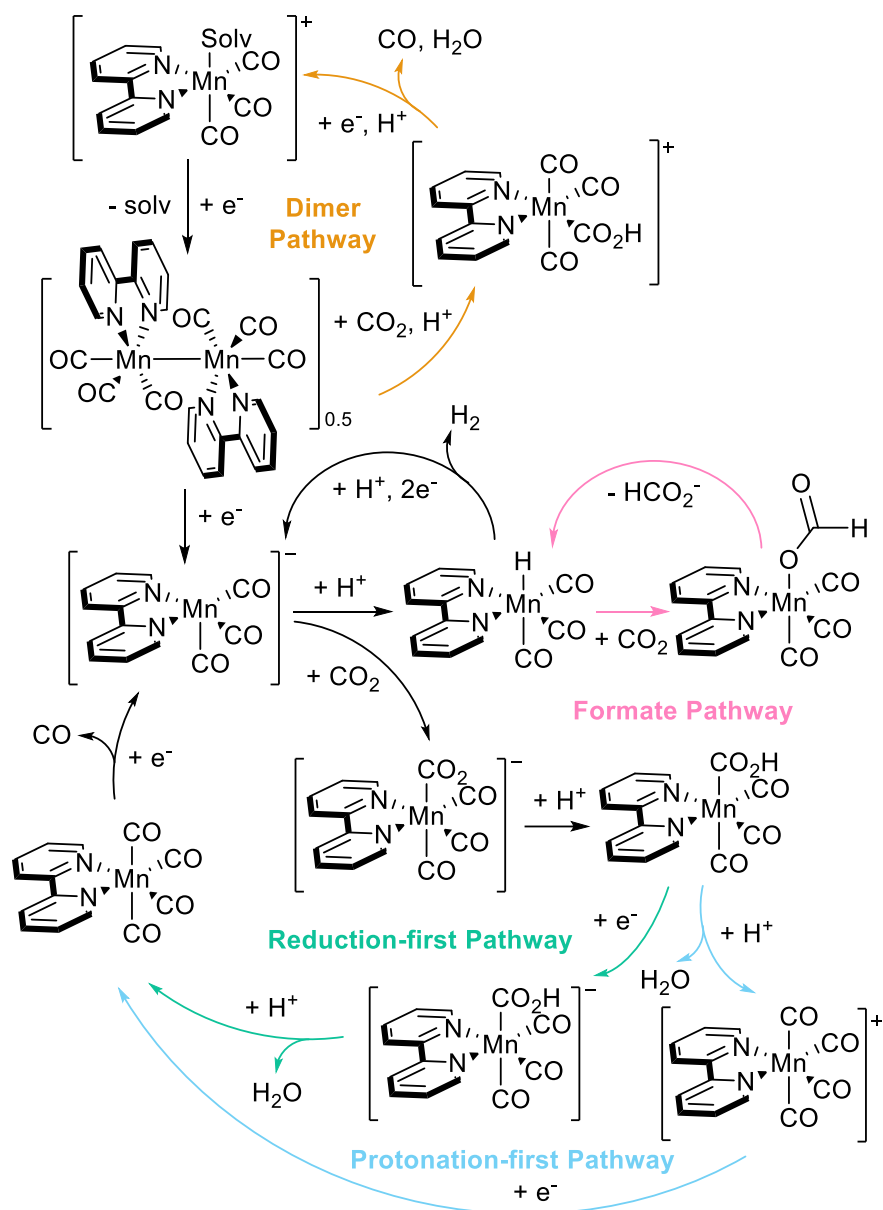


Figure 6 Simplified catalytic cycle for Mn(bpy) catalysts reproduced from literature.^{43,55}

Like the Fe tetraphosphine, bipyridine complexes have also recently gained interest in integrated CO₂ capture and reduction. The Ishitani group revisited the role of triethanolamine (TEA),^{56,57} where they established spectroscopically the coordination of TEA to the metal centre. The group also showed CO₂ inserted into the M-O bond (see **Figure 7**) where it is reduced effectively even at CO₂ concentrations as low as 1%.^{58,59} Bhattacharya *et al.* also reported the effect of amine addition on Mn bipyridine catalysts, where they reported a shift in the CO₂ reduction pathway from CO to formate production.⁶⁰

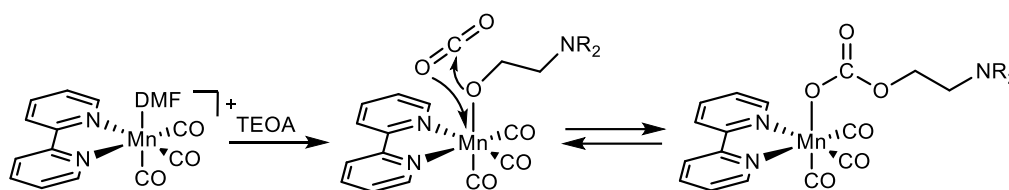


Figure 7 Coordination of TEOA and possible mechanism of CO_2 insertion into the $\text{M}-\text{O}$ bond to form the carbonate ligand. Reproduced from Ishitani et al.⁵⁷

1.4.4 Cyclams

$\text{Ni}(\text{cyclam})$ (cyclam = 1,4,8,11-tetraazacyclotetradecane) is a low-cost, well known electrocatalyst for CO_2 reduction, showing high selectivity for CO in aqueous electrolyte.^{61–64} The first cyclam-type catalysts shown to reduce CO_2 were reported by Fisher and Eisenberg in 1980,⁶¹ before $\text{Ni}(\text{cyclam})$ was named and shown to produce almost FE_{CO} 100% with a Hg working electrode at low overpotentials ($-1.00 \text{ V}_{\text{NHE}}$) by the Sauvage group.⁶² Both its catalytic and deactivation mechanism have been studied extensively, and the key proposed steps are shown in **Figure 8**.^{64–66} It has also been established that not only is $\text{Ni}(\text{cyclam})$ remarkably acid tolerant,⁶⁷ but a proton source is necessary to observe catalytic CO_2 reduction with $\text{Ni}(\text{cyclam})$ at reasonable potentials, as the second reduction of the CO_2 adduct only occurs after protonation.⁶⁸

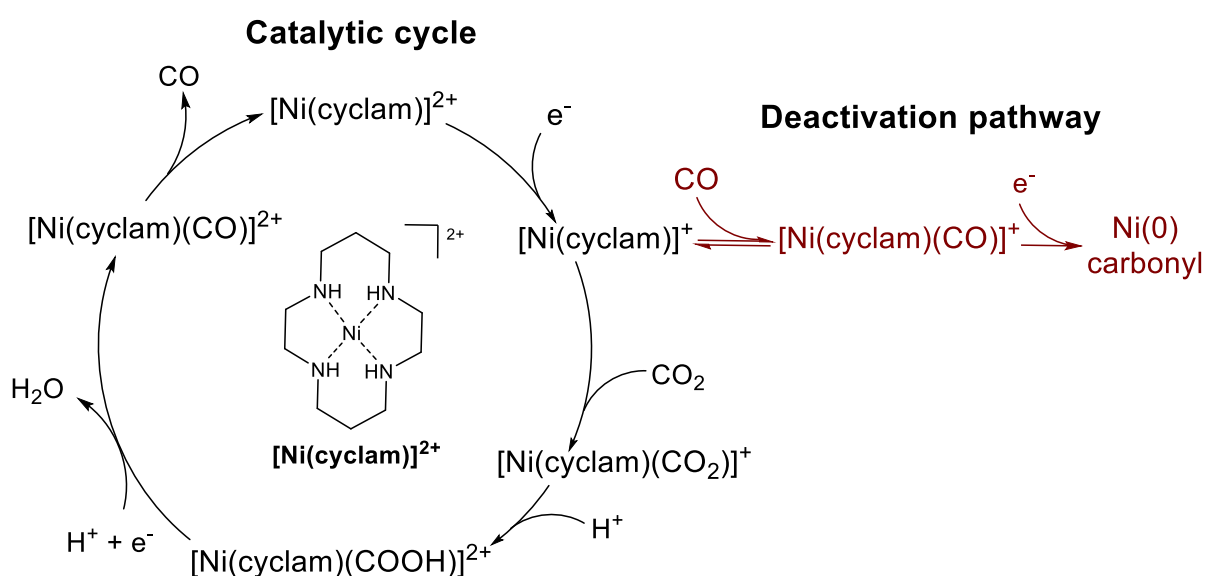


Figure 8 Reported catalytic cycle and deactivation pathway of $\text{Ni}(\text{cyclam})$.^{68,69}

Ni(cyclam) was initially studied on Hg electrodes, originally due to the extensive solvent window of the Hg electrode in aqueous media.^{62,64} However, it was quickly established that the catalyst underwent reductive adsorption on the Hg electrode surface to give the active adsorbed $[\text{Ni}(\text{cyclam})]^+$ species at potentials significantly positive of the formal redox couple.⁷⁰⁻⁷³ Adsorption onto the Hg electrode surface has been shown to aid the catalyst in electrochemical CO_2 reduction through structural rearrangement to the active conformer and/or repressing of the catalyst deactivation pathway.⁷⁴

Ni(cyclam) exists in solution as a mixture of five possible conformers (**Figure 9**), with *trans*-III and *trans*-I being the most abundant, making up ~15% and ~85% respectively.⁷⁵⁻⁷⁷ While it is agreed that the adsorbed, active catalyst on Hg electrodes is a single conformer, whether it is *trans*-III or *trans*-I is disputed in literature. Earlier DFT calculations done by Schneider *et al.* suggested the active catalyst is the *trans*-I isomer due to the four N-H protons on the same side of the macrocycle permitting hydrogen bonding and stabilisation of the CO_2 adduct.⁷⁸ However Wu *et al.* claimed instead, that the *trans*-III conformer is the active form, as DFT calculations suggest the Ni-CO bond is much weaker, disfavouring CO poisoning of the complex which is a key step in the deactivation of Ni(cyclam) (**Figure 8**).⁷⁴

The deactivation pathway of Ni(cyclam) has been studied extensively first by Balazs *et al.* on Hg and later by Froehlich *et al.* on carbon electrodes, shown in **Figure 8**. While Ni(cyclam) is proposed to be more stable on Hg electrodes, both show the catalyst to suffer from CO poisoning, due to the high CO binding constant to the active $[\text{Ni}(\text{cyclam})]^+$ species ($K_{\text{CO}} = 7.5 \times 10^5$, $K_{\text{CO}_2} = 16$),⁶⁸ followed by overreduction, significantly limiting its catalytic activity, which is discussed in more detail in Chapter 3.^{68,79-81}

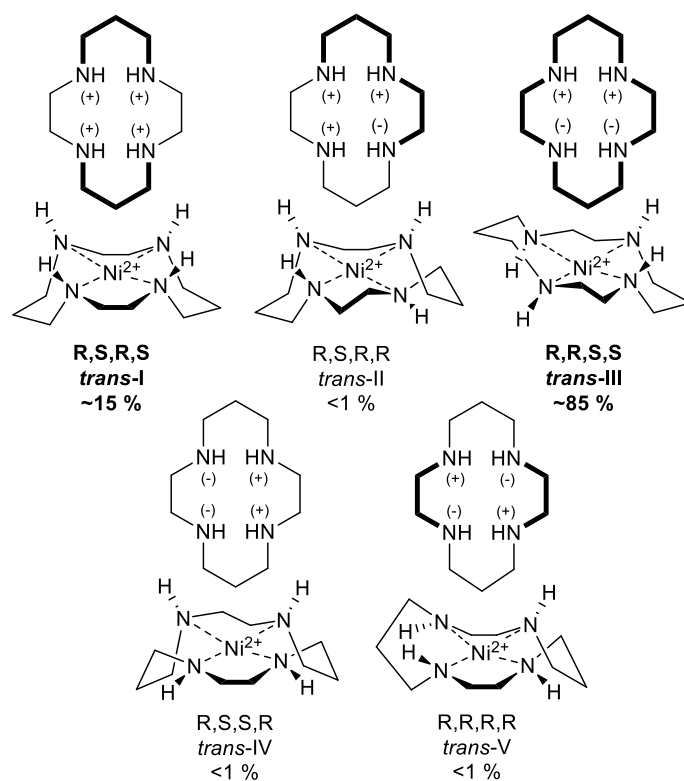


Figure 9 Possible conformers of Ni(cyclam) in solution, drawn in both common conventions with relative abundances given below. (+) indicates the hydrogen of the amine group is above the macrocycle plane whereas (-) indicates the amine hydrogen is below the macrocycle plane.

While Ni(cyclam) is most active on mercury electrodes, the complex is also electrocatalytic for CO₂ reduction at non-toxic metals,^{74,82} and carbon electrodes,⁶⁹ both homo- and heterogeneously which is discussed in the next section.

1.5 Heterogeneous molecular catalysis

As the field of electrochemical CO₂ reduction has advanced, literature has shifted to consider the impact of scaling up these reactions, identifying limiting factors to reach more industrially relevant current densities and yields. Significant strides have involved removing diffusion limitations of both substrate and catalyst. To overcome the low solubility of CO₂ in water, the desired green solvent, GDEs were developed. Here, rather than relying on dissolved CO₂ diffusing to the electrode through the electrolyte, a porous (usually carbon) working electrode is used and CO₂ is delivered directly through the back of the electrode to the electrode/electrolyte interface (see **Figure 10**).^{13,83–85} While this has shown to greatly improve the selectivity and current densities achieved at metallic electrodes, it is less explored with molecular complexes.

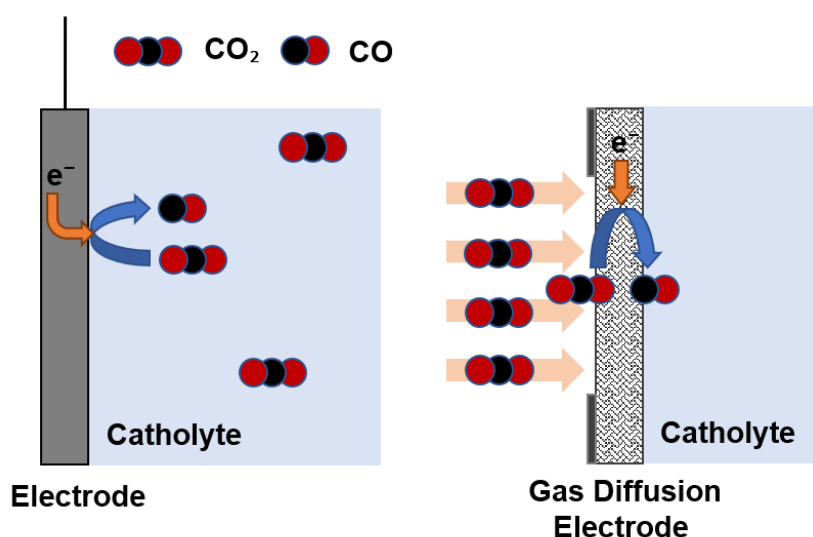


Figure 10 Schematic of a standard electrode (left) compared to a gas diffusion electrode (right).

In addition to the implementation of GDEs, cell structures have also been adapted to minimise ohmic resistance by moving away from liquid catholyte, instead, opting for membrane-electrode assembly or zero-gap setup.^{67,86} Zero-gap electrolyzers are characterised by both the cathode and anode being pressed either side of an anion exchange membrane (see **Error! Reference source not found.**), decreasing the distance ions are required to transfer, increasing current densities achievable. As zero-gap electrolyzers are optimised for product production, they are often ran as two electrode measurements which limits the insight achievable in this setup, thus are used in tandem with other methods to analyse electrocatalytic activity in this thesis.

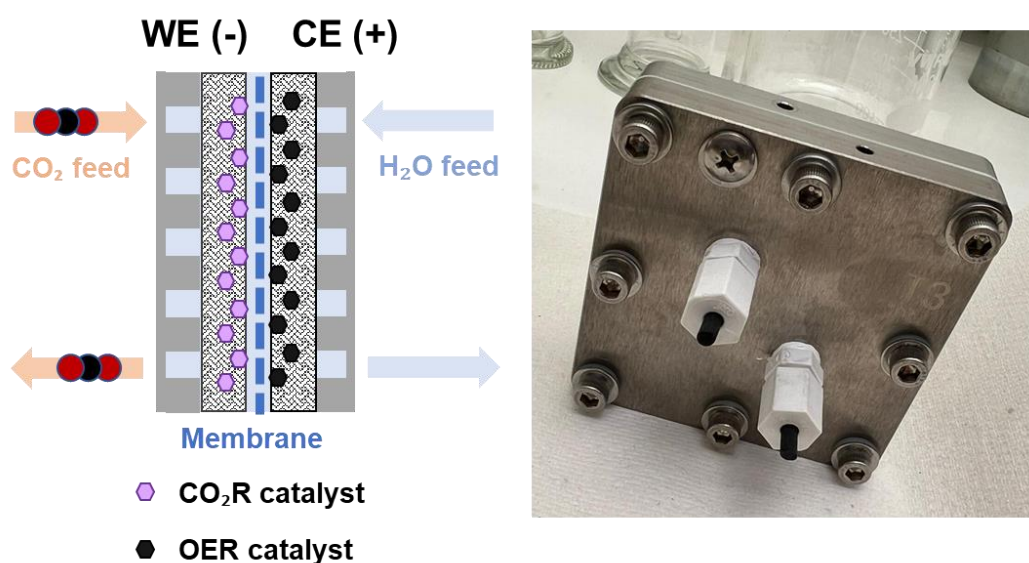


Figure 11 Schematic (left) and photograph of a zero-gap cell.

More recently, molecular electrocatalyst literature has moved away from homogeneous catalysis, instead increasing focus on incorporating catalysts onto these electrode surfaces, to increase contact between the catalyst and electrode, allowing significantly less catalyst to be used, overcoming catalyst solubility issues and sometimes even shifting the electrocatalytic behaviour. Lu *et al.* were the first to immobilise a CoPc molecular catalyst on a GDE on a flow cell, achieving a current density of 33 mAcm^{-2} with FE_{CO} of 90%.³⁴ Ren *et al.* expanded on this significantly, where CoPc was shown to give FE_{CO} of over 95% at 150 mAcm^{-2} in a zero-gap electrolyser cell, demonstrating that molecular electrocatalysts can work efficiently, on par with metal electrodes, at these operating conditions.³⁵ This has since been shown not to be limited to CoPc, as a range of metal complexes have been shown to work in these electrolyser setups, including FeP,^{19,36} Mn(bpy),^{87,88} and Ni(cyclam).^{67,89}

Many different strategies have been employed to immobilise a variety of molecular catalysts onto electrodes for CO₂ reduction, such as integration into a porous or polymer support,^{72,90–92} direct grafting via covalent bonding,^{52,87,93,94} or simple physical adsorption via weak interactions.^{89,95–98} The latter being the most straightforward immobilisation method, usually exploiting the sp² carbon structure of carbon electrodes, non-covalent π - π interactions are used to adhere a complex to the surface via the ligand, improving both selectivity and stability. In some cases, products have even been shown to vary with immobilisation, for example Wu *et al.* reporting methanol production by CNT immobilised CoPc as a result of effective electron transfer over prolonged electrolysis, allowing the catalyst to reduce CO to methanol before becoming over reduced itself.⁹⁵ While Pc ligands have sufficient sp² structure already, other catalysts have been modified with pyrene units, which has also shown to be successful in both organic and aqueous electrolyte.^{89,96–100}

References

- 1 IEA, *CO2 Emissions in 2022*, IEA Publications, 2023.
- 2 D. M. Etheridge, L. P. Steele, R. L. Langenfelds, R. J. Francey, J. M. Barnola and V. I. Morgan, *Journal Of Geophysical Research-Atmospheres*, 1996, **101**, 4115–4128.
- 3 J. Blunden, T. Boyer and E. Bartow-Gillies, *Bull Am Meteorol Soc*, 2023, **104**, 1–516.
- 4 A. S. Agarwal, Y. Zhai, D. Hill and N. Sridhar, *ChemSusChem*, 2011, **4**, 1301–1310.
- 5 N. Corbin, J. Zeng, K. Williams and K. Manthiram, *Nano Res*, 2019, **12**, 2093–2125.
- 6 E. E. Benson, C. P. Kubiak, A. J. Sathrum and J. M. Smieja, *Chem Soc Rev*, 2009, **38**, 89–99.
- 7 M. Aresta and A. Dibenedetto, *Dalton Trans.*, 2007, 2975–2992.
- 8 W. H. Wang, Y. Himeda, J. T. Muckerman, G. F. Manbeck and E. Fujita, *Chem Rev*, 2015, **115**, 12936–12973.
- 9 J. Qiao, Y. Liu, F. Hong and J. Zhang, *Chem. Soc. Rev.*, 2014, **43**, 631–675.
- 10 L. Sun, V. Reddu, A. C. Fisher and X. Wang, *Energy Environ Sci*, 2020, **13**, 374–403.
- 11 Y. Hori, in *Modern Aspects of Electrochemistry*, Springer, New York, 2008, vol. 42, pp. 89–189.
- 12 G. Zhao, X. Huang, X. Wang and X. Wang, *J. Mater. Chem. A*, 2017, **5**, 21625–21649.
- 13 T. Burdyny and W. A. Smith, *Energy Environ Sci*, 2019, **12**, 1442–1453.
- 14 Y. Hori, H. Wakebe, T. Tsukamoto and O. Koga, *Electrochim Acta*, 1994, **39**, 1833–1839.
- 15 Y. Hori, K. Kikuchi, A. Murata and S. Suzuki, *Chem Lett*, 1986, **15**, 897–898.
- 16 R. M. Arán-Ais, F. Scholten, S. Kunze, R. Rizo and B. Roldan Cuenya, *Nat Energy*, 2020, **5**, 317–325.
- 17 R. Casebolt, K. Levine, J. Suntivich and T. Hanrath, *Joule*, 2021, **5**, 1987–2026.
- 18 T. Liu, J. Wang, X. Yang and M. Gong, *Journal of Energy Chemistry*, 2021, **59**, 69–82.

- 19 K. Torbensen, D. Joulié, S. Ren, M. Wang, D. Salvatore, C. P. Berlinguette and M. Robert, *ACS Energy Lett*, 2020, **5**, 1512–1518.
- 20 P. Saha, S. Amanullah and A. Dey, *Acc Chem Res*, 2022, **55**, 134–144.
- 21 N. W. Kinzel, C. Werlé and W. Leitner, *Angewandte Chemie International Edition*, 2021, **60**, 11628–11686.
- 22 D. L. DuBois, A. Miedaner and R. C. Haltiwanger, *J Am Chem Soc*, 1991, **113**, 8753–8764.
- 23 P. Kang, C. Cheng, Z. Chen, C. K. Schauer, T. J. Meyer and M. Brookhart, *J Am Chem Soc*, 2012, **134**, 5500–5503.
- 24 S. T. Ahn, E. A. Bielinski, E. M. Lane, Y. Chen, W. H. Bernskoetter, N. Hazari and G. T. R. Palmore, *Chemical Communications*, 2015, **51**, 5947–5950.
- 25 P. Kang, T. J. Meyer and M. Brookhart, *Chem Sci*, 2013, **4**, 3497–3502.
- 26 J. Bi, P. Hou, F. W. Liu and P. Kang, *ChemSusChem*, 2019, **12**, 2195–2201.
- 27 S. Meshitsuka, M. Ichikawa and K. Tamaru, *J Chem Soc Chem Commun*, 1974, 158.
- 28 K. Takahashi, K. Hiratsuka, H. Sasaki and S. Toshima, *Chem Lett*, 1979, **8**, 305–308.
- 29 K. Hiratsuka, K. Takahashi, H. Sasaki and S. Toshima, *Chem Lett*, 1977, **6**, 1137–1140.
- 30 I. Bhugun, D. Lexa and J. M. Savéant, *J Am Chem Soc*, 1994, **116**, 5015–5016.
- 31 M. Hammouche, D. Lexa, J. M. Savéant and M. Momenteau, *J Am Chem Soc*, 1991, **113**, 8455–8466.
- 32 C. Costentin, S. Drouet, M. Robert and J.-M. Savéant, *Science (1979)*, 2012, **338**, 90–94.
- 33 C. Costentin, M. Robert, J. Savéant and A. Tatin, *Proceedings of the National Academy of Sciences*, 2015, **112**, 6882–6886.
- 34 X. Lu, Y. Wu, X. Yuan, L. Huang, Z. Wu, J. Xuan, Y. Wang and H. Wang, *ACS Energy Lett*, 2018, **3**, 2527–2532.
- 35 S. Ren, D. Joulié, D. Salvatore, K. Torbensen, M. Wang, M. Robert and C. P. Berlinguette, *Science (1979)*, 2019, **365**, 367–369.

- 36 K. Torbensen, C. Han, B. Boudy and N. Von Wolff, *Chemistry - A European Journal*, 2020, **26**, 3034–3038.
- 37 K. Torbensen, B. Boudy, D. Joulié, N. von Wolff and M. Robert, *Curr Opin Electrochem*, 2020, **24**, 49–55.
- 38 J. Hawecker, J.-M. Lehn and R. Ziessel, *J. Chem. Soc., Chem. Commun.*, 1984, 328–330.
- 39 J. M. Smieja and C. P. Kubiak, *Inorg Chem*, 2010, **49**, 9283–9289.
- 40 K.-Y. Wong, W.-H. Chung and C.-P. Lau, *Journal of Electroanalytical Chemistry*, 1998, **453**, 161–170.
- 41 M. Bourrez, F. Molton, S. Chardon-Noblat and A. Deronzier, *Angewandte Chemie - International Edition*, 2011, **50**, 9903–9906.
- 42 F. P. A. Johnson, M. W. George, F. Hartl and J. J. Turner, *Organometallics*, 1996, **15**, 3374–3387.
- 43 G. Neri, P. M. Donaldson and A. J. Cowan, *Physical Chemistry Chemical Physics*, 2019, **21**, 7389–7397.
- 44 J. A. Keith, K. A. Grice, C. P. Kubiak and E. A. Carter, *J Am Chem Soc*, 2013, **135**, 15823–15829.
- 45 C. Riplinger, M. D. Sampson, A. M. Ritzmann, C. P. Kubiak and E. A. Carter, *J Am Chem Soc*, 2014, **136**, 16285–16298.
- 46 Y. C. Lam, R. J. Nielsen, H. B. Gray and W. A. Goddard, *ACS Catal*, 2015, **5**, 2521–2528.
- 47 J. J. Walsh, G. Neri, C. L. Smith and A. J. Cowan, *Chemical Communications*, 2014, **50**, 12698–12701.
- 48 J. J. Walsh, C. L. Smith, G. Neri, G. F. S. Whitehead, C. M. Robertson and A. J. Cowan, *Faraday Discuss*, 2015, **183**, 147–160.
- 49 M. D. Sampson, A. D. Nguyen, K. A. Grice, C. E. Moore, A. L. Rheingold and C. P. Kubiak, *J Am Chem Soc*, 2014, **136**, 5460–5471.

- 50 J. M. Smieja, M. D. Sampson, K. A. Grice, E. E. Benson, J. D. Froehlich and C. P. Kubiak, *Inorg Chem*, 2013, **52**, 2484–2491.
- 51 G. Neri, J. J. Walsh, G. Teobaldi, P. M. Donaldson and A. J. Cowan, *Nat Catal*, 2018, **1**, 952–959.
- 52 F. M. Stuardi, A. Tiozzo, L. Rotundo, J. Leclaire, R. Gobetto and C. Nervi, *Chemistry – A European Journal*, 2022, **28**, 1–9.
- 53 M. R. Madsen, M. H. Rønne, M. Heuschen, D. Golo, M. S. G. Ahlquist, T. Skrydstrup, S. U. Pedersen and K. Daasbjerg, *J Am Chem Soc*, 2021, **143**, 20491–20500.
- 54 M. H. Rønne, D. Cho, M. R. Madsen, J. B. Jakobsen, S. Eom, É. Escoudé, H. C. D. Hammershøj, D. U. Nielsen, S. U. Pedersen, M. Baik, T. Skrydstrup and K. Daasbjerg, *J Am Chem Soc*, 2020, **142**, 4265–4275.
- 55 B. Siritanaratkul, C. Eagle and A. J. Cowan, *Acc Chem Res*, 2022, **55**, 955–965.
- 56 T. Morimoto, T. Nakajima, S. Sawa, R. Nakanishi, D. Imori and O. Ishitani, *J Am Chem Soc*, 2013, **135**, 16825–16828.
- 57 H. Koizumi, H. Chiba, A. Sugihara, M. Iwamura, K. Nozaki and O. Ishitani, *Chem Sci*, 2019, **10**, 3080–3088.
- 58 H. Kumagai, T. Nishikawa, H. Koizumi, T. Yatsu, G. Sahara, Y. Yamazaki, Y. Tamaki and O. Ishitani, *Chem Sci*, 2019, **10**, 1597–1606.
- 59 T. Nakajima, Y. Tamaki, K. Ueno, E. Kato, T. Nishikawa, K. Ohkubo, Y. Yamazaki, T. Morimoto and O. Ishitani, *J Am Chem Soc*, 2016, **138**, 13818–13821.
- 60 M. Bhattacharya, S. Sebghati, R. T. VanderLinden and C. T. Saouma, *J Am Chem Soc*, 2020, **142**, 17589–17597.
- 61 B. J. Fisher and R. Eisenberg, *J Am Chem Soc*, 1980, **102**, 7361–7363.
- 62 M. Beley, J. Collin, R. Ruppert and J. Sauvage, *J. Chem. Soc., Chem. Commun.*, 1984, **2**, 1315–1316.
- 63 J. P. Collin, A. Jouaiti and J. P. Sauvage, *Inorg Chem*, 1988, **27**, 1986–1990.
- 64 M. Beley, J. P. Collin, R. Ruppert and J. P. Sauvage, *J Am Chem Soc*, 1986, **108**, 7461–7467.

- 65 C. A. Kelly, E. L. Blinn, N. Camaioni, M. D'Angelantonio and Q. G. Mulazzani, *Inorg Chem*, 1999, **38**, 1579–1584.
- 66 C. A. Kelly, Q. G. Mulazzani, E. L. Blinn and M. A. J. Rodgers, *Inorg Chem*, 1996, **35**, 5122–5126.
- 67 B. Siritanaratkul, M. Forster, F. Greenwell, P. K. Sharma, E. H. Yu and A. J. Cowan, *J Am Chem Soc*, 2022, **144**, 7551–7556.
- 68 J. D. Froehlich and C. P. Kubiak, *J Am Chem Soc*, 2015, **137**, 3565–3573.
- 69 J. D. Froehlich and C. P. Kubiak, *Inorg Chem*, 2012, **51**, 3932–3934.
- 70 M. Fujihira, Y. Hirata and K. Suga, *Journal of Electroanalytical Chemistry*, 1990, **292**, 199–215.
- 71 K. Bujno, R. Bilewicz, L. Siegfried and T. A. Kaden, *Journal of Electroanalytical Chemistry*, 1998, **445**, 47–53.
- 72 A. Jarzebinska, P. Rowainki, I. Zawisza, R. Bilewicz, L. Siegfried and T. Kaden, *Anal Chim Acta*, 1999, **396**, 1–12.
- 73 G. B. Balazs and F. C. Anson, *Journal of Electroanalytical Chemistry*, 1992, **322**, 325–345.
- 74 Y. Wu, B. Rudshiteyn, A. Zhanaidarova, J. D. Froehlich, W. Ding, C. P. Kubiak and V. S. Batista, *ACS Catal*, 2017, **7**, 5282–5288.
- 75 E. Joseph Billo, P. J. Connolly, D. J. Sardella, J. P. Jasinski and R. J. Butcher, *Inorganica Chim Acta*, 1995, **230**, 19–28.
- 76 E. Fujita, J. Haff, R. Sanzenbacher and H. Elias, *Inorg Chem*, 1994, **33**, 4627–4628.
- 77 J. Schneider, H. Jia, K. Kobiuro, D. Cabelli, J. Muckerman and E. Fujita, *Energy Environ Sci*, 2012, **5**, 9502–9510.
- 78 J. Schneider, H. Jia, J. T. Muckerman and E. Fujita, *Chem. Soc. Rev.*, 2012, **41**, 2036–2051.
- 79 G. B. Balazs, PhD Thesis, California Institute of Technology, 1993.
- 80 G. B. Balazs and F. C. Anson, *Journal of Electroanalytical Chemistry*, 1993, **361**, 149–157.

- 81 J. D. Froehlich, PhD Thesis, University of California, 2015.
- 82 G. Neri, I. M. Aldous, J. J. Walsh, L. J. Hardwick and A. J. Cowan, *Chem Sci*, 2016, **7**, 1521–1526.
- 83 Y. Gu, J. Wei, X. Wu and X. Liu, *Sci Rep*, 2021, **11**, 1–10.
- 84 D. Higgins, C. Hahn, C. Xiang, T. F. Jaramillo and A. Z. Weber, *ACS Energy Lett*, 2019, **4**, 317–324.
- 85 H. Rabiee, L. Ge, X. Zhang, S. Hu, M. Li and Z. Yuan, *Energy Environ Sci*, 2021, **14**, 1959–2008.
- 86 B. Siritanaratkul, P. K. Sharma, E. H. Yu and A. J. Cowan, *Adv Mater Interfaces*, 2023, **10**, 1–10.
- 87 J. Filippi, L. Rotundo, R. Gobetto, H. A. Miller, C. Nervi, A. Lavacchi and F. Vizza, *Chemical Engineering Journal*, 2021, 416.
- 88 C. Eagle, G. Neri, V. L. Piercy, K. Younis, B. Siritanaratkul and A. J. Cowan, *Sustain Energy Fuels*, 2023, **7**, 2301–2307.
- 89 S. Pugliese, N. T. Huan, A. Solé-Daura, Y. Li, J.-G. Rivera de la Cruz, J. Forte, S. Zanna, A. Krief, B.-L. Su and M. Fontecave, *Inorg Chem*, 2022, **61**, 15841–15852.
- 90 T. Yoshida, K. Tsutsumida, S. Teratani, K. Yasufuku and M. Kaneko, *J. Chem. Soc., Chem. Commun.*, 1993, 631–633.
- 91 J. Choi, J. Kim, P. Wagner, J. Na, G. G. Wallace, D. L. Officer and Y. Yamauchi, *J Mater Chem A Mater*, 2020, **8**, 14966–14974.
- 92 S. Sato, B. J. McNicholas and R. H. Grubbs, *Chemical Communications*, 2020, **56**, 4440–4443.
- 93 A. Zhanaidarova, C. E. Moore, M. Gembicky and C. P. Kubiak, *Chemical Communications*, 2018, **54**, 4116–4119.
- 94 G. Neri, J. J. Walsh, C. Wilson, A. Reynal, J. Y. C. Lim and A. J. Cowan, *Physical Chemistry Chemical Physics*, 2015, **17**, 1562–1566.
- 95 Y. Wu, Z. Jiang, X. Lu, Y. Liang and H. Wang, *Nature*, 2019, **575**, 639–642.

- 96 B. Reuillard, K. H. Ly, T. E. Rosser, M. F. Kuehnel, I. Zebger and E. Reisner, *J Am Chem Soc*, 2017, **139**, 14425–14435.
- 97 P. Kang, S. Zhang, T. J. Meyer and M. Brookhart, *Angewandte Chemie - International Edition*, 2014, **53**, 8709–8713.
- 98 S. Pugliese, N. T. Huan, J. Forte, D. Grammatico, S. Zanna, B.-L. Su, Y. Li and M. Fontecave, *ChemSusChem*, 2020, **13**, 6449–6456.
- 99 J. D. Blakemore, A. Gupta, J. J. Warren, B. S. Brunschwig and H. B. Gray, *J Am Chem Soc*, 2013, **135**, 18288–18291.
- 100 A. Maurin and M. Robert, *J Am Chem Soc*, 2016, **138**, 2492–2495.

Chapter 2 Noncovalent immobilization of a Ni(cyclam) catalyst on carbon electrodes

The material for this chapter comes from the manuscript “Noncovalent Immobilization of a Nickel Cyclam Catalyst on Carbon Electrodes for CO₂ Reduction Using Aqueous Electrolyte” by Francesca Greenwell, Gaia Neri, Verity Piercy and Alexander J. Cowan, published in *Electrochimica Acta*, 2021, 392, 139015. The thesis author is the primary investigator and author of this publication, completing experiment design, catalyst synthesis and electrochemical analysis in half cell. Ligand synthesis and conceptualisation was done by Gaia Neri, flow cell electrochemistry and XPS analysis done by Verity Piercy and supervision, experimental design and conceptualisation by Alexander J. Cowan.

2.1 Scope of the chapter

As discussed in chapter 1, nickel cyclams (cyclam = 1,4,8,11-tetraazacyclotetradecane) are a successful, affordable branch of CO₂ reduction catalysts that work well in aqueous electrolyte,¹⁻⁴ at a range of electrode materials,^{5,6} including carbon.⁷ Incorporating Ni(cyclam) onto a low cost, non-toxic electrode surface, such as a carbon felt, has since been of great interest as a route to developing practical electrode structures, for example a gas diffusion electrode (GDE) for use in a CO₂/water co-electrolysis device.⁸⁻¹¹ Our group demonstrated the wider potential of Ni(cyclam) in more industrially relevant settings by using deposited Ni(cyclam) in a zero-gap cell with a reverse bias bi-polar membrane (BPM). Bipolar membranes consist of a cation exchange membrane (CEM) and an anion exchange membrane (AEM) with water dissociation occurring in between them. In the reverse-bias configuration the membrane constantly supplies protons to the cathode, combatting the rising pH with as protons are consumed with both CO₂ reduction and hydrogen production. The reverse-bias BPM also pumps hydroxide to the anode for efficient water oxidation.

In this work was it demonstrated that Ni(cyclam) was able to operate at higher current densities and took advantage of the higher selectivity of Ni(cyclam) in acidic environments, where Ni(cyclam) was able to outperform Ag. This is important as many electrochemical CO₂ reduction (eCO₂R) catalysts are only selective at higher pH where proton concentration and hydrogen production is significantly lower, however at pHs >6 there are large losses of CO₂ to the bicarbonate equilibrium, shown below (Eq (7) – (9)). As eCO₂R proceeds, protons are consumed, see Eq (2) - (5), and if these protons are not replaced this causes a significant rise

Chapter 2 Noncovalent immobilisation of a Ni(cyclam) catalyst on carbon electrodes

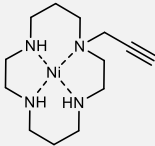
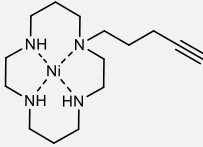
in the pH at the electrode resulting in more CO₂ lost to bicarbonate than can be converted to useful product, detrimentally decreasing the CO₂ conversion efficiency.¹²



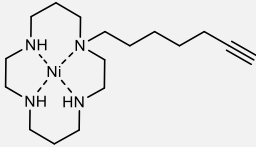
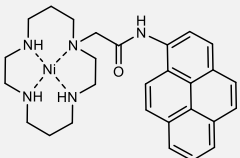
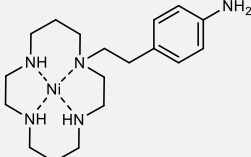
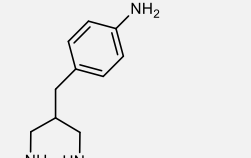
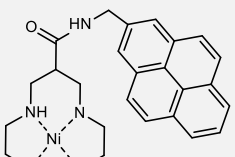
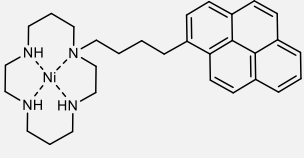
While Siritanaratkul *et al.* demonstrated Ni(cyclam) as a functional catalyst in this setup, two distinct limitations of the study were noted: catalyst poisoning over time and a significantly smaller amount of electroactive catalyst when compared to that deposited.¹³

N-alkylated Ni(cyclam) immobilisation to carbon electrodes has been shown to anchor and improve electroactivity of the deposited catalyst (see **Table I**). Particular success is observed with a pyrene immobilisation done by Pugliese *et al.* where they show FE of 90% towards CO in CH₃CN with 1% water (**4** in **Table 1**).^{14,15} However, in the interest of moving towards more industrially relevant conditions an alternative pyrene functionalised nickel cyclam, Ni²⁺(1-(4-(pyren-1-yl)butyl)-1,4,8,11-tetraazacyclotetradecane, labelled hereafter, Ni(CycPy) is assessed in fully aqueous conditions, immobilised onto a gas diffusion electrode allowing direct delivery of higher concentrations of CO₂ to the catalyst.

Table 1 Alkylated Ni(cyclam) catalysts immobilised onto carbon electrodes for eCO₂R. N or C refers to alkylation from a nitrogen or carbon atom on the cyclam. NA refers to data being unavailable. ^a Approximately converted from original Fc/Fc⁺ reference by adding +0.4 V.

Entry	Catalyst	E (V) (vs Ag/AgCl)	J (mAcm ⁻²)	Electrolyte	WE	FE _{CO} (%)	FE _{H₂} (%)	Ref.
1	Ni(N-propargyl-cyclam) 	-2.0 ^a	NA	0.1 M TBA PF ₆ in MeCN (20% H ₂ O)	GCE	7	87	¹⁴
2	Ni(N-pentynyl-cyclam) 	-2.0 ^a	1.8	0.1 M TBA PF ₆ in MeCN (20% H ₂ O)	GCE	8	89	¹⁴
3	Ni(N-hexynyl-cyclam)	-2.0 ^a	NA	0.1 M TBA PF ₆ in	GCE	7	91	¹⁴

Chapter 2 Noncovalent immobilisation of a Ni(cyclam) catalyst on carbon electrodes

				MeCN (20% H ₂ O)				
4	Ni(<i>N</i> -pyrenyl-amide cyclam) 	-2.3 ^a	>10	0.1 M TBA PF ₆ MeCN (1% H ₂ O)	CNT/ carbon cloth	90	11	¹⁵
5	Ni(<i>N</i> -4-ethylaniline cyclam) 	-1.3	NA	0.2 M NaHCO ₃ (aq)	GCE	12	29	¹⁶
6	Ni(<i>C</i> -4-methylaniline cyclam) 	-1.3	0.7	0.2 M NaHCO ₃ (aq)	GCE	56	11	¹⁶
7	Ni(<i>C</i> -pyrenyl-amide cyclam) 	-1.4	~5.0	0.1 M KHCO ₃ (aq)	CNT/ carbon cloth	90	10	¹⁷
8	Ni(CycPy) 	-1.4	0.3	0.5 M KHCO ₃ (aq)	GCE	0.8	86	This work

While writing this thesis, immobilisation of C-alkylated Ni(cyclam) catalysts has since been achieved (Entry 6 and 7 in **Table I**).^{16,17} The resulting complexes yield much higher activity for CO₂ reduction, even in aqueous electrolyte as C-alkylation prevents the loss of a N-H group, which are proposed to aid in coordinating incoming CO₂ to the metal centre through hydrogen bonding.^{18,19} While these complexes are definitely more active than N-alkylated analogues, alkylating at the carbon backbone of the cyclam is synthetically much more challenging, thus Ni(CycPy) was synthesised via the nitrogen atom.

Ni(CycPy) was initially chosen as a target complex due to previous success of pyrene immobilisation to carbon electrodes in aqueous electrolyte.²⁰⁻²³ Pugliese *et al* also showed that in immobilising a nickel cyclam catalyst this way, the catalyst remains active despite loss of activity through alkylation of the nitrogen atoms in the cyclam ring.^{7,10,15,24} In the beginning of this chapter the synthesis of Ni(CycPy) is described, followed by electrochemical analysis of the synthesised complex in a mixed electrolyte of MeCN with 10% water and in fully aqueous electrolyte. The complex was immobilised on a variety of carbon supports, where its catalytic behaviour on the electrode is analysed via electrochemical methods and XPS both pre- and post-electrolysis. Finally, results are shown of the first nickel cyclam immobilised onto a gas diffusion electrode, tested in both a zero-gap and fully aqueous flow cell where we observe FE of over 60% toward CO.

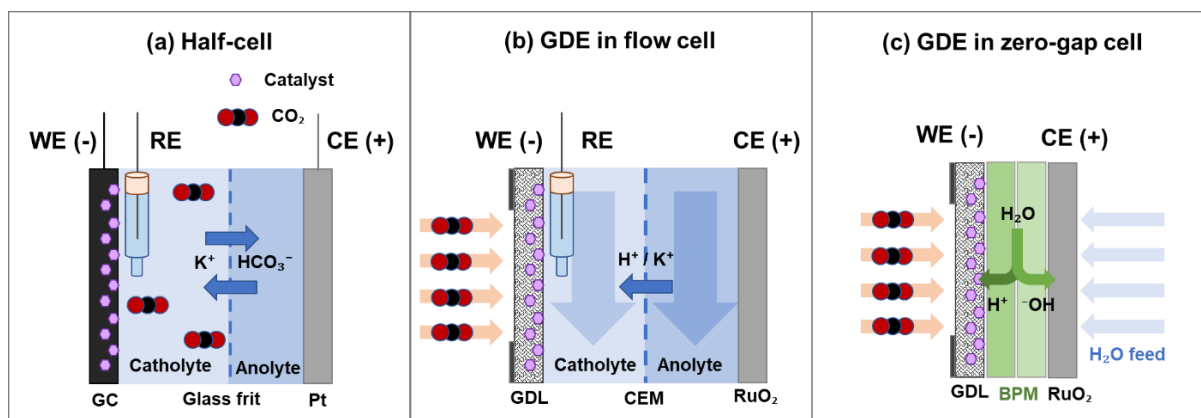


Figure 12 Diagram showing the different types of electrochemical cell used in this chapter

2.2 Synthesis and Characterisation

The synthesis and characterisation of 1-(4-(pyren-1-yl)butyl)-1,4,8,11-tetraazacyclotetradecane (CycPy) is described in more detail in Chapter 6 and shown in **Figure 13**. A commercial pyrenebutanol was oxidised to the aldehyde (**1**, **Figure 13**, yield: 75%)

Chapter 2 Noncovalent immobilisation of a Ni(cyclam) catalyst on carbon electrodes

before undergoing reductive amination with a Boc-protected cyclam, the cyclam-pyrene (**2**, **Figure 13**, yield: 83%) was then deprotected before insertion of the Ni²⁺ centre with addition of NiCl₂ (**4**, **Figure 13**, yield: 54%). The geometry of final complex was investigated with UV/Vis.

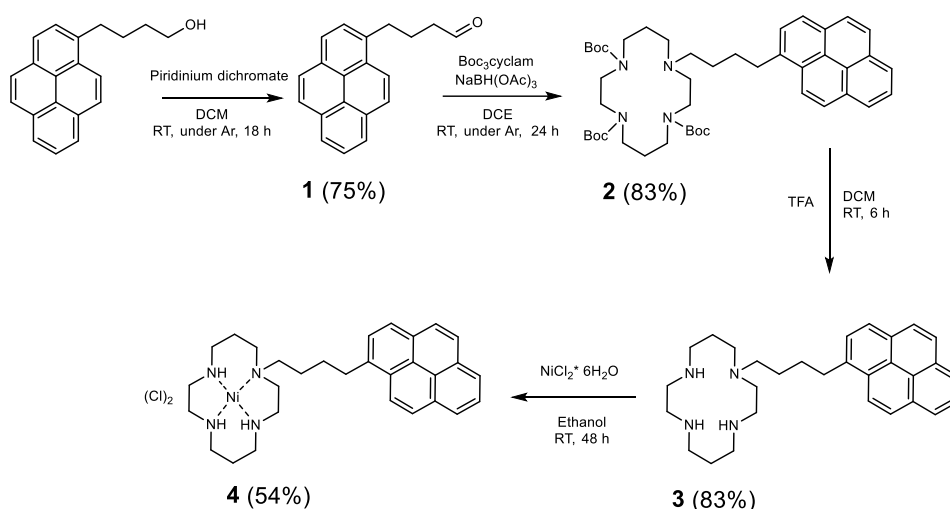


Figure 13 Synthetic pathway to form Ni(CycPy)

Crystal field theory (CFT) can be used to describe the loss of degeneracy of the d orbitals as metal ions coordinate to ligands. As ligands donate electron density to the metal ion, the d electrons oppose this, leading to an increase in their energy. However, as d orbitals are not spherically symmetrical, the extent of their interaction with the ligands is different, creating a split in the energy degeneracy of the d orbitals, called crystal field splitting (see **Figure 14**). Assuming the ligands are point charges, the splitting of the d orbitals is different depending on the number and positions of the ligands in the complex.

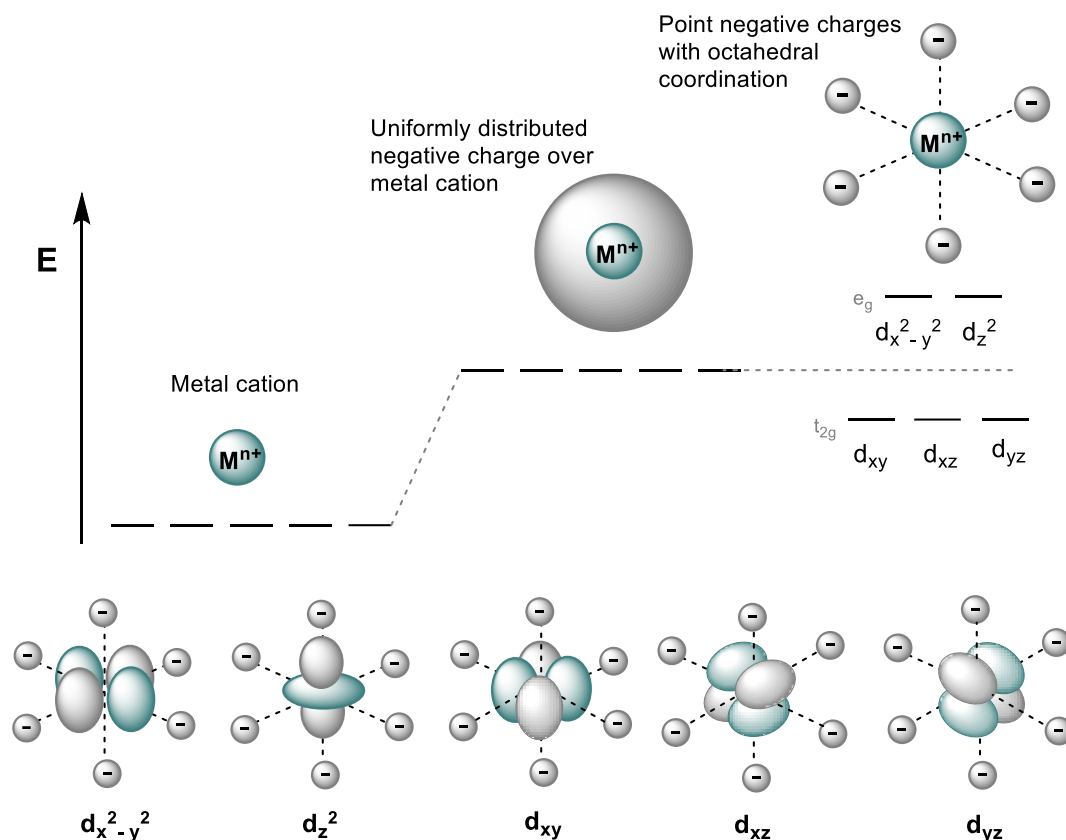


Figure 14 Schematic of the change in the energy of *d*-orbitals of metal ion with coordination of negative ligands first as a uniformed sphere and then as individual point charges with octahedral coordination which leads to a loss of degeneracy (top). Spatial arrangement of octahedral ligands with respect to the *d*-orbitals (bottom).

As Ni^{2+} complexes have eight electrons in its *d* orbitals, weak, *d-d* transitions can be observed with ultraviolet/visible (UV/Vis) spectroscopy which can give insight into the geometry of the complex. Ni macrocycles are able to interconvert geometries based on the coordination strength of the solvent (see **Figure 15**).^{25,26} In strongly coordinating solvents, two solvent molecules coordinate at the axial positions of the distorted octahedron and the nickel is in a high spin state; here the d_z^2 and $d_{x^2-y^2}$ orbitals are of a similar energy and thus are singly occupied making the complex paramagnetic. In weakly coordinating solvents the axial positions remain unoccupied giving the complex square planar geometry; this simultaneously stabilises the d_z^2 orbital while destabilising the $d_{x^2-y^2}$ causing the metal centre to assume the low spin state.

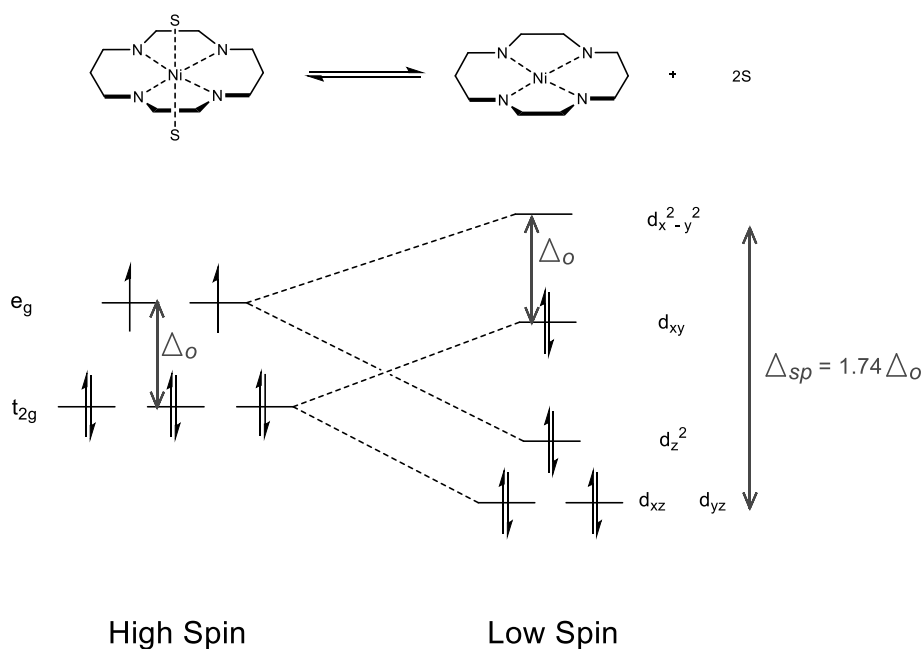


Figure 15 Spin interconversion in Ni cyclam (top) and d orbital splitting for the octahedral and square planar geometries (bottom)

Figure 16 shows the UV/Vis spectra of 1 mM Ni(CycPy), compared to CycPy and NiCl₂, here Ni(CycPy) shows absorbance peaks at 463 nm, characteristic of Ni cyclam in square planar configuration, and at shorter wavelengths (<390 nm) from the attached pyrene. The spectra show no remnant of NiCl₂ in the final complex. Spectra of 1 mM Ni(CycPy) was taken in a variety of solvents where the peak at 463 nm is consistently observed in water, methanol and a solvent mix of CH₃CN with 10% H₂O, suggesting the complex exists primarily in the low spin, square planar form with minimal contribution from the distorted octahedral form with either solvent or chloride in the axial positions (**Figure 16**). In dichloromethane (DCM) UV/Vis spectroscopy shows Ni(CycPy) preferentially forms the 6-coordinate octahedral species, where we see an absorbance at 550 nm.¹¹ This is similar to the behaviour of the parent Ni(cyclam) which exists in a mix of octahedral to square planar geometries in water at 25°C at a ratio of 29% and 71% respectively.²⁷

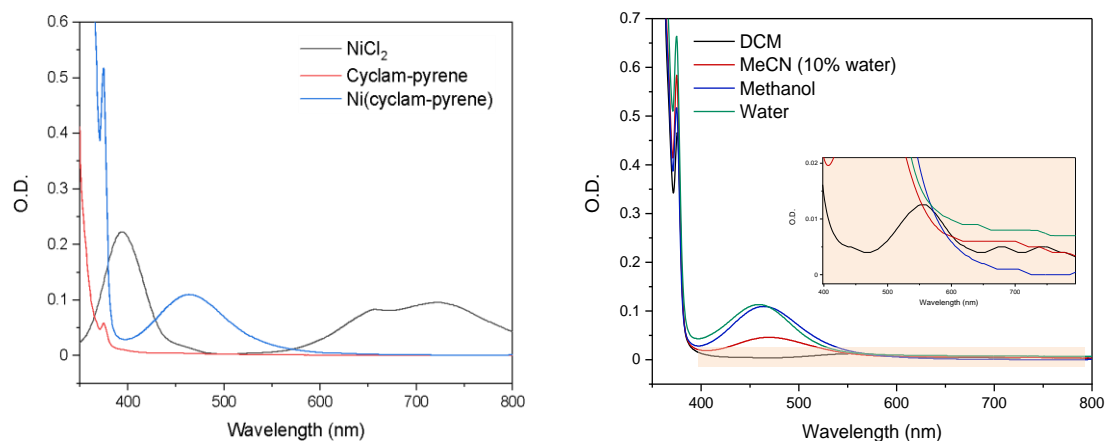


Figure 16 UV/Vis spectrum of 1mM CycPy, Ni(CycPy) and NiCl₂ in water (left) and 1 mM Ni(CycPy) in various solvents. Inset shows magnification of Ni(CycPy) in DCM (right). Pathlength 10 mm.

2.3 Electrochemistry in solution

Electrochemical studies of Ni(CycPy) in solution were carried out to examine the effect of addition of the pyrene group through alkylating one of the N atoms in the cyclam ring. Cyclic voltammetry (CV) was recorded in 1 mM solutions of catalyst in CH₃CN with 10% water using a glassy carbon electrode as the working electrode, **Figure 17a**. The complex was not fully soluble in CH₃CN in the absence of water. We also present the electrochemistry of the unmodified parent complex, under the same conditions, Ni(cyclam), **Figure 17b**. The CVs under nitrogen show a reversible redox couple at -1.31 V_{Ag/AgCl} which can be assigned to the Ni^{III/I} reduction through comparison to the CV of Ni(cyclam) (-1.44 V_{Ag/AgCl}) and to literature.^{7,10,11} Using CVs at variable scan rates under N₂ (**Figure 18**) and the Randles-Ševčík equation (Eq 10) where F is Faraday's constant, R is the universal gas constant, T is temperature, n is the number of electrons, D_O is the diffusion coefficient and C_O is the molar concentration of the redox active species. Here, the peak current density (j_p) can be plotted against the square-root of scan rate ($v^{1/2}$) shown in **Figure 19**. The linear relationship shows that the Ni^{III/I} couple of Ni(CycPy) was dominated by freely diffusing species in solution and not by any adsorbed on the electrode surface.

$$j_p = 0.4463 \left(\frac{F^3}{RT} \right)^{\frac{1}{2}} n^{\frac{3}{2}} D_O^{\frac{1}{2}} C_O^* v^{\frac{1}{2}} \quad (10)$$

Chapter 2 Noncovalent immobilisation of a Ni(cyclam) catalyst on carbon electrodes

The Ni^{II/I} couple of Ni(CycPy) was *ca.* 150 mV more positive than the parent complex as a result of alkylating one of the N atoms in the cyclam ring, in-line with past studies which show similar positive shifts in the couple following substitution.^{7,28} This potential shift is a result of the ratio of stability constants of the Ni^{II} and Ni^I species decreasing with N-alkylation, according to:

$$E_{\frac{1}{2} \frac{\text{NiCycPy}^{\text{II}}}{\text{NiCycPy}^{\text{I}}}} = E_{\frac{1}{2} \frac{\text{NiCyc}^{\text{II}}}{\text{NiCyc}^{\text{I}}}} - \left(\frac{RT}{nF}\right) \ln \left(\frac{\beta_{\text{NiCycPy}^{\text{II}}}}{\beta_{\text{NiCycPy}^{\text{I}}}}\right) \quad (11)$$

Where $E_{\frac{1}{2} \frac{\text{NiCycPy}^{\text{II}}}{\text{NiCycPy}^{\text{I}}}}$ and $E_{\frac{1}{2} \frac{\text{NiCyc}^{\text{II}}}{\text{NiCyc}^{\text{I}}}}$ are the formal Ni^{II/I} redox couples of Ni(CycPy) and Ni(cyclam). $\beta_{\text{NiCycPy}^{\text{II}}}$ and $\beta_{\text{NiCycPy}^{\text{I}}}$ are the stability constants of the oxidised Ni^{II}(CycPy) and reduced Ni^I(CycPy) respectively. Fujita *et al.* proposed by modifying Ni(cyclam) different conformers are preferred which can increase or decrease their stability.¹⁸ Bujno *et al.*, found through subsequent N-alkylation's of the cyclam ring, both the stability of Ni^I and Ni^{II} is compromised.²⁸ The decrease in stability of Ni^I has been linked to lower catalytic activity, caused by increased deactivation through both CO poisoning and over reduction to Ni(0) which can deposit on the electrode and increase HER, discussed in more detail in Chapter 3.

Interestingly, both the parent Ni(cyclam) and Ni(CycPy) show onset of HER at slower scan rates under N₂ (**Figure 18a** & **Figure 20a**). This suggests the generation of a moiety following the reduction of the Ni^{II/I} which is able to reduce protons, only observable at slow scan rates.

Under CO₂, the Ni^{II/I} reduction becomes irreversible and an increase in current density was measured demonstrating that CO₂ catalysis was occurring. Comparison of the peak current density under catalytic conditions (j_c), and in the absence of the substrate (where redox couple is reversible) (j_p), provides a comparative measure of catalytic activity.^{29,30} The j_c / j_p was calculated to be 1.7 for Ni(CycPy) and 3.1 for Ni(cyclam). Although the parent complex shows a larger catalytic current enhancement under CO₂, the pyrene-modified cyclam has an electrocatalytic onset *ca.* 50 mV positive. Overall the CV analysis showed that in CH₃CN/H₂O solution the electrochemical behaviour of the Ni(CycPy) complex was similar to that of the parent Ni(cyclam) complex with a slight decrease in catalytic activity, anticipated from past studies which show lower stability and lower CO₂ binding constant upon modification of the N-H groups of cyclam.^{10,24,31}

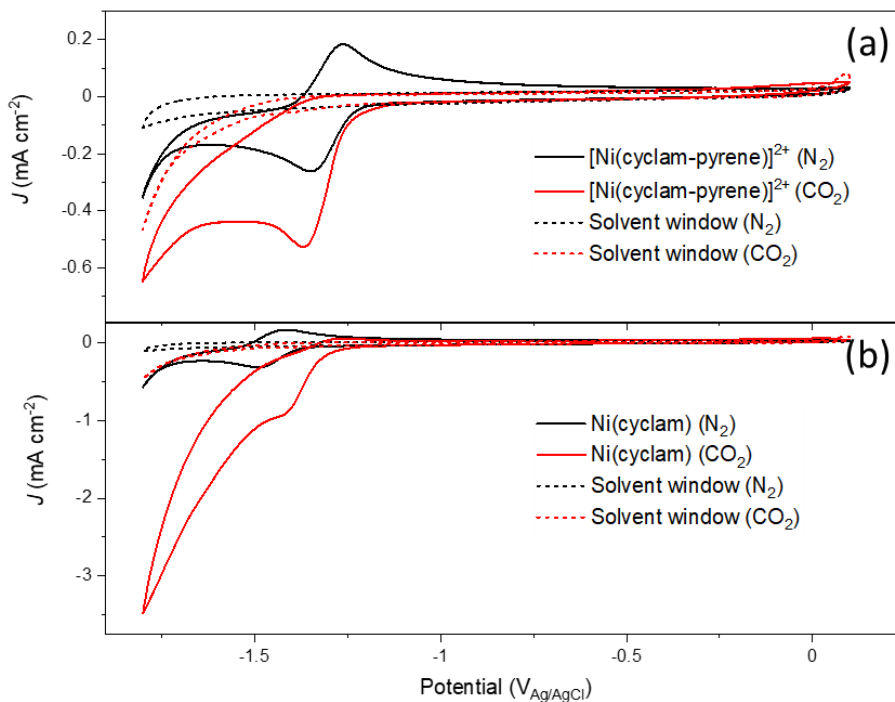


Figure 17 CVs of 1mM Ni(CycPy) (top) and Ni(cyclam) (bottom) in 0.1M TBA PF₆ CH₃CN with 10% water using a GCE; 100mV/s under N₂ (black) and CO₂ (red). The solvent window recorded under the same conditions in the absence of the catalysts is shown with dashed lines.

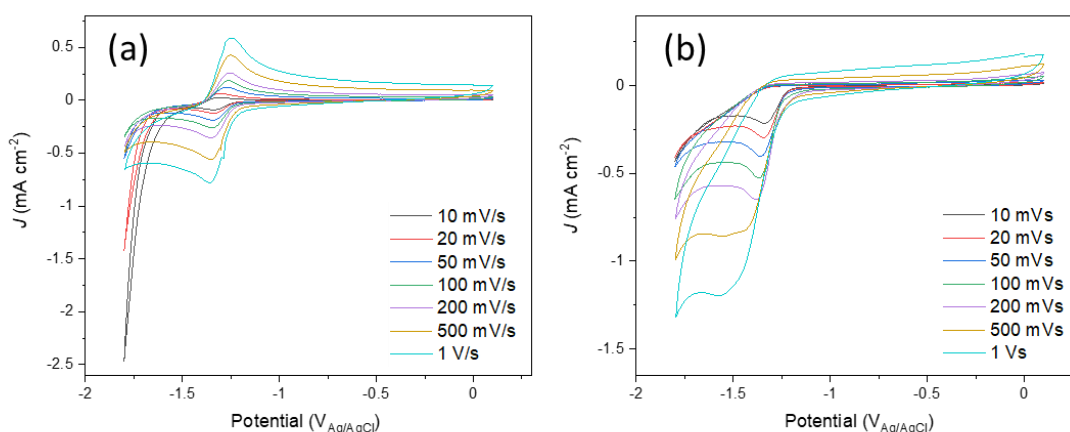


Figure 18 CVs of 1mM Ni(CycPy) in 0.1M TBA PF₆ CH₃CN with 10% water using a GCE under N₂ (a) and CO₂ (b).

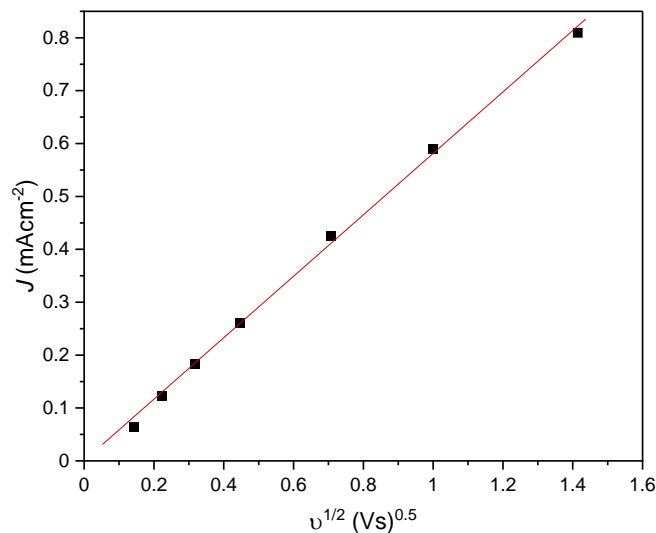


Figure 19 Scan rate dependence of the peak current density of the Ni^{II/I} reduction of 1mM Ni(CycPy) in 0.1M TBA PF₆ CH₃CN with 10% water using a GCE under N₂.

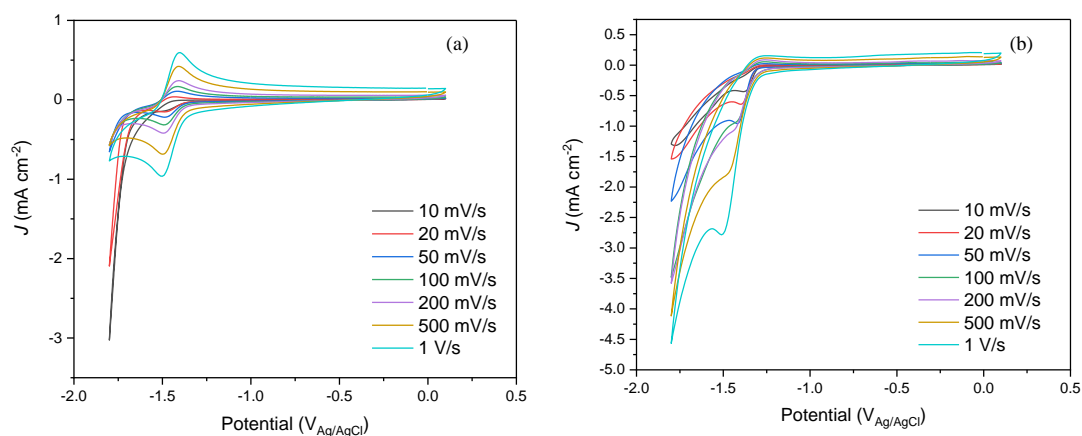


Figure 20 CVs of 1mM Ni(cyclam) in 0.1M TBA PF₆ CH₃CN with 10% water using a GCE under N₂ (a) and CO₂ (b).

CVs in aqueous electrolyte (0.5 M KHCO₃) are shown in Fig. 6 for Ni(CycPy) at a GCE. KHCO₃ was chosen as an electrolyte as it is commonly used in electrolysis with immobilised CO₂ reduction catalysts.^{22,23} In aqueous electrolyte, under N₂, the Ni^{II/I} reduction becomes obscured by hydrogen production of the GCE in the aqueous electrolyte, **Figure 21**. While the

Chapter 2 Noncovalent immobilisation of a Ni(cyclam) catalyst on carbon electrodes

proximity of the solvent window to the $\text{Ni}^{\text{II/I}}$ reduction peak makes it hard to distinguish if electrocatalytic CO_2 reduction occurs from CV analysis alone, the $\text{Ni}^{\text{II/I}}$ reduction peak shifts from $-1.41 \text{ V}_{\text{Ag}/\text{AgCl}}$ (N_2) to -1.36 V (CO_2) which may suggest preferential CO_2 binding, stabilising the formation of reduced (Ni^{I}) catalyst in aqueous solvents.^{19,29}

Experiments in aqueous solvent under both N_2 and CO_2 were restricted to $-1.6 \text{ V}_{\text{Ag}/\text{AgCl}}$. At potentials negative of this the electrochemical features of the Ni(CycPy) catalyst became diminished and could only be recovered following polishing of the glassy carbon electrode, indicating electrode fouling, possibly caused by nickel-derived species due to degradation of the Ni(CycPy).^{30,32} Interestingly in the mixed solvent ($\text{CH}_3\text{CN}/\text{Water}$ (10%)) CV's were recorded to $-1.8 \text{ V}_{\text{Ag}/\text{AgCl}}$ with no sign of catalyst degradation.

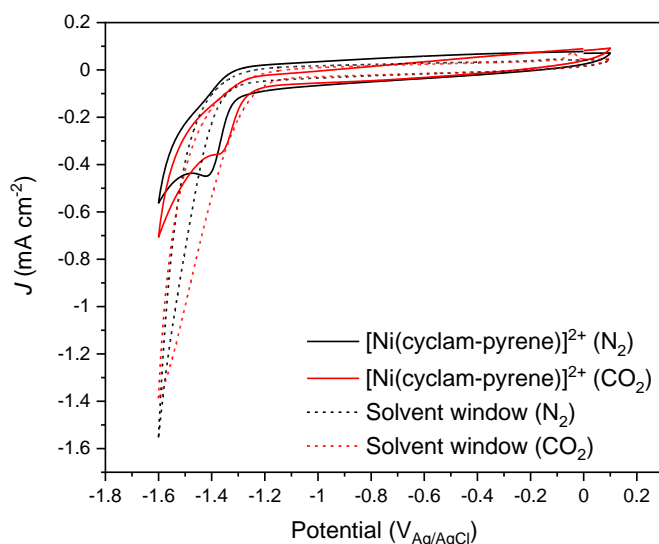


Figure 21 CVs of 1 mM NiCycPy) in 0.5 M KHCO_3 at 100 mV/s under N_2 (black) and CO_2 (red) using a GCE. The solvent window recorded under the same conditions in the absence of the catalysts is shown with dashed lines.

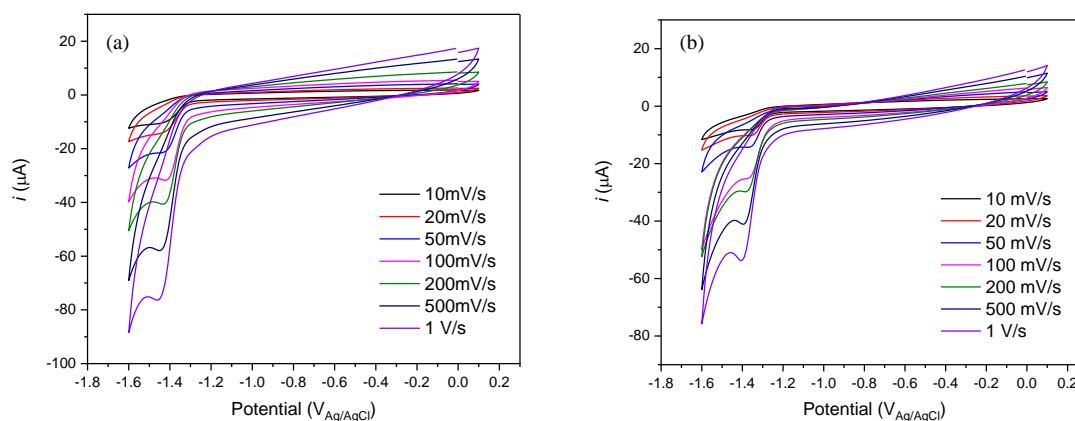
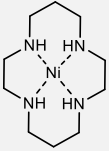
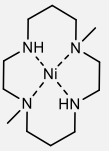
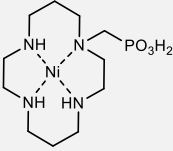
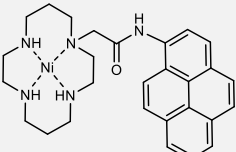
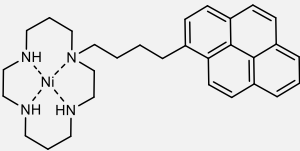


Figure 22 CVs of 1mM Ni(CycPy) in 0.5M KHCO₃ under N₂ (a) and CO₂ (b).

Electrocatalytic CO₂ reduction with the complex was confirmed with bulk electrolysis experiments using Ni(CycPy) (0.2 mM) in 0.5 M KHCO₃ for 2 hours at -1.4 V_{Ag/AgCl}. Electrolysis gave an average current density of 0.17 mA cm⁻² and CO and H₂ as the sole reaction products formed in a 1:1 ratio (CO:H₂, total Faradaic Efficiency 92%). These results are compared to both the parent Ni(cyclam) and other N-alkylated Ni(cyclam in **Table 2**. Here selectivity is decreased compared to the 4.5:1 reported for 1 mM unmodified Ni(cyclam) in 0.5 M KCl at a GCE²⁹ but is comparable or higher than other N-alkylated analogous in aqueous electrolyte, indicating that the addition of the pyrene group has not turned off CO₂ catalysis in water.

Table 2 *N*-alkylated and unmodified Ni(cyclam) catalysts used homogenously for *eCO*₂*R*

Catalyst	E (V) (vs ref)	<i>J</i> (mAcm ⁻²)	Electrolyte	WE	FE _{CO} (%)	FE _{H2} (%)	Ref.
1mM Ni(cyclam) 	-1.60 (vs NHE)	2.8	0.1 M KCl (aq)	GCE	90	20	29
	-1.61 (vs NHE)	4.5	0.8 M TBA PF ₆ in MeCN (20% H ₂ O)	GCE	60	10	29
1mM Ni(DMC) 	-1.63 (vs NHE)	3.8	0.8 M TBA PF ₆ in MeCN (20% H ₂ O)	GCE	20	80	29
1mM Ni(cycP) 	-1.20 (vs NHE)	~0.9	0.1 M NaClO ₄ (aq) (pH 5)	Au /Hg	22	22	33
1mM Ni(pyrenyl- amide cyclam) 	-2.54 (vs Fc ⁺ /Fc ⁰)	0.3	0.1 M TBA PF ₆ in DMF (2 M H ₂ O)	GCE	96	0	15
0.2mM Ni(CycPy) 	-1.4 (vs Ag/AgCl)	0.17	0.5 M KHCO ₃ (aq)	GCE	46	46	This work

2.4 Ni(CycPy) immobilisation onto carbon electrodes

2.4.1 Immobilisation on glassy carbon electrodes (GCE) and carbon nanotubes (CNT)

To test if the Ni(CycPy) catalyst can form a non-covalent interaction with carbon supports electrodes were prepared by soaking either carbon nanotubes (CNT) or glassy carbon plates in solutions of 1 mM Ni(CycPy) in methanol. The CNT or GCE plates were then washed in triplicate with methanol followed by distilled water. For the CNT electrode, a solution of 1 mg CNTs and 50 μ L 5 wt% Nafion in 1 mL MeCN was made up before 10 μ L was drop casted onto a clean GCE. The resulting Ni(CycPy) modified GCE's were analysed by X-ray photoelectron spectroscopy (XPS).

XPS of the Ni(CycPy) powder shows a Ni 2p_{3/2} signal at 854.9 eV with broad satellite peaks (857-861 eV) due to the Ni²⁺, with the binding energy being in very good agreement with the previous reported spectrum of Ni(cyclam) **Figure 23**.³⁴ The XPS spectrum of the as prepared GCE/[Ni(CycPy)] electrode shows a Ni 2p_{3/2} signal at 856.2 eV. A previously reported Ni cyclam modified with pyrene on carbon nanotubes had a Ni²⁺ 2p_{3/2} binding energy of 856.0 eV.¹⁵ The shift to higher binding energies of the Ni 2p_{3/2} peaks upon immobilisation suggest an electron density shift away from the Ni centre to the carbon support upon immobilisation. Whilst the XPS data of the GCE/[Ni(CycPy)] electrode provides good evidence of a redistribution of electron density from the Ni centre to the carbon electrode/pyrene group the formal oxidation state of the Ni centre of GCE/[Ni(CycPy)] during the XPS measurement is not assigned. However, electrochemical data recorded once the electrode is in solution suggests that the first reduction upon initiating a negative sweep from close to the open circuit potential is the Ni^{II/I} reduction.

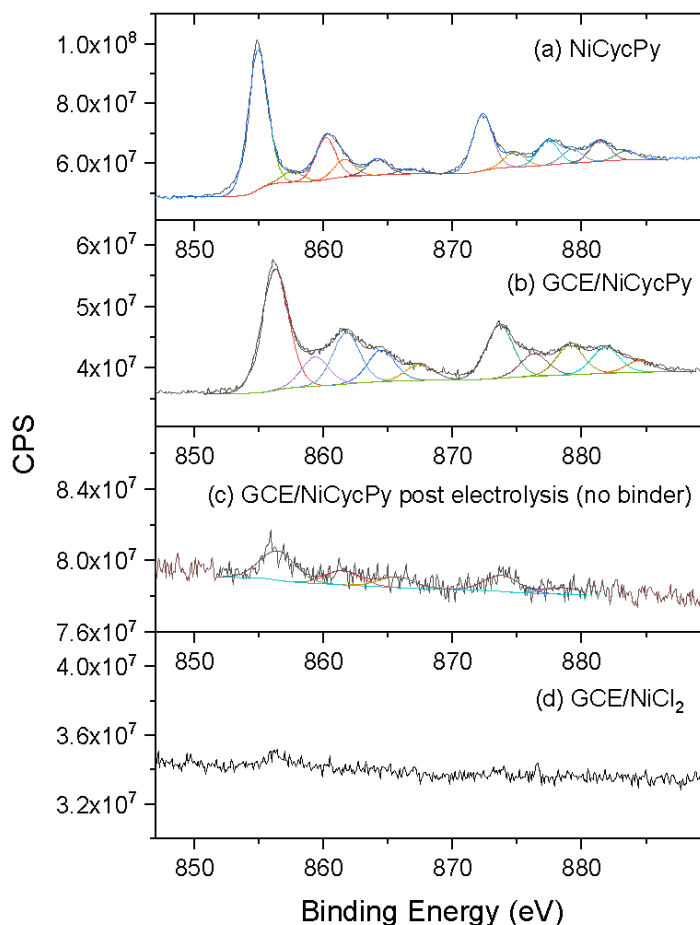


Figure 23 Experimental and simulated XPS spectra of Ni $2p_{3/2}$ and $2p_{1/2}$ signal of powder sample of Ni(CycPy) (a), Ni(CycPy) immobilised to GCE before (b) and after 1 h electrolysis at $-1.4V_{Ag/AgCl}$ (here “no binder” refers to the immobilisation method using no additional polymer) (c) GCE after soaking in 1 mM NiCl₂

The presence of the cyclam ligand was also confirmed through the observation of the N 1s signal at 400.3 eV (**Figure 24**) confirming the successful immobilisation of the Ni cyclam pyrene complex on the GCE. Control XPS experiments where the Ni(CycPy) was replaced with NiCl₂ in the soaking solution showed that following washing no significant concentration of Ni was retained on the electrode surface, **Figure 23**.

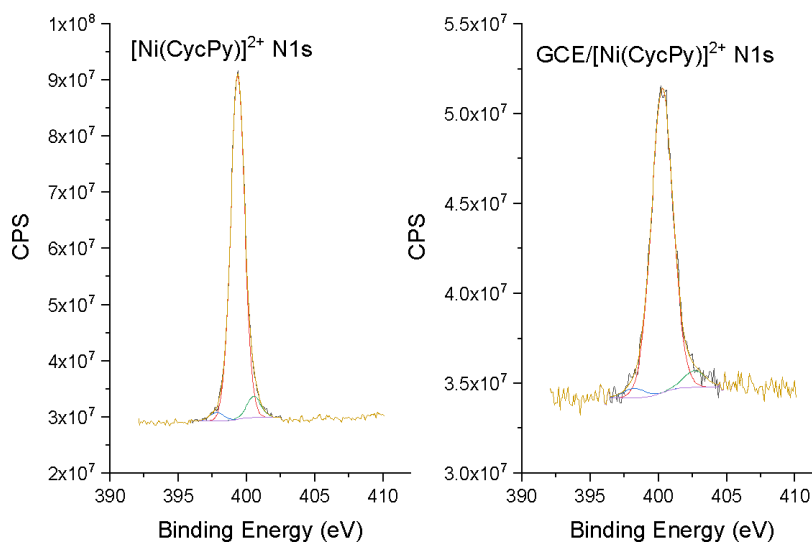


Figure 24 Experimental and simulated XPS spectra of N1s signal of powder sample of Ni(CycPy) (left) and Ni(CycPy) after immobilisation onto GCE (right)

In **Figure 23c** the XPS spectrum of a GCE post electrolysis in KHCO₃ electrolyte (-1.4 V_{Ag/AgCl} for 1 h) shows a clear loss of Ni from the electrode surface. This suggests the pyrene immobilisation alone is not enough to stop the water soluble complex from dissolving off the electrode surface in aqueous electrolyte, proving detrimental to catalysis of the GCE/Ni(CycPy) discussed later in this section. Despite an obvious drop in the intensity, no significant shift in the binding energies are observed when compared to the pre-electrolysis GCE/Ni(CycPy) electrode.

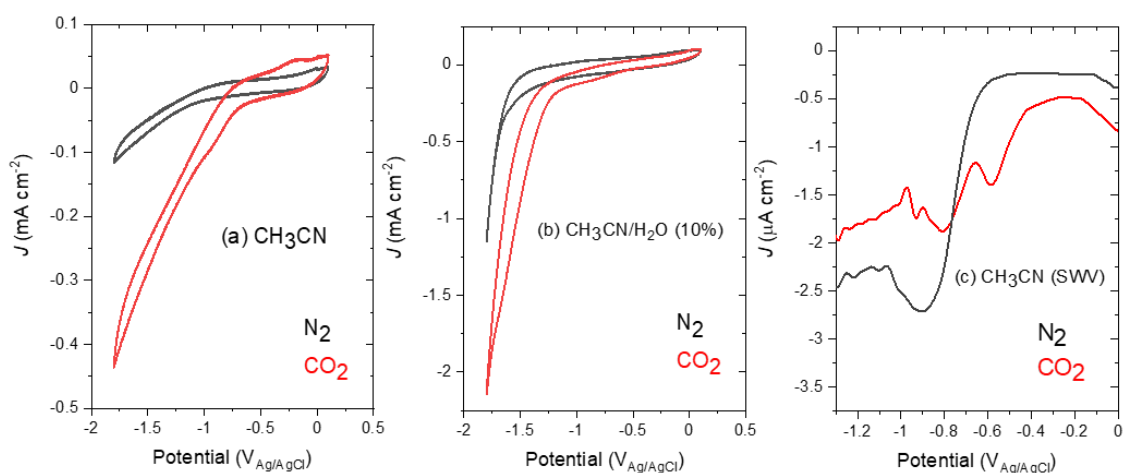


Figure 25(a) CVs of GCE/[Ni(CycPy)] electrode in 0.1M TBA PF₆ in CH₃CN and (b) 0.1M TBA PF₆ in CH₃CN/H₂O (10%) at 100 mV/s under N₂ (black) and CO₂ (red). (c) SWV of GCE/[Ni(CycPy)] electrode in 0.1M TBA PF₆ in CH₃CN at 5Hz under N₂ (black) and CO₂ (red).

CVs of the GCE/[Ni(CycPy)] electrodes under N₂ and CO₂ (**Figure 25a**) in CH₃CN show clear differences to an unmodified GCE (see solvent window in **Figure 17a**) also confirming the presence of the catalyst. Under N₂ we find that the current density becomes increasingly negative at < -0.95 V. Square wave voltammetry (SWV, **Figure 25c**) shows the presence of a reduction at -0.90 V which was proposed to be the Ni^{III} reduction of immobilised Ni(CycPy) due its sensitivity to CO₂.

The Ni^{III} reduction was shifted *ca.* 450 mV positive upon immobilisation under N₂ demonstrating that the Ni(CycPy) complex interacts strongly with the carbon surface. This was supported by the XPS data which suggested a decrease in electron density at the Ni centre upon immobilisation. A similar shift in the reduction potential was observed by Pugliese and co-workers upon immobilisation of a modified Ni cyclam complex on a carbon nanotube electrode.¹⁵ The very large shift in reduction potential upon immobilisation therefore appears to be a common feature of this class of catalysts that requires further investigation. On mercury electrodes the Ni^{III} couple was also shifted positive due to the reduced Ni^I state being stabilised through interaction with the metal surface and a beneficial effect on the onset of CO₂ catalysis occurs.³⁵ Indeed here we find under CO₂ that the current density increases slightly at potentials negative of -0.8 V, with a larger increase in current density with applied potential negative of -1.1V. The increased current density at -0.8 V suggests that immobilisation offers a way to achieve a significant decrease in overpotential for catalysis. Although no proton source has been deliberately added in the experiment shown in **Figure 25a**, residual water particularly

Chapter 2 Noncovalent immobilisation of a Ni(cyclam) catalyst on carbon electrodes

after the CO₂ purge will be present. Addition of 10% water leads to a large increase in current density for CVs recorded under CO₂ using the GCE/Ni(CycPy) electrode at potentials negative of -1.1 V when compared to the same electrode under CO₂ in CH₃CN alone, **Figure 25b**. The oxidation at -0.2 V under CO₂ (**Figure 25a**) was similar to that seen for Ni(cyclam) at carbon electrodes under similar conditions (see Chapter 3). This feature has been assigned to the oxidation of a Ni⁰-carbonyl complex formed by reduction of [Ni(Cyc)(CO)]⁺.³² CO was present in the experiments as it is formed through CO₂ reduction. SWV shows reductions at -0.58 V and at -0.81 V under CO₂. The reduction at -0.81 V was proposed to be due to the Ni^{III/I} reduction of Ni(CycPy) which is accompanied by CO₂ binding, whilst the peak at -0.58 V was proposed to be due to the formation of a CO bound Ni^I complex.³² The large binding constant of Ni^I cyclams towards CO (for [Ni(Cyc)]⁺ in CH₃CN, $K_{CO} = 2.8 \pm 0.6 \times 10^5 \text{ M}^{-1}$, $K_{CO_2} = 4 \pm 2 \text{ M}^{-1}$)^{24,36} means that even trace amounts can lead to large shifts in the Ni^{III/I} reduction potential.

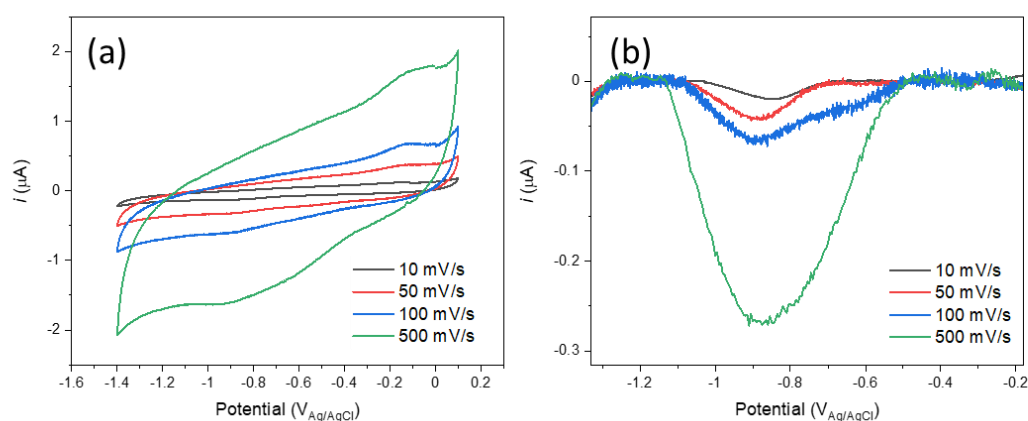


Figure 26(a) Variable scan rate CVs of GCE/[Ni(CycPy)] in 0.1M TBA PF₆ CH₃CN under N₂.
(b) inset of the Ni^{III/I} reduction peak at -0.90 V after subtracting the capacitive current

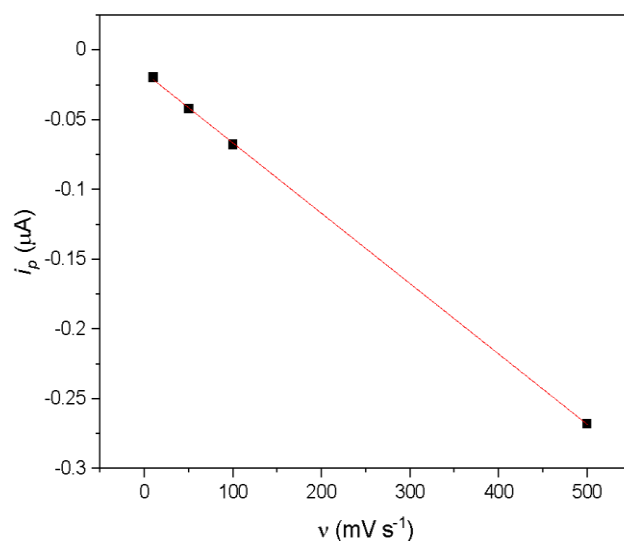


Figure 27 Peak current at -0.9 V from CV vs scan rate of GCE/Ni(CycPy) in 0.1M TBA PF₆ CH₃CN under N₂.

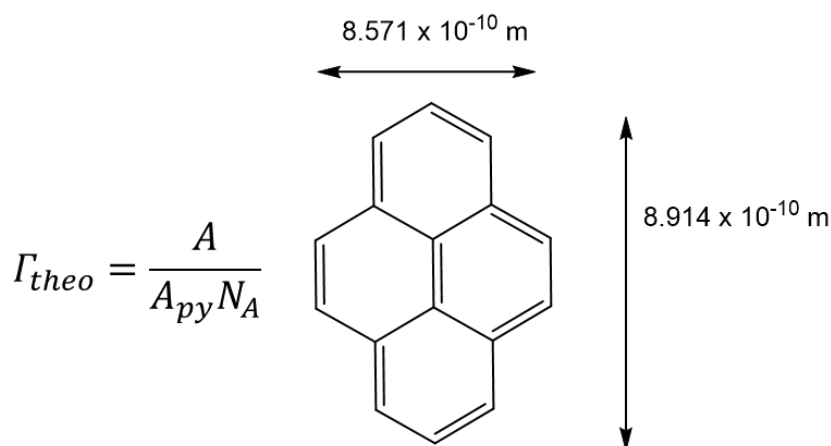


Figure 28 Calculation used to estimate a theoretical surface coverage for a monolayer of [Ni(CycPy)] (Γ_{theo}). Where A is area of the electrode, A_{py} is the area of the pyrene foot print (estimated as shown) and N_A is Avogadro's constant. We assume that the pyrene group lies parallel to the electrode surface and that the closest packing structure can be calculated by approximating the pyrene foot-print to a rectangle. This estimation does not consider the space required by the C4 linker or the cyclam complex itself. As electrochemical and XPS measurements show that the Ni centre of the cyclam complex is interacting strongly with the carbon surface we know that our estimated catalyst foot-print is an under estimation, in-line with the measured coverage being ~0.5 that of the estimation.

Chapter 2 Noncovalent immobilisation of a Ni(cyclam) catalyst on carbon electrodes

From the electrochemical data (**Figure 26** and **Figure 27**) we measure a surface coverage of $1.1 \times 10^{-10} \text{ mol cm}^{-2}$ for Ni(CycPy) on the glassy carbon electrode using equation (12).

$$i_p = \frac{n^2 F^2 \nu A \Gamma}{4RT} \quad (12)$$

Where i_p is the peak current in A, n is number of electrons, F is the faraday constant, ν is the scan rate in V/s, A is the electrode area in cm^2 , Γ is surface coverage in mol cm^{-2} , R is the gas constant and T is temperature in K. This is similar to the surface coverage achieved by Kubiak and co-workers using an electrografting approach for cyclam complexes, where values of 1.3×10^{-10} to $2.3 \times 10^{-10} \text{ mol cm}^{-2}$ were measured, which was calculated to be equivalent to monolayer coverages.¹⁴ Assuming that the pyrene group is laid flat on the electrode surface, and that no other part of the complex is in-contact with the electrode surface, we estimate the theoretical maximum monolayer coverage to be $2.8 \times 10^{-10} \text{ mol cm}^{-2}$, **Figure 28**. This is an estimated maximum surface coverage as in reality the presence of the alkyl chain and cyclam group will increase the effective footprint of the catalyst on the surface. The measured value of $1.1 \times 10^{-10} \text{ mol cm}^{-2}$ for Ni(CycPy) is on the order expected based on both this calculation and past experimental reports. Variable scan rate studies confirm that the reduction was due to a surface confined process, confirming its assignment to the Ni(CycPy) complex, **Figure 27**.

In 2022, a publication by Kaminsky *et al.*, showed an interesting solvent dependence of electrochemical behaviour of an immobilised CoP on carbon electrode.³⁷ In MeCN, where the complex is soluble, the discrete electronic structure is intact thus electron transfer from the electrode to CoP is observed. However, when solvent is switched to where the complex is insoluble, it can fully adsorb, creating direct contact between the metal centre and the electrode leading to a loss in defined redox features in a CV, making it difficult to quantify them electrochemically, **Figure 29**. While a redox feature is visible, attributed to the $\text{Ni}^{2+/+}$ reduction, it's important to acknowledge that this may be an underestimate of the electrochemically active coverage, especially as this was done in MeCN where the complex is not soluble.

Chapter 2 Noncovalent immobilisation of a Ni(cyclam) catalyst on carbon electrodes

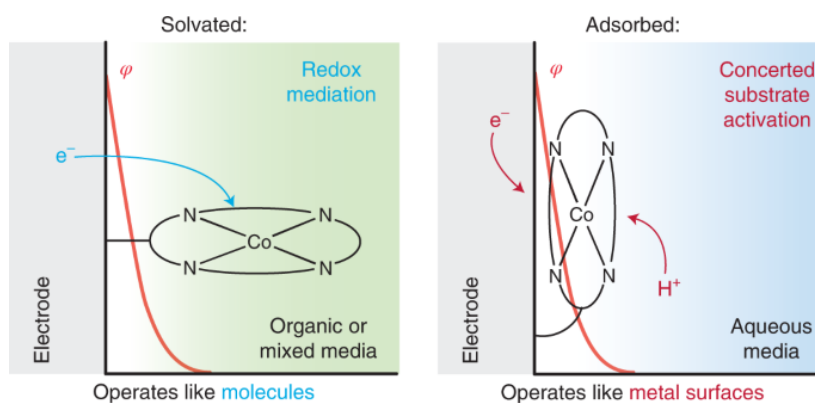


Figure 29 Cartoon model for the electron transfer behaviour of immobilised CoP in MeCN (left) and water (right). From Kaminsky *et al.*³⁷

As Ni(CycPy) appears to retain its activity towards CO_2 upon immobilisation to GCEs, the modified electrodes were next assessed in aqueous electrolyte. In 0.5 M $KHCO_3$ the CVs of the immobilised complex shows current increase under CO_2 at potentials negative of -1.1 V when compared to N_2 (**Figure 30**) however no clear $Ni^{II/I}$ reduction features could be observed. Two attempts to carry out bulk electrolysis for 2h at -1.25 $V_{Ag/AgCl}$ and -1.40 $V_{Ag/AgCl}$ using the immobilised catalyst on a GCE both gave H_2 as the dominant (>76% Faradaic efficiency) product with Faradaic efficiencies of *ca.* 0.6% and 0.8% for CO respectively, with no other products detected by IC. XPS post electrolysis demonstrates that the majority of the Ni(CycPy) complex was lost from the electrode surface during bulk electrolysis, Fig. 9. These results show that the non-covalent interaction between the pyrene group and the carbon surface is insufficient to prevent desorption of the majority of the catalyst over prolonged periods at potentials negative of OCP in solvents in which the complex readily dissolves.

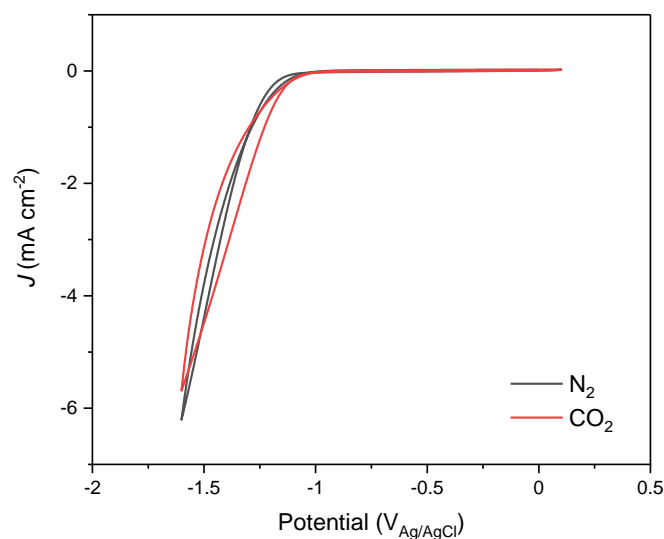


Figure 30 CVs GCE/Ni(CycPy) in 0.5 M KHCO_3 under N_2 and CO_2 .

Ni(CycPy) was also immobilised to carbon nanotubes (CNTs) before drop casting them onto a GCE to see if the immobilisation occurs on different carbon substrates and if we could improve the loading. Here the Ni(CycPy) was loaded onto the CNTs in the same way by soaking them in a solution of 1 mM Ni(CycPy) in methanol for 24 h. CVs of this electrode were ran in both aqueous and non-aqueous solvents and the latter is shown in **Figure 31**.

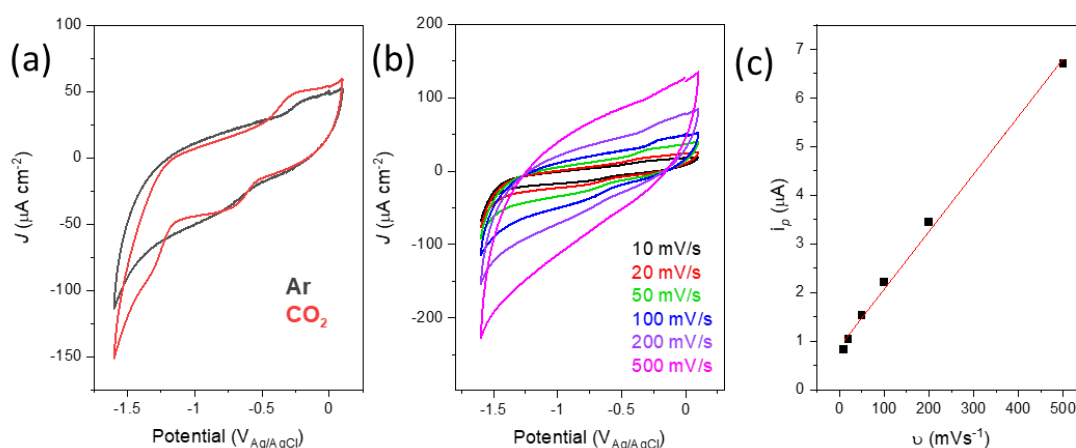


Figure 31 CVs of CNT/GCE/Ni(CycPy) in 0.1 M TBA PF_6 in MeCN (a) Comparison under Ar and CO_2 at 100 mV/s (b) Scan rate comparison under Ar (c) Peak current vs scan rate from reduction at $-0.9 \text{ V}_{\text{Ag}/\text{AgCl}}$

Chapter 2 Noncovalent immobilisation of a Ni(cyclam) catalyst on carbon electrodes

We do see a similar small reduction at $-0.9 \text{ V}_{\text{Ag}/\text{AgCl}}$ on the Ni(CycPy) modified CNT electrode which becomes more defined and is followed by an increase in current under CO_2 as is observed on the glassy carbon. From the scan rate dependence and Eq(12) we were able to calculate the electroactive coverage to be $1.7 \times 10^{-10} \text{ mol cm}^{-2}$, showing no significant increase over the glassy carbon substrate alone. The CNTs also complicated stability runs as they would dislodge from the electrode during experiments, while this could have been limited through optimisation of the drop casting ink, we instead decided to move to a gas diffusion layer substrate with the aim of using it as a gas diffusion electrode.

2.4.2 Immobilisation onto a gas diffusion electrode (GDE)

2.4.2.1 Flow-cell

Although the pyrene-carbon electrode interaction was insufficient alone to prevent desorption, the electrochemical data indicates that the immobilisation offers an advantage through the modification of the $\text{Ni}^{\text{II/I}}$ reduction potential. Although weak, the XPS of the post electrolysis sample also showed that the remaining Ni was in a similar form to the sample pre-electrolysis. Therefore Ni(CycPy) was also tested on a GDE support in a gas flow through structure. In a GDE structure the wetting of the catalyst layer is limited by the additional polytetrafluoroethylene (PTFE) added to the catalyst ink used when preparing the electrode which was hoped would improve the electrode stability. Furthermore, the GDE structure allows for delivery of a high CO_2 concentration and removal of CO produced at the electrode which would help overcome CO poisoning, a known limitation of this class of catalysts, especially in N-alkylated analogues.^{7,15,32,38}

The results for the GDE/Ni(CycPy) electrode held at $-1.4 \text{ V}_{\text{Ag}/\text{AgCl}}$ for 2.5 h in a flow cell with 0.5 M KHCO_3 electrolyte (flowing at 22 mLmin^{-1} and 12 mLmin^{-1} over the anode and cathode respectively) under CO_2 flow of 20 mLmin^{-1} shown in **Figure 32**. While additional experiments using a carbon filler in the catalyst ink to increase the current density of the GDE/Ni(CycPy) electrode are shown in **Figure 33**. **Figure 33** shows the addition of Enasco 350G carbon support gives higher currents but slightly lower selectivity towards CO. As this does not show a significant improvement, carbon powder was excluded from the GDEs.

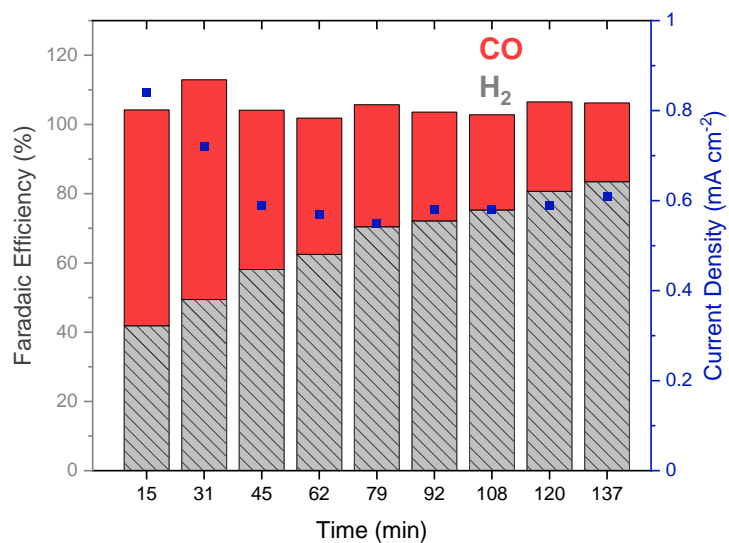


Figure 32 Electrolysis data from a Ni(CycPy) GDE at $-1.4V_{Ag/AgCl}$ used in $0.5 M KHCO_3$ with a CO_2 flow rate of $20 ml min^{-1}$.

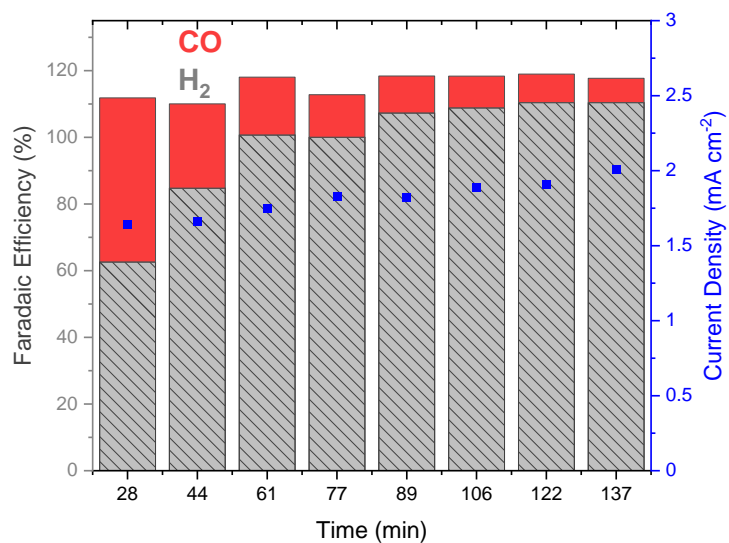


Figure 33 Electrolysis data from a Ni(CycPy) GDE synthesised with additional Ensaco carbon support at $-1.4V_{Ag/AgCl}$ in $0.5 M KHCO_3$ with a CO_2 flow rate of $20 ml min^{-1}$.

Chapter 2 Noncovalent immobilisation of a Ni(cyclam) catalyst on carbon electrodes

For the duration of the experiment significant CO was detected (starting FE_{CO} 61% or 2.3 $\mu\text{mol}/\text{min}$ at total initial current of 10.5 mA) indicating that the Ni(CycPy) electrode was able to electrocatalytically reduce CO_2 when immobilised on the GDE support using an aqueous catholyte. In **Figure 32** and **Figure 33** the total faradaic efficiency is recorded as over 100%, this arises due to error in product detection and quantification.

The initial turnover frequency of the catalyst was calculated to be $\sim 55 \text{ hr}^{-1}$ based off the measured catalyst concentration on the electrode surface, **Figure 34a**. The peak at $-0.95 \text{ V}_{\text{Ag}/\text{AgCl}}$ on **Figure 34a** has been used to calculate the electrochemically active surface coverage of Ni(CycPy) on modified GDE. We measure the surface coverage to be $1.84 \times 10^{-7} \text{ mol cm}^{-2}$ giving us a minimum TON of 13.8 for CO after 15 minutes. This result is benchmarked against other Ni(cyclam) catalysts immobilised on carbon electrodes in **Table 1**. Here GDE/Ni(CycPy) outperforms all N-alkylated analogous except the Ni(pyrenyl-amide cyclam) complex by Pugliese *et al.*,¹⁵ which, while showing high selectivity at high current densities, is ran in predominantly organic solvent (MeCN 1% H_2O), where proton concentration, and thus HER is significantly lower. It is important to note that none of the other catalysts reported in **Table 1** have been used in gas diffusion set-up, where less CO_2 is available to the catalyst which may be the cause of their much lower selectivity, highlighting the advantages of gas diffusion electrodes for CO_2 reduction with Ni(cyclam) catalysts.

Chapter 2 Noncovalent immobilisation of a Ni(cyclam) catalyst on carbon electrodes

While initially active for $e\text{CO}_2\text{R}$, CO production by GDE/Ni(CycPy) quickly drops off throughout the reaction. CVs shown in **Figure 34b** show the GDE (in 0.5 M KHCO_3 conventional electrochemical cell set-up) before and after electrolysis at -1.4 V for 45 minutes. While the catalyst appears stable in the solution at open circuit (solutions are purged for 30 minutes with CO_2 prior to use), post electrolysis a loss of current is observed indicating, despite additional PTFE, catalyst loss from the GDE structure. This was confirmed by running a clean GCE in the electrolyte post electrolysis, where we see a peak at -1.36 V indicating the Ni(CycPy) catalyst was in solution. This suggests the decline in CO production of GDE/Ni(CycPy) over time was likely due to the pyrene unit being unable to immobilise the catalyst to the carbon support when using a solvent, such as water, where Ni(CycPy) is soluble. Although pyrene groups can play an important role in directing the orientation of interaction between an electroactive species and the carbon support, they alone are not sufficiently stable under reductive conditions to prevent detachment of a soluble catalyst.

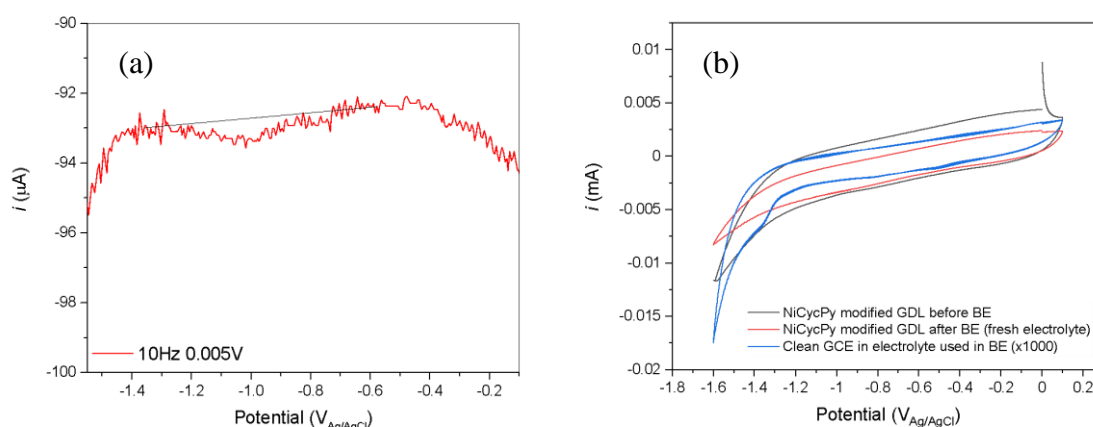


Figure 34(a) SWV of Ni(CycPy) modified GDE in 0.1M TBA PF_6 CH_3CN under N_2 **(b)** CV comparison of Ni(CycPy) modified GDE in 0.5M KHCO_3 (aq) in a standing cell under CO_2 before bulk electrolysis (BE), after BE in fresh electrolyte and a clean GCE (scaled up) in the electrolyte used for BE to show loss of the catalyst from the electrode into the electrolyte.

The catalyst loss from the surface highlights an important wider issue for the electrochemistry community. π - π stacking of pyrene groups on carbon supports is widely used as a simple way to non-covalently modify electrodes in the sensing and catalysis communities, particularly for CO_2 reduction,^{20,21,23,39} but desorption is not commonly discussed. Here, we find that although stable at open circuit conditions, under an applied bias the pyrene modified species desorbs. One study on 1-pyrenecarboxylic acid on graphite showed that at negative potentials (-0.8 $\text{V}_{\text{Ag}/\text{AgCl}}$) over 90% of the species desorbs after 1 minute at pH 7. This loss occurred at lower

Chapter 2 Noncovalent immobilisation of a Ni(cyclam) catalyst on carbon electrodes

levels at lower pH but at high pH's the pyrene group was completely removed, attributed to the deprotonation of the carboxylic acid group, making the molecule anionic, repelling it from the electrode at negative potentials.⁴⁰ While we would not expect Ni(CycPy) to take on an overall negative charge, during catalysis the complex does become reduced in oxidation state which may affect the adsorption of the complex when we deviate from OCP. Even the lower desorption rate of neutral pyrene shows increasing desorption with increasingly negatively applied potentials showing 5% loss after 1 minute at $-0.8 \text{ V}_{\text{Ag}/\text{AgCl}}$. During CO_2 reduction experiments, such as those reported here, potentials are significantly negative of $-0.8 \text{ V}_{\text{Ag}/\text{AgCl}}$, local pH in rises due to formation of hydroxide ions during both CO_2R and HER,⁴¹ and experiments are ran for significantly longer making even a slower desorption rate lead to significant losses over the course of the experiment.

The first reports of the use of molecular electrocatalysts on GDE structures have only been made recently and to date these have focussed on the Fe and Co macrocyclic complexes, particularly porphyrins.⁴²⁻⁴⁴ Production of significant levels of CO using a Ni(CycPy) GDE in 0.5 M KHCO_3 proved that this class of catalysts has potential for use in complete aqueous electrolyzers. Since writing this thesis, a Ni(cyclam) complex was modified with a pyrene unit via the carbon by Pugliese *et al.*, here the activity of the complex was shown to be significantly improved compared to the previous N-alkylated analogues.¹⁷

It is clear that the pyrene group can play an important role in controlling the orientation of interaction of the catalyst with the electrode surface, and in facilitating electron transfer, and here its presence leads to a +0.45 V shift in the $\text{Ni}^{\text{II/I}}$ reduction potential, however in-itself it is insufficient to ensure stable immobilisation under aqueous, catalytic conditions.

2.4.2.2 Zero-gap cell

In an attempt to exploit the proposed improved catalyst-electrode interaction the pyrene unit provide, Ni(CycPy) was also ran in a zero-gap reverse bias BPM cell by Dr Bhavin Siritanaratkul. Here the zero-gap cell configuration does not require flowing catholyte so loss of the catalyst via dissolution is hopefully minimised. The GDE was made by spray coating a catalyst ink onto 5 cm^2 Sigracet 39 BB carbon paper. Here PTFE was excluded from the catalyst ink which was made up of 5 mg of Ni(CycPy) to 1 mL H_2O , 1 mL isopropyl alcohol and 80 μL of 5% Nafion solution.

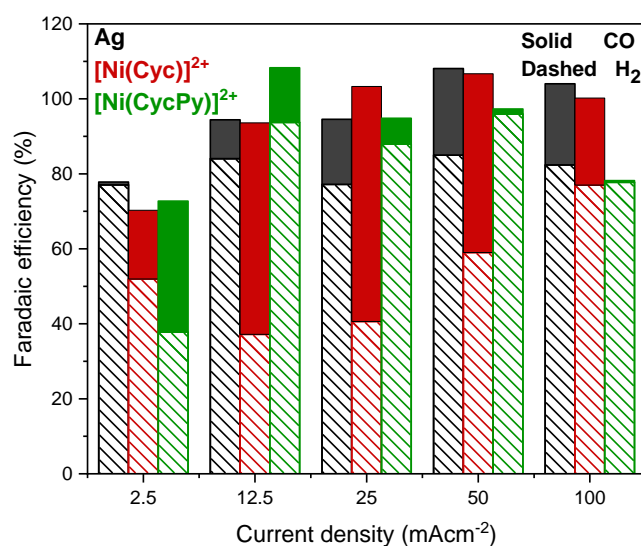


Figure 35 Faradaic efficiencies of a Ni(CycPy) modified GDE in a zero-gap reverse bias BPM set up at a range of current densities after 12 min.

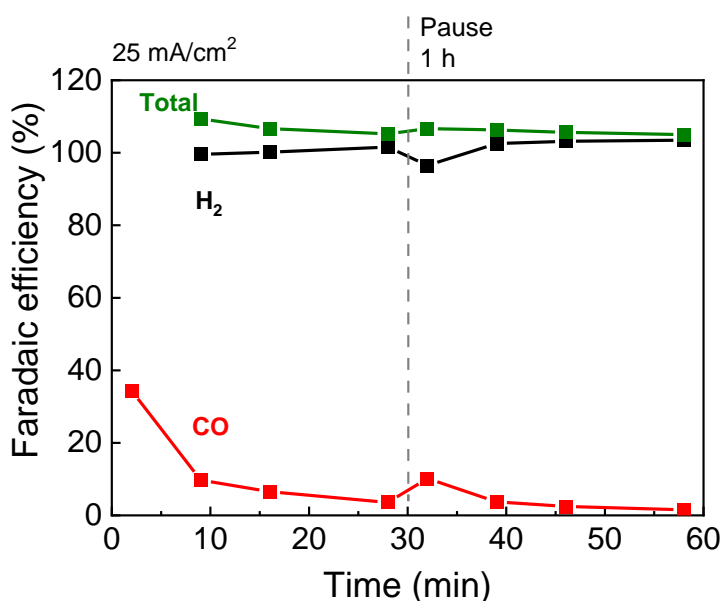


Figure 36 FE's of a Ni(CycPy) modified GDE in zero-gap reverse bias BPM at 25 mAcm⁻² over the course of 1 h.

In **Figure 35** the comparison of Ni(CycPy) compared to the performance of Ag and parent complex, Ni(cyclam), previously reported by Siritanaratkul *et al* at a range of current densities from lowest to highest.¹³ Each current density was held for 12 minutes with a 30-minute resting period in between to allow generated CO to desorb. Here we see that at 2.5 mAcm⁻² Ni(CycPy) was able to produce FE_{CO} of 38%, almost twice that of Ni(cyclam). Interestingly the selectivity remains close to that achieved in the flow cell at a similar current density where proton

Chapter 2 Noncovalent immobilisation of a Ni(cyclam) catalyst on carbon electrodes

concentration, thus competing hydrogen evolution reaction (HER) is expected to be much lower than with the reverse-bias BPM (**Figure 33**). This demonstrates the acid tolerance of Ni(CycPy), which is able to reduce CO₂ even at this lower pH. However very quickly we see CO production fall off as we reach higher current densities. As there was limited catholyte, loss of the catalyst via dissolution is unlikely, instead it is proposed that the stability of Ni(CycPy) towards poisoning and deactivation at higher currents is compromised as a result from functionalising one of the nitrogen's in the macrocycle. A stability run, where a current density of 25 mAcm⁻² was applied for one hour is shown in **Figure 36**. Here again we see a similar trend where CO was only able to be produced for the first 15 minutes of the reaction before dropping off. After 30 minutes of electrolysis, a one-hour break was used where gas was still flowing, here we see partial recovery of CO production from <5 % to 10%, a similar magnitude of recovery was reported in the parent complex (though overall CO production was much higher for Ni(cyclam)) suggesting that part of this drop off was caused by reversible CO poisoning, followed by irreversible second reduction to Ni(0) carbonyl compound. This is a common deactivation pathway for all Ni(cyclam) catalysts, though is proposed to be worse in the N-alkylated analogues, where we see significant positive shifts in the Ni^{2+/+} reduction.^{28,45}

CVs of the Ni(CycPy) modified electrodes were ran in 0.1 M TBAPF₆ in MeCN where the Ni^{2+/3+} couple which was used to estimate the electroactive coverage to be 1.2x10⁻⁸ mol cm⁻² (**Figure 37**). This coverage was on a similar order of magnitude to the unmodified parent complex made up in the same way, suggesting that the pyrene modification had not significantly increased the electroactive coverage on this electrode.¹³ The electrode was also analysed post-electrolysis where no redox features can be observed suggesting no catalyst was present (**Figure 38**). It was observed that due to the nature of the zero-gap cell, often significant catalyst was lost during disassembly of the cell, thus it is difficult to assign if this loss is an effect of prolonged electrolysis or mechanical removal during disassembly.

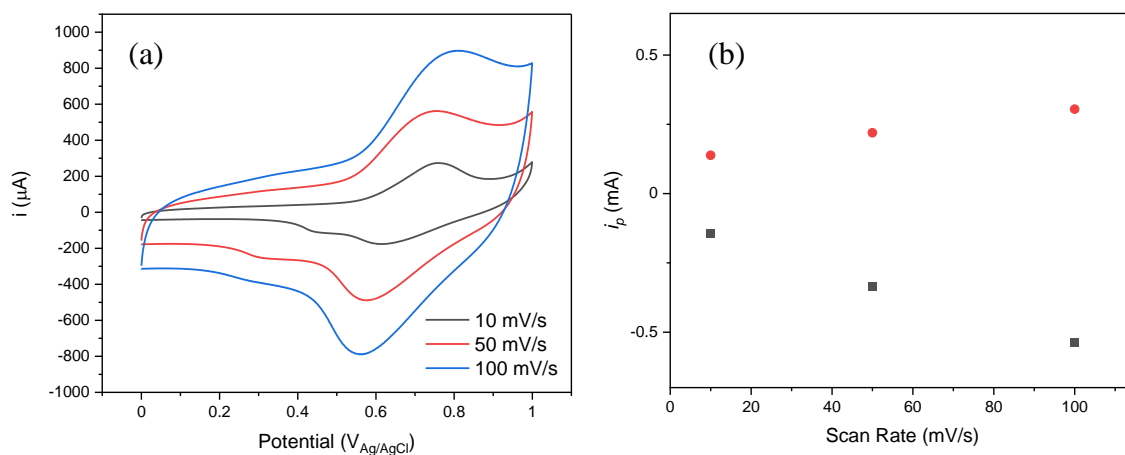


Figure 37 Cyclic voltammetry of a Ni(CycPy) modified GDE (geometric area 0.25 cm^2) in MeCN with 0.1 M TBAPF_6 under Ar.

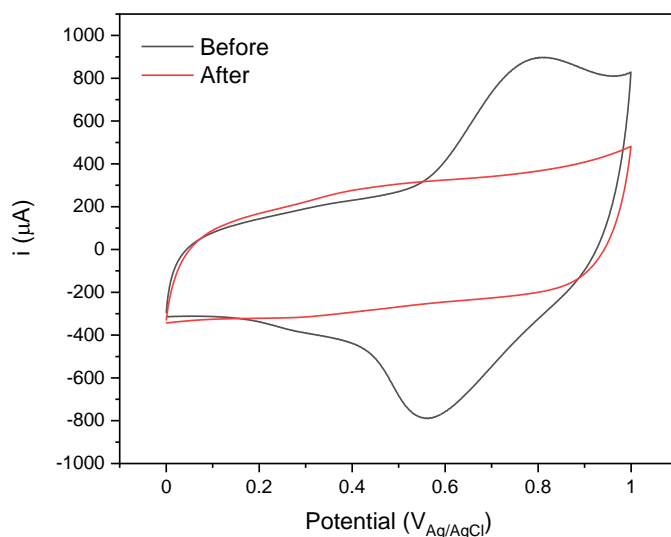


Figure 38 CV of a Ni(CycPy) modified GDE (geometric area 0.25 cm^2) in MeCN with 0.1 M TBAPF_6 under Ar before and after 1 h electrolysis at 25 mAcm^2 .

2.5 Conclusions

A pyrene modified Ni cyclam complex (Ni(CycPy)) has been synthesised and electrochemically characterised in both aqueous and mixed solvents (CH₃CN/H₂O (10%)). XPS and electrochemical measurements show that the pyrene group enables immobilisation onto a range of carbon surfaces. Although the strength of the non-covalent π - π interaction was insufficient to prevent the complex from desorbing in an aqueous solvent upon application of a reducing potential it was shown from experiments in mixed solvents that immobilisation leads to a large (+0.45 V) positive shift in the potential of the Ni^{II/I} reduction. In a flow cell set-up the stability of the immobilised Ni(CycPy) electrode was increased and preliminary studies using an aqueous electrolyte are possible. This is important as past studies using immobilised cyclams had focussed on mixed solvents. Here we provide the first report using an immobilised cyclam complex on a GDE support in aqueous electrolyte that shows that FE_{CO} of 60% can be obtained initially at 0.9 mAcm⁻², however activity decreases due to catalyst loss from the surface caused by catalyst solubility in water and reductive desorption of the pyrene unit. We propose that when working with aqueous catholyte, reducing catalyst solubility is very important to retain the catalyst on the surface.

Experiments in the zero-gap cell move away from a liquid catholyte and analyse the behaviour of Ni(CycPy) in a more acidic environment with a reverse-bias BPM where Ni(CycPy) shows good selectivity towards CO at low current densities, however this quickly drops off with increasing current and time of electrolysis. Additionally, analysis of the Ni(CycPy) modified GDE showed no significant increase in electroactive coverage compared to Ni(cyclam) deposited in the same way.

Ni(CycPy) is an active catalyst for CO₂ reduction, although selectivity and stability are decreased when compared to the parent complex, Ni(cyclam), likely due to the loss of one of the 4 N-H groups on the cyclam ligand which are known to aid CO₂ binding while reducing CO poisoning and overreduction when compared with alkylated analogues.^{10,14,24,46} This has since been confirmed by Pugliese *et al* where a Ni(cyclam) complex was modified with a pyrene unit via the carbon, here the activity of the complex was shown to be significantly improved compared to the previous N-alkylated analogues, however, CO poisoning and deactivation remains an issue for this catalyst class.¹⁷

2.6 References

- 1 B. J. Fisher and R. Eisenberg, *J Am Chem Soc*, 1980, **102**, 7361–7363.
- 2 J. P. Collin, A. Jouaiti and J. P. Sauvage, *Inorg Chem*, 1988, **27**, 1986–1990.
- 3 M. Beley, J. Collin, R. Ruppert and J. Sauvage, *J Chem Soc, Chem Commun*, 1984, **2**, 1315–1316.
- 4 M. Beley, J. P. Collin, R. Ruppert and J. P. Sauvage, *J Am Chem Soc*, 1986, **108**, 7461–7467.
- 5 G. Neri, I. M. Aldous, J. J. Walsh, L. J. Hardwick and A. J. Cowan, *Chem Sci*, 2016, **7**, 1521–1526.
- 6 Y. Wu, B. Rudshiteyn, A. Zhanaidarova, J. D. Froehlich, W. Ding, C. P. Kubiak and V. S. Batista, *ACS Catal*, 2017, **7**, 5282–5288.
- 7 J. D. Froehlich and C. P. Kubiak, *Inorg Chem*, 2012, **51**, 3932–3934.
- 8 Y. J. Leem, K. Cho, K. H. Oh, S. Han, K. M. Nam and J. Chang, *Chem Soc Rev*, 2017, **53**, 3454–3457.
- 9 C. R. Schneider and H. S. Shafaat, *Chem Commun*, 2016, **52**, 9889–9892.
- 10 A. Jarzebinska, P. Rowainiski, I. Zawisza, R. Bilewicz, L. Siegfried and T. Kaden, *Anal Chim Acta*, 1999, **396**, 1–12.
- 11 G. Neri, J. J. Walsh, C. Wilson, A. Reynal, J. Y. C. Lim, X. Li, A. J. P. White, N. J. Long, J. R. Durrant and A. J. Cowan, *Phys Chem Chem Phys*, 2014, **17**, 1562–1566.
- 12 J. A. Rabinowitz and M. W. Kanan, *Nat Commun*, 2020, **11**, 5231.
- 13 B. Siritanaratkul, M. Forster, F. Greenwell, P. K. Sharma, E. H. Yu and A. J. Cowan, *J Am Chem Soc*, 2022, **144**, 7551–7556.
- 14 A. Zhanaidarova, C. E. Moore, M. Gembicky and C. P. Kubiak, *Chem Commun*, 2018, **54**, 4116–4119.
- 15 S. Pugliese, N. T. Huan, J. Forte, D. Grammatico, S. Zanna, B.L. Su, Y. Li and M. Fontecave, *ChemSusChem*, 2020, **13**, 1–9.

Chapter 2 Noncovalent immobilisation of a Ni(cyclam) catalyst on carbon electrodes

- 16 A. Forget, M. Regnacq, C. Orain, E. Touzé, E. Lelong, C. Brandily, H. Bernard, R. Tripier and N. Le Poul, *Chem Commun*, 2022, **58**, 6785–6788.
- 17 S. Pugliese, N. T. Huan, A. Solé-Daura, Y. Li, J.G. Rivera de la Cruz, J. Forte, S. Zanna, A. Krief, B.-L. Su and M. Fontecave, *Inorg Chem*, 2022, **61**, 15841–15852.
- 18 E. Fujita, J. Haff, R. Sanzenbacher and H. Elias, *Inorg Chem*, 1994, **33**, 4627–4628.
- 19 J. Schneider, H. Jia, K. Kobihiro, D. Cabelli, J. Muckerman and E. Fujita, *Energy Environ Sci*, 2012, **5**, 9502–9510.
- 20 J. D. Blakemore, A. Gupta, J. Warren, B. S. Brunshwig and H. B. Gray, *J. Am. Chem. Soc.*, 2013, **135**, 18288–18291.
- 21 P. Kang, S. Zhang, T. J. Meyer and M. Brookhart, *Angew Chem, Int Ed*, 2014, **53**, 8709–8713.
- 22 A. Maurin and M. Robert, *J Am Chem Soc*, 2016, **138**, 2492–2495.
- 23 B. Reuillard, K. H. Ly, T. E. Rosser, M. F. Kuehnel, I. Zebger and E. Reisner, *J Am Chem Soc*, 2017, **139**, 14425–14435.
- 24 D. J. Szalda, E. Fujita, R. Sanzenbacher, H. Paulus and H. Elias, *Inorg Chem*, 1994, **33**, 5855–5863.
- 25 M. Boiocchi, L. Fabbrizzi, F. Foti and M. Vázquez, *Dalton Tran*, 2004, 2616–2620.
- 26 A. Anichini, L. Fabrizzi, P. Paoletti and R. M. Clay, *Inorganica Chim Acta*, 1977, **25**, 1.
- 27 A. Evers and R. D. Hancock, *Inorganica Chim Acta*, 1989, **160**, 245–248.
- 28 K. Bujno, R. Bilewicz, L. Siegfried and T. A. Kaden, *J Electroanal Chem*, 1998, **445**, 47–53.
- 29 J. D. Froehlich and C. P. Kubiak, *Inorg Chem*, 2012, **51**, 3932–3934.
- 30 G. B. Balazs and F. C. Anson, *J Electroanal Chem*, 1993, **361**, 149–157.
- 31 J. Song, E. L. Klein, F. Neese and S. Ye, *Inorg Chem*, 2014, **53**, 7500–7507.
- 32 J. D. Froehlich and C. P. Kubiak, *J Am Chem Soc*, 2015, **137**, 3565–3573.
- 33 G. Neri, PhD Thesis, University of Liverpool, 2016.

Chapter 2 Noncovalent immobilisation of a Ni(cyclam) catalyst on carbon electrodes

- 34 S. P. Roe, J. O. Hill and J. Liesegang, *Transition Met. Chem.*, 1985, **10**, 100–106.
- 35 C. A. Kelly, E. L. Blinn, N. Camaioni, M. D'Angelantonio and Q. G. Mulazzani, *Inorg Chem*, 1999, **38**, 1579–1584.
- 36 M. Hammouche, D. Lexa, J. M. Savêant and M. Momenteau, *J Am Chem Soc*, 1991, **113**, 8455–8466.
- 37 C. J. Kaminsky, S. Weng, J. Wright and Y. Surendranath, *Nat Catal*, 2022, **5**, 430–442.
- 38 S. L. Behnke, A. C. Manesis and H. S. Shafaat, *Dalton Trans.*, 2018, **47**, 15206–15216.
- 39 L. A. Paul, Sheida Rajabi, Christian Jooss, Franc Meyer, Fatemeh Ebrahimi and Inke Siewert, *Dalton Trans*, 2020, **49**, 8367–8374.
- 40 M. Cao, A. Fu, Z. Wang, J. Liu, N. Kong, X. Zong, H. Liu and J. J. Gooding, *J Phys Chem C*, 2014, **118**, 2650–2659.
- 41 H. Rabiee, L. Ge, X. Zhang, S. Hu, M. Li and Z. Yuan, *Energy Environ Sci*, 2021, **14**, 1959–2008.
- 42 K. Murata, H. Tanaka and K. Ishii, *J Phys Chem C*, 2019, **123**, 12073–12080.
- 43 S. Ren, D. Joulié, D. Salvatore, K. Torbensen, M. Wang, M. Robert and C. P. Berlinguette, *Science*, 2019, **365**, 367–369.
- 44 K. Torbensen, D. Joulié, S. Ren, M. Wang, D. Salvatore, C. P. Berlinguette and M. Robert, *ACS Energy Lett*, 2020, **5**, 1512–1518.
- 45 M. Fujihira, Y. Hirata and K. Suga, *J Electroanal Chem*, 1990, **292**, 199–215.
- 46 E. S. Rountree, B. D. Mccarthy, T. T. Eisenhart and J. L. Dempsey, *Inorg Chem*, 2014, **53**, 9983–10002.

Chapter 3 Pulsed electrolysis on Ni(cyclam)

The material for this chapter comes from the manuscript “Pulsed Electrolysis with a Nickel Molecular Catalyst Improves Selectivity for Carbon Dioxide Reduction.” By Francesca Greenwell, Bhavin Siritanaratkul, Preetam K. Sharma, Eileen H. Yu and Alexander J. Cowan, published in *Journal of American Chemistry Society*, 2023, 145, 28, 15078–15083. The thesis author is the primary investigator and author of this publication, completing conceptualisation and experiment design, all electrochemical analysis, electrolysis and product analysis. Catalyst synthesis and experiment design was done by Bhavin Siritanaratkul. XPS analysis was done by Preetam K. Sharma and Eileen H. Yu. Supervision, experimental design and conceptualisation by Alexander J. Cowan.

3.1 Scope of the chapter

As well as developing new electrocatalysts for CO₂ reduction, research efforts are focusing on understanding and controlling the electrode-electrolyte interface with existing catalysts to understand and improve their catalytic behaviour. This includes engineering of the electrochemical cell,¹⁻³ altering electrolyte concentrations and composition,⁴⁻⁷ and more recently changing electrolysis techniques.⁸⁻¹⁰ Electrolysis experiments are typically carried out under potentiostatic (or galvanostatic) conditions. However recent studies on metal electrodes have utilized pulsed electrolysis as a way to influence and improve reaction selectivity and stability in electrochemical CO₂R.^{8,9} There are multiple proposed effects of using a pulsed voltage depending on the system and pulse parameters used. The parameters used are the cathodic and anodic potentials applied (or currents in the case of chronopotentiometry) which are denoted at E_C and E_A (or i_C and i_A) and the length of time each potential (or current) is applied (t_C or t_A) as illustrated in Figure 39b. The reasons for improved CO₂ reduction with pulsed electrolysis range from surface oxidation or roughening,¹¹⁻¹⁶ rearrangement of surface coverage,^{15,17-19} altering the local pH and CO₂ concentration at the electrode,²⁰⁻²³ and inhibiting catalyst poisoning,^{11-13,24,25} (shown in **Figure 39c**).

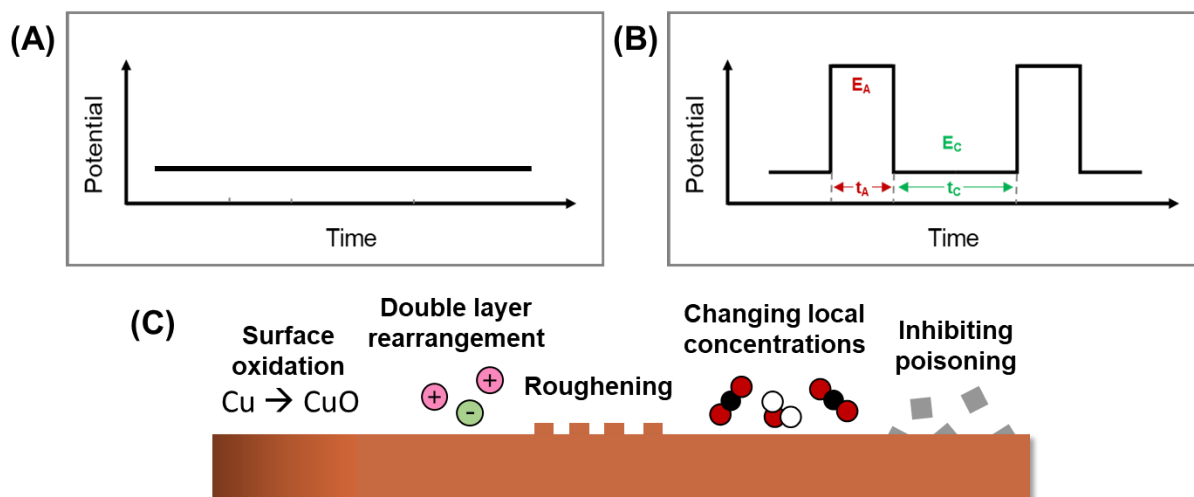


Figure 39 Schematic of potential-time profile during (a) potentiostatic and (b) pulsed electrolysis. (c) illustration of different mechanisms as a result of pulsed electrolysis on a Cu electrode. Reproduced from Casebolt et al.⁸

The previous chapter introduced nickel cyclams (cyclam = 1,4,8,11-tetraazacyclotetradecane) as well studied electrocatalysts for CO production in aqueous electrolytes.^{26–33} Recently $[Ni(cyclam)]^{2+}$ has also been found to be selective for CO production when used on gas diffusion electrodes in H-cells,^{34,35} and higher current density electrolyzers,^{31,36} notably even at low pH.³⁶ However, despite good initial selectivity, Ni(cyclam) suffers from self-poisoning through the formation of $[Ni(cyclam)(CO)]^+$ as a result of the high CO binding constant to $[Ni(cyclam)]^+$ ($K_{CO} = 7.5 \times 10^5$, $K_{CO_2} = 16$) leading to a second reduction forming Ni(0) carbonyl (**Figure 40**). This has been proposed to be the limiting factor in stability and selectivity of the catalyst both at GCE and gas diffusion electrodes.^{34,36,37} More widely CO poisoning and overreduction of intermediates has been proposed to limit stable electrochemical CO_2R in a range of molecular catalysts, with metal centres including Ni,^{38,39} Fe,^{40,41} Co etc.^{42–44} Remediation methods have included removal of CO with scavengers or increased gas flow,^{36,37} modifications to the catalyst structure,^{40–44} or incorporating long periods (minutes-hours) for recovery/regeneration, which only leads to a temporary recovery in activity.^{34,36}

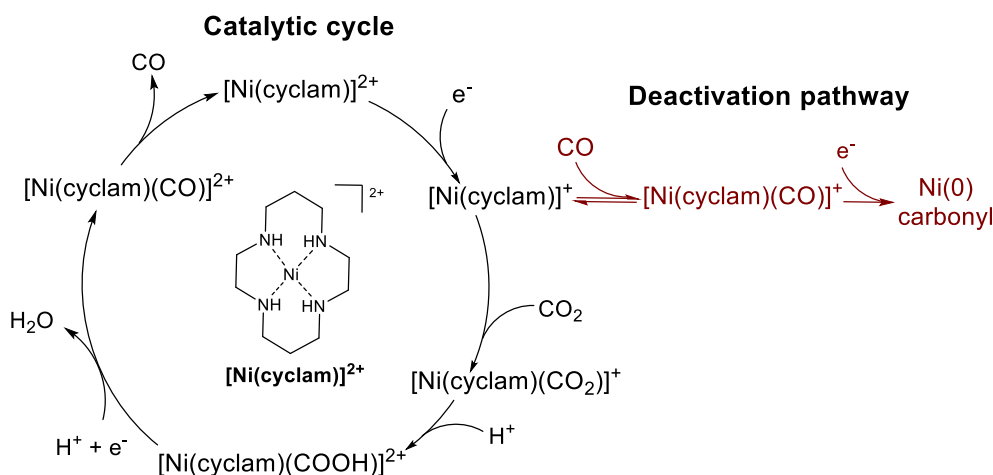


Figure 40 Reported catalytic cycle and deactivation pathway of $[\text{Ni}(\text{cyclam})]^{2+}$.³⁰

While there are many pulsed studies on different metal electrodes for CO_2R , we are not aware of any where the impact of short (ms-s) voltage pulses is examined with homogenous molecular catalysts despite it offering a potential way to modify catalytic activity and stability. In this work we report a pulse electrolysis study on a homogenous molecular catalyst for CO_2R with an inert glassy carbon working electrode (GCE).

3.2 Ni(cyclam) mechanism and degradation

As discussed, early experiments with $[\text{Ni}(\text{cyclam})]^{2+}$ were carried out where the catalyst would reductively adsorb onto Hg electrodes, however more recently it has been shown that $[\text{Ni}(\text{cyclam})]^{2+}$ can also be used with a GCE.^{30,45} Here Faradaic efficiencies for CO are typically lower as it is proposed that the catalyst does not adsorb,³⁰ this was tested using double potential step chronocoulometry (DPSC) where the adsorbed species can be quantified following methods from literature which will be briefly explained below.^{32,46}

In a solution 0.1 mM Ni(cyclam) a potential of interest was held for 30 s to allow any reductive adsorption of $[\text{Ni}(\text{cyclam})]^+$ onto the GCE surface to occur. At time 0 (shown on **Figure 41a**) the potential was jumped to +0.2 V_{NHE} in the first step, assuming only $[\text{Ni}(\text{cyclam})]^+$ was absorbed, the resulting charge can be thought of as made up from faradaic contributions from oxidation of $[\text{Ni}(\text{cyclam})]^+$ both dissolved in solution ($\frac{2nFAD^{1/2}C_0t^{1/2}}{\pi^{1/2}}$) and adsorbed onto the electrode ($Q_{ads} = nF\Gamma$) in addition to the capacitive charge from the double layer (Q_c). This charge passed over the first 10 ms in this step (Q1, **Figure 41**) was plotted vs $t^{1/2}$ to give a linear plot (**Figure 41c**) where the intercept corresponds to Q_c and Q_{ads} .

To determine an independent estimate of Q_c , the potential is then stepped back to the initial value, at time τ (**Figure 41a**), where any capacitive change should be the same however there should be no surface species present to provide any Faradaic contributions. Here the charge passed over 10 ms in the second step (Q2, **Figure 41**) was plotted vs $[\tau^{1/2} + (t-\tau)^{1/2} - t^{1/2}]$ where τ is the duration of the first step and t is the time. The difference of the forward and reverse intercepts gives charge of adsorbed species, Q_{ads} , from which the surface coverage, Γ , was calculated using: $\Gamma = \frac{Q_{ads}}{FnA}$ for each potential across a potential range where F the Faraday constant, n the number of electrons and A the electrode area in cm^2 . The resulting plot is shown in **Figure 42**.

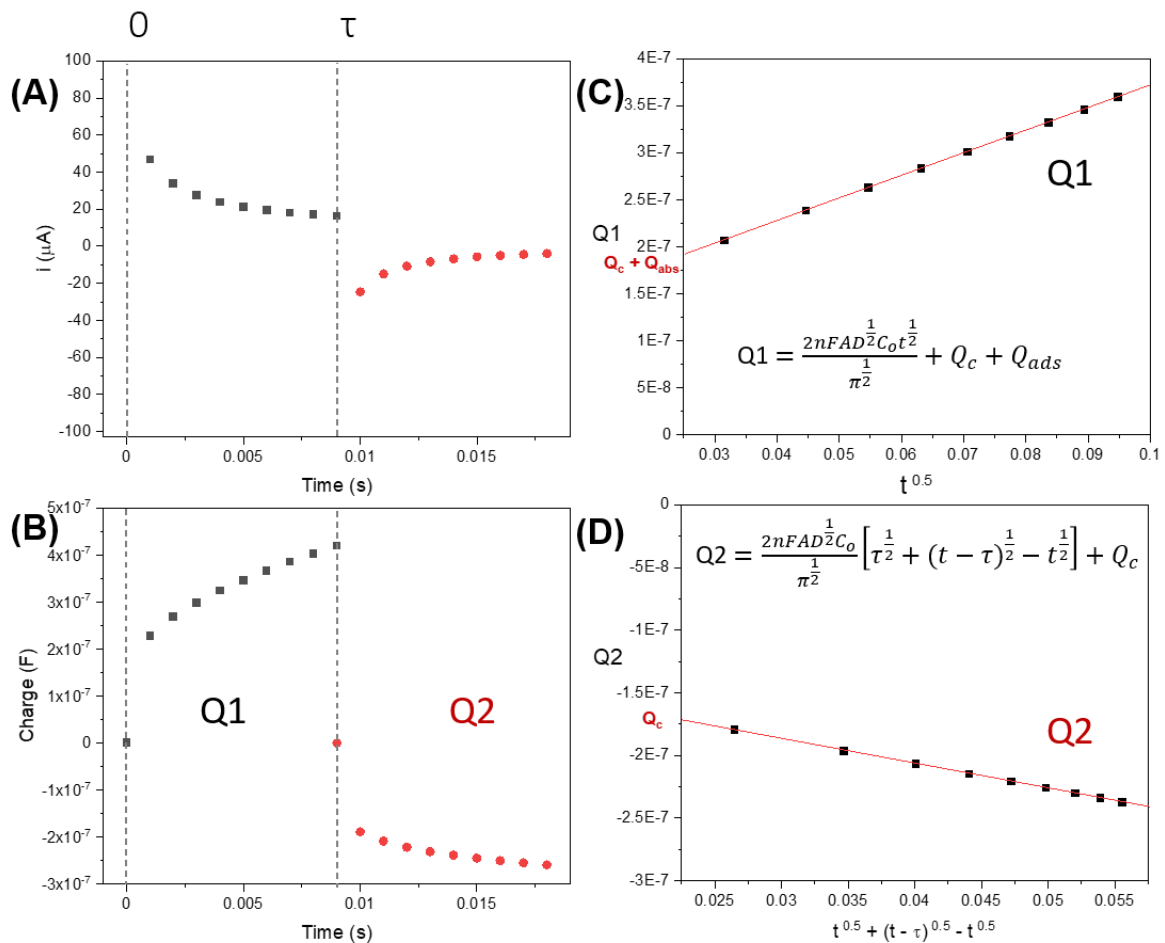


Figure 41 Representative DPSC experiment (a) current plot (b) charge plot (c) linear plot between Q_1 (from current response of first step) and $t^{0.5}$ (d) linear plot between Q_2 (from current response of second step) and $[\tau^{1/2} + (t-\tau)^{1/2} - t^{1/2}]$

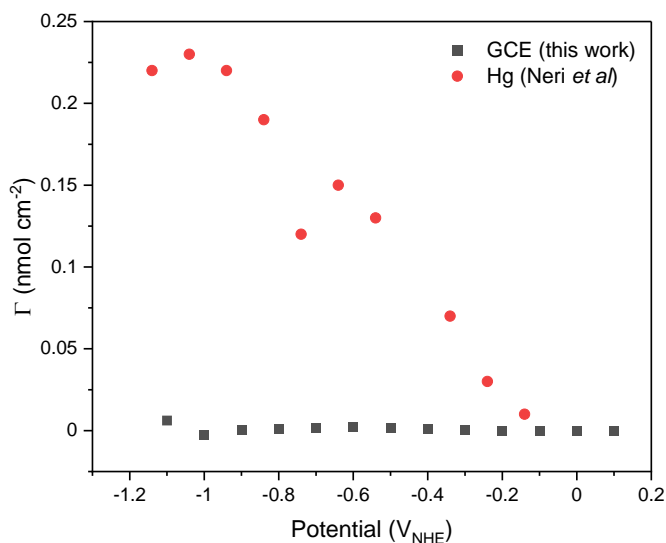


Figure 42 Dependence of the surface coverage of 0.1 mM Ni(cyclam) on GCE in 0.5 M NaCl (black square) compared with 0.1 mM Ni(cyclam) on Hg drop in 0.1 M NaClO₄, pH 2 (red circle). Hg data reproduced from Neri et al with permission.³²

Figure 42 shows that there is no significant charge assignable to adsorption process for Ni(cyclam), thus surface coverage is minimal at GCE (unlike on Hg), making it a simpler molecular catalyst/electrode system to study the effects of pulsed electrolysis on.

Next, we examine the electrochemical response of Ni(cyclam) under CO₂ and Ar. **Figure 43(A)** shows a cyclic voltammogram (CV) of 1 mM [Ni(cyclam)]²⁺ in 0.5 M NaCl using a GCE. Under Ar the CV remains fairly featureless as hydrogen evolution obscures the Ni(II)/(I) couple in aqueous electrolyte.³⁰ Under CO₂ we see a significant increase in current at -1.5 V vs Ag/AgCl indicating CO₂R and the appearance of two small anodic features at -1.3 V (i) and -0.5 V (ii), assigned to the oxidation of deactivated catalyst species [Ni(cyclam)(CO)]⁺ and further irreversibly reduced Ni(0) carbonyl respectively.³⁷

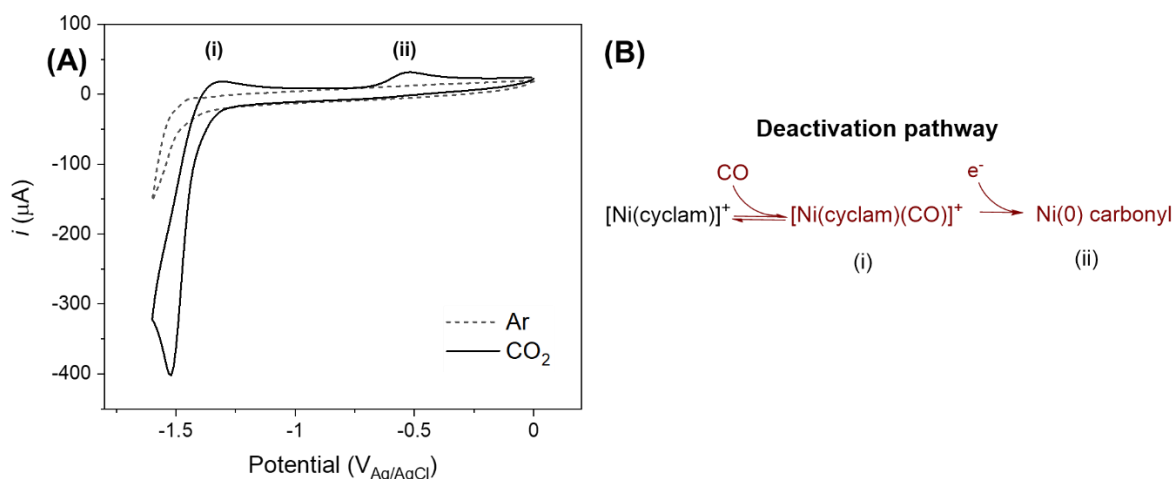


Figure 43(A) CV of 1 mM $[\text{Ni}(\text{cyclam})]^{2+}$ in 0.5 M NaCl at a GCE at 1 V/s (0 V to -1.6 V to 0 V) under Ar and CO_2 vs. Ag/AgCl, Pt counter separated by vycor frit, recorded without iR compensation. Plotted using IUPAC convention (B) Deactivation pathway of Ni(cyclam)

To investigate this peak assignment CVs of the complex were ran in MeCN with and without 1% water under Ar and CO_2 where scans were periodically stepped out (scanning negatively) to observe when oxidation features formed with a wider solvent window. In **Figure 45** under CO_2 with 1% H_2O a peak at -1.2 $V_{\text{Ag wire}}$ (attributed to oxidation of $[\text{Ni}(\text{cyclam})(\text{CO})]^+$) is observed only once the potential is swept to -1.4 $V_{\text{Ag wire}}$. The reduction potential needs to reach -1.6 $V_{\text{Ag wire}}$ before oxidation features at -0.4 V and another feature at -0.7 V appear on the return scan, indicating that these features are the product of a further reduced species, in line with the literature assignment of Ni(0) carbonyl. Interestingly, under Ar with 1% water addition, a similar trend is observed, suggesting that in scanning to -1.4 V the Ni(I) species is formed and that going down to -1.8 V formed different Ni(0) species resulting in three oxidation features on the returning scan (**Figure 44**). Under Ar it is assumed that no CO production occurs and thus suggests that other Ni(0) compounds, other than Ni(0) carbonyl, reported in literature can also be formed. When comparing the CV of the Ni(cyclam) to that of the solvent window (**Figure 46**) in the absence of catalyst, the current is significantly higher, suggesting that Ni(cyclam), or more likely Ni(0) compounds produced via Ni(cyclam) reduction, are able to act as a HER catalyst.

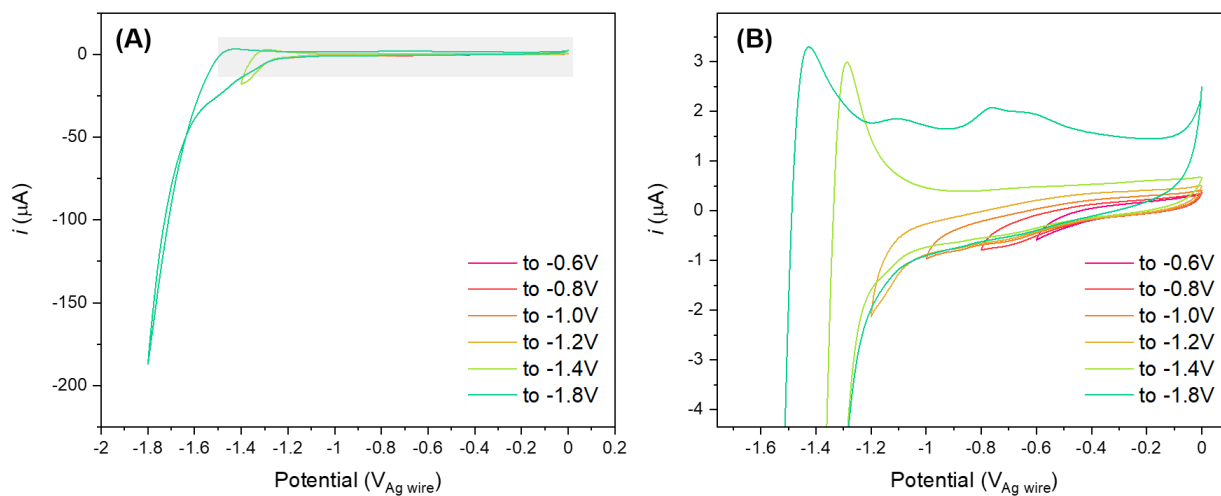


Figure 44(A) CV of $1 \text{ mM } [\text{Ni}(\text{cyclam})]^{2+}$ at a GCE in 0.1 M TBA PF_6 in MeCN with 1% water at 50 mV/s under Ar vs Ag wire. (B) Close up of inset in the grey box.

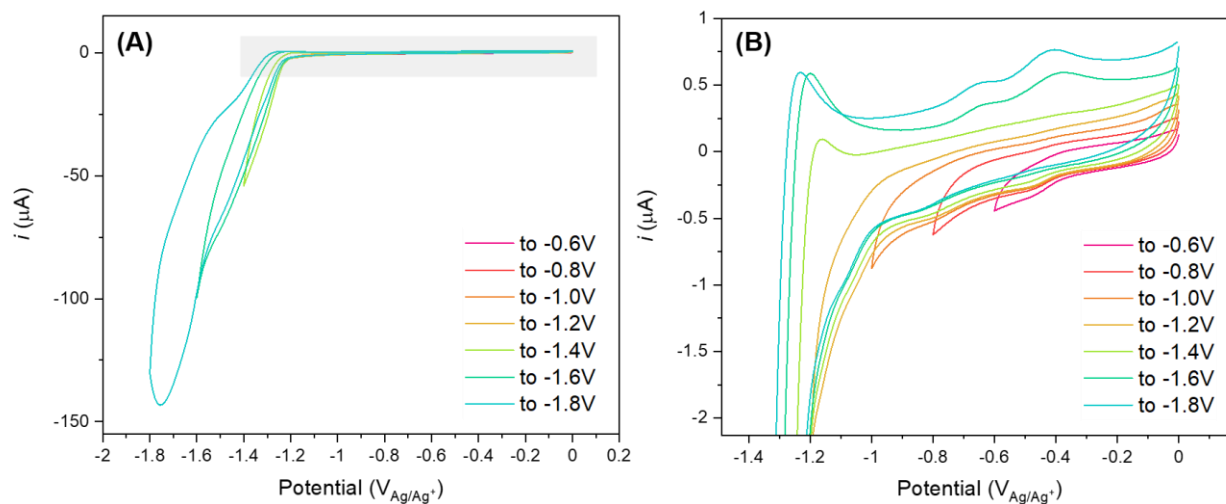


Figure 45(A) CV of $1 \text{ mM } [\text{Ni}(\text{cyclam})]^{2+}$ at a GCE in 0.1 M TBA PF_6 in MeCN with 1% water at 50 mV/s under CO_2 vs Ag wire. (B) Close up of inset in the grey box

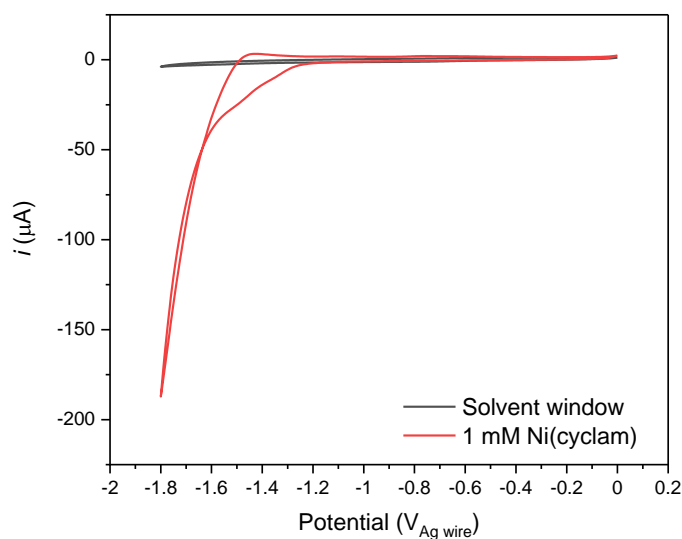


Figure 46 CV of 0.1 M TBA PF₆ in MeCN with 1% water at 50 mV/s with and without 1 mM [Ni(cyclam)]²⁺ under Ar

When the same experiment is ran in dry MeCN without additional water (**Figure 47** & **Figure 48**), the oxidation peak at -0.4 V_{Ag wire} is not visible under either Ar or CO₂ even after scanning to -1.8 V_{Ag wire}, this could suggest that the degradation pathway of Ni(cyclam) shown in **Figure 43** (B) is a proton coupled process. Under N₂ the Ni^{2+/+} couple is completely reversible whereas under CO₂ the reversibility disappears, however the currents remain small, demonstrating the need for a proton source for the system to turn over significant quantities for CO₂.

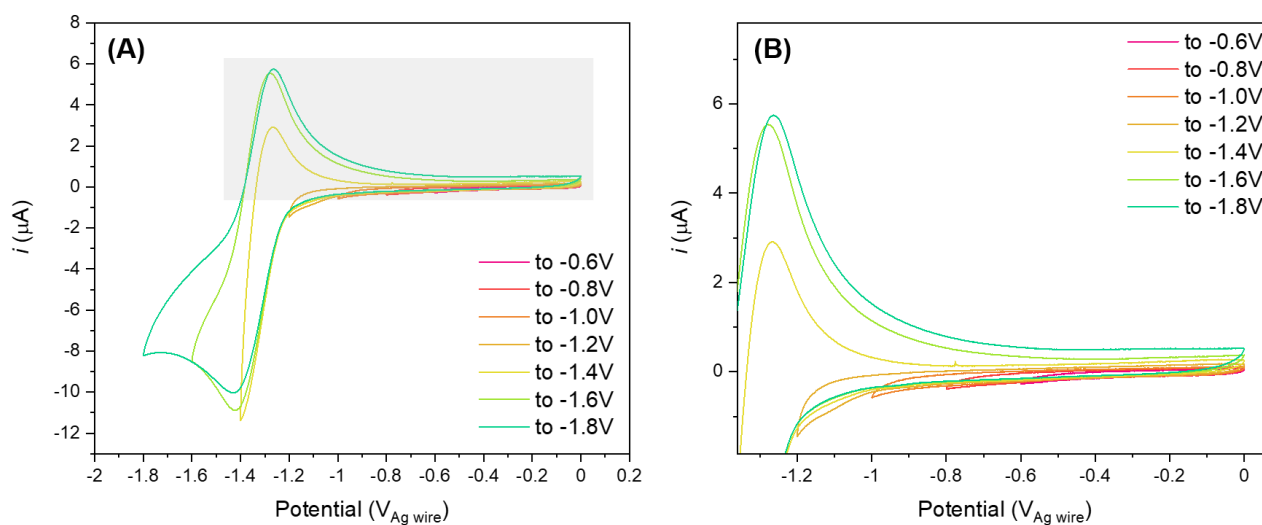


Figure 47 CV of 1 mM [Ni(cyclam)]²⁺ at a GCE in 0.1 M TBA PF₆ in dry MeCN 50 mV/s under Ar vs Ag wire. (B) Close up of inset in the grey box.

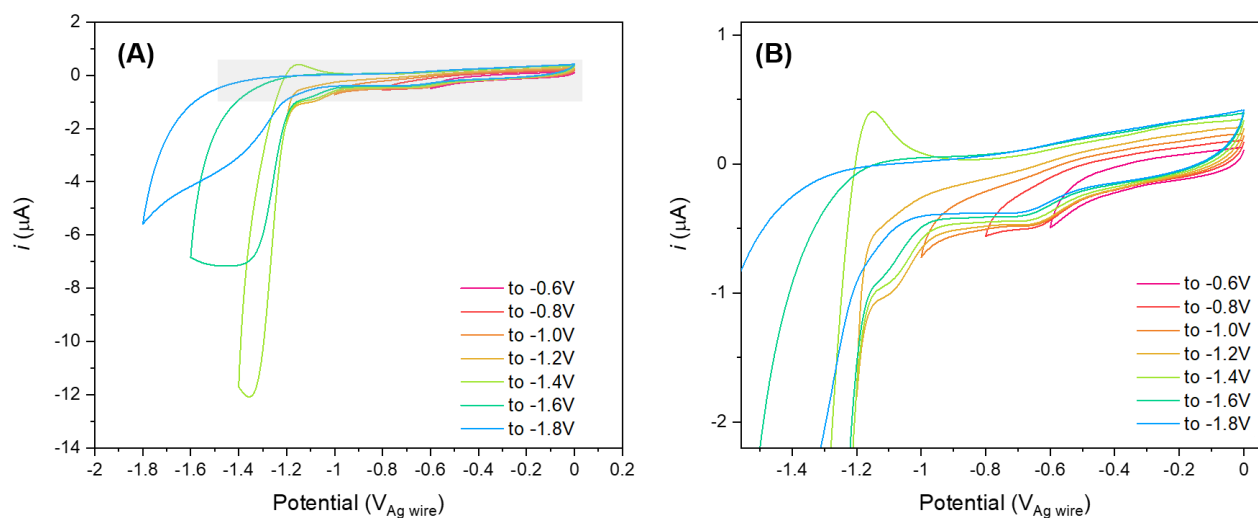


Figure 48 CV of 1 mM $[\text{Ni}(\text{cyclam})]^{2+}$ at a GCE in 0.1 M TBA PF₆ in dry MeCN at 50 mV/s under CO₂ vs Ag wire. (B) Close up of inset in the grey box.

3.3 Pulsed electrolysis on Ni(cyclam)

Using a GCE as the working electrode in an aqueous solution of 0.1 mM Ni(cyclam) in CO₂ saturated 0.5 M NaCl, short (ms) asymmetric anodic pulses (E_A) were applied throughout electrolysis. **Figure 49** shows a comparison between a potentiostatic (denoted as Standard) and pulsed electrolysis. The standard electrolysis was held at a cathodic potential (E_C) of -1.6V vs Ag/AgCl throughout. For initial pulsed electrolysis studies E_C was held for 5s (t_C) before an anodic potential (E_A) of -1.0V vs Ag/AgCl was applied for 0.2s (t_A). The pulsed voltage profile led to a four-fold increase in selectivity for CO ($\text{CO}/\text{H}_2 = 2.42 \pm 0.10$), that was stable over three hours, compared with the standard run ($\text{CO}/\text{H}_2 = 0.63 \pm 0.21$). The pH of the electrolyte was measured before and after electrolysis, where a slight increase was observed post-electrolysis (from 6.3 to 7.8 (standard), 7.7 (pulsed)) in both the standard and pulsed run.

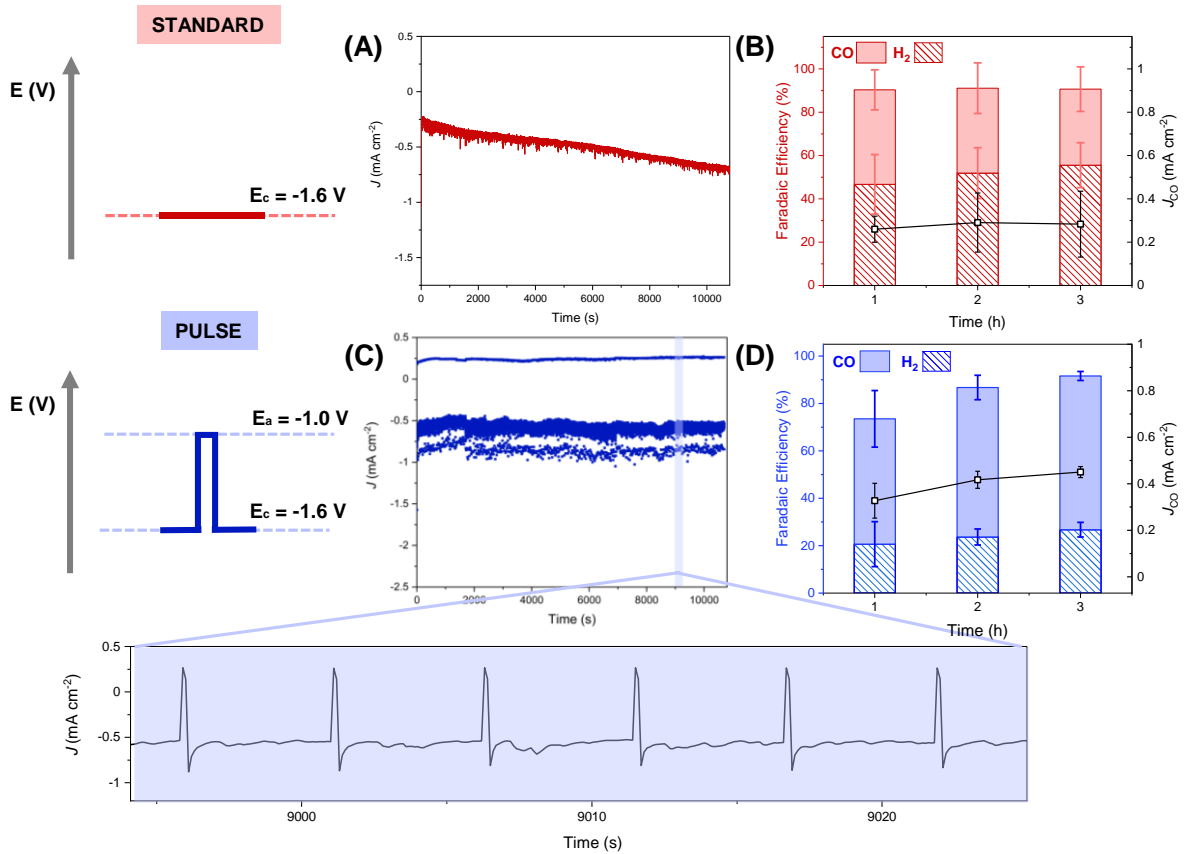


Figure 49 Comparison of standard ($E_C = -1.6 \text{ V}_{\text{Ag}/\text{AgCl}}$) and pulsed ($E_C[t_C] = -1.6 \text{ V}_{\text{Ag}/\text{AgCl}}$ [5 s]; $E_A[t_A] = -1.0 \text{ V}_{\text{Ag}/\text{AgCl}}$ [0.2s] electrolysis of $0.1 \text{ mM} [\text{Ni}(\text{cyclam})]^{2+}$ in $0.5 \text{ M NaCl}(\text{aq})$ over 3h. (A) Chronoamperometry trace of standard run (B) FEs and CO partial current densities of standard run (C) Chronoamperometry trace of pulse run (D) FEs and CO partial current densities of pulse run.

To give some insight into the energy required to instate these pulses the total cell voltage and energy efficiency was calculated for both the standard and the pulse run using the equations below and is shown in

Table 3.

$$\text{Full Cell Voltage Efficiency: } VE_{full\ cell} = \frac{(E_{OER}) + (-E_{CO})}{(E_{full\ cell})} \quad (13)$$

$$\text{CO Full Cell Energetic Efficiency: } EE_{full\ cell} = VE_{full\ cell} \times FE_{CO} \quad (14)$$

Where $E_{full\ cell}$ is the full cell applied potential; $E_{CO} = -0.109 \text{ V}$ and $E_{OER} = +0.817$ are the thermodynamic potentials (vs RHE at pH 7) of CO_2 reduction to CO and the oxygen evolution reaction respectively, and FE_{CO} is the measured CO Faradaic efficiency as a percentage.⁴⁷ The

full cell voltage efficiency for the pulsed system is lower than for the standard system due to a higher overall cell potential however total cell energy efficiency for CO₂ to CO of the pulse system is almost double that of the standard experiment demonstrating that any energy losses associated with the voltage pulse are offset by the increased FE for CO and higher CO production rate. The limitations of this method of investigating the energy requirements of pulsed electrolysis are that it only takes into account cell potential and faradaic efficiency, other methods such as calculating anodic charge and duty cycle are also quantified later in the chapter.

Sample	Av. E _{WE} (V)	Av. E _{CE} (V)	E _{full cell} (V)	VE _{full cell}	FE _{CO} (%)	EE _{full cell} (%)
Standard	-1.60	1.32	2.92	0.32	35.12	11.23
Pulsed (E _a = -1.0V)	-1.58	1.56	3.14	0.29	64.86	18.81

Table 3 Full cell energy efficiencies of standard and pulse electrolysis of 0.1 mM NiCyc and 0.5 M NaCl

The longevity of this effect was measured in extended electrolysis experiments shown in **Figure 50** and **Figure 51**. In both cases pulsed electrolysis shows significantly better selectivity over longer time scales, achieving CO/H₂ > 1 after 12 h without stopping electrolysis or using a CO scavenger. However, while reproducibility was very high up to 3 h the two datasets vary in stability at longer times suggesting further experimentation is required to quantitatively effect the durability of this system.

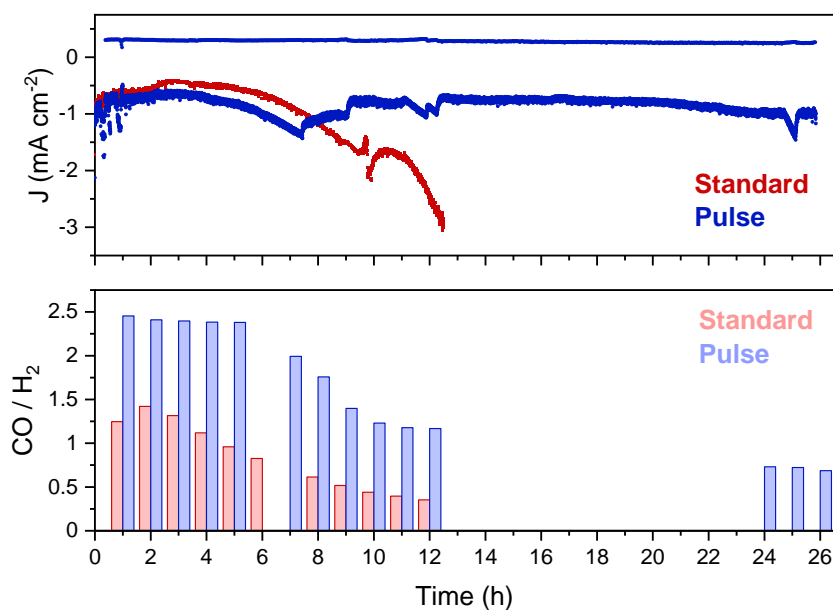


Figure 50 Selectivities (columns) and current densities (symbol) of standard and pulse electrolysis of 0.1 mM Ni(cyclam) in 0.5 M NaCl (aq) over 12 to 26 h. Standard electrolysis ($E = -1.6$ V) (red) and pulse electrolysis ($E_c = -1.6$ V (5s) $E_a = -1.0$ V (0.2 s)) (blue). The standard experiment was stopped after 12 hours due to the rapid increase in current due to increased hydrogen evolution.

comparison of a clean GCE and an electrode post 3 h standard electrolysis (fouled) is shown in 0.5 M NaCl, here the fouled electrode shows a significantly earlier onset for hydrogen evolution.

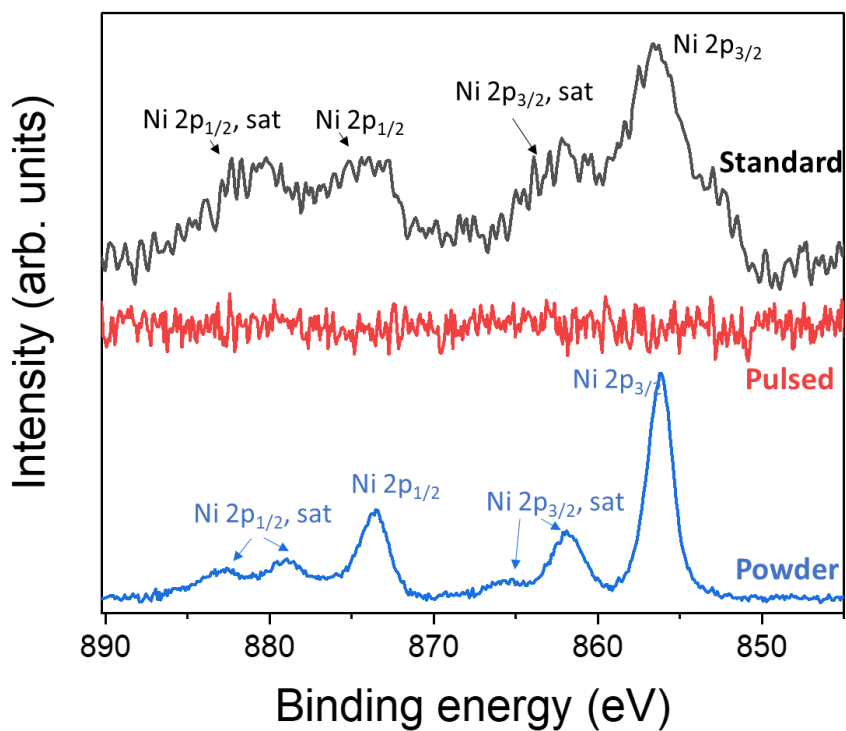


Figure 52 Ni 2p XPS spectra for glassy carbon substrate post 3 h standard (black) and pulse electrolysis (red). The spectrum of Ni(cyclam) powder (blue) is added at the bottom for reference.

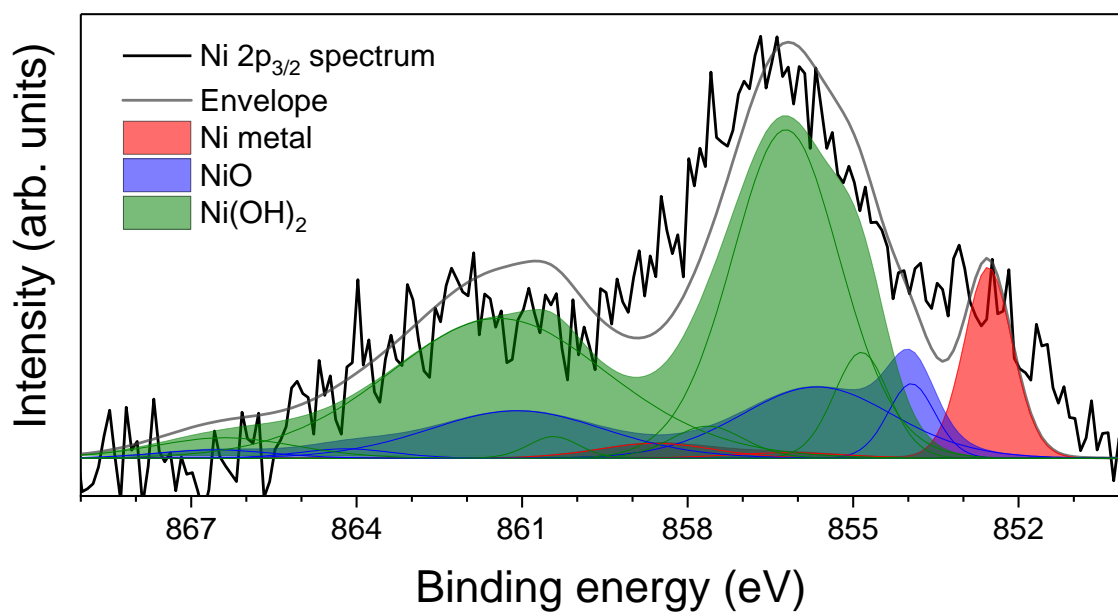


Figure 53 Deconvolution of Ni 2p XPS spectra of glassy carbon substrate post 3 h standard electrolysis showing peaks corresponding to Ni, NiO and Ni(OH)₂

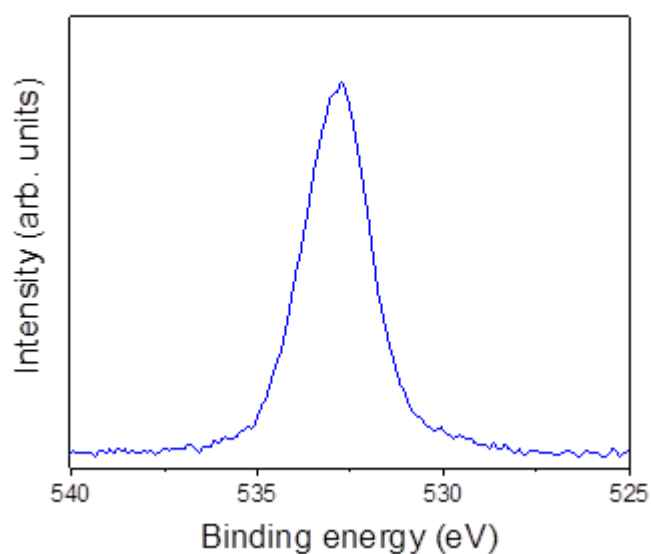


Figure 54 O 1s spectrum for glassy carbon substrate post 3 h standard electrolysis

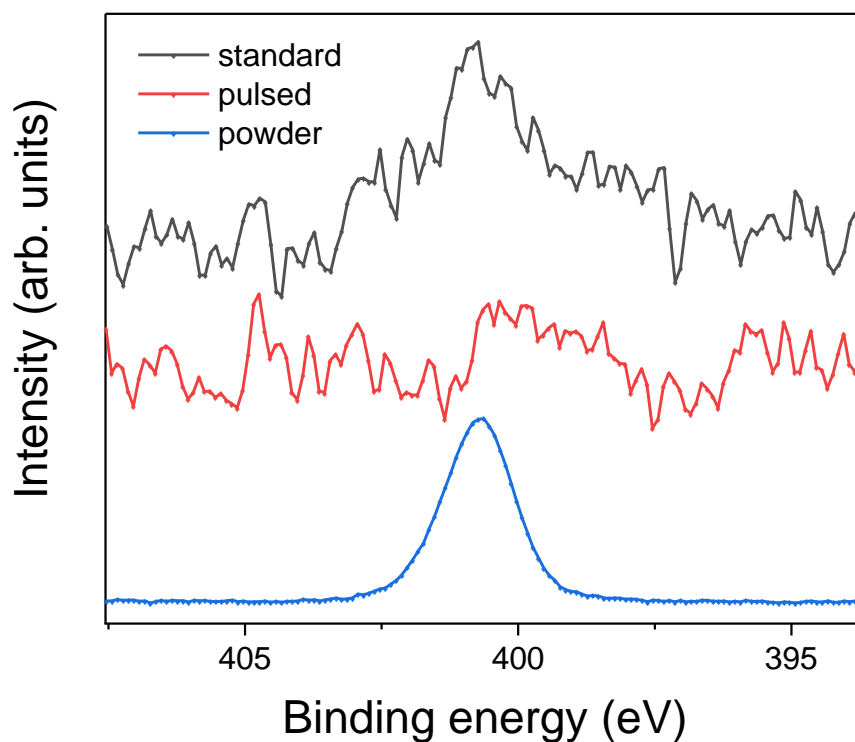


Figure 55 *N 1s* XPS spectra for glassy carbon substrate post 3 h standard (black) and pulse electrolysis (red). The spectrum of Ni(cyclam) powder (blue) is added at the bottom for reference.

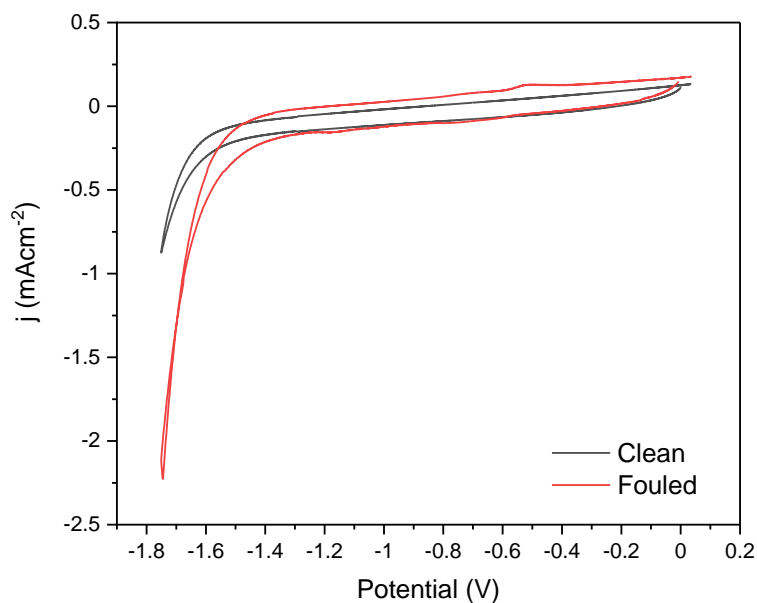


Figure 56 CVs of GCE in 0.5 M NaCl(aq) under Ar both before (Clean) and after (Fouled) 3 h standard electrolysis in 0.1 mM Ni(cyclam) in 0.5 M NaCl(aq) at $-1.6 V_{Ag/AgCl}$

3.3.1 Potential dependence of pulsed electrolysis

The XPS analysis suggests that pulsing prevents the decomposition and over reduction of Ni(cyclam) leading to increased CO selectivity when compared to the potentiostatic run. This prevention of Ni deposition could be achieved through Faradaic or non-Faradaic mechanisms. To probe this, a series of electrolysis experiments were run with varying E_A , the results of which are shown in **Figure 57-Figure 59** and CO / H₂ compared at 3 h of electrolysis in **Figure 63**. The selectivity of the pulse runs where $E_A > -1.3 \text{ V}_{\text{Ag}/\text{AgCl}}$ show much greater CO / H₂ when compared to the standard run however show no significant effect of E_A from $-1.0 \text{ V}_{\text{Ag}/\text{AgCl}}$ to $-0.3 \text{ V}_{\text{Ag}/\text{AgCl}}$. When $E_A = -1.3 \text{ V}_{\text{Ag}/\text{AgCl}}$ the positive effect of pulsing disappears and the CO / H₂ drops to ~ 0.7 , within the error of standard electrolysis run.

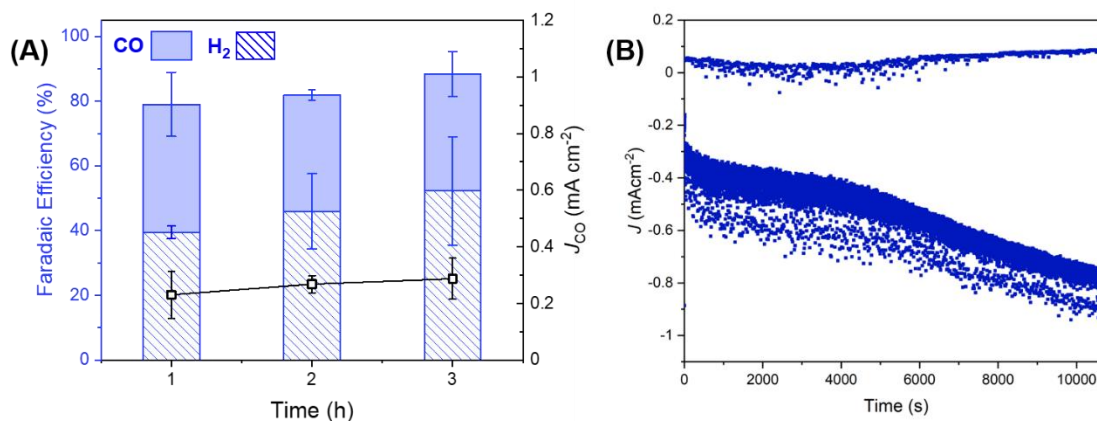


Figure 57(A) FEs and CO partial current densities (B) Chronoamperometry trace of pulsed electrolysis where $E_c = -1.6 \text{ V}_{\text{Ag}/\text{AgCl}}$ and $E_A = -1.3 \text{ V}_{\text{Ag}/\text{AgCl}}$

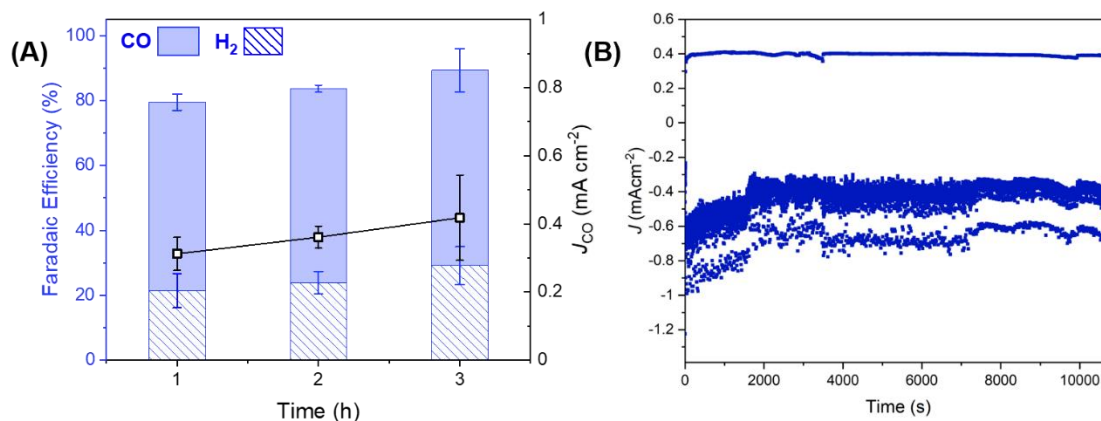


Figure 58(A) FEs and CO partial current densities (B) Chronoamperometry trace of pulsed electrolysis where $E_c = -1.6 V_{Ag/AgCl}$ and $E_A = -0.8 V$

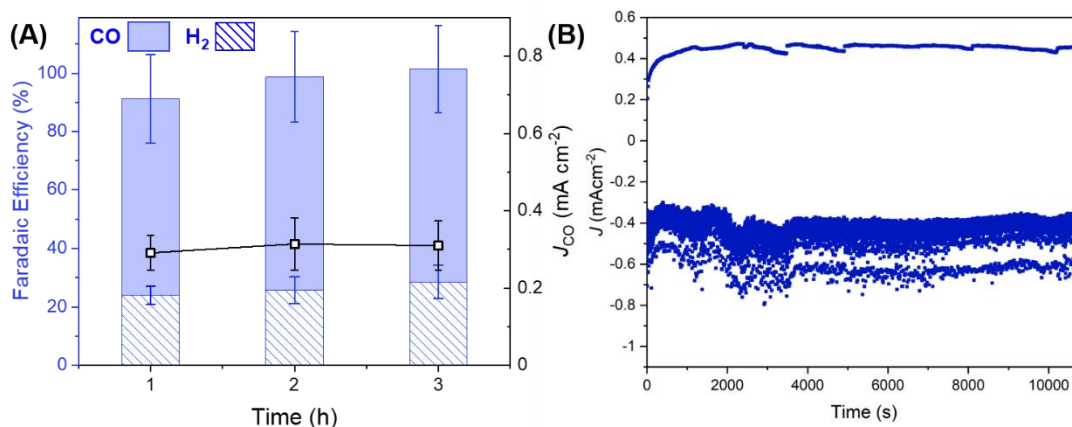


Figure 59(A) FEs and CO partial current densities (B) Chronoamperometry trace of pulsed electrolysis where $E_c = -1.6 V_{Ag/AgCl}$ and $E_A = -0.3 V$

To investigate this observation, firstly non-Faradaic processes were considered to assess if the voltage step could lead to a rearrangement of the electrolyte, refreshing the catalyst/CO₂ at the GCE surface and remove species such as [Ni(cyclam)(CO)]⁺, prior to their irreversible reduction. The largest rearrangement of the electrolyte would be expected to occur if the potential was stepped across the potential of zero charge (pzc) where the charge on the electrode would flip.

To calculate the pzc, first the double-layer capacitance (C_{dl}) is calculated from measurements were taken of the GCE in 0.1 and 1 mM NaCl electrolyte using impedance spectroscopy. The C_{dl} can be expressed as the composition of two components: C_H which is capacitance of the

charges at the outer Helmholtz plane and is independent of electrode potential and electrolyte concentration and C_D which is the capacitance of the diffuse charge which increases with increasing electrolyte concentration and electrode polarizations (see Eq (15)). The C_{dl} is dominated by the smaller of the two components, thus when larger electrolyte concentrations used C_D becomes so large, only the C_H is observed, thus lower electrolyte concentrations were used.

$$\frac{1}{C_{dl}} = \frac{1}{C_H} + \frac{1}{C_D} \quad (15)$$

Fundamentals of electrochemical impedance spectroscopy and the methods used to extract differential capacitance are given in much better detail in the literature,^{50,51} however a brief overview is given below.

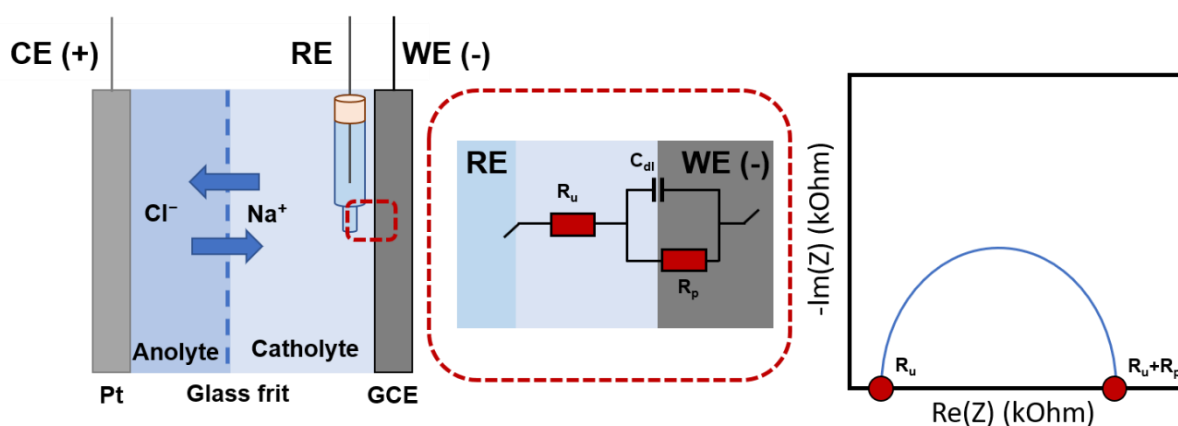


Figure 60 Schematic of a 3-electrode setup with inset showing the equivalent circuit (left) with the corresponding Nyquist plot (right).

Figure 60 shows a 3-electrode cell set-up, where a known potential difference is applied between the reference and working electrode. The resulting current is impeded by three equivalent circuit components (i) the ohmic resistance of the electrolyte between the working and the reference electrode known as uncompensated resistance (R_u) (ii) the polarisation resistance (R_p) which is the resistance of species to charge transfer assessing the changes in voltage compared to current at steady state ($R_p = \Delta V/\Delta i$) and (iii) the capacitive component arising as a result of the charging and discharging of the electrical double layer (C_{dl}).

To measure the pzc of our cell, the C_{dl} needs to be measured across a potential range, as the pzc is approached we expect the C_{dl} to be at a minimum as no excess charge prevails at the electrode. This is related to measured impedance as follows:

Ideal Capacitance (C_{dl}) from measured impedance:

$$Z = Z_{Re} + iZ_{Im} = R + (iC\omega)^{-1} \quad (16)$$

$$C_{dl} = -(\omega Z_{Im})^{-1} \text{ where } \omega = 2\pi f \quad (17)$$

Where Z is the impedance of the interfacial region between the working and reference electrode, where Z_{Re} and Z_{Im} are the real and imaginary parts respectively; ω is the angular frequency of the ac perturbation; f is the frequency. Here the capacitance is calculated using the single-frequency impedance over a potential range of +0.6 V_{Ag/AgCl} to -1.2 V_{Ag/AgCl} as described in literature.⁵⁰ To do this a full range frequency scan was ran at OCP (-0.2 V_{Ag/AgCl}) and fitted to an equivalent circuit (**Figure 61b** and c), here the Nyquist plot shows a large, depressed semi-circle with an R1 of 6.9 kOhm (attributed to R_U). The depressed nature of the semicircle indicates that our system was not acting as an ideal capacitor (denoted as Q) and thus capacitance is more accurately calculated with the equation below.

Non – ideal Capacitance (Q) from measured impedance:

$$Q = \frac{\omega^{\alpha-1}}{Z_0 \sin \frac{\pi}{2} \alpha} \quad (18)$$

Here Z_0 and α are positive constants, α being a value from 0 to 1 where the closer the value to 1, the closer the system is to behaving as an ideal capacitor,⁵² here $\alpha = 0.85$. Values for Z_0 and α were obtained from the fit, shown in **Figure 61b** and c, and Q was calculated for each frequency using Eq(18). This was compared to ideal capacitance (C) values calculated using Eq (17) (plotted in **Figure 61d**). Single frequencies were chosen where the variation between ideal and non-ideal capacitance values showed little variation. From here the capacitance was calculated using the single-frequency chose previously and Eq (17). Impedance measurements were ran every 36 mV over a potential range of +0.6 to -1.2 V_{Ag/AgCl} with 1-minute equilibration time between each potential with an amplitude (V_a) of 10 mV (shown in **Figure 62**).

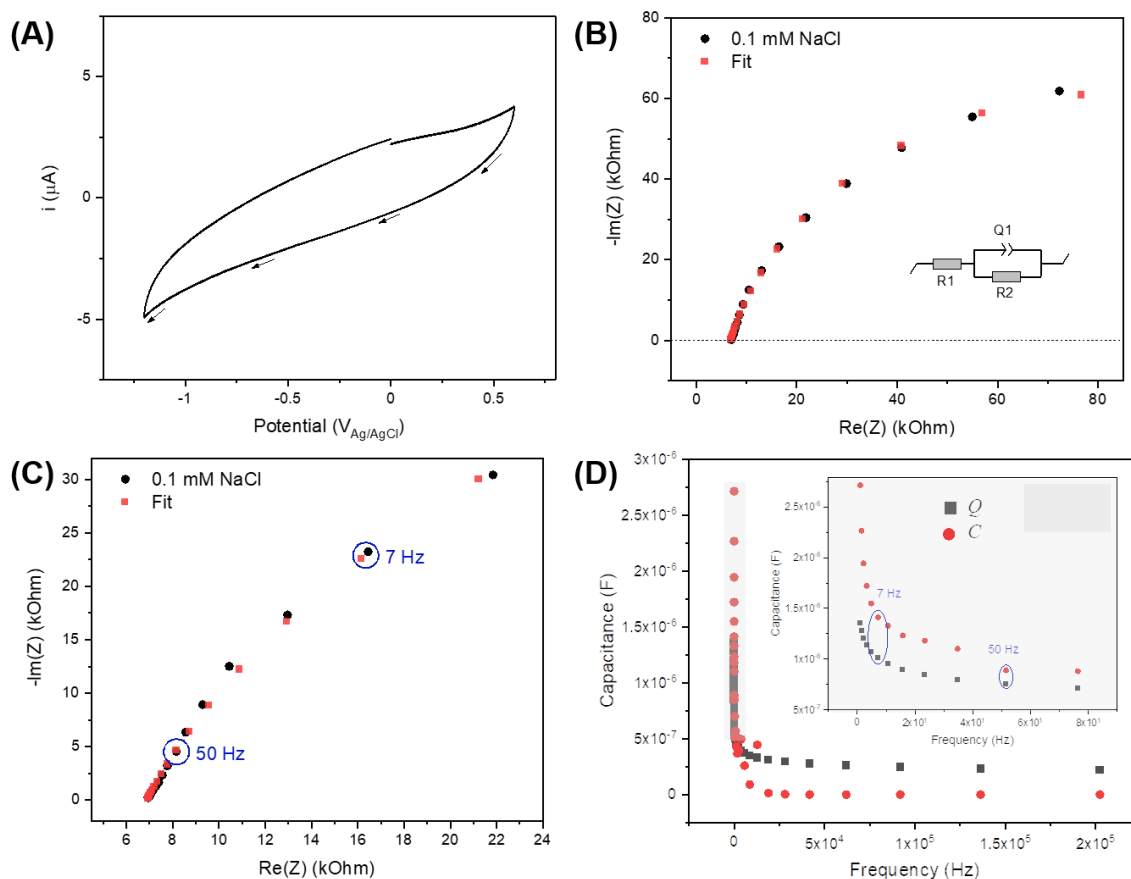


Figure 61 *0.1 mM NaCl(aq) on GCE under N₂ (A) CV at scan rate of 100 mV/s (B) Nyquist plot from 300 kHz to 1 Hz at OCP with equivalent circuit shown (C) Zoom in of capacitive region of Nyquist plot (D) Plot of both ideal, C, and non-ideal, Q, capacitance over the range of frequencies. Single frequencies chosen for further analysis are circled.*

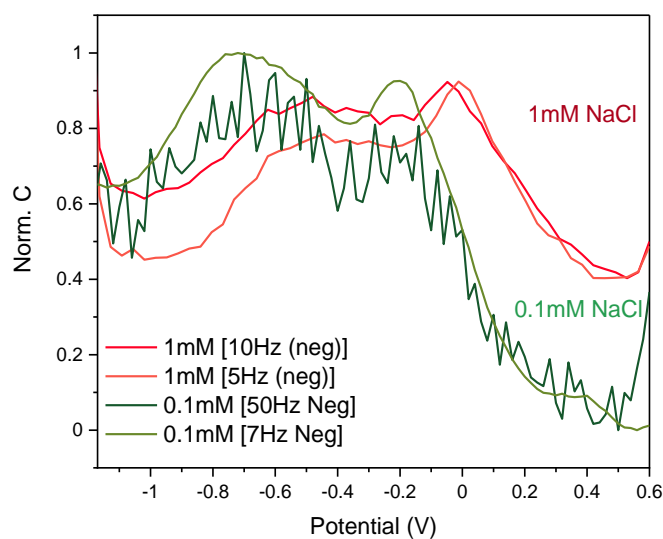


Figure 62 Normalised differential capacitance curves of GCE in NaCl (aq)

Double layer capacitance measurements establish the pzc to be +0.4 V vs Ag/AgCl, in line with other reports (**Figure 62**). The pzc is significantly positive of the values of E_A (-0.3 to -1.0 V) where we see a beneficial effect of pulsing (**Figure 63**).^{53,54} Some changes in the differential capacitance do occur between -0.3 and -1.0 V but it is notable that the selectivity for CO production is approximately constant when E_A is varied between these voltages (CO/H₂ ~ 2.0 to 2.5, **Figure 63**) therefore the lack of Ni deposition and increase in selectivity for CO₂RR is unlikely to be caused by double layer rearrangement.

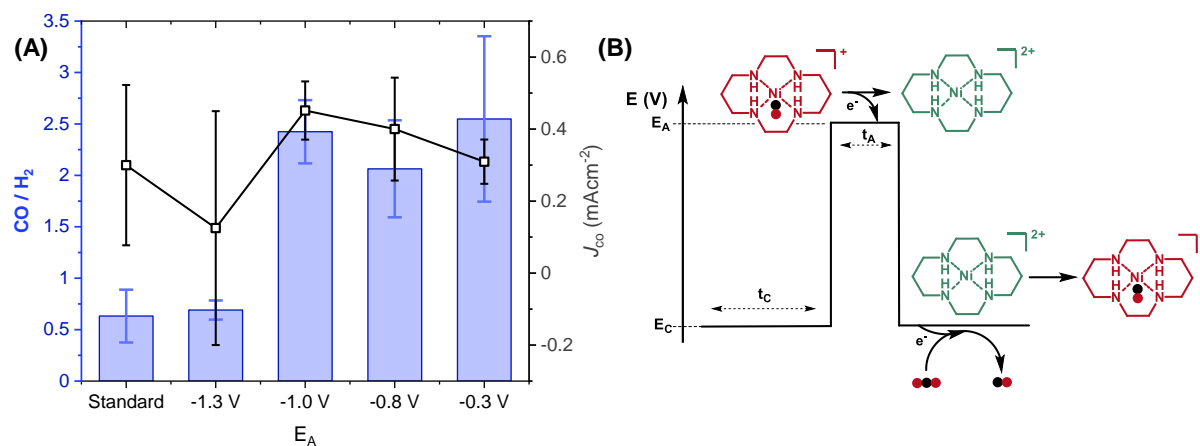


Figure 63(A) Comparison of CO/H₂ and CO partial current densities after 3 h electrolysis of 0.1 mM [Ni(cyclam)]²⁺ in 0.5 M NaCl(aq) where E_c[t_c] = -1.6 V_{Ag/AgCl} [5 s]; t_A = 0.2 s with changing E_A (B) Schematic illustrating the proposed mechanism of how pulsed electrolysis can reduce catalyst degradation.

We next consider if a Faradaic process is occurring during the anodic pulse. **Figure 63** shows that when E_A is positive of the oxidation of the Ni(0) species (-0.55 V **Figure 43**) no additional increase in selectivity for CO₂RR is observed when compared to experiments with E_A at -1.0 V suggesting that oxidation of Ni(0) carbonyl is not significantly contributing to increased selectivity. However, when E_A = -1.3 V the CO/H₂ drops to 0.7 ± 0.1, equal to that measured under standard electrolysis conditions. The selectivity for CO is greater for pulsed runs with E_A > -1.3V, but J_{CO} remains the same within error. This is due to an overall increase in current associated with increased hydrogen evolution when E_A = -1.3 V (or when potentiostatic conditions are used). The oxidation at -1.35 V in **Figure 43** is assigned to [Ni(cyclam)(CO)]⁺ to [Ni(cyclam)]²⁺.³⁷ Therefore we conclude that pulsing decreases the concentration of [Ni(cyclam)(CO)]⁺ at the electrode surface, preventing subsequent reduction to Ni(0), **Figure 63b**. One past study employed a prolonged (10 minute) oxidation of a cyclam complex at very positive potentials (+0.8 V vs RHE, approximately +0.2 V vs Ag/AgCl). This led to a short-lived recovery in the rate of CO production (~ 20 minutes) but there was no significant decrease in hydrogen evolution demonstrating the importance of continuous removal of [Ni(cyclam)(CO)]⁺ using the pulsed voltage profile.³⁴

3.3.2 Time dependence of pulsed electrolysis

The time dependence of the anodic (t_A) pulse duration was also investigated whilst keeping t_C constant at 5 s, **Figure 64**. It is desirable to minimize t_A to increase the duty cycle (percentage of time that the device is held at operating potential (Eq (19))).

$$Duty\ Cycle\ (\%) = \frac{t_C}{T} \times 100 \quad (19)$$

Where t_c is time spent at the cathodic potential (undergoing eCO_2R) and T is total time of cycle. The shortest t_A value we could achieve during a prolonged electrolysis experiment with our apparatus was 40 ms corresponding to a duty cycle of >99% (**Table 4**). Even with this very short pulse duration we see an increase in selectivity ($CO/H_2 = 1.86 \pm 0.16$) when compared to the potentiostatic experiment ($CO/H_2 = 0.63 \pm 0.21$). While extending t_A to 1 s leads to a small but measurable increase in selectivity compared with shorter pulses ($CO/H_2 = 3.62 \pm 0.87$, $FE_{CO} \sim 80\%$, **Figure 64**), further suggesting the improvement is driven by a Faradaic process.

Another parameter previously used for assessing pulse profiles during CO_2R at metals is cathodic charge fraction (Q_C) shown below.¹⁶

$$Q_{total} = q_C + q_A \quad (20)$$

$$Q_C (\%) = \frac{q_C}{Q_{total}} \times 100 \quad (21)$$

$$Q_A (\%) = \frac{q_A}{Q_{total}} \times 100 \quad (22)$$

Where q_C is all cathodic charge passed, q_A is all anodic charge passed and Q_{total} is all charge passed. Q_C highlights the benefit of both reducing t_A ($Q_C = 91.2\%$, 96.3% and 97.5% for $t_A = 1.0$ s, 0.2 s and 0.04 s, **Table 4**) and opting for a less positive E_A ($Q_C = 96.3\%$ and 98.7 for $E_A = -0.3$ V and -1.0 V, **Table 4**).

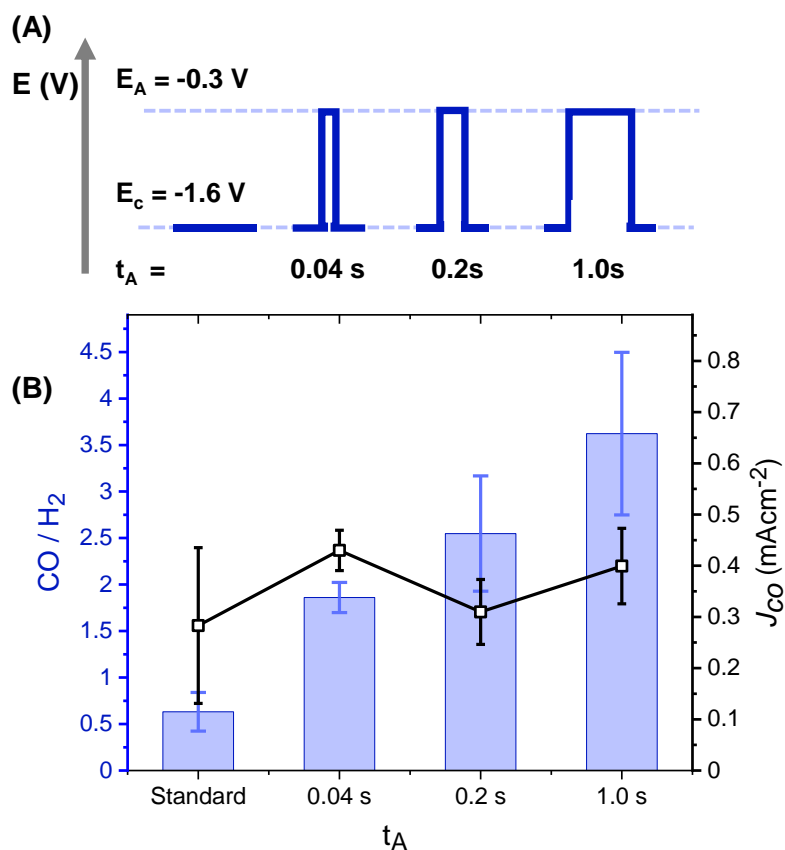


Figure 64 (A) Schematic of different pulse profiles with increasing t_a (not to scale) (B) Comparison of CO / H₂ and CO partial current densities after 3 h electrolysis of 0.1 mM [Ni(cyclam)]²⁺ in 0.5 M NaCl(aq) where $E_c[t_c] = -1.6 V_{Ag/AgCl}$ [5 s]; $E_A = -0.3 V_{Ag/AgCl}$ with changing t_A .

Table 4 The effective charge in both the cathodic and anodic regions

E_c (V) [t_c]	E_A (V) [t_A]	Q_c (%)	Q_A (%)	Duty Cycle (%)
-1.6 [5.0s]	-0.3 [0.2 s]	96.3	3.7	96.2
	-0.8 [0.2 s]	97.9	2.1	96.2
	-1.0 [0.2 s]	98.7	1.3	96.2
	-0.3 [0.04 s]	97.5	2.5	99.2
	-0.3 [1.0 s]	91.2	8.8	83.3

To qualitatively analyse the Faradaic and non-Faradaic current contributions of the pulse, short (< 1 min) pulsed electrolysis was ran to achieve higher time resolution (**Figure 65**) following methods by Kimura *et al.*⁵⁵. The pulse profile shown in **Figure 65** was the average of ten pulses. Here the initial current is expected to be dominated by the non-Faradaic (capacitive) current, whereas at longer times, Faradaic currents govern the overall response. An ideal capacitor would show a linear response when the natural log of current density is plotted against time, while it's important to note this system is not an ideal capacitor, a good linear relationship is observed at initial times which begins to deviate at longer times. At ~ 10 ms after the pulse the experimental data shows a 10% deviation from the linear fit which could suggest the Faradaic current is significant here, explaining how CO/H₂ is increased even at t_A 40 ms.

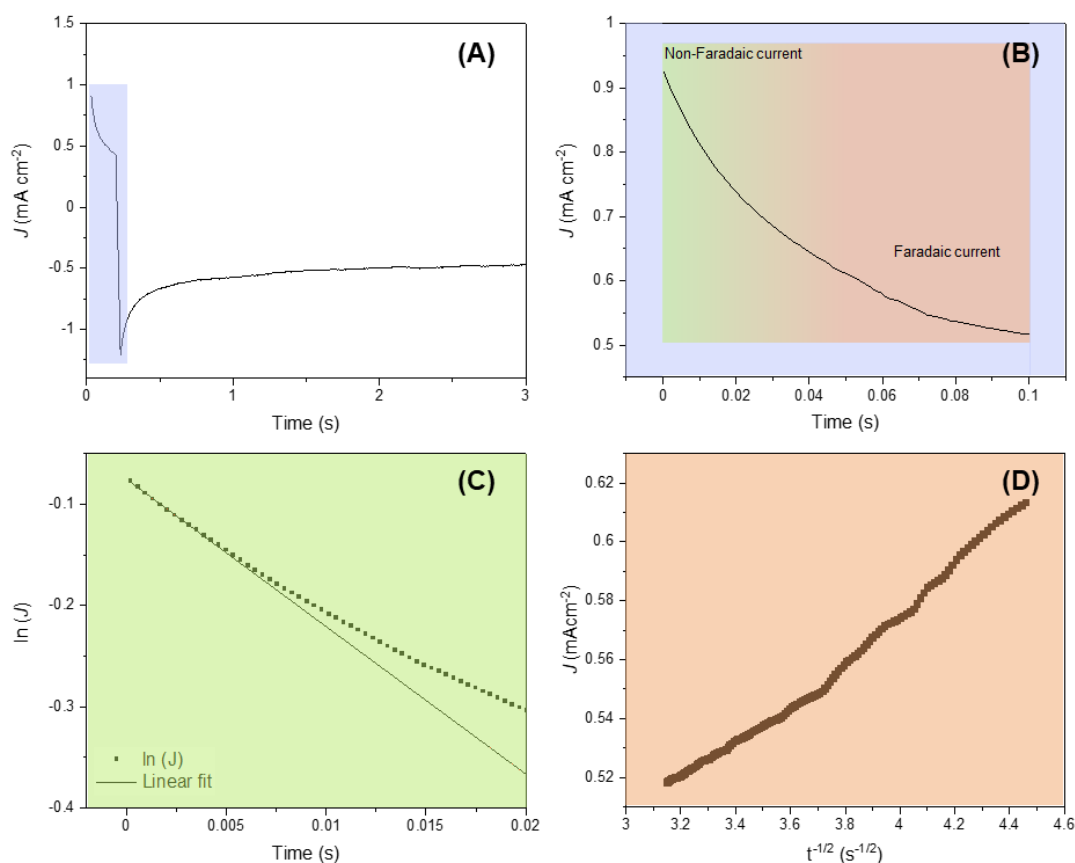


Figure 65 (A) Full pulse profile ($t_a = 200$ ms; $E_a = -0.3$ V vs Ag/AgCl; $t_c = 5$ s; $E_c = -1.6$ V vs Ag/AgCl). (B) Total anodic current averaged over 10 pulses. (C) Natural log of anodic current showing non-Faradaic current in the linear regime. (D) Faradaic current plotted against $t^{-1/2}$. Green represents non-Faradaic contributions and pink represents Faradaic contributions to total current.

3.3.3 Testing pulsed electrolysis on zero-gap cell

Finally, pulsed electrolysis was tested in a zero-gap reverse bias BPM cell by Dr Bhavin Siritanaratkul, who previously demonstrated CO poisoning was an issue in static electrolysis conditions with Ni(cyclam). Where the cathode comprised of 5 mg Ni(cyclam) 1 mL H₂O, 1 mL isopropyl alcohol and 80 μ L of 5% Nafion solution was sprayed onto carbon paper, the anode was RuO₂ on carbon paper, separated by a Fumasep BPM.

As the zero-gap is a two-electrode setup, chronopotentiometry was used where cathodic current density (i_c) of -25 mAcm^{-2} was used throughout for the standard electrolysis run. For the pulsed run the same i_c was held for 5 s before anodic current (i_A) of $+10 \text{ mAcm}^{-2}$ was applied for 1 s. From the previous pulsed chronoamperometry data (**Figure 49** & **Figure 57-Figure 59**), the anodic current was significantly positive in all runs, with the exception of when $E_A = -1.3 \text{ V}$ where i_A rose only slightly positive of zero and the resulting CO/H₂ selectivity showed no improvement when compared to standard electrolysis. As there was no way to control the potential of the working electrode, i_A was ensured to be significantly positive at $+10 \text{ mAcm}^{-2}$. A longer t_A was selected to ensure enough time for the cell to respond to the pulse as the surface area of the GDE was over 70x larger than the GCE used previously, the time constant of the zero-gap cell was significantly larger. The total cell potentials and CO/H₂ data is shown in **Figure 66**.

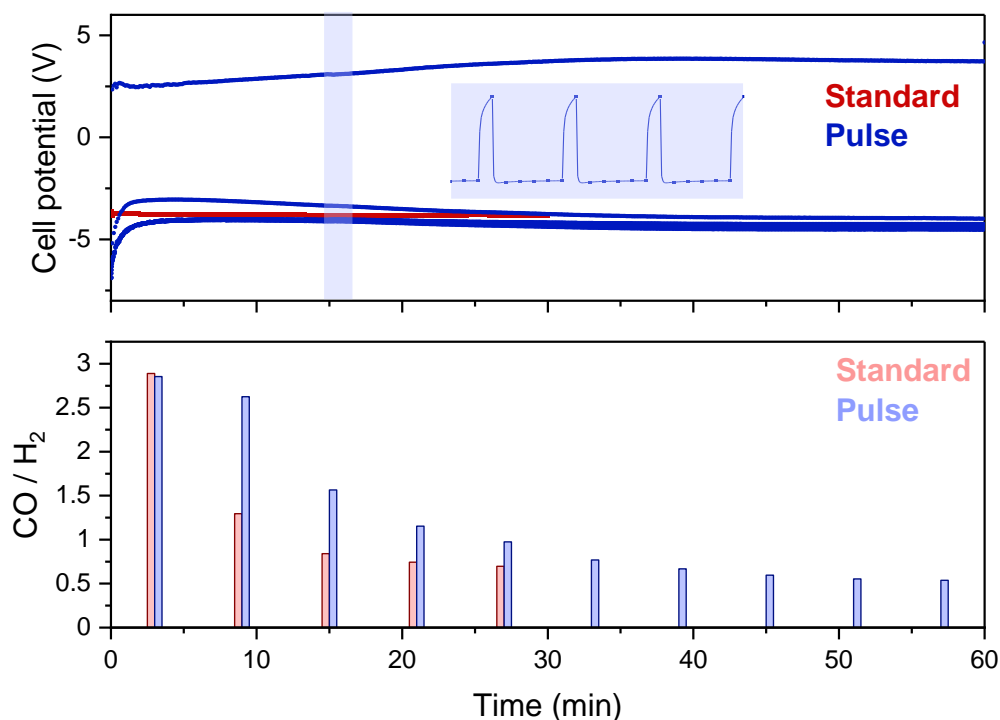


Figure 66 Comparison of standard (-25 mAcm^{-2}) and pulsed run ($i_c [t_c] = -25 \text{ mAcm}^{-2} [5 \text{ s}]$; $i_A [t_A] = +10 \text{ mAcm}^{-2}$) on reverse-bias BPM electrolyser. Blue inset shows zoomed in pulse.

Figure 66 shows the initial CO/H₂ selectivity of pulsed and standard runs are very similar, as the electrolysis proceeds the pulsed run shows a marginally slower decline. However, by 30 min the CO/H₂ for both the pulsed and standard runs had dropped from ~ 3 to ~ 1 suggesting that the pulsing was not able to increase the stability of the catalyst for very long. There could be many explanations for this, a large limitation is the 2-electrode set-up which gives us no control of the potential applied to the working electrode, a parameter that has shown to be crucial in improving the selectivity through pulsing. Here the catalyst is also deposited rather than homogeneously in solution as in previous experiments, this could mean that even if $[\text{Ni}(\text{cyclam})(\text{CO})]^+$ was regularly oxidised by the pulse, the mass transport is not sufficient to move the recovered catalyst from the electrode before further reduction. A third possibility is that the zero-gap cell is ran at significantly larger currents leading to much larger CO production, thus pulsing (under conditions showed) cannot keep up with the increase in catalyst deactivation as a result.

As with all electrochemistry experiments, pulse electrolysis is heavily dependent on the cell setup used. While the customisability of pulsed electrolysis through amending parameters such

as E_A and t_A makes it an incredible tool, it also requires significant investigation and optimisation for each individual system, which unfortunately was beyond the scope of this chapter.

3.4 Conclusions and Future Work

To conclude, this chapter has shown that short (ms - s) asymmetric voltage pulse profiles can be used to improve the selectivity and achieve stable operation of the molecular catalyst, Ni(cyclam) for CO₂R to CO. A theory for the mechanism was proposed through electrochemical investigation and ex-situ XPS, that the anodic pulse worked by rapidly removing [Ni(cyclam)(CO)]⁺, preventing the complex from undergoing irreversible reduction to degradation product, Ni(0) carbonyl which when formed acts as a HER catalyst. This led to a four-fold increase in the CO selectivity with pulsed electrolysis compared to potentiostatic over the first three hours of the reaction, however at longer reaction times this effect becomes less pronounced and reproducible.

The duration of the anodic pulse was also investigated, here Faradaic contributions were shown to dominate the current after only 10 ms, leading to observable improvements in selectivity in pulsed electrolysis with anodic pulse durations of just 40 and 200 ms, corresponding to impressive duty cycles of >99 % and 96% respectively. Finally, pulsed electrolysis was attempted on the zero-gap cell, where, unfortunately an increase in selectivity was not sustained. As many different variables could account for this, future experiments deconvoluting these would be extremely useful.

More widely the use of short asymmetric pulse profiles may offer a way to modify the activity and stability of a wider range of molecular catalysts through both the in-situ regeneration of activate catalytic species and possible non-Faradic processes such as modifying the local pH and CO₂ concentration at the electrode.

3.5 References

- 1 K. J. P. Schouten, *Nat Energy*, 2021, **6**, 335–336.
- 2 D. Higgins, C. Hahn, C. Xiang, T. F. Jaramillo and A. Z. Weber, *ACS Energy Lett*, 2019, **4**, 317–324.
- 3 J. A. Rabinowitz and M. W. Kanan, *Nat Commun*, 2020, **11**, 10–12.
- 4 I. Bhugun, D. Lexa and J.-M. Savéant, *J Phys Chem*, 1996, **100**, 19981–19985.
- 5 K. Guo, H. Lei, X. Li, Z. Zhang, Y. Wang, H. Guo, W. Zhang and R. Cao, *Chin J Catal*, 2021, **42**, 1439–1444.
- 6 M. König, J. Vaes, E. Klemm and D. Pant, *iScience*, 2019, **19**, 135–160.
- 7 Y. Q. Wang, X. H. Dan, X. Wang, Z. Y. Yi, J. Fu, Y. C. Feng, J. S. Hu, D. Wang and L. J. Wan, *J Am Chem Soc*, 2022, **144**, 20126–20133.
- 8 R. Casebolt, K. Levine, J. Suntivich and T. Hanrath, *Joule*, 2021, **5**, 1987–2026.
- 9 T. Liu, J. Wang, X. Yang and M. Gong, *J Energy Chem*, 2021, **59**, 69–82.
- 10 C. Kim, J. C. Bui, X. Luo, J. K. Cooper, A. Kusoglu, A. Z. Weber and A. T. Bell, *Nat Energy*, 2021, **7**, 116–116.
- 11 R. Shiratsuchi, Y. Aikoh and G. Nogami, *J Electrochem Soc*, 1993, **140**, 3479–3482.
- 12 J. Lee and Y. Tak, *Electrochim Acta*, 2001, **46**, 3015–3022.
- 13 J. Yano and S. Yamasaki, *J Appl Electrochem*, 2008, **38**, 1721–1726.
- 14 B. Jermann and J. Augustynski, *Electrochim Acta*, 1994, **39**, 1891–1896.
- 15 S. C. Lin, C. C. Chang, S. Y. Chiu, H. T. Pai, T. Y. Liao, C. S. Hsu, W. H. Chiang, M. K. Tsai and H. M. Chen, *Nat Commun*, 2020, **11**, 1–12.
- 16 X.-D. Zhang, T. Liu, C. Liu, D.-S. Zheng, J.-M. Huang, Q.-W. Liu, W.-W. Yuan, Y. Yin, L.-R. Huang, M. Xu, Y. Li and Z.-Y. Gu, *J Am Chem Soc*, 2023, **145**, 2195–2206.
- 17 C. F. C. Lim, D. A. Harrington and A. T. Marshall, *Electrochim Acta*, 2016, **222**, 133–140.

- 18 S. H. Lee, I. Sullivan, D. M. Larson, G. Liu, F. M. Toma, C. Xiang and W. S. Drisdell, *ACS Catal*, 2020, **10**, 8000–8011.
- 19 R. Casebolt, K. W. Kimura, K. Levine, J. A. Cimada DaSilva, J. Kim, T. A. Dunbar, J. Suntivich and T. Hanrath, *ChemElectroChem*, 2021, **8**, 681–688.
- 20 T. Oguma and K. Azumi, *Electrochemistry*, 2020, **88**, 451–456.
- 21 J. C. Bui, C. Kim, A. Z. Weber and A. T. Bell, *ACS Energy Lett*, 2021, **6**, 1181–1188.
- 22 H. S. Jeon, J. Timoshenko, C. Rettenmaier, A. Herzog, A. Yoon, S. W. Chee, S. Oener, U. Hejral, F. T. Haase and B. Roldan Cuenya, *J Am Chem Soc*, 2021, **143**, 7578–7587.
- 23 N. Gupta, M. Gattrell and B. MacDougall, *J Appl Electrochem*, 2006, **36**, 161–172.
- 24 P. Friebe, P. Bogdanoff, N. Alonso-Vante and H. Tributsch, *J Catal*, 1997, **168**, 374–385.
- 25 C. W. Lee, N. H. Cho, K. T. Nam, Y. J. Hwang and B. K. Min, *Nat Commun*, 2019, **10**, 1–8.
- 26 B. J. Fisher and R. Eisenberg, *J Am Chem Soc*, 1980, **102**, 7361–7363.
- 27 M. Beley, J. P. Collin, R. Ruppert and J. P. Sauvage, *J Am Chem Soc*, 1986, **108**, 7461–7467.
- 28 M. Beley, J. Collin, R. Ruppert and J. Sauvage, *J. Chem. Soc., Chem. Commun.*, 1984, **2**, 1315–1316.
- 29 J. P. Collin, A. Jouaiti and J. P. Sauvage, *Inorg Chem*, 1988, **27**, 1986–1990.
- 30 J. D. Froehlich and C. P. Kubiak, *Inorg Chem*, 2012, **51**, 3932–3934.
- 31 F. Greenwell, G. Neri, V. Piercy and A. J. Cowan, *Electrochim Acta*, 2021, **392**, 139015.
- 32 G. Neri, I. M. Aldous, J. J. Walsh, L. J. Hardwick and A. J. Cowan, *Chem Sci*, 2016, **7**, 1521–1526.
- 33 G. Neri, J. J. Walsh, C. Wilson, A. Reynal, J. Y. C. Lim and A. J. Cowan, *Phys Chem Chem Phys*, 2015, **17**, 1562–1566.
- 34 S. Pugliese, N. T. Huan, A. Solé-Daura, Y. Li, J.-G. Rivera de la Cruz, J. Forte, S. Zanna, A. Krief, B.-L. Su and M. Fontecave, *Inorg Chem*, 2022, **61**, 15841–15852.

- 35 M. Fontecave, S. Pugliese, N. T. Huan, J. Forte, D. Grammatico, S. Zanna, B.-L. Su and Y. Li, *ChemSusChem*, 2020, **13**, 1–9.
- 36 B. Siritanaratkul, M. Forster, F. Greenwell, P. K. Sharma, E. H. Yu and A. J. Cowan, *J Am Chem Soc*, 2022, **144**, 7551–7556.
- 37 J. D. Froehlich and C. P. Kubiak, *J Am Chem Soc*, 2015, **137**, 3565–3573.
- 38 G. B. Balazs and F. C. Anson, *J Electroanal Chem*, 1993, **361**, 149–157.
- 39 C. A. Kelly, Q. G. Mulazzani, E. L. Blinn and M. A. J. Rodgers, *Inorg Chem*, 1996, **35**, 5122–5126.
- 40 A. W. Nichols, S. Chatterjee, M. Sabat and C. W. Machan, *Inorg Chem*, 2018, **57**, 2111–2121.
- 41 C. Cometto, L. Chen, P. K. Lo, Z. Guo, K. C. Lau, E. Anxolabéhère-Mallart, C. Fave, T. C. Lau and M. Robert, *ACS Catal*, 2018, **8**, 3411–3417.
- 42 A. N. Marianov, A. S. Kochubei, T. Roman, O. J. Conquest, C. Stampfl and Y. Jiang, *ACS Catal*, 2021, **11**, 3715–3729.
- 43 J. Jiang, A. J. Matula, J. R. Swierk, N. Romano, Y. Wu, V. S. Batista, R. H. Crabtree, J. S. Lindsey, H. Wang and G. W. Brudvig, *ACS Catal*, 2018, **8**, 10131–10136.
- 44 Y. Wu, Z. Jiang, X. Lu, Y. Liang and H. Wang, *Nature*, 2019, **575**, 639–642.
- 45 A. Zhanaidarova, C. E. Moore, M. Gembicky and C. P. Kubiak, *Chem Commun*, 2018, **54**, 4116–4119.
- 46 G. B. Balazs and F. C. Anson, *J Electroanal Chem*, 1992, **322**, 325–345.
- 47 C. M. Gabardo, A. Seifitokaldani, J. P. Edwards, C. T. Dinh, T. Burdyny, M. G. Kibria, C. P. O’Brien, E. H. Sargent and D. Sinton, *Energy Environ Sci*, 2018, **11**, 2531–2539.
- 48 M. C. Biesinger, B. P. Payne, A. P. Grosvenor, L. W. M. Lau, A. R. Gerson and R. St. C. Smart, *Appl Surf Sci*, 2011, **257**, 2717–2730.
- 49 B. D. McCarthy, C. L. Donley and J. L. Dempsey, *Chem Sci*, 2015, **6**, 2827–2834.
- 50 V. Lockett, R. Sedev, J. Ralston, M. Horne and T. Rodopoulos, *J Phys Chem C*, 2008, **112**, 7486–7495.

- 51 A. C. Lazanas and M. I. Prodromidis, *ACS Meas Sci Au*, 2023, **3**, 162–193.
- 52 T. Pajkossy, *J Electroanal Chem*, 1994, **364**, 111–125.
- 53 J.-P. Randin and E. Yeager, *J Electroanal Chem Interfacial Electrochem*, 1975, **58**, 313–322.
- 54 H. R. Zebardast, S. Rogak and E. Asselin, *J Electroanal Chem*, 2014, **724**, 36–42.
- 55 K. W. Kimura, K. E. Fritz, J. Kim, J. Suntivich, H. D. Abruña and T. Hanrath, *ChemSusChem*, 2018, **11**, 1781–1786.

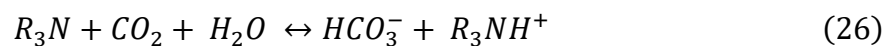
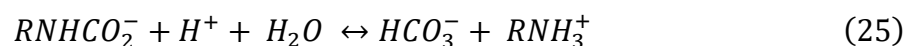
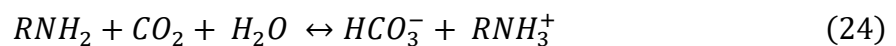
Chapter 4 Integrating CO₂ capture and electrocatalytic conversion

4.1 Scope of the chapter

4.1.1 Equilibria and speciation involved in amine-based CO₂ capture solutions

Direct conversion of captured CO₂ is of significant interest to overcome the cost and energy demands of regeneration of capture mix and CO₂ compression. While this field is still emerging, there have been studies showing both improvement and insight into CO₂ conversion in capture solutions. Though there is a variety of different capture media (e.g. aqueous alkaline solutions and ionic liquids),^{1,2} the focus of this chapter is on integrated conversion of amine-based capture of CO₂, which is currently the most commercially available scrubbing agent.³

Here we focus on the species formed in aqueous solution using 20-30 wt % amine, typically used in the CO₂ capture process. For primary and secondary amines, CO₂ capture goes through two absorption stages: first forming the carbamate, Eq (23), then going on to form bicarbonate ions, Eq (24) and (25). Tertiary amines are unable to form carbamates, instead acting as a base and forming only bicarbonate ions (Eq 26).



Lv *et al* utilised ¹³C NMR to describe the mechanisms of CO₂ absorption and desorption in primary amine, monoethanolamine (MEA) over different conditions including CO₂ loading, pH and temperature.⁴ Aqueous solutions of primary and secondary amines have a maximum CO₂ loading of mol_{CO₂}/ mol_{amine} 0.5 due their requirement to form carbamate anion and ammonium cation pairs. Here Lv *et al*. reported that as CO₂ is loaded up to 0.4 mol_{CO₂}/ mol_{MEA} (often the loading limit in typical CO₂ capture processes), the pH drops rapidly from pH 12 to pH 10 and the temperature of the system increased by ~15 K due to the exothermic nature of forming the carbamate species. Eq (23). As the loading exceeds >0.4 mol_{CO₂}/ mol_{MEA}, the pH continues to drop and the carbamate begins to undergo hydrolysis into bicarbonate anions and ammonium cations, Eq (25). Due to the difference in speciation, CO₂ capture with aqueous tertiary amines, Eq (26), have a higher maximum CO₂ loading per amine of 1:1.

The species that are able to form during CO₂ capture also are depend on the solvent and salts present with the amine. In non-aqueous media speciation will vary, for example hydrolysis of the carbamate to bicarbonate is impossible, while some solvents can also stabilise the carbamic acid species, preventing it from forming the carbamate/ammonium ion pair.⁵ Khurram et al found this when using 2-ethoxyethylamine (EEA) in neat DMSO, where the carbamic acid was unable to dissociate until alkali metal salts were added. While the authors found little dependence of the anion, there was a strong dependence on the cation where carbamic acid dissociation increased with increasing Lewis acidity of the cation.⁶

Understanding the different species formed in these amine mixes is integral if we hope to utilise them directly for integrated CO₂ capture and conversion, however for now investigations into the equilibriums involved in amine-based CO₂ capture are complex and ongoing.

4.1.2 Types of CO₂ amine

A relatively wide range of amines (typically alkanolamines) either on their own or in specific mixtures are used for CO₂ capture, a selection of the more common is tabulated below.^{2,7-10} MEA is the first-generation of amine for gas purification and is still the most frequently used, due to its reactivity and moderately high CO₂ loading however it suffers significantly with thermal and oxidative degradation. Generally primary and secondary amines have high reactivity with CO₂ at relatively fast rates however, due to carbamate formation, requires higher heat of CO₂ absorption and thus significantly larger heat duty to regenerate the amine. Tertiary amines and those with significant steric hinderance such as 2-amino-2-methyl-1-propanol

(AMP) have lower heat of regeneration however usually have lower levels of CO₂ binding due to the slower kinetic process.¹¹

Table 5 Some common amines used in CO₂ capture

Name (abbr.)	Structural formulae	CO ₂ loading (molCO ₂ /mol _{amine})	Stripper T (°C)
Monoethanol amine (MEA)	OHCH ₂ CH ₂ NH ₂	0.4-0.5 ^{2,8,12}	111-125 ^{10,13}
Diglycol amine (DGA)	(HOC ₂ H ₄)-O- (C ₂ H ₄ NH ₂)	0.25-0.35 ²	132 ^{10,13}
Diethanol amine (DEA)	(CH ₂ CH ₂ OH) ₂ NH	0.2-0.5 ^{8,12}	103-105 ^{10,14}
Diisopropanol amine (DIPA)	(CH ₃ CHOHCH ₂) ₂ NH	0.43-0.22 ²	110 ²
Methyl diethanol amine (MDEA)	CH ₃ N(C ₂ H ₄ OH) ₂	0.1-0.4 ^{2,12}	119-129 ^{10,13,14}
Triethanol amine (TEA)	N(C ₂ H ₄ OH) ₃	0.08-0.3 ^{8,12}	77 ¹⁵
2-amino-2-methyl-1- propanol (AMP)	NH ₂ C(CH ₃) ₂ CH ₂ OH	0.3-0.65 ^{8,12}	123-140 ¹⁰
Morpholine (MORPH)	O(CH ₂ CH ₂) ₂ NH	0.2-0.5 ⁹	<160 ^{9,13}

While the literature on CO₂ capture is extensive and constantly expanding with new amines mixtures and engineering strategies to lower overall regeneration costs, another approach is to integrate CO₂ capture and electrochemical conversion to minimise energy losses.

4.1.3 Electrochemical CO₂ reduction in amine solution

4.1.3.1 Metal catalysts

Chen *et al.* were the first to report electrochemical CO₂ reduction in an amine mixture where they screened a range of metal electrodes in 30 wt % MEA (4.9 M), which initially resulted in poor selectivity towards CO₂ reduction products, attributed to free, dissolved CO₂ acting as the only carbon source.¹⁶ This was recently supported in a thorough study by Shen *et al* who

identified both computationally and experimentally that dissolved CO₂ is the primary reactant undergoing conversion in electrocatalytic reduction in capture mixes on silver electrodes.¹⁷

Thus, the field has moved towards engineering strategies to achieve CO₂ conversion in amine mixtures by liberating CO₂ from amine mixture at the electrode in order to achieve reasonable CO₂ reduction. This involves shifting the equilibrium away from carbamates and bicarbonates and back towards the amine and free CO₂ and can be done by controlling the pH, temperature and pressure. Providing a supply of protons to the amine mixture can drive CO₂ desorption from the captured mix. Inspired by bicarbonate electrolyzers,¹⁸ a cation exchange membrane (CEM) or bipolar membrane (BPM) in the reverse-bias configuration which continually pumps protons onto the cathode side. This shifts the amine-carbamate equilibrium, keeping dissolved CO₂ concentrations high at the cathode, increasing electrochemical CO₂ reduction rates (eCO₂R) at metallic electrodes.^{19–21}

Increasing temperature increases the rate of the carbamate/bicarbonate equilibrium and shifts it towards free CO₂. It has been shown that even moderately higher temperatures lead to a large increase in eCO₂R. For example, Pérez-Gallent and co-workers demonstrated a six-fold increase in current density when increasing the temperature of the system from 15°C to 70°C on a Pb electrode.²² Lee *et al.* also showed an increase in FE_{CO} from <5 % at room temperature to 72% at 60 °C on a Ag electrode in 30 wt% MEA(aq).²⁰

Other optimisation strategies that have been developed involve moving away from electrode and electrochemical cells that benefit a gas-fed configuration. This includes maximising electrode surface area and increasing electrode wetting to gain better contact between the substrate and electrode. Another limitation of working in amine mixtures is the lower conductivity without added electrolyte salts, an effect which can be minimized by using a zero-gap cell.²¹

Alternatively, electrolyte addition may improve both conductivity and selectivity in integrated electrochemical conversion, without hampering the capturing ability of the amine with initial reports by Lee *et al.* showed good recycling performance of the capture solution of up to 10 cycles of 2M KCl in 2M MEA. The authors also report an increase in FE_{CO} from <5% to ~10% through the addition of 2M K⁺ cations. With selectivity increasing with increasing size of alkali cation (decreasing size of the hydrated cation), up to FE_{CO} 30% achieved with 2M CsCl. This cation trend is observed consistently in electrochemical CO₂ reduction with metal electrodes and is usually attributed to one of three theories: buffering the local pH, stabilising reduction

intermediates or modifying the electric field of the electrode/electrolyte interface^{23–25} The latter of which, Lee et al attributes to the increased CO selectivity on Ag in MEA, claiming the increased strength of the electric field stabilises adsorption of reactant and improves electron transfer to the carbamate. The authors argue that in MEA-CO₂ alone, under a negative bias, the primary species in the electrochemical double layer (EDL) is the larger ethanolammonium cation which hampers accessibility of the carbamate to the electrode, this can then be overcome with tailoring the EDL with addition of KCl electrolyte (**Figure 67**).²⁰ Kim and co-workers also showed this trend on Ag, using it to benchmark against the proficient CO selectivity the group achieved with a single Ni atom catalyst (FE_{CO} up to 78.3%) in 5M MEA-CO₂ which the authors attributed to the insensitivity of the catalyst towards this cation effect.²¹

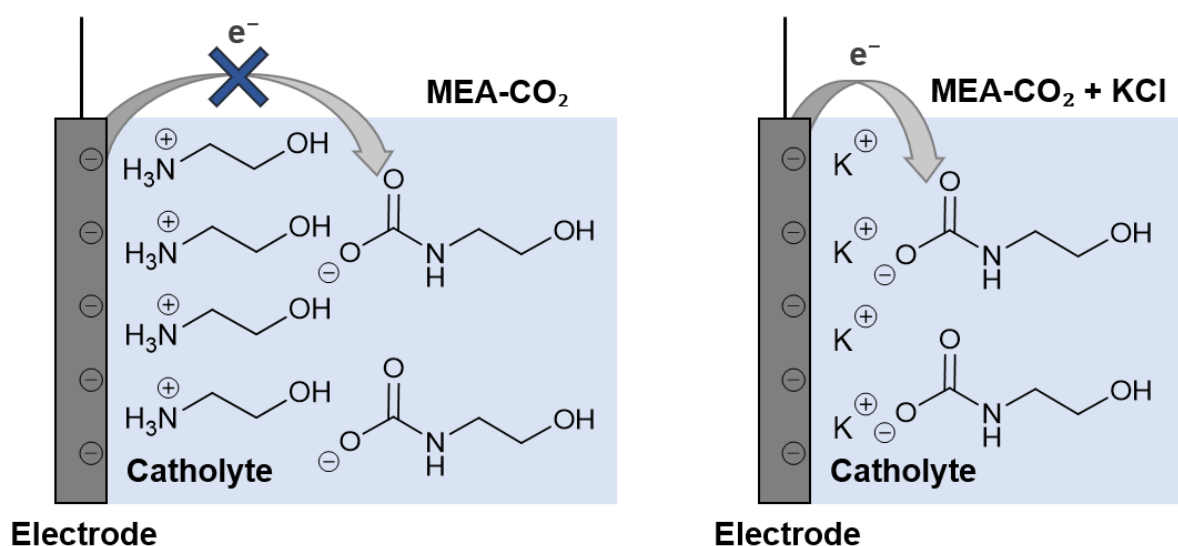


Figure 67 Proposed interfacial structure near the electrode surface of MEA-CO₂ electrolyte (left) with alkali salt addition (right). Reproduce from Lee et al.²⁰

4.1.3.2 Molecular catalysts

An alternative approach is to utilise the selectivity and tunability of molecular complexes to give higher product yields in carbon capture mixes, however there a limited number of studies on this. In 2019 Bi et al first showed electrochemical CO₂ reduction via the carbamate using an iron tetradentate phosphine complex in MeCN with 1% water.²⁶ With 1-10 vol% DEA (0.1-

1 M) present, the iron complex was shown to produce methanol as its primary product (up to FE_{methanol} of 68.8%) whereas, without amine, formate was the main product of eCO₂R. This change in selectivity was attributed to the catalyst reducing the carbamate directly to form a formamide which could then be converted to methanol by the complex. This study demonstrated the value of using catalysts that interact with the carbamate directly over those which simply tolerate it.

In the same year publications by Kumagai *et al.* and Koizumi *et al.* showed that triethanolamine (TEA) can coordinate to Re and Mn bipyridine tricarbonyl CO₂ reduction complexes by FTIR spectroscopy. It was proposed that the complexes were able to capture CO₂ via the amine coordinated species leading to significant CO₂-to-CO conversion even at CO₂ concentrations of <1% (see **Figure 7**).^{27,28} Bhattacharya *et al.* later performed electrolysis with Mn(bpy) where a change in selectivity was observed in the presence of a low concentration (0.1 M) of the amine, morpholine (MORPH) in MeCN.²⁹ With morpholine, the primary products for CO₂ reduction became formic acid and hydrogen as opposed to CO which is commonly the main product with this catalyst. The authors attribute this selectivity change to the carbamic acid (MORPH-COOH), which exists due to limited deprotonation to the carbamate in MeCN, or ammonium cation (MORPH-H⁺) species protonating the catalyst to form the hydride which can either undergo a second protonation producing hydrogen or dissolved CO₂ insertion to lead to formic acid (see **Figure 68**). It is important to note that the group did show that formic acid is also produced through electrolysis of a range of other amines without the catalyst, however this remained at a significantly lower level.³⁰ A publication by Stuardi *et al.* also showed an effect on formate production with Mn(bpy) and low concentrations (1 mM) of amine additives in methanol. While both of these studies claim the source of formate is CO₂ rather than the captured species, Stuardi *et al.* dispute Bhattacharya's hydride transfer theory, instead claiming that the amine assists in coordinating to CO₂, lowering the energy required for Mn(bpy) to convert CO₂ to formate.³¹

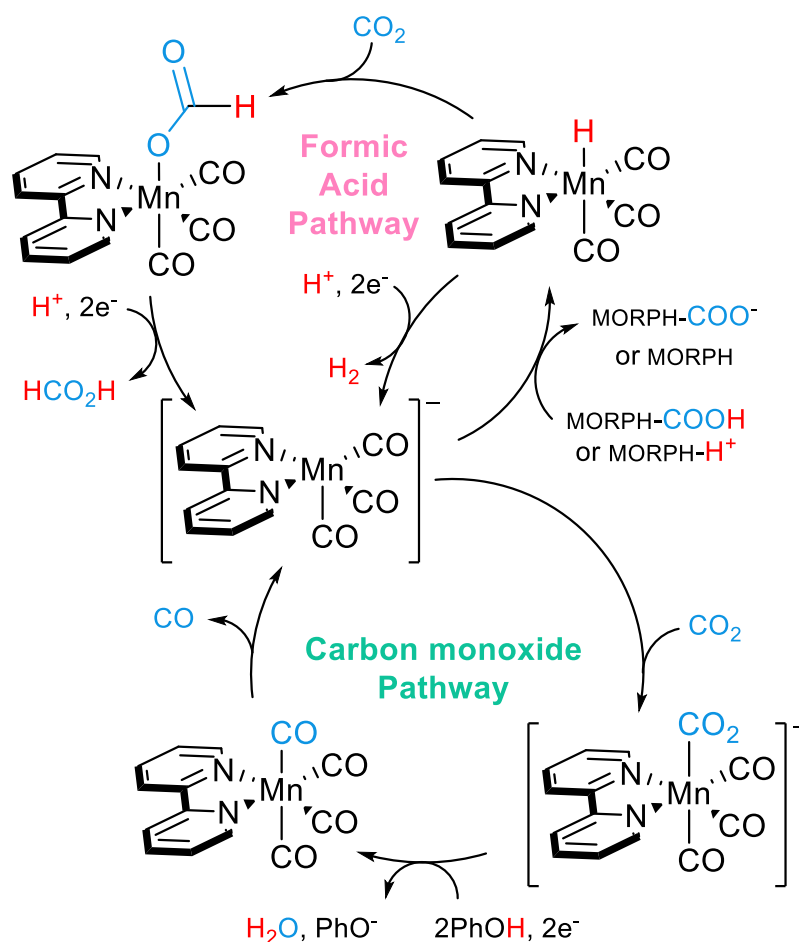


Figure 68 Proposed mechanism for the electrocatalytic reduction of CO₂ to formic acid (top) or carbon monoxide (bottom) reproduced from Bhattacharya *et al.*²⁹

While these papers demonstrate the possibility of combining CO₂ capture amines and electrocatalytic conversion with molecular complexes, there are some limitations. All of the studies are done with lower amine concentrations (0.1-1 M) in organic solvents. This is a stark contrast to amine-based capture mixes which are 30 wt% amine in water (3-5 M). This is important as the solvent not only drastically changes the behaviour of the catalyst but also the amine species present in solution. Recently Kar *et al.* published a study using a cobalt(II) phthalocyanine (CoPc) immobilised to a photocathode where they show electrochemical conversion in aqueous capture media. Of the amines tested 1 M TEA showed the best selectivity giving FE_{CO} = 46%, followed by DEA (17%) and MEA (10%), the authors attribute this to TEA-CO₂ having lower thermodynamic stability, making it easier to reduce.³² While the authors use lower amine concentrations than in traditional capture mixes, this work demonstrates a molecular electrocatalyst able to produce CO in aqueous conditions. However,

like the metal catalysts, results indicate that the CoPc is able to endure the amine-CO₂ mixture as opposed to utilising it as the complexes discussed previously.

4.1.3.3 [Mn^I(bpy-(COOH)₂)(CO)₃Br] (where bpy-(COOH)₂ = 4,4'-dicarboxy-2,2'-bipyridine)

Previously in the Cowan group, the first homogeneous studies of a modified Mn bipyridine complex in aqueous electrolyte were reported. The complex, [Mn^I(bpy-(COOH)₂)(CO)₃Br] (where bpy(COOH)₂ = 4,4'-dicarboxy-2,2'-bipyridine), (from now on abbreviated to Mn(bpy-COOH)) showed reduced activity when compared with the parent complex in organic solvent however, in aqueous electrolyte the complex displays a high level of selectivity towards CO₂ reduction.^{33,34} This water-soluble analogue of Mn(bpy) is of interest to investigate whether a catalyst/amine-CO₂ interaction is observed and what this means for electrolysis of more industrially relevant CO₂ capture mixes with this complex.

In this chapter, first the amine, morpholine, under CO₂ is investigated to assess its speciation. Spectroscopy is then used in an attempt to observe direct interaction between the catalyst and morpholine, before electrochemical investigating of the complex in the morpholine-CO₂ mix. The chapter concludes with preliminary tests of Mn(bpy-COOH) with other, more conventional, CO₂ capture amines.

4.2 Species breakdown of morpholine-CO₂

Morpholine is a secondary cyclic amine with an ether group at the 4 position of the ring (shown in **Figure 69(A)**). As discussed previously, secondary amines react upon exposure to CO₂, to form carbamic acid, in aqueous solutions this carbamic acid dissociates immediately to the carbamate, with the proton preferentially sitting on the unreacted amine, Eq (23). Throughout this chapter a concentration of 30 wt% of morpholine is taken as a standard as used in the capture literature,^{4,9} which equates to 3.4 M. ¹H NMR spectra of 30 wt% morpholine in water, adjusted to pH 8.8 from 11.5 with HCl, is shown in **Figure 69(B)**. ¹H NMR (400 MHz, D₂O):

δ 3.72 (t, J = 4.8, 4H, α), δ 2.94 (t, J = 4.9 4H, β). Spectra of a second solution of 30 wt% morpholine after purging and reacting with CO₂ (pH 8.6) is shown in **Figure 69(C)**. ¹H NMR (400 MHz, D₂O): δ 3.66 (t, J = 4.8, 4H, α), δ 3.49 (t, J = 4.5, 4H, γ), δ 3.21 (t, J = 4.5, 4H, Δ), δ 2.89 (t, J = 4.8 4H, β). The singlet peak at $\delta \sim 2.6$ ppm is DMSO, added to samples for proton quantification.

Here the shifts of the protonated and unprotonated morpholine are indistinguishable due to the rapid proton transfer between the two species. The total amine in solution is the sum of unprotonated amine (MORPH), protonated amine (MORPH-H⁺) and carbamate (MORPH-COO⁻).^{35,36} From integrating γ and Δ peaks as a fraction of the total integrated peaks, 29 % is the carbamate species in this solution. The ratio of both MORPH and MORPH-H⁺ can be determined from the pH of the solutions. The pK_a of MORPH-H⁺ is 8.36 in thus K_a = 10^{-pK_a} = 4.36x10⁻⁹. The pH 8.8 in MORPH and 8.6 in MORPH-CO₂ thus [H₃O]⁺ = 10^{-pH} thus is 1.58x10⁻⁹ M and 2.5x10⁻⁹ M respectively. The ratio of MORPH/MORPH-H⁺ is 2.76 (73% MORPH (2.5M) & 27% MORPH-H⁺ (0.9M)) for MORPH-AIR and 1.74 (45% MORPH (1.5M), 26% MORPH-H⁺ (0.9M) & 29% MORPH-COO⁻ (1.0M)) for MORPH-CO₂.

$$\frac{[MORPH][H_3O^+]}{[MORPH - H^+]} = K_a \quad (28)$$

As well as identifying species present in MORPH-CO₂, integration can give quantitative insight into the CO₂ loading into amine. To compare CO₂ loadings into capture amines, the ratio between the moles of CO₂ and amine are used. This was done using integration of ¹H NMR of three separate solutions where average mol_{CO₂}/ mol_{MORPH} is 0.24± 0.11. The mol_{CO₂}/ mol_{MORPH} value was also calculated by weight increase with CO₂ purging giving mol_{CO₂}/ mol_{MORPH} of 0.34± 0.11. The loading values obtained through ¹H NMR integration are lower on average, here only the carbamate species are counted whereas some CO₂ is expected to react with water to form bicarbonate, or exist unreacted in solution (though the levels of dissolved CO₂ are <0.03 M so this contribution is expected to be very small). With either method the error value is similar suggesting that the bigger source of error in mol_{CO₂}/ mol_{MORPH} comes from the way the solution is made up over method of measuring. Despite attempts to keep purging times (3 min/ mL) and flow rates (40 sccm) consistent, higher control is needed to obtain consistent CO₂ loading.

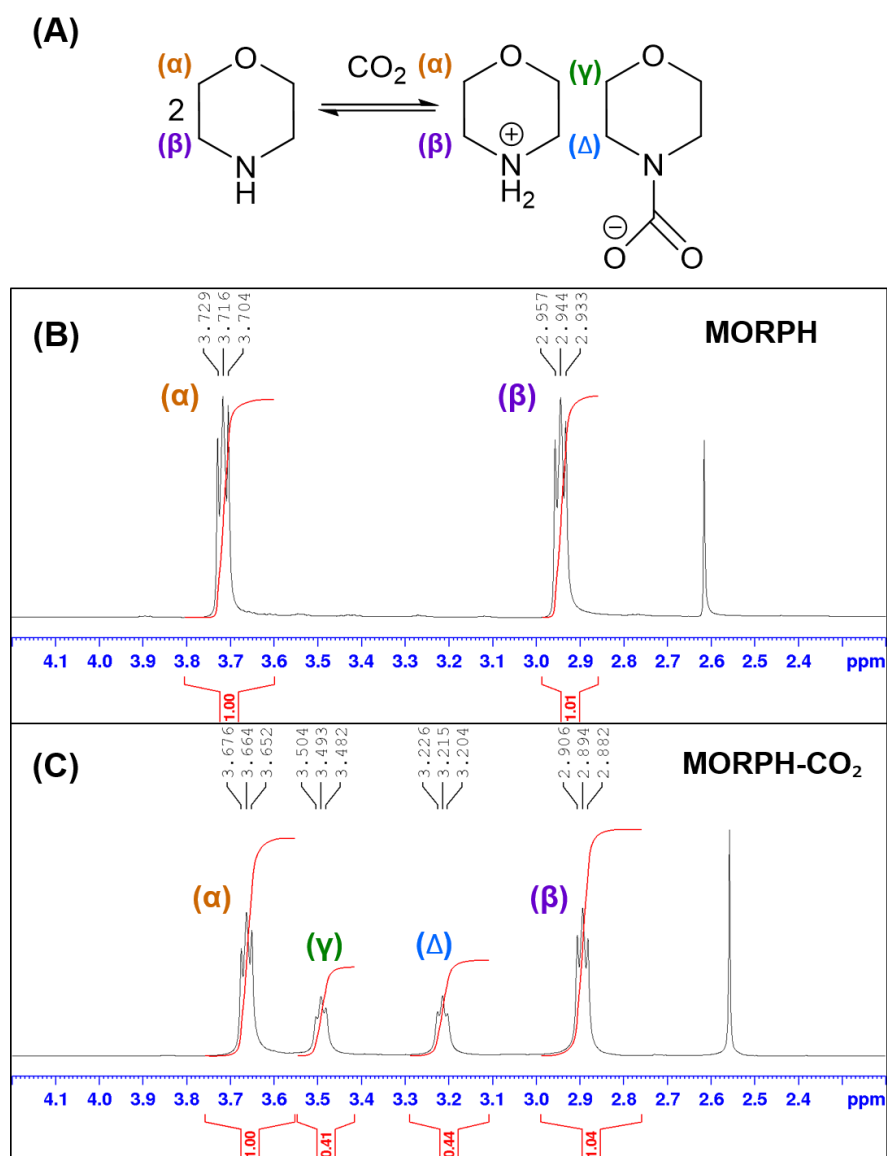


Figure 69 (A) Schematic equilibria of morpholine reacting with CO₂ (B)&(C) ¹H NMR of 30 wt% morpholine with and without CO₂ purging

4.3 Spectroscopy of Mn(bpy-COOH) in morpholine

4.3.1 FTIR

To establish Mn(bpy-COOH) complex showed any interaction with amine or carbamate species at the industrially relevant concentrations, FTIR spectroscopy was used to observe any changes in the CO vibrations of the catalyst in the presence of morpholine. Four aqueous solutions of 5 mM Mn(bpy-COOH) were made, two with 0.5 M NaHCO₃ with and without CO₂ purging (denoted as H₂O-AIR and H₂O-CO₂ respectively), and two with 30 wt%

morpholine with and without CO₂ (denoted as MORPH-AIR and MORPH-CO₂). The pH of each solution was measured to be 8.5 (H₂O-AIR), 7.8 (H₂O-CO₂), 8.8 (lowered from 11.5 with HCl for better experimental control) (MORPH-AIR) and 8.6 (MORPH-CO₂). At these pH's, the carboxylic acid groups of Mn(bpy-COOH) are both expected to be deprotonated (pK_a's are 2.86 & 2.36) giving the catalyst form [Mn^I(bpy(COO⁻)₂)(CO)₃H₂O]⁻ in solution. FTIR measurements used a Harrick cell with 50 μm spacer. Before each measurement the background was ran with the same solution with no catalyst before running the sample with a resolution of 2 cm⁻¹ with 124 scans. Spectra was recorded at 0, 10, 20 and 60 minutes from assembly, with the exception of H₂O-CO₂ where only spectra recorded to 20 minutes is shown. Here there appears to be little variation in frequencies over the course of an hour, suggesting that coordination occurs quickly (**Figure 70**).

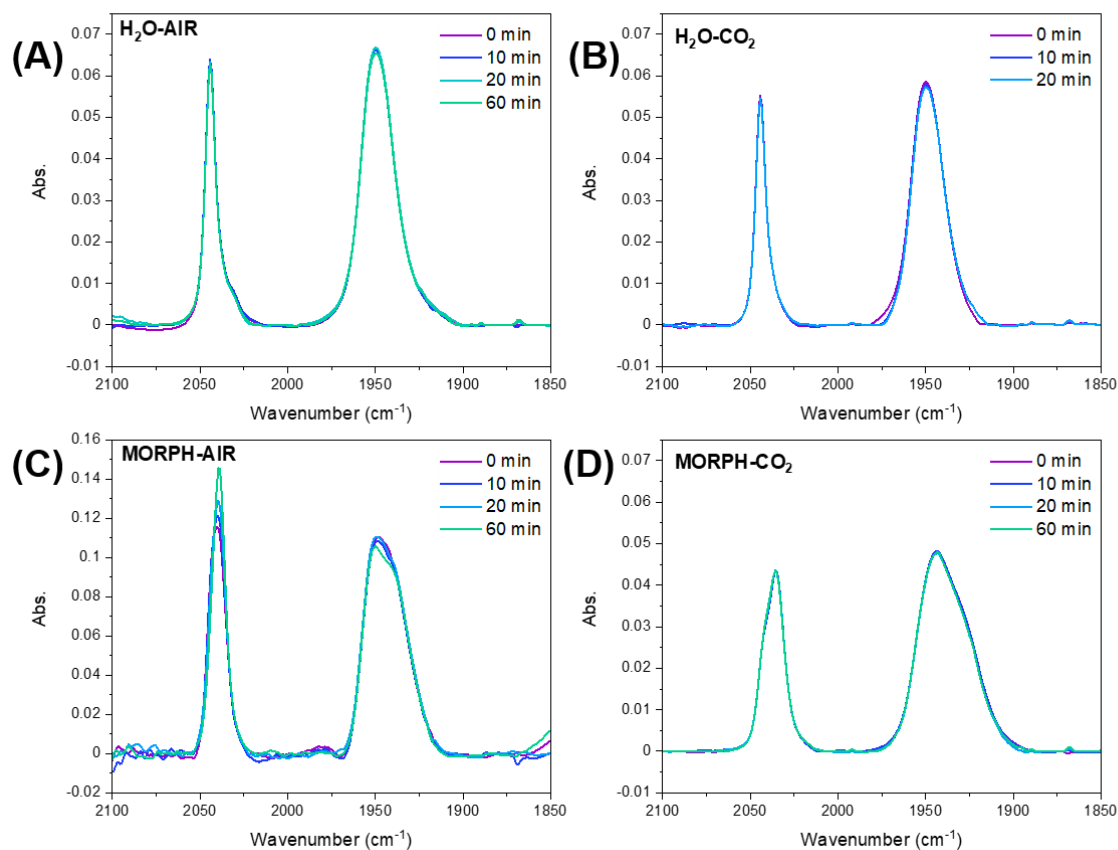


Figure 70 FTIR spectra of aqueous solutions 5 mM Mn(bpy-COOH) both with and without 30% morpholine under air or CO₂ over time.

The assignment of the C-O stretches of *fac*-tricarbonyl manganese(I) complexes is explained in further detail by Ault *et al.*,³⁷ though a summary is given here. Three carbonyl ligands on the same face of an octahedral is said to have local C_{3v} symmetry where we would expect to see two carbonyl stretching bands with FTIR, attributed to A₁ and doubly degenerate E band. However, Mn(bpy-COOH), like many *fac*-tricarbonyl complexes, lack C₃ symmetry so actually belong to point group C_s. Thus, the doubly degenerate E band splits into two, and the resulting FTIR spectra shows three carbonyl stretching bands: A' mode from A₁ of C_{3v}, A' mode and A'' mode from E of C_{3v}. The FTIR spectra of 5 mM Mn(bpy-COOH) with the corresponding stretching assignments is shown below in **Figure 71**. It is important to note that there is not unanimous agreement on the assignment of the lower frequency bands in the literature, which overlap significantly in the spectra of Mn(bpy-COOH) and thus are just labelled together.

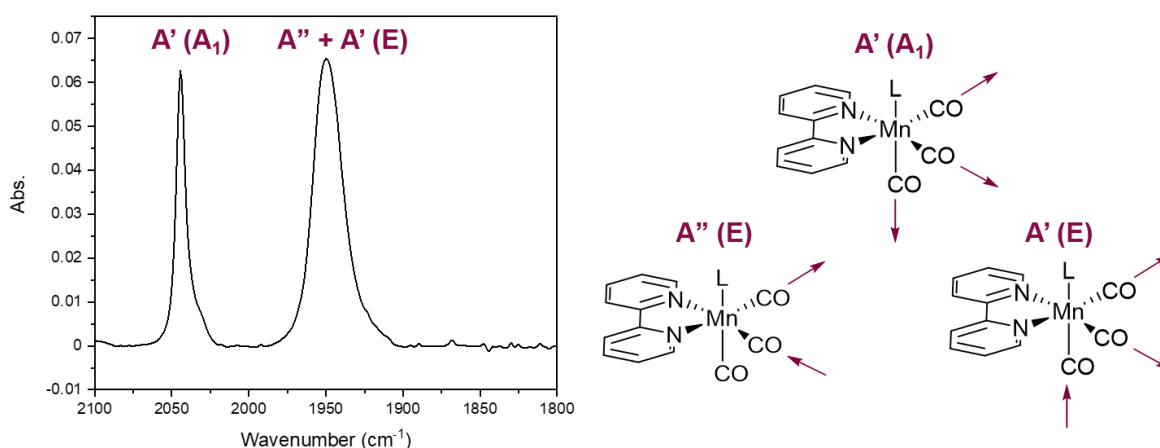


Figure 71 FTIR spectra of 5 mM Mn(bpy-COOH) in water assigned to $[Mn^I(bpy(COO^-)_2)(CO)_3H_2O]^-$ with the corresponding C-O stretches labelled and depicted.

The normalised FTIR of 5 mM Mn(bpy-COOH) after 20 min both with and without capture amines is shown in **Figure 72**, with the fits shown in **Figure 73**. Without amine, the A' (A₁) carbonyl stretching frequencies are similar both with and without CO₂, showing a majority peak at $\nu_{CO} = 2044 \text{ cm}^{-1}$ assigned to $[Mn^I(bpy-COO^-)(CO)_3H_2O]^-$ from literature,³⁴ with a small shoulder at $\nu_{CO} = 2036.6 \text{ cm}^{-1}$ and $\nu_{CO} = 2039.2 \text{ cm}^{-1}$ respectively. Despite the sensitivity of this catalyst to pH, the variation from pH 8.5 to 7.8 seems to show little effect on ν_{CO} , as this is the largest pH difference between the solutions the effect of pH on ν_{CO} can be discounted. The CO stretch frequency is very sensitive to the nature of the ligand L, which is proposed to be water. The lack of change in the carbonyl stretches when CO₂ is purged with the catalyst in

water allows us to conclude that ligand substitution with the replacement of the water by CO₂ or bicarbonate/carbonate does not occur.

By contrast, in 30 wt% morpholine the $\nu_{\text{CO}} = 2044 \text{ cm}^{-1}$ drops in intensity, becoming the shoulder to a larger peak at $\nu_{\text{CO}} = 2039.6 \text{ cm}^{-1}$ suggesting that morpholine could be occupying the axial site of the catalyst. Since the pH of the MORPH-AIR solution was acidified to 8.8, just higher than the pK_a of conjugate acid of morpholine (pK_a morpholinium = 8.4 in water³⁸) we would expect both morpholine and morpholinium to be present in solution. However, as the ν_{CO} shifts to lower wavenumbers, it suggests that a more electron donating species is coordinating to the Mn metal centre inserting charge density into the π^* antibonding orbitals of the C-O (see **Figure 74**) suggesting coordination of morpholine over the positively charged morpholinium species.

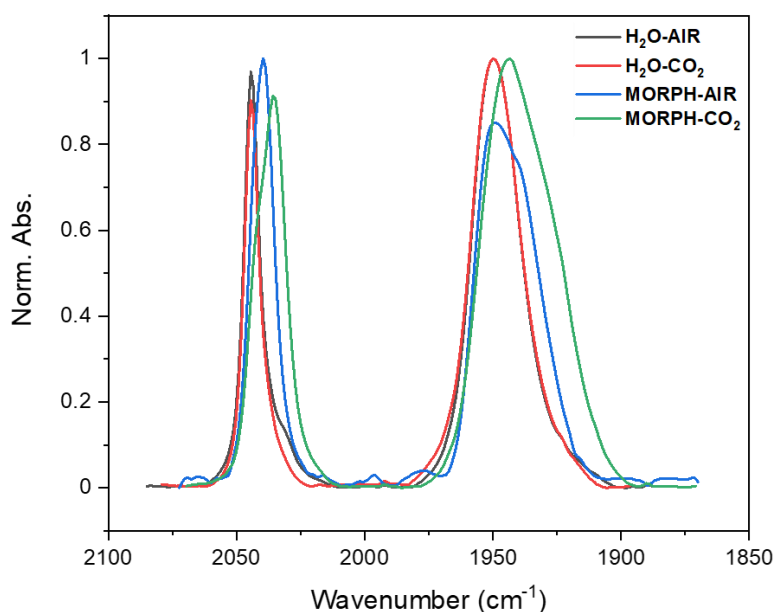


Figure 72 Comparison of the FTIR spectra with normalised absorbance of aqueous solutions 5 mM Mn(bpy-COOH) both with and without 30% morpholine under air or CO₂ after 20 min.

The FTIR spectrum of Mn(bpy-COOH) in MORPH-CO₂ shows two A' (A₁) carbonyl shifts shifted lower again at $\nu_{\text{CO}} = 2042.6 \text{ cm}^{-1}$ and $\nu_{\text{CO}} = 2035.6 \text{ cm}^{-1}$ with the latter having the higher intensity. From the ¹HNMR the MORPH-CO₂ is expected to contain significant fractions of morpholine and morpholinium cation, as well as the carbamate anion.³⁹ As the ν_{CO} is shifted further towards lower wavenumbers than observed in MORPH-AIR, indicating coordination to a different, more electron donating species and thus is proposed to be the carbamate.

From the A' stretch, at least two different species are present thus at least four peaks are expected to make up the broad peak at ~1950 cm⁻¹. However due to the breadth of these bands, it isn't possible to fit the overlapping features correctly, thus the minimum number of peaks has been used to obtain a good fit of the experimental data. While the focus of analysis and discussion is on the totally symmetric A' (A₁) stretch due to clearer fitting and easier peak assignment, the A'' (E) and A'(E) stretches also show a similar trend. Without amine, the spectra don't appear to shift significantly with the addition of CO₂. However, as amine is added, lower frequency peaks become more prominent. In MORPH-CO₂ ν_{CO} shifts lower again, at a different frequency to morpholine alone suggesting that there is interaction between the carbamate and Mn(bpy-COOH).

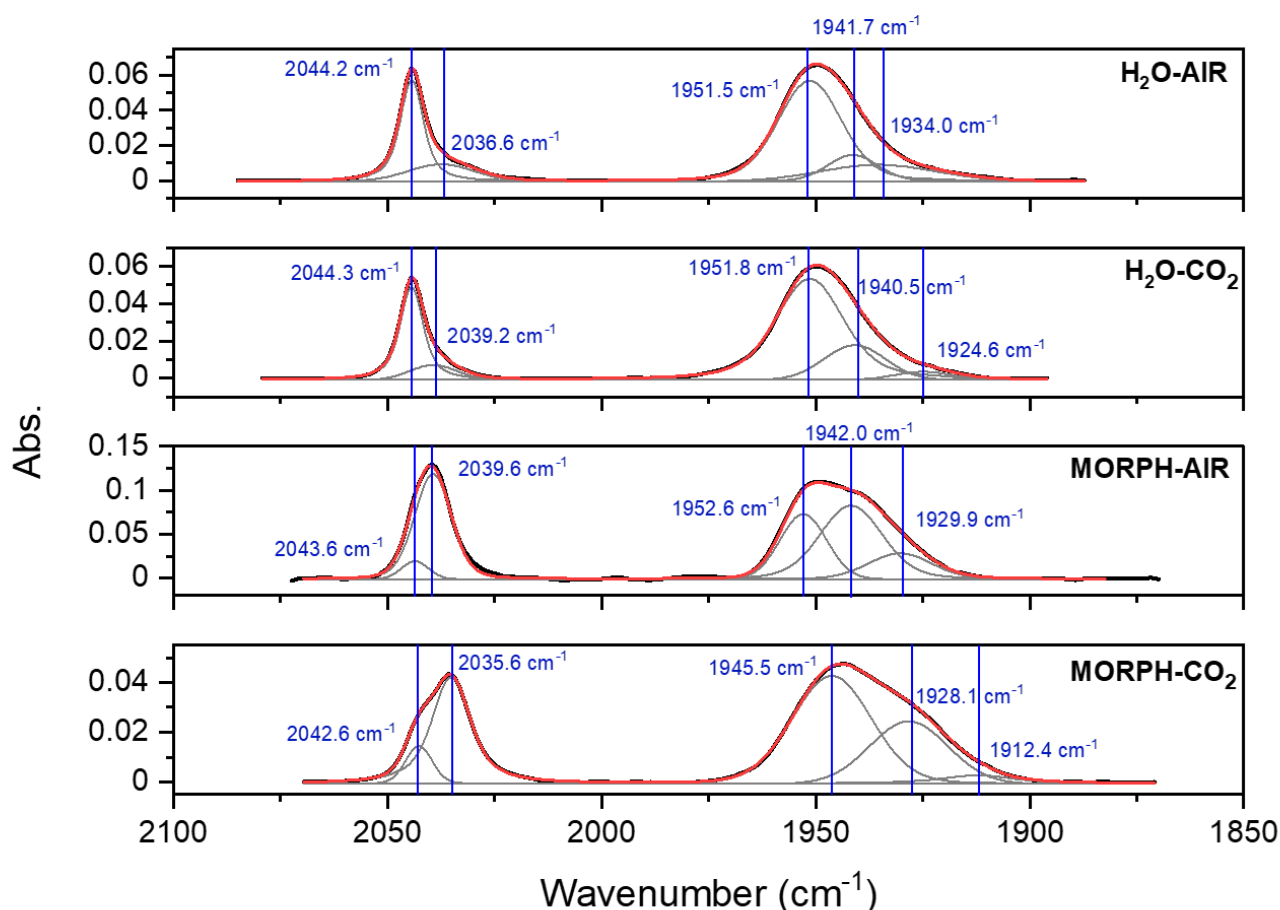


Figure 73 FTIR spectra of aqueous solutions 5 mM Mn(bpy-COOH) both with and without 30% morpholine under air or CO₂ after 20 min. The recorded spectra is shown in black, and the fitting (red) represents the sum of individual fit peaks (grey). Fitted to the Voigt function.

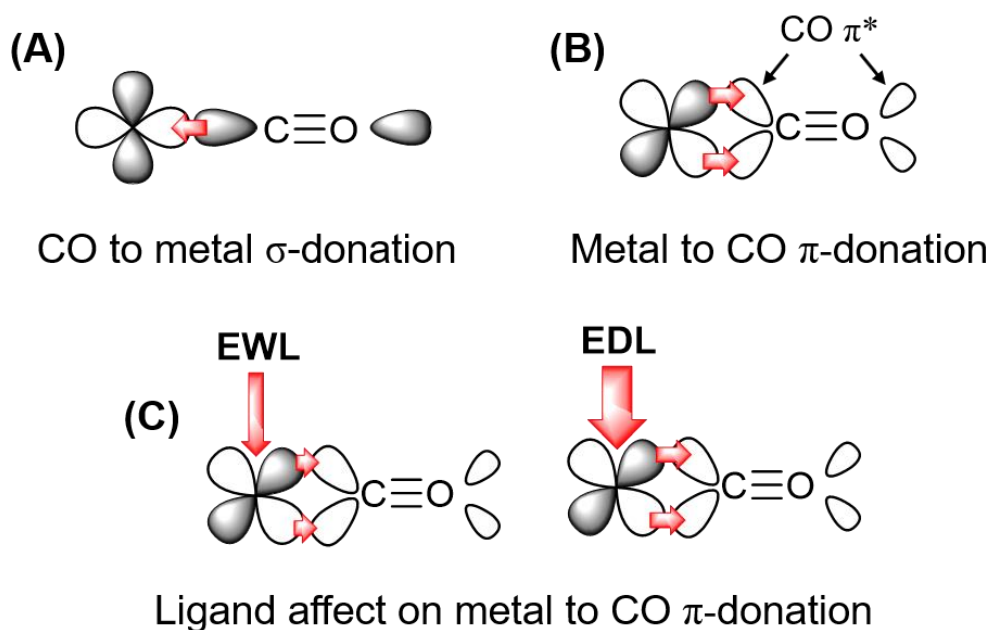


Figure 74 Orbital schematic showing (a) CO ligand to metal σ -donation (b) metal to CO ligand π -donation (c) the effect of electron-withdrawing (EWL) or electron-donating ligands (EDL) on decreasing or increasing metal to CO ligand π -donation where red arrows represent electron donation.

Koizumi *et al* previously showed IR spectra of *fac*-[Mn(bpy)(CO)₃(MeCN)]⁺ in DMF with 1.3 M triethanolamine (TEA).²⁸ Over the course of 30 min they observed a small shoulder appear at ν_{CO} over 20 wavenumbers lower, which they attributed to the coordination of TEA. When the solution was purged with CO₂ the totally symmetric stretch shifted from $\nu_{\text{CO}} = 2039\text{cm}^{-1}$ to $\nu_{\text{CO}} = 2028\text{cm}^{-1}$. While this study also observes shifts to lower frequencies with coordination with TEA and TEA-CO₂, the shifts in wavenumber are significantly larger than what is observed with Mn(bpy-COOH) in MORPH-AIR and MORPH-CO₂.

Koizumi *et al* proposed that TEA bonds to Mn metal through the deprotonated alcohol group. As morpholine has an ether group, it is unable to undergo deprotonation and unlikely to coordinate via the oxygen. Instead, morpholine could be imagined coordinating via the lone pair on the nitrogen atom as shown in **Figure 75**. It's important to note this ligand is neutral, thus it is proposed that the Mn(I) centre is balanced by the bromide or other anion in proximity. When purged with CO₂ Koizumi *et al* proposes CO₂ inserts into the metal-oxygen bond (**Figure 75** left) as TEA is a tertiary amine and unable to form carbamates. In our case, CO₂ insertion would give rise to a three bonded oxygen atom, or have to break the morpholine ring which is unlikely, thus we propose coordination of the carbamate anion directly to the Mn centre.

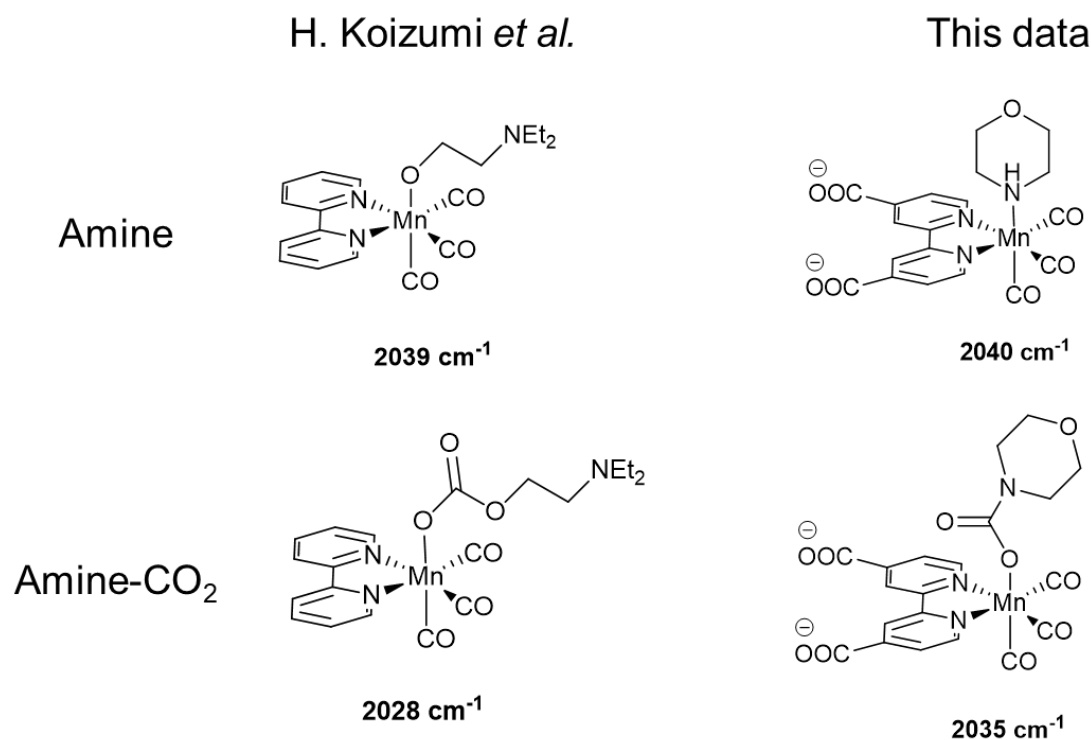


Figure 75 Possible structures of amine and amine-CO₂ coordinated Mn(bpy) proposed by Koizumi *et al.*²⁸ (left) and this work (right).

4.3.2 UV/Vis & ¹H NMR

To gain further insight into the coordination of MORPH and MORPH-CO₂ to Mn(bpy-COOH) UV/Vis and ¹H NMR spectra were ran. UV/Vis spectra were taken of three solutions (pH ranging 7.8-8.8) of 5 mM Mn(bpy-COOH) in 0.5 M NaHCO₃ purged with CO₂ (H₂O-CO₂), 30 wt% MORPH and MORPH-CO₂ respectively, and is shown in **Figure 76**. Previously Walsh *et al.* reported a shift in the metal-to-ligand charge transfer (MLCT) band of Mn(bpy-COOH) from $\lambda_{\text{max}} = 460$ nm in MeCN to $\lambda_{\text{max}} = 393$ nm in H₂O attributed to exchange of the axial bromide ligand with water.³⁴ However in **Figure 76** the MLCT of Mn(bpy-COOH) stay at $\lambda_{\text{max}} \sim 410$ nm in all three solutions suggesting any coordination of MORPH or MORPH-CO₂ has minimal effect on the MLCT of Mn(bpy-COOH).

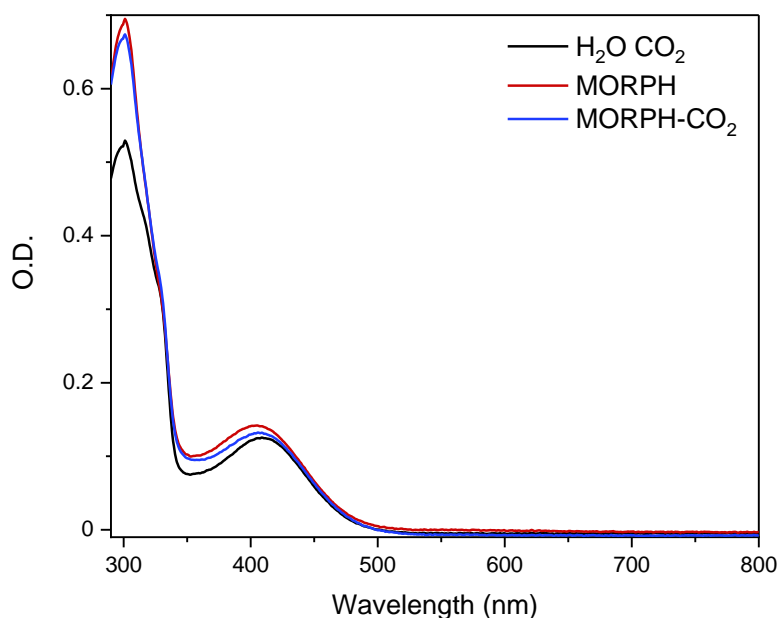


Figure 76 UV/Vis spectrum of 5 mM Mn(bpy-COOH) in the following aqueous solutions: 0.5 M NaHCO₃ purged with CO₂ (H₂O-CO₂), 30 wt% MORPH and 30 wt% MORPH-CO₂. Pathlength of 10 mm.

¹H NMR samples of aqueous solutions of 5 mM Mn(bpy-COOH) containing no amine, 5 mM MORPH and 5 mM MORPH-CO₂ are shown in **Figure 77**. Samples were made up with 5 mM Mn(bpy-COOH), 5 mM MORPH or MORPH-CO₂ if stated, 5 mM DMSO for quantification and 10% D₂O. Samples were also made immediately before running and prepared in amber tubes to limit light exposure to the complex which is reported to form radicals upon excessive light exposure. 0.5 mM Mn(bpy-COOH) in H₂O (**Figure 77(A)**): ¹H NMR (400 MHz, D₂O): δ 9.27 (s, 2H, α), δ 8.62 (s, 2H, β), δ 7.89 (s, 2H, γ). Additional small peaks are observed, this

could correspond to a small amount of the complex coordinating to DMSO in the sample or indicate some catalyst degradation through light exposure. 0.5 mM Mn(bpy-COOH) in MORPH (**Figure 77(B)**): ¹H NMR (400 MHz, D₂O): δ 9.27 (s, 2H, α), δ 8.63 (s, 2H, β), δ 7.89 (s, 2H, γ). 0.5 mM Mn(bpy-COOH) in MORPH-CO₂ (**Figure 77(C)**): ¹H NMR (400 MHz, D₂O): δ 9.26 (s, 2H, α), δ 8.63 (s, 2H, β), δ 7.88 (s, 2H, γ). Here the expected splitting of the peaks is not resolved, for example protons assigned α and γ are expected to be doublets however appear as singlets. When comparing spectra of Mn(bpy-COOH) in MORPH/ MORPH-CO₂, no additional peaks or shifting is observed, however the β proton appears to broaden significantly though the reason or significance of this is unclear.

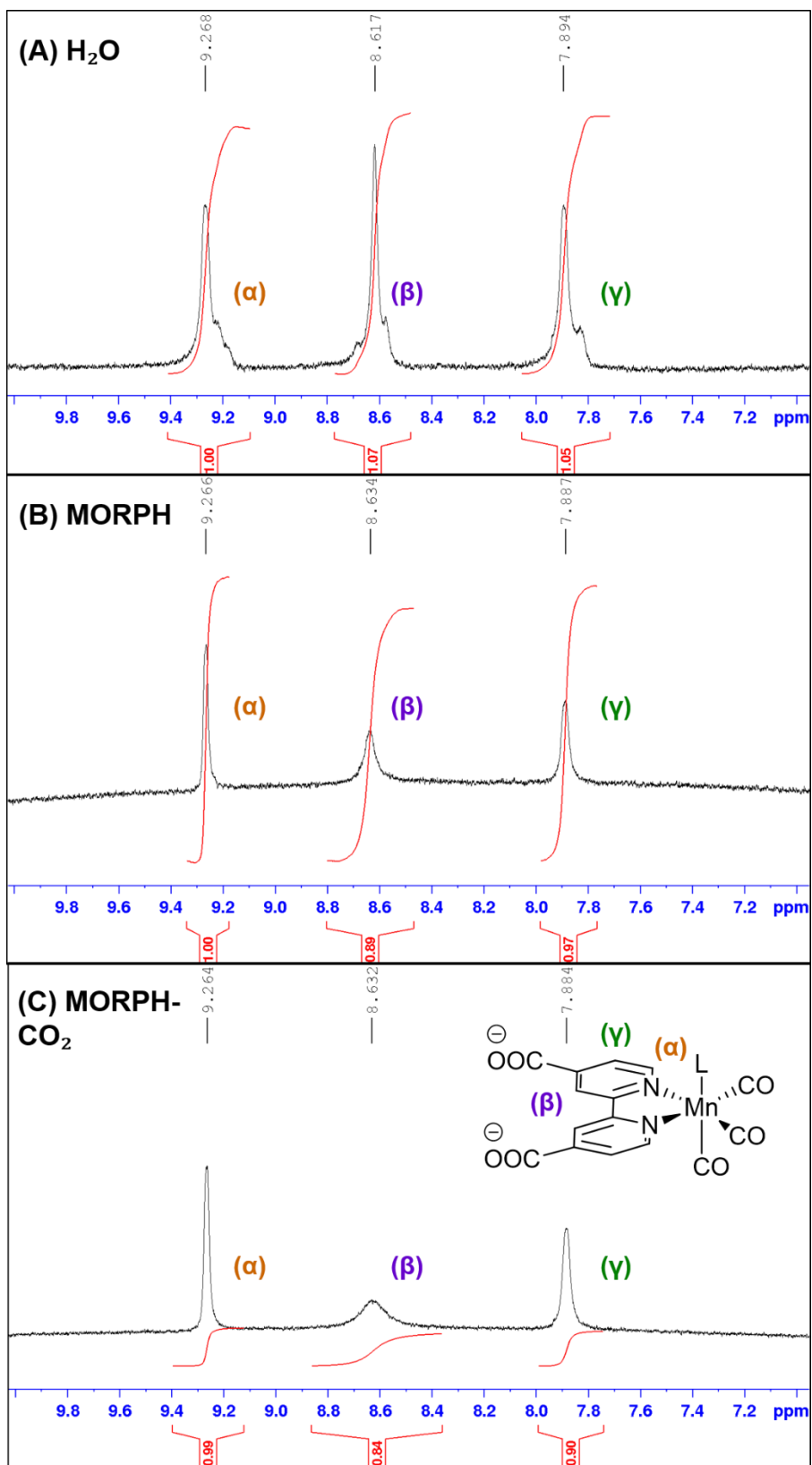


Figure 77 ¹H NMR samples of aqueous solutions of 5 mM Mn(bpy-COOH) containing no amine (H₂O), 5 mM MORPH and 5 mM MORPH-CO₂

The morpholine protons in these samples are also analysed and compared to samples of 5 mM MORPH and MORPH-CO₂ solutions made up in the same way without 5 mM catalyst in **Figure 78** & **Figure 79**. MORPH no catalyst (**Figure 78**): ¹H NMR (400 MHz, D₂O): δ 3.82 (t, 4H, J = 4.9), δ 3.12 (t, 4H, J = 4.9). MORPH with catalyst (**Figure 78**): ¹H NMR (400 MHz, D₂O): δ 3.85 (t, 4H, J = 5.0), δ 3.20 (t, 4H, J = 4.5). The catalyst containing sample shows a slight downfield shift compared to without catalyst, with the NCH₂ protons shifting further ($\Delta\delta = 0.071$ ppm) than the OCH₂ protons ($\Delta\delta = 0.0293$ ppm). This could be an effect of the pH lowering as catalyst is added, increasing the fraction of MORPH-H⁺ where the electron withdrawing ammonium group shifts NCH₂ protons downfield,³⁵ or could suggest electron donation of the amine group to the metal centre. Another observation is a reduction in the J coupling constant of the NCH₂ protons, an effect not seen with pH changes, which could suggest the coupling of these protons has changed.

MORPH-CO₂ no catalyst (**Figure 79**): ¹H NMR (400 MHz, D₂O): δ 3.86 (t, 4H, J = 5.0), δ 3.21 (t, 4H, J = 5.0). MORPH-CO₂ with catalyst (**Figure 79**): ¹H NMR (400 MHz, D₂O): δ 3.86 (t, 4H, J = 4.9), δ 3.20 (t, 4H, J = 5.0). Interestingly, at these low concentrations of morpholine, the carbamate species is not visible in either sample. The shifts and J coupling of the protonated and unprotonated morpholine vary very little when catalyst is added.

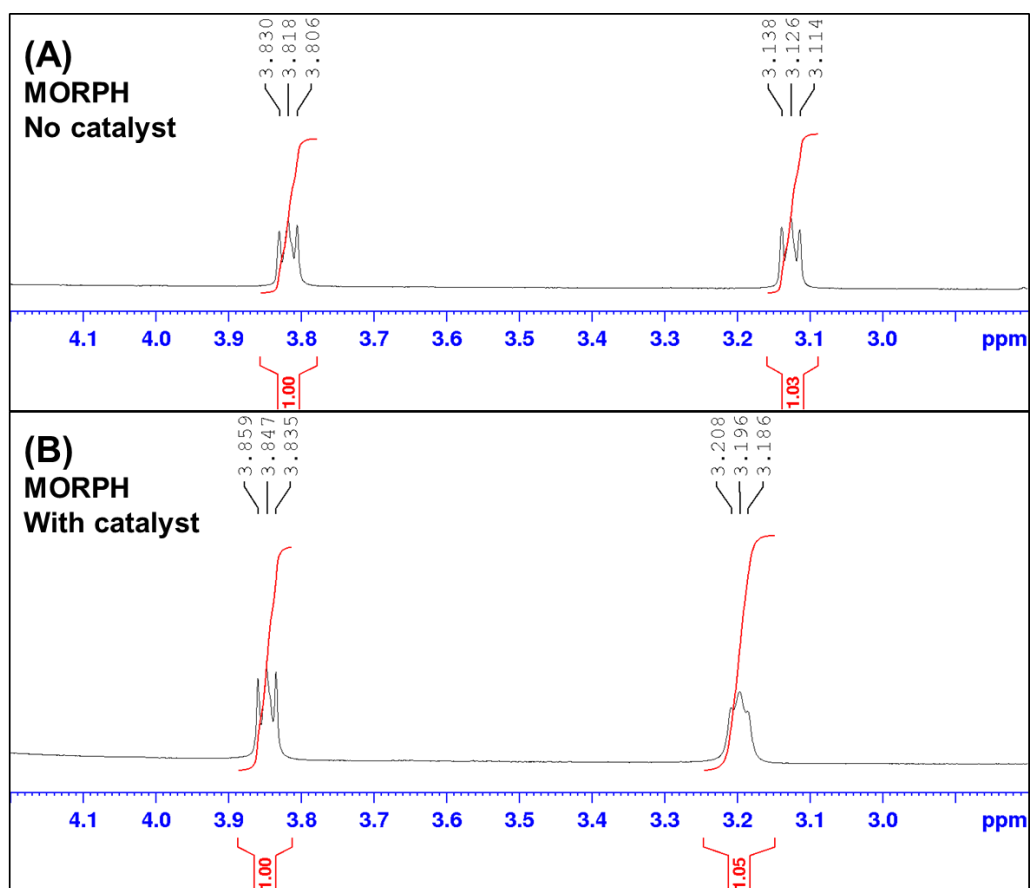


Figure 78 ¹H NMR samples of aqueous solutions of 5 mM MORPH with and without 5 mM Mn(bpy-COOH)

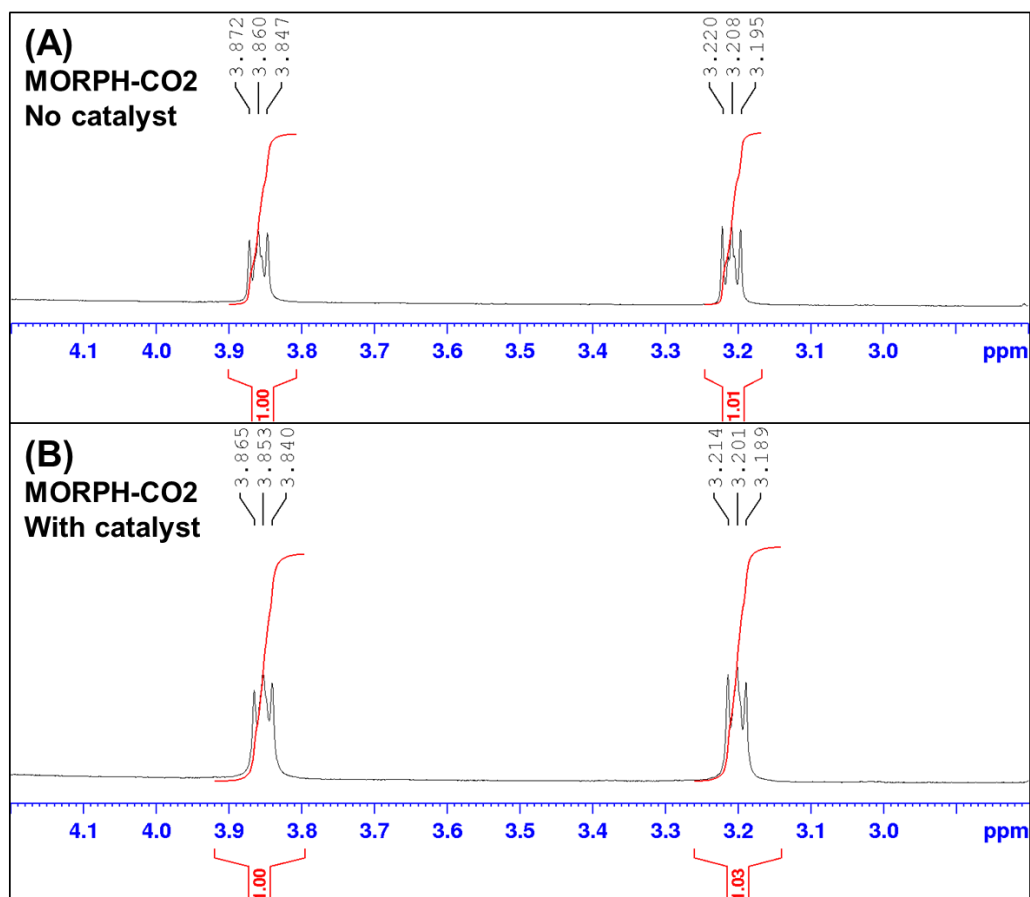


Figure 79 ¹H NMR samples of aqueous solutions of 5 mM MORPH-CO₂ with and without 5 mM Mn(bpy-COOH)

FTIR spectroscopy shows that there is interaction between Mn(bpy-COOH) and both MORPH and MORPH-CO₂ however further analysis with UV/Vis and ¹H NMR spectroscopy gave limited insight into the nature of this interaction. While an interaction between the starting complex, Mn(bpy-COOH) and morpholine-CO₂ may not necessarily lead to catalytic activity, it provides a point of interest to begin electrolysis in aqueous CO₂ capture solutions at relevant amine concentrations.

4.4 Electrochemistry of Mn(bpy-COOH) in morpholine

All electrochemistry is reported in one compartment electrochemical cell using a glassy carbon working electrode (GCE), an Ag/AgCl reference electrode and a Pt mesh counter behind a Vycor frit. All electrochemistry was run at room temperature and pressure (see Chapter 6 for further details).

4.4.1 CV Analysis

To get an initial assessment of the electrochemistry of Mn(bpy-COOH) in morpholine, cyclic voltammograms (CV's) of 0.5 mM Mn(bpy-COOH) in 30 wt% aqueous morpholine solutions with 0.5 M NaHCO₃ supporting electrolyte were obtained under Ar and CO₂ using a glassy carbon working electrode, **Figure 80**. While MORPH-CO₂ is conductive enough without supporting electrolyte, NaHCO₃ was added to lower the resistance of MORPH-Ar, making it possible to do CV analysis. The morpholine solution under Ar and CO₂ was pH 11.5 to 8.6 respectively both with and without catalyst. This response was compared to the catalyst response with no amine, in 0.5 M NaHCO₃ electrolyte where the pH is 8.6 and 7.5 under Ar and CO₂ respectively (**Figure 80**). In both cases, we observe two irreversible reductions at around -1.1 V_{Ag/AgCl} and -1.4 V_{Ag/AgCl}.

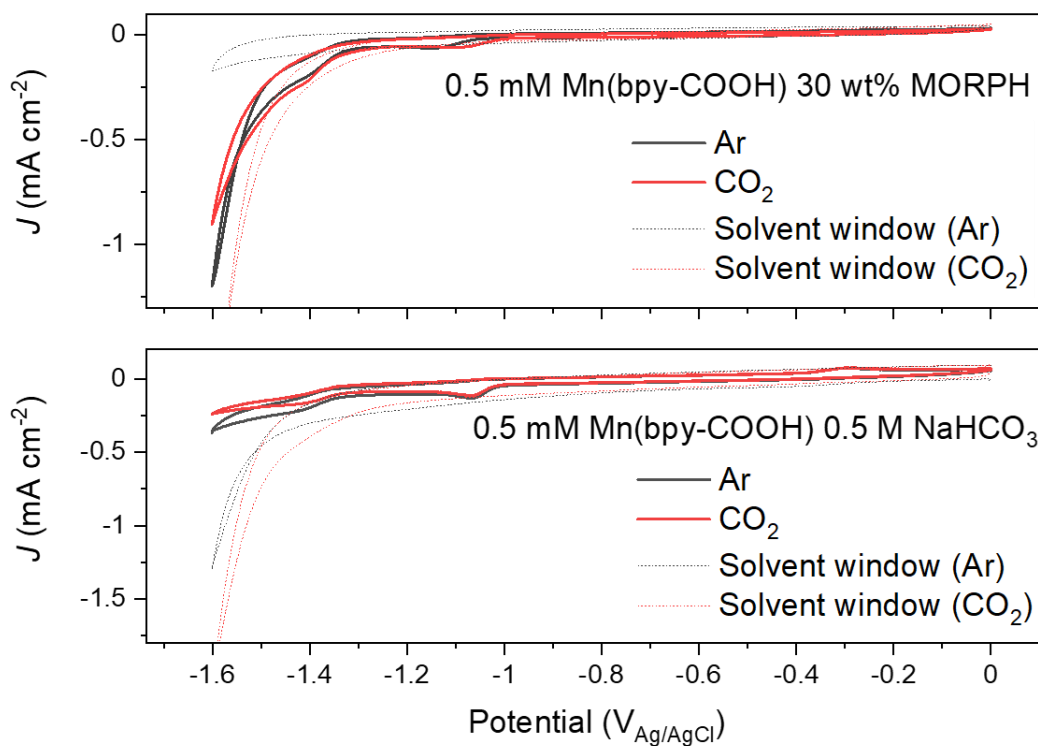


Figure 80 CVs of 0.5 mM Mn(bpy-COOH) in 30 wt% morpholine (top) (pH 11.5(Ar) & pH 8.6(CO₂)) and 0.5 M NaHCO₃ (bottom) (pH 8.6(Ar) & pH 7.5(CO₂)) at 50 mV/s. The solvent window is recorded under the same conditions in the absence of the catalyst (dashed). No iR compensation.

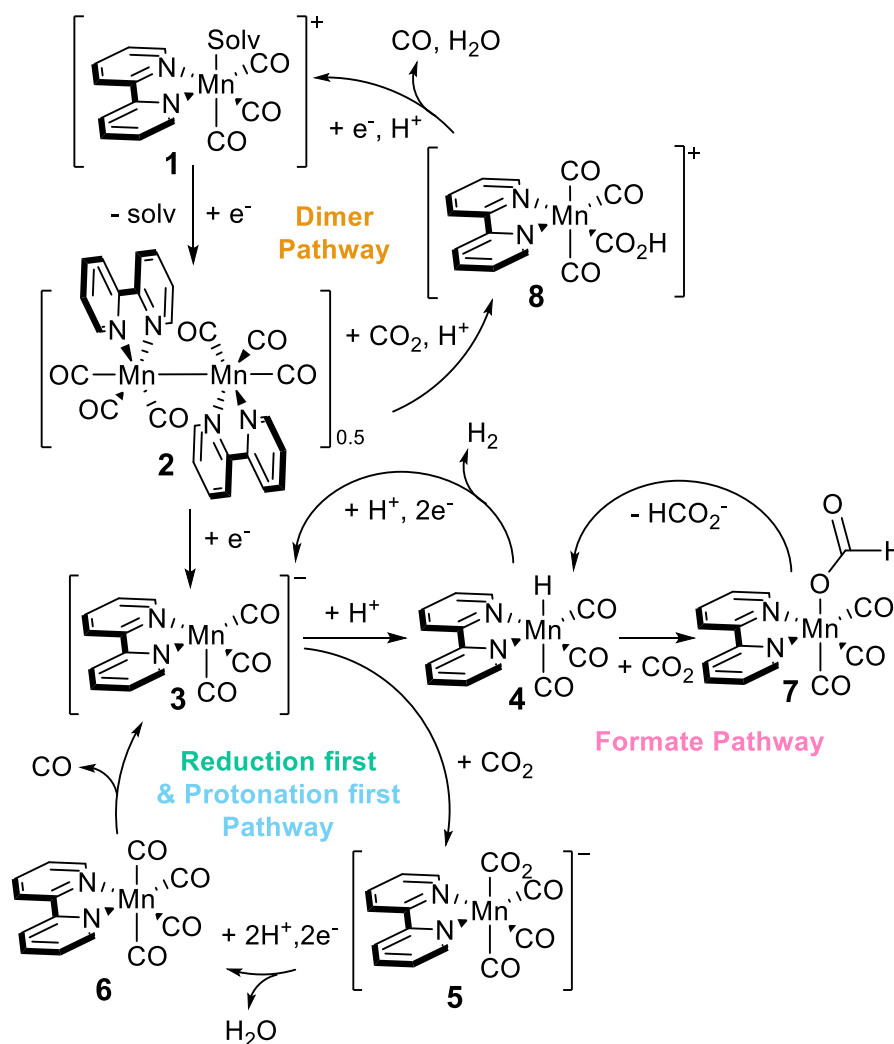


Figure 81 Simplified catalytic cycle for $Mn(bpy)$ catalysts reproduced from literature.^{29,40,41}

The first reduction at around $-1.1 V_{Ag/AgCl}$ is attributed to the first reduction of **1** (Figure 81), upon reduction the solvent ligand is lost and the complex undergoes dimerization to the dimer species (**2**, Figure 81). With no amine present the coordinated solvent is expected to be H₂O from the FTIR, this reduction occurs at $-1.08 V_{Ag/AgCl}$ under both Ar and CO₂. In 30 wt% MORPH-CO₂ solution, this reduction also occurs at a similar potential of $-1.09 V_{Ag/AgCl}$ however is shifted slightly more negative to $-1.16 V_{Ag/AgCl}$ in MORPH under Ar, which could be a result of the higher pH in this solution,³⁴ or suggest a small stabilisation of the starting species due to solvent coordination of morpholine, requiring a slightly higher potential to reduce the species and displace the solvent.

The second reduction at $-1.4 V_{Ag/AgCl}$ is assigned to the 2-electron reduction of the dimer to give two equivalents of active catalyst $[Mn^0(bpy(COO^-)_2)(CO)_3]^{3-}$ (**3**, Figure 81). This reduction feature shows very little shift in the different solvents, however with no amine, the

formation of **3**, is followed by a plateau current of -0.3 mAcm^{-2} and -0.2 mAcm^{-2} under both Ar (pH 8.6) and CO₂ (pH 7.5) respectively. This response is similar in shape to that reported by Walsh *et al.* of the complex in 0.1 M KCl + 0.5 M K₂CO₃ electrolyte on GCE at pH 7. However, Walsh *et al.* observed an increase in current under CO₂, which is not seen here, though this may be convoluted by the changing pH in this study as higher currents under both Ar and CO₂ were reported at pH 9 compared to pH 7 on GCE.³⁴

In morpholine, the current increases significantly after the reduction feature at $-1.4 \text{ V}_{\text{Ag}/\text{AgCl}}$ suggesting reduction of species not limited by diffusion. This points to either direct reduction of water, morpholine or carbamate species which are available in high enough concentration to be reduced. In **Figure 80**, the solvent windows of the GCE without catalyst show, with the exception 30 wt% MORPH under Ar which is at a higher pH, the onset of hydrogen evolution. When the catalyst is added, the solvent window of the GCE appears to be pushed back, especially in NaHCO₃, possibly caused by the competition between the catalyst and background HER for electrons and/or protons, this was also observed on GCE by Walsh *et al.*³⁴

As the potential is scanned positive, a small oxidation feature corresponding to the oxidation of the dimer ($-1.04 \text{ V}_{\text{Ag}/\text{AgCl}}$) is observed in NaHCO₃, under both Ar and CO₂, especially at higher scan rates (see **Figure 82**). However, dimer formation appears to be almost completely irreversible in morpholine (**Figure 83**), even at scan rates as high as 1 V/s, suggesting the rate of the subsequent reaction following the formation of the active catalyst is much larger than the reduction occurring in NaHCO₃. The same is true of the oxidation feature at $-0.25 \text{ V}_{\text{Ag}/\text{AgCl}}$ which follows a similar trend. While there is significant pH variation between the solutions (pH 11.5 and pH 8.6 in NaHCO₃ and MORPH under Ar respectively) this response is the opposite of the pH trend of the catalyst shown by Walsh *et al.* where at the highest pH (MORPH under Ar), the catalyst is expected to show the most reversibility, suggesting this is not a result of a pH.³⁴

The CV analysis shows little difference between Ar and CO₂, both due the lack of experimental control over changing pH between purging and the equilibrium between bicarbonates, Eq (27), and/or carbamates, Eq (23), to CO₂ which would mean even when the solution was purged with Ar, small amounts of CO₂ would still be present. While CV provides insight into the reaction rates through measured current density, it gives limited information related to the reduction reaction taking place at a given potential. Due to the complexity of the amine-catalyst mixture,

chronoamperometry and product analysis was used to differentiate between hydrogen production and eCO₂R.

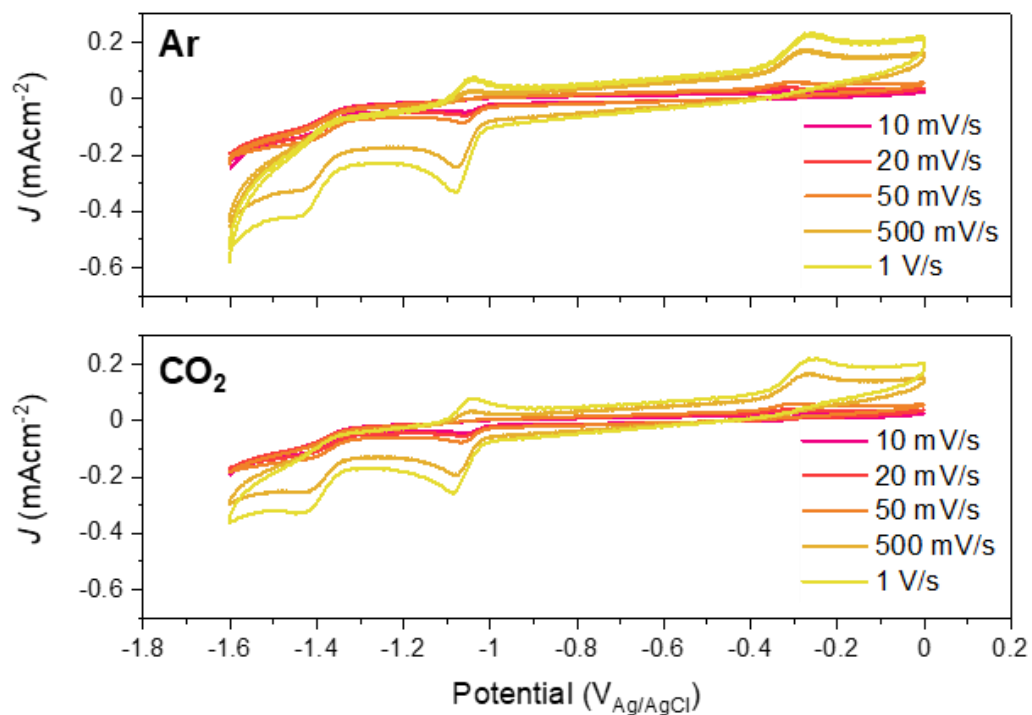


Figure 82 CVs of 0.5 mM Mn(bpy-COOH) at a range of scan rates in 0.5 M NaHCO₃ under Ar (top) (pH 8.6) and CO₂ (bottom) (pH 7.5). No iR compensation.

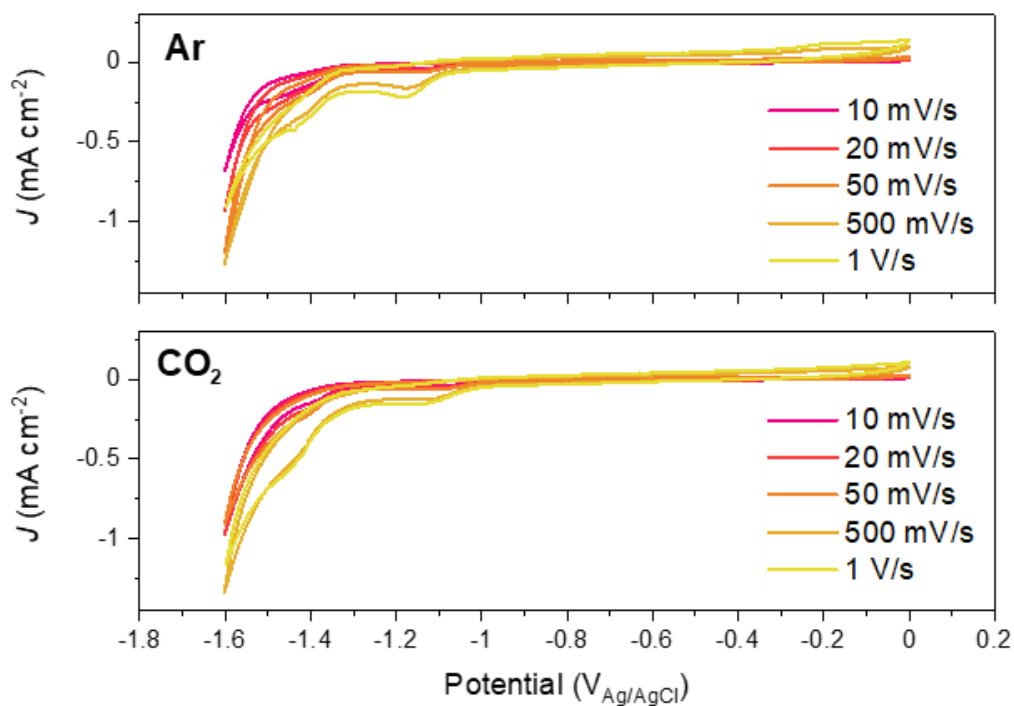


Figure 83 CVs of 0.5 mM Mn(bpy-COOH) at a range of scan rates in 30 wt% morpholine under Ar (top) (pH 11.5) and CO₂ (bottom) (pH 8.6) with 0.5 M NaHCO₃ supporting electrolyte. No iR compensation.

4.4.2 Bulk Electrolysis

Initial electrolysis results for Mn(bpy-COOH) in 30 wt% MORPH-CO₂ appeared very promising however the following limitations of this data are acknowledged. The first is that Faradaic efficiencies are variable and often low. The primary way to measure products is by GC but we have also investigated if the missing charge is being used to generate alternative (not CO, H₂) liquid products through analysis of the solutions via IC, GC-MS and ¹H NMR and no further products, or degradation products of the morpholine were found (see appendix). Possible explanations include cell design (half-cell) at low overpotentials giving rise to very low currents and low moles of product (~0.2 μmol CO produced after 2 h electrolysis at -1.3 V_{Ag/AgCl}) leading to large errors between experiments.

The solubility of different gasses in the amine mixtures was also observed to cause issues in the product detection by changing the partitioning of the species between the solution and headspace. Normally cells are purged with CO₂ or N₂ with 1% CH₄ used as an internal calibrant (tracer) to account for leak losses over the course of electrolysis through fittings, however the large difference of solubility of CO₂ compared with CH₄ in the capture mixture causes large errors. To mitigate this as best as possible solutions were pre-purged with CO₂ to convert as much of the amine to carbamate as possible before a second short purge with the tracer containing gas focussed in the head space.

Reproducibility was also an issue with large discrepancies between data take in 2021 to data taken in 2023 shown in **Figure 84**. FTIR and electrochemical analysis of the catalyst suggested that no degradation had taken place of the stored catalyst. ¹H NMR of the amine mixture showed no identifiable amine degradation either. Other parameters such a purging time, lab temperature and light exposure were controlled as best as possible however no cause for this was identified within the time frame of this project. To ensure the most accurate data analysis and discussion possible, all subsequent data comparisons are made between data which was recorded within April to December 2021 and the reader should be aware that whilst initial studies do tentatively support the conclusion that the Mn catalyst may be able to operate in capture media there are clearly parameters in the experiment that are poorly understood and not controlled.

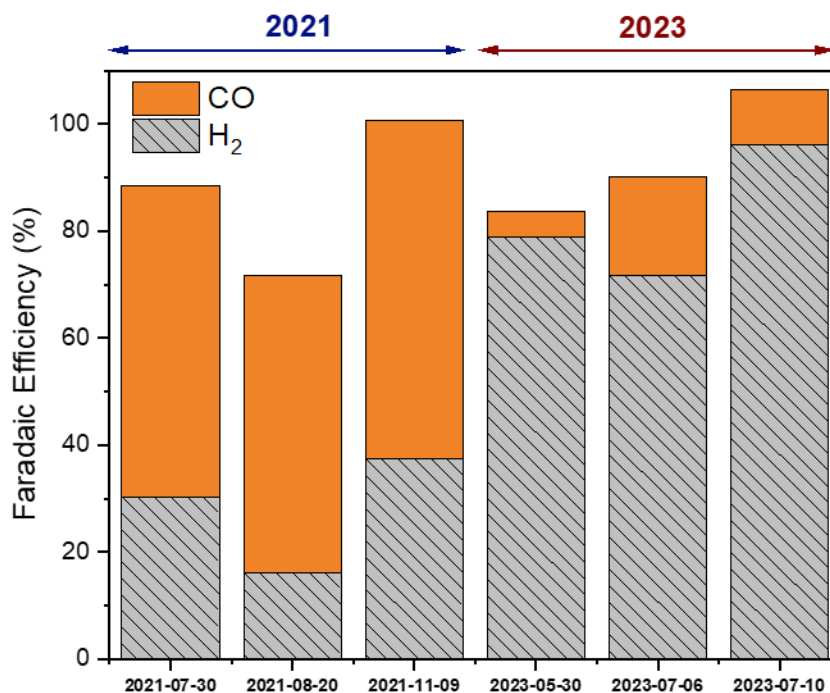


Figure 84 Faradaic efficiencies of 0.5 mM Mn(bpy-COOH) in 30 wt% morpholine-CO₂ with no supporting electrolyte at -1.3 V_{Ag/AgCl} showing discrepancies between data taken in 2021 vs 2023. Experiments were carried out in a stirred half-cell with GC working electrode, Ag/AgCl reference and Pt counter electrode at 2 h.

4.4.2.1 Initial electrolysis of Mn(bpy-COOH) in MORPH-CO₂

Electrolysis experiments of 0.5 mM Mn(bpy-COOH) in 30 wt% morpholine were ran, holding at -1.3 V_{Ag/AgCl} (shown in **Figure 85**) and -1.4 V_{Ag/AgCl} (shown in **Figure 87**) for 2 hours. Here, no supporting electrolyte was used as the charged species formed upon reaction of the amine with CO₂ is sufficiently conductive enough to perform electrolysis. The total FE is shown to increase overtime, a trend observed across electrolysis data, which is attributed to sufficient build-up of products in the head space. At -1.3 V, the current is more stable and the rate of CO production is significantly higher when compared to applying a higher overpotential. At -1.3 V_{Ag/AgCl} the potential is not sufficiently negative to reduce the dimer and form [Mn⁰(bpy(COO)₂)(CO)₃]³⁻ (complex **3**, **Figure 81**) thus it is proposed that CO production is occurring through the dimer pathway where a FE_{CO} of approximately 50% is achieved, which

is stable for 2 hrs.^{42–45} While electrolysis is performed at room temperature and pressure, where there is a significantly higher concentration of carbamate than free dissolved CO₂ at these conditions, it is still not clear which is the carbon source, especially as Mn(bpy) catalysts are reportedly selective even at low CO₂ concentrations.²⁷

While it is not clear whether CO is produced through reduction of the carbamate or dissolved CO₂, catalyst degradation is shown not to be the major source of CO through electrolysis at -1.3 V for 2 h in 30% MORPH-N₂. Here the pH of solution was corrected from 11.0 to 9.0 with HCl and 0.5 M KCl supporting electrolyte is added to ensure solution is conductive and comparable to conditions ran under CO₂. While the total faradaic efficiency is low, the FE_{CO} is less than 2%, indicating CO from catalyst degradation is minimal (**Figure 86**).

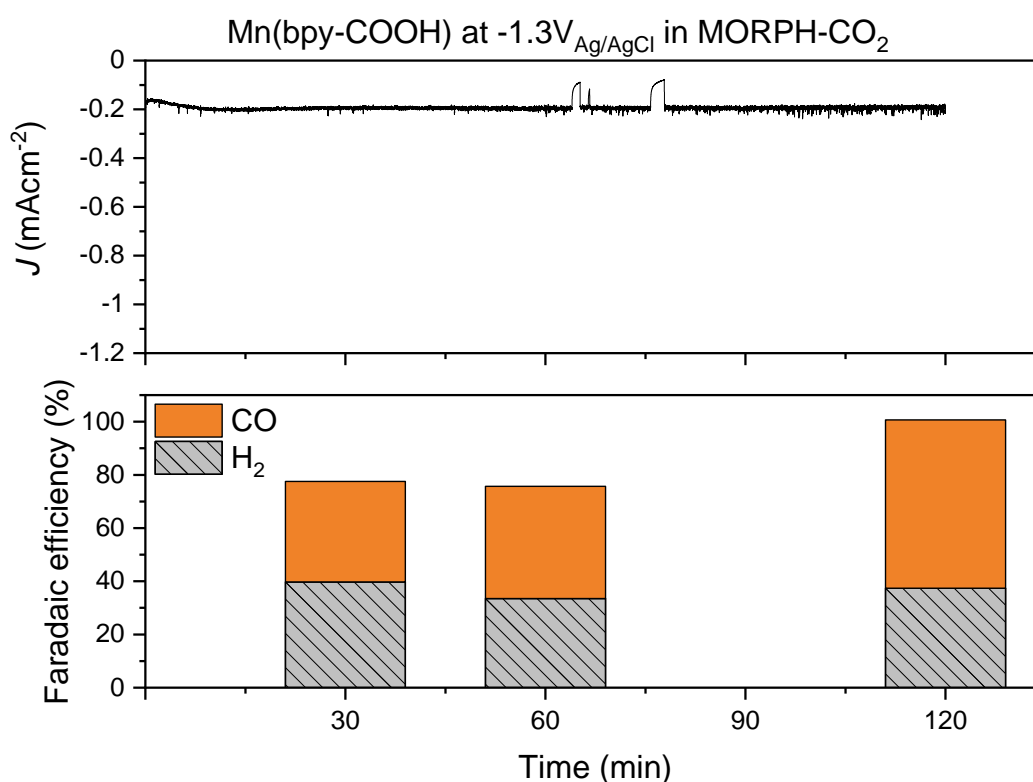


Figure 85 Electrolysis data of 0.5 mM Mn(bpy-COOH) at -1.3 V_{Ag/AgCl} over 2 h in 30 wt% MORPH-CO₂ (pH 8.6)

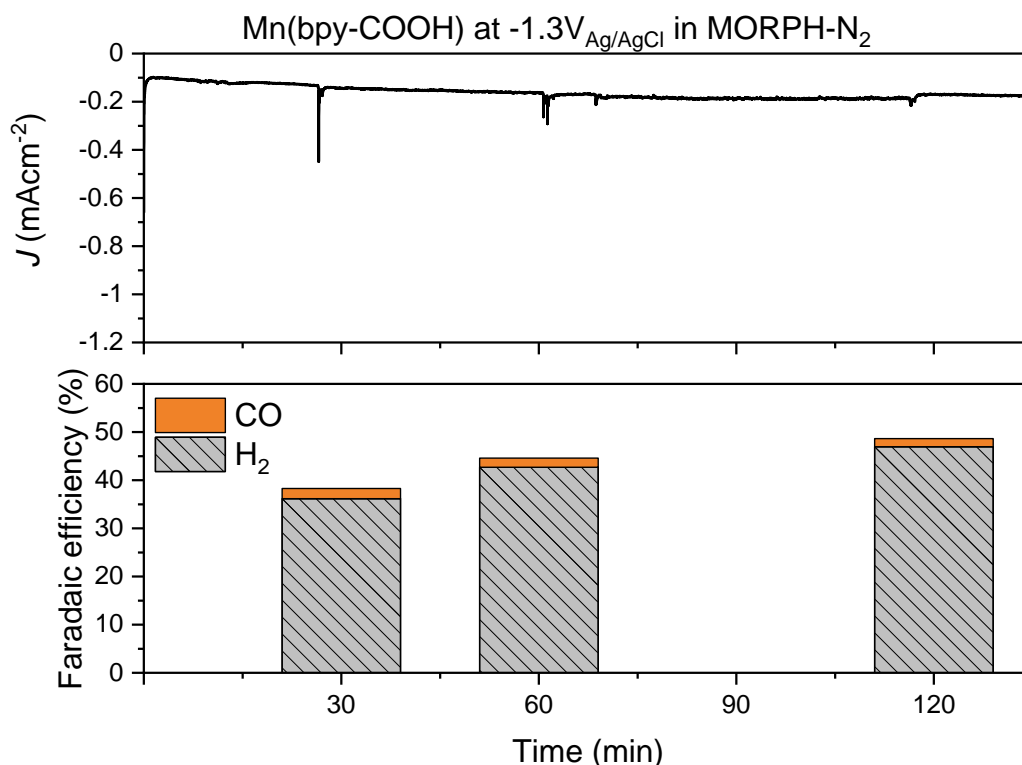


Figure 86 Electrolysis data of 0.5 mM Mn(bpy-COOH) at $-1.3 V_{Ag/AgCl}$ over 2 h in 30 wt% MORPH-N₂ with 0.5 M KCl (pH 9.0).

At $-1.4 V_{Ag/AgCl}$ (**Figure 87**) the FE_{CO} drops sharply to $< 5\%$, this suggests that following the formation of $[Mn^0(bpy(COO)_2)(CO)_3]^{3-}$ (**3**, **Figure 81**), it becomes protonated to the Mn-hydride (**4**, **Figure 81**) which goes on to catalytically produce hydrogen. This is in partial agreement with Bhattacharya *et al.* who previously proposed that morpholine promotes the formation of Mn-hydride through protonation of Mn(bpy) by the corresponding carbamic acid of morpholine (MORPH-COOH) or protonated morpholine (MORPH-H⁺) in dry MeCN.²⁹ While we would expect MORPH-COOH to be fully dissociated to the carbamate in aqueous solution, it is possible that MORPH-H⁺ could be fulfilling this role as an effective proton source that pre-associates to the complex. Bhattacharya *et al.* observed formate production as a result of Mn-hydride formation, however in this work no formate production was observed via ion chromatography or ¹H NMR at either potential. In a fully aqueous system, there are significantly larger concentrations of proton donors present, increasing the likelihood of protonation, over CO insertion into Mn-H which could explain the predominant formation of hydrogen over formate in this study.

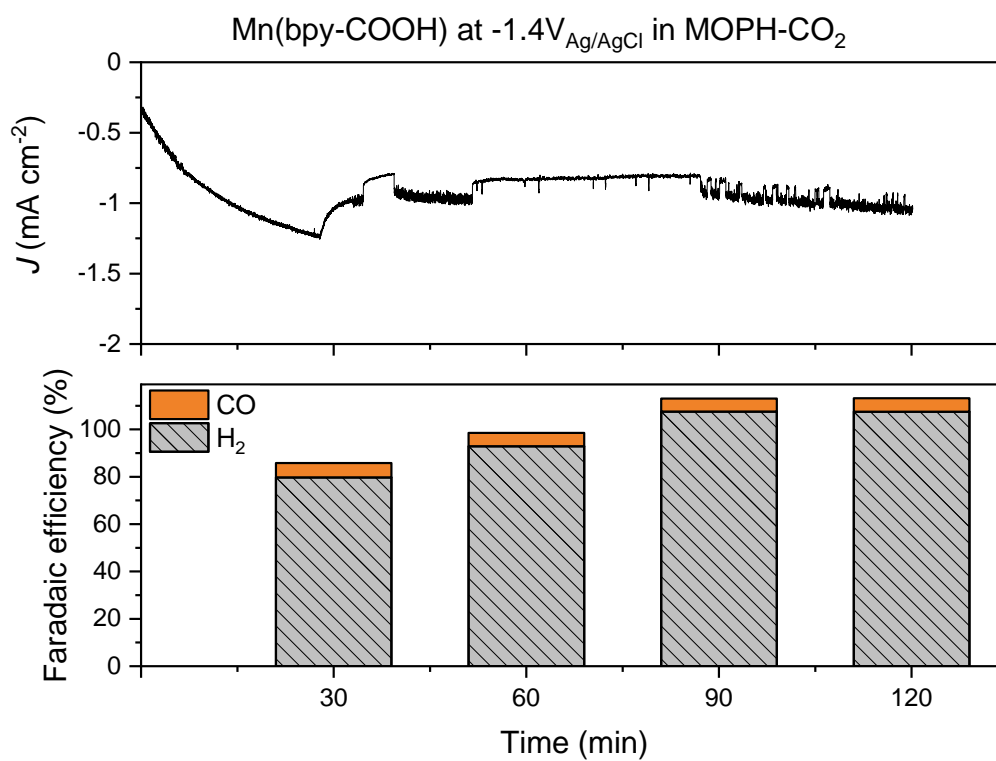


Figure 87 Electrolysis data of 0.5 mM Mn(bpy-COOH) at $-1.4 V_{Ag/AgCl}$ over 2 h in 30 wt% MORPH-CO₂ (pH 8.6)

While formate was not produced in the 30 wt% MORPH-CO₂ solution, initially electrolysis experiments showed CO production at $-1.3 V_{Ag/AgCl}$ was significant, giving an average FE_{CO} of 59 ± 4 after 2 hours. Error bars are the result of triplicate experiments where values were averaged and error for FE_{H_2} and FE_{CO} was calculated with one standard deviation. Error for values which combine uncertainties (such as J_{CO}) was calculated with Propagation of Error.

In **Figure 88**, the Faradaic efficiencies of 0.5 mM Mn(bpy) on GCE is compared to Ag wire in 30 wt% morpholine. While previous studies have proposed Ag to be one of the more CO selective metal catalysts in amine solutions, this is mainly achieved by releasing CO₂ at the electrode by shifting the carbamate equilibrium by increasing proton concentrations and/or temperatures or tailoring the EDL with additional cations. Without these modifications, selectivity remains low, with FE_{CO} ranging from 6% in literature,^{16,20} to 1% in this work (**Figure 88**). While the total currents for Mn(bpy-COOH) are much lower than for Ag (0.2 mA cm^{-2} compared to 2 mA cm^{-2} respectively), Mn(bpy-COOH) appears more selective for integrating CO₂ capture and conversion compared to conventional Ag electrodes which make almost exclusively hydrogen.

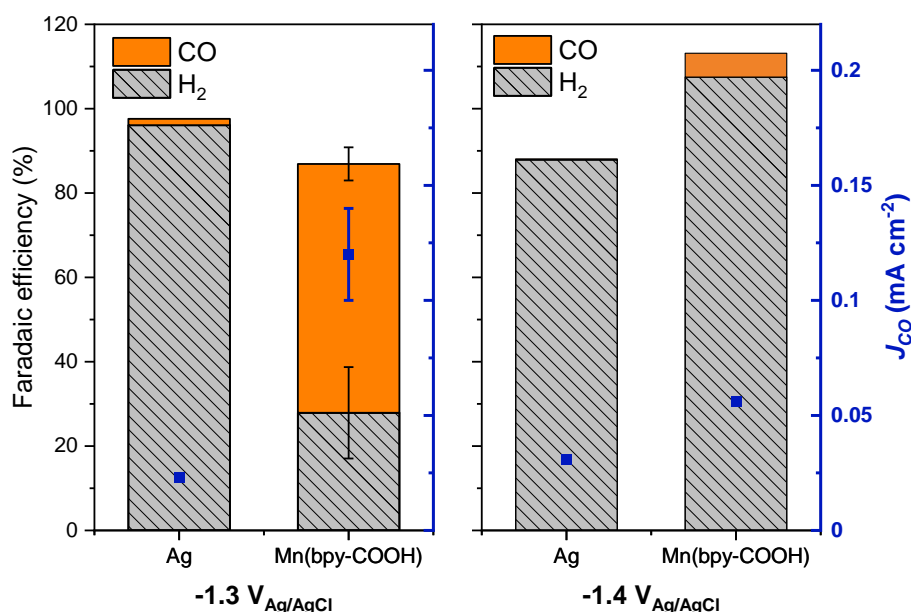


Figure 88 Faradaic efficiencies of Ag wire compared with 0.5 mM Mn(bpy-COOH) in 30 wt% MORPH-CO₂ (pH 8.6) after 2 h electrolysis at $-1.3 V_{Ag/AgCl}$ or $-1.4 V_{Ag/AgCl}$

The electroactivity of Mn(bpy-COOH) is compared in **Figure 89** in 30 wt % MORPH-CO₂ (pH 8.4) with no supporting electrolyte to in CO₂ purged 0.5 M NaHCO₃ (pH 7.7) with no amine where CO/H₂ is 2.1 and 3.8 respectively after 2 h electrolysis at $-1.3 V_{Ag/AgCl}$. Here the

selectivity of Mn(bpy-COOH) is remarkably similar, despite the two very different environments. As discussed previously, MORPH-CO₂ is a more complex mixture which will contain high concentrations of carbamates (~1.0M), ammonium ions (~1.0M) and unreacted morpholine (~1.4M) alongside the bicarbonate and dissolved CO₂ also present in 0.5M NaHCO₃.

Because of the large disparity in both species type and molarity between the two solutions, the concentration of dissolved CO₂ present is also estimated. While both solutions are expected to be saturated with dissolved CO₂, this saturation value varies with ion types and is expected to decrease with increasing salt concentration, an effect known as “salting-out”.⁴⁶ The maximum gas solubility in salt solutions (c_G) (kmolm⁻³) is calculated using the Sechenov relation below:

$$\log\left(\frac{c_{G,o}}{c_G}\right) = \sum(h_i + h_G)c_i \quad (29)$$

Where $c_{G,o}$ is gas solubility in pure water (0.033 kmolm⁻³ for CO₂), h_i is the ion specific parameter (m³ kmol⁻¹) (also known as the van Krevelen coefficient), h_G is the gas specific parameter (-0.017 m³ kmol⁻¹ for CO₂⁴⁶) and c_i is the concentration of the ion (kmolm⁻³). Unfortunately the van Krevelen coefficients for morpholine carbamate (MORPH-COO⁻) and morpholinium (MORPH-H⁺) have not been reported, so these values for DEA (another secondary alkanolamine) experimentally derived by Browning and Weiland are used (see **Table 6**) to estimate the solubility of CO₂ in 30 wt% MORPH(aq) at 298.15 K.⁴⁷

Table 6 *van Krevelen coefficients and concentrations used to estimate the concentration of dissolved CO₂ in aqueous solutions of 30wt% MORPH-CO₂ compared with 0.5 M NaHCO₃*

Ion	h_i (m ³ kmol ⁻¹)	c_i (kmol m ⁻³)
MORPH-H ⁺	0.047	1.0
MORPH-COO ⁻	0.043	1.0
Na ⁺	0.114	0.5
HCO ₃ ⁻	0.073	0.5

From this, the maximum solubility of CO₂ in 30 wt% MORPH-CO₂ and 0.5 M NaHCO₃ was estimated to be 0.029 M and 0.028 M respectively, showing very little difference in the availability of dissolved CO₂ to Mn(bpy-COOH) in either solution which may account for the similar activity in both solutions.

Another important difference is the nature of the cation species in each solution. Unlike in 0.5M NaHCO₃, there are no alkali metal cations in MORPH-CO₂ with the only cation species present being the morpholinium which has previously been suggested to hamper CO production in amine-CO₂ solutions, however, interestingly CO production is still significant with Mn(bpy-COOH). Though the relationship between both cation species and dissolved CO₂ concentration on the activity of Mn(bpy-COOH) in 30 wt% MORPH-CO₂ is further explored in the next section.

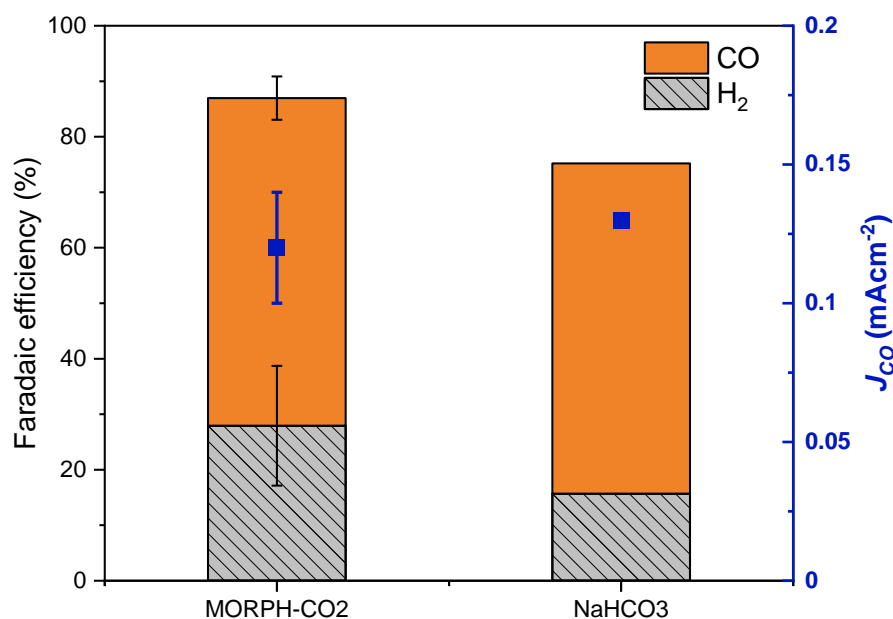


Figure 89 Faradaic efficiencies and partial current densities of 0.5 mM Mn(bpy-COOH) in 30 wt % MORPH-CO₂ (pH 8.6) and 0.5 M NaHCO₃ (pH 7.5) after 2 h electrolysis at -1.3 V_{Ag/AgCl}.

4.4.2.2 Effects of electrolyte addition

Previously Lee *et al.* reported improved activity for Ag electrodes in MEA-CO₂ with addition of 2 M KCl, proposing that the presence of alkali metal cations tailored the EDL, providing the carbamate species with better access the electrode. With a homogenous catalyst and an inert working electrode material, direct electron transfer from the electrode to the carbamate is not expected in this system. However, it is feasible that if the protonated amine is blocking the

electrode, that it would also hamper electron transfer to Mn(bpy-COOH) thus electrolysis of 0.5 mM Mn(bpy-COOH) at -1.3 V_{Ag/AgCl} in 30 wt% MORPH-CO₂ with the addition of 2 M KCl electrolyte is shown in **Figure 90**.

Here the FE_{CO} is 101% (here FE_{total} is higher than 100% due to error in product detection) and the FE_{H₂} is very low at only 12%. With the addition of 2M KCl, the current density is comparable (~0.2 mA cm⁻²) however the CO/H₂ increases significantly from 2.1 to 8.6, suggesting the addition of 2M KCl increases CO production as opposed to suppressing HER. The increase in CO production also indicates that any decrease in solubility of dissolved CO₂ (CO₂ solubility estimated to reduce from 0.028 M (MORPH-CO₂) to 0.012 M (MORPH-CO₂ with 2M KCl) has minimal effect compared to the increase in activity with 2M KCl addition.

Interestingly this is not observed in our control with Ag working electrode (**Figure 91**), which displays higher current densities but no increase FE_{CO}, contrary to what was reported by Lee *et al.*²⁰ This may suggest an alternative cause for the improved selectivity for Mn(bpy-COOH) in MORPH-CO₂ rather than improved access to the electrode. There are a limited number of studies on the cation effect for CO₂ reduction with molecular catalysts compared to metals, though the addition of alkali metal cations has been seen to increase CO production,⁴⁸⁻⁵⁰ with a study on a Mn bipyridine complex by Sato *et al.* suggesting a synergistic effect between potassium cations and carbon support lowering the overpotential for CO₂ reduction.⁵¹ While initial experiments appear to suggest a significant improvement with cation addition to Mn(bpy-COOH) in MORPH-CO₂, further studies are required to deconvolute the mechanism by which this occurs.

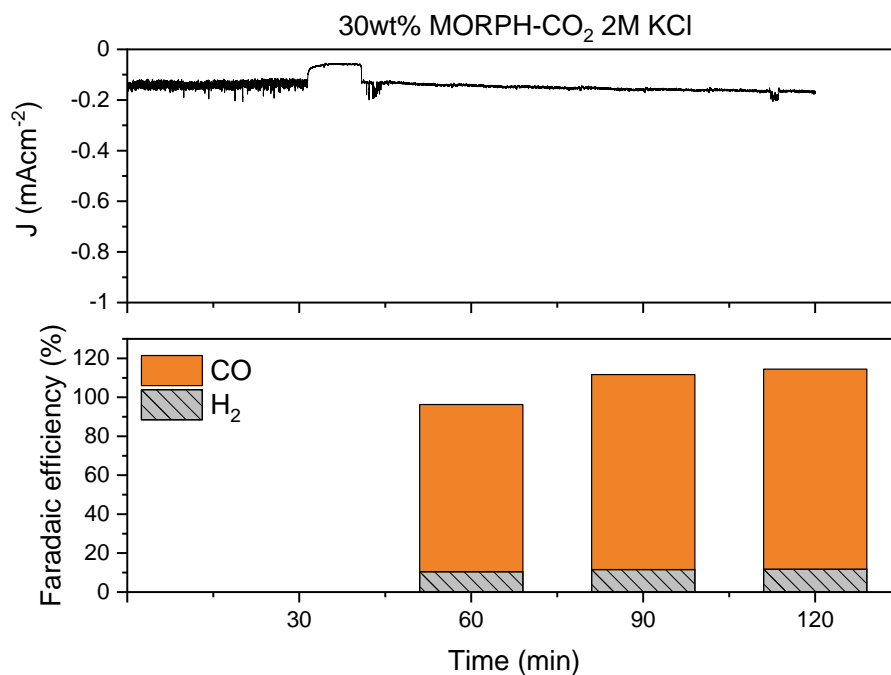


Figure 90 Electrolysis data of 0.5 mM Mn(bpy-COOH) at $-1.3 V_{Ag/AgCl}$ over 2 h in 30 wt% MORPH-CO₂ with the addition of 2M KCl

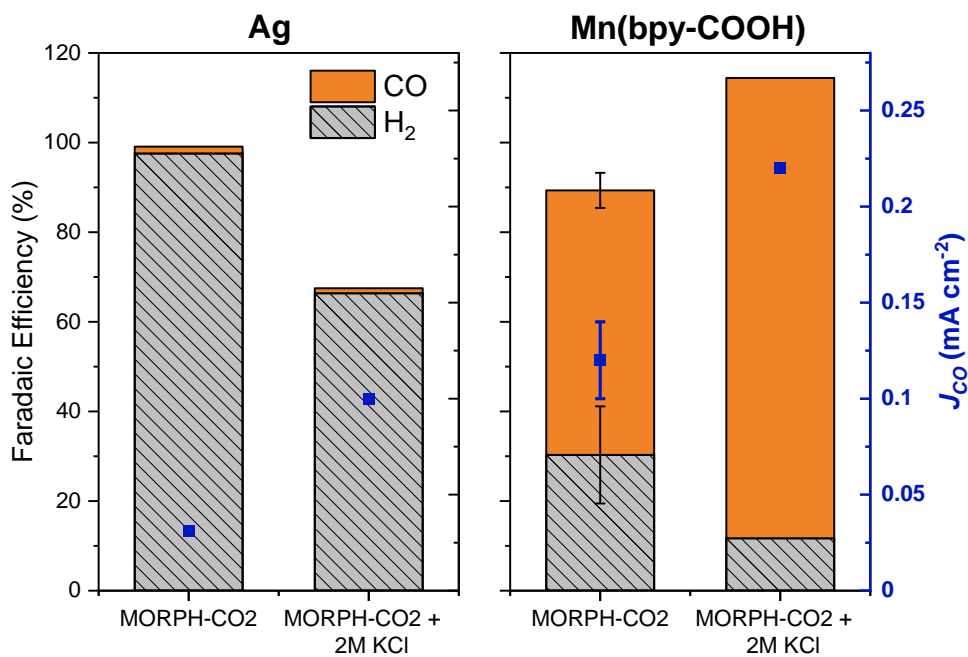


Figure 91 Faradaic efficiencies of Ag wire compared with 0.5 mM Mn(bpy-COOH) in 30 wt% MORPH-CO₂ with and without the addition of 2M KCl after 2 h electrolysis at $-1.3 V_{Ag/AgCl}$

In line with literature conventions, the activity of Mn(bpy-COOH) in MORPH-CO₂ with 2M KCl was assessed after a second 15-minute purge with N₂ (denoted as MORPH-CO₂-N₂) (**Figure 92**). While the concentration of dissolved CO₂ has been estimated to change with no obvious effect on CO production so far, the values are all in the range 10-30 mM dissolved CO₂. This value is expected to drop significantly lower with a N₂ purge, with Shen *et al.* reporting a concentration of dissolved CO₂ as low as 0.08 mM (though this was achieved after six hours of purging with N₂, which is significantly longer than is reported here or elsewhere in literature).¹⁷ After removing most of the dissolved CO₂, the only carbon source for CO production is carbamates/bicarbonates, thus if activity is retained, it suggests conversion of the carbamate (or bicarbonate) directly.

The Faradaic efficiencies and partial current densities of 0.5 mM Mn(bpy-COOH) in MORPH-CO₂ and MORPH-CO₂-N₂ after 2 h electrolysis at -1.3 V_{Ag/AgCl} are shown in **Figure 93**. Here the J_{CO} halves as CO/H₂ drops from 8.6 to 1.6 with the N₂ purge suggesting that while Mn(bpy-COOH) shows binding to carbamate species, it may not be the preferred substrate for CO production. Despite selectivity decreasing with the decreased concentration of dissolved CO₂, a FE_{CO} value of 55% is obtained in 30 wt% MORPH-CO₂-N₂ with 2 M KCl, showing CO production competitive with literature in an amine-based CO₂ capture solution.

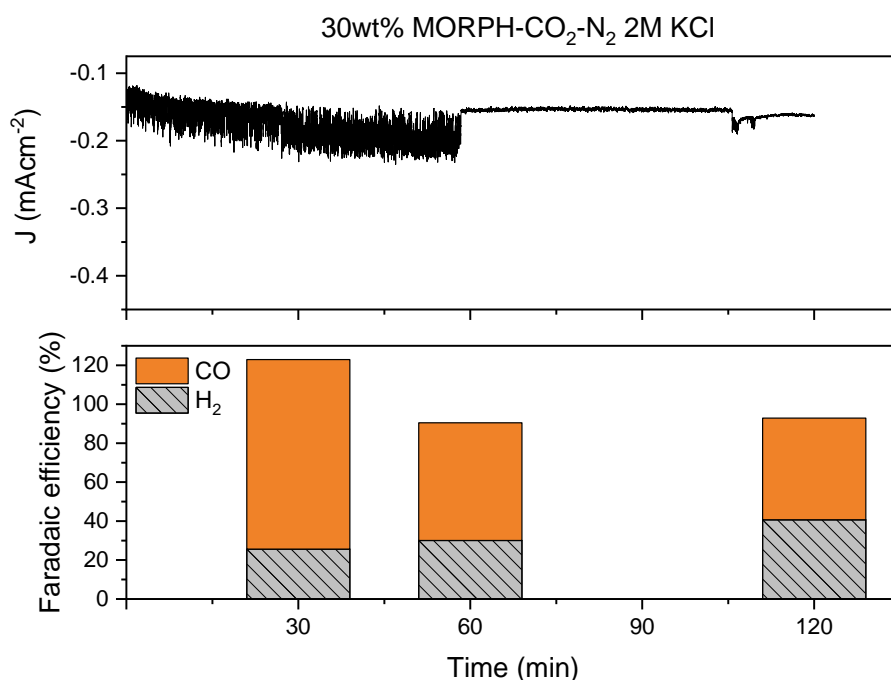


Figure 92 Electrolysis data of 0.5 mM Mn(bpy-COOH) at -1.3 V_{Ag/AgCl} over 2 h in 30 wt% MORPH-CO₂-N₂ with the addition of 2M KCl

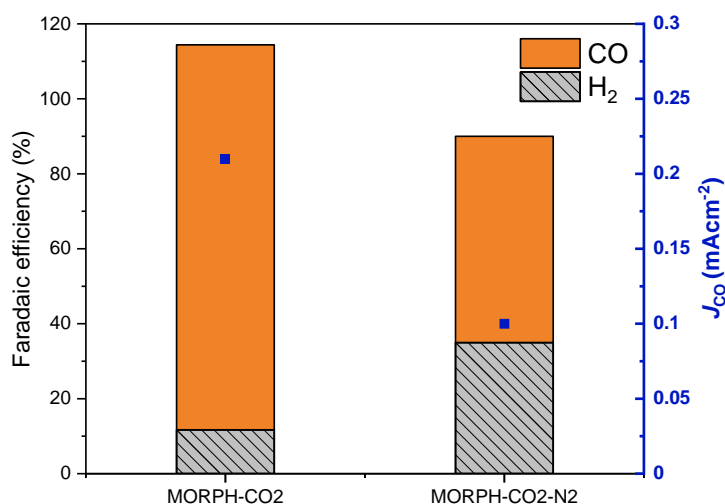


Figure 93 Faradaic efficiencies of 0.5 mM Mn(bpy-COOH) in 30 wt% MORPH-CO₂ compared with 30 wt% MORPH-CO₂-N₂ with 2M KCl after 2 h electrolysis at -1.3 V_{Ag/AgCl}

4.5 Electrochemistry in other capture amines: MEA and DEA

From initial investigations Mn(bpy-COOH) shows significant CO selectivity in 30 wt% morpholine, while the carbon source is unclear, the CO production in an industrially relevant amine mixture is competitive of what is seen in literature. To explore if this activity is specific to morpholine, the electrochemistry of 0.5 mM Mn(bpy-COOH) was also assessed in more conventional capture amines: monoethanolamine (MEA) and diethanolamine (DEA).

As with morpholine, initially CVs were ran of Mn(bpy-COOH) in aqueous solutions 30 wt% of either MEA (4.9 M) or DEA (2.9 M). The pH of MEA was 12.0 and 10.3 under N₂ and CO₂ respectively. In MEA the electrochemical behaviour appears quite different (**Figure 94** & **Figure 95**), with the first reduction of Mn(bpy-COOH) is at -1.30 V_{Ag/AgCl} (N₂) or -1.24 V_{Ag/AgCl} (CO₂). This is almost a 200 mV negative shift compared with NaHCO₃, MORPH or DEA suggesting a stabilisation of the starting catalyst species in MEA to reduction. The second reduction of the dimer is small, and shifts significantly less at -1.45 V_{Ag/AgCl} under both N₂ and CO₂. After this reduction a small increase in current is observed under CO₂ as well as a smaller oxidation of the dimer on the reverse scan, while this could suggest catalysis under CO₂ in MEA, caution should be taken as this catalyst behaviour is also observed as pH is increased, a parameter that was not controlled here.

Under DEA (pH 11.8 and 8.9 under N₂ and CO₂ respectively), the redox features on Mn(bpy-COOH) are less pronounced (**Figure 94** & **Figure 96**), however the first reduction occurs at -1.10 V_{Ag/AgCl}, more in line with what was observed in morpholine and NaHCO₃. Under N₂ the second reduction occurs at -1.40 V_{Ag/AgCl}, however is completely obscured under CO₂ by the onset of a large current. Like in morpholine, the oxidation features of Mn(bpy-COOH) in DEA appear significantly smaller even at high scan rates, suggesting fast subsequent reactions involving the catalyst.

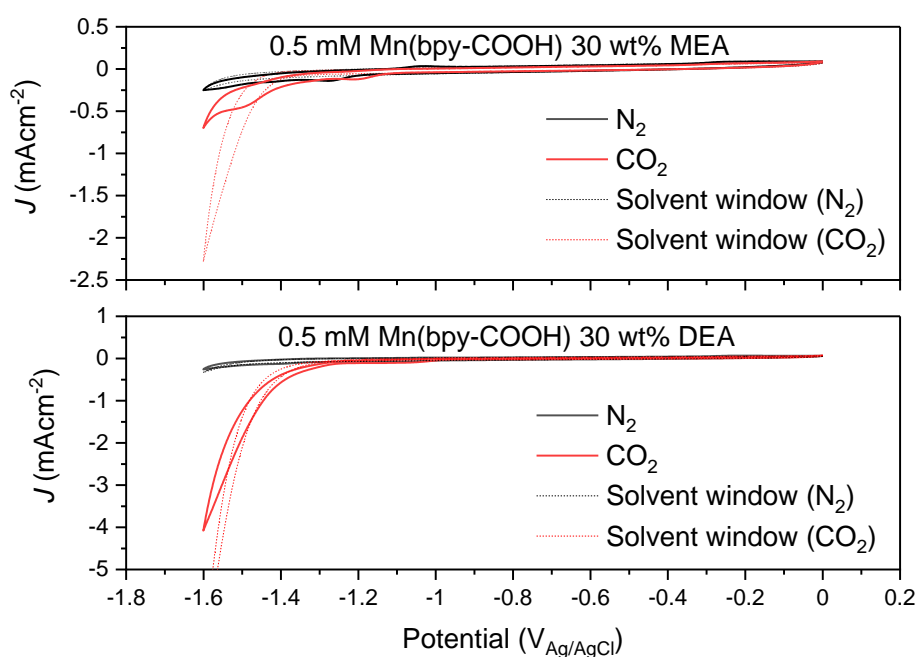


Figure 94 CVs of 0.5 mM Mn(bpy-COOH) in 30 wt% MEA (top) (pH 12.0(N₂) & pH 10.5(CO₂)) and 30 wt% DEA (bottom) (pH 11.8(N₂) & pH 8.9(CO₂)) at 50 mV/s. The solvent window is recorded under the same conditions in the absence of the catalyst (dashed).

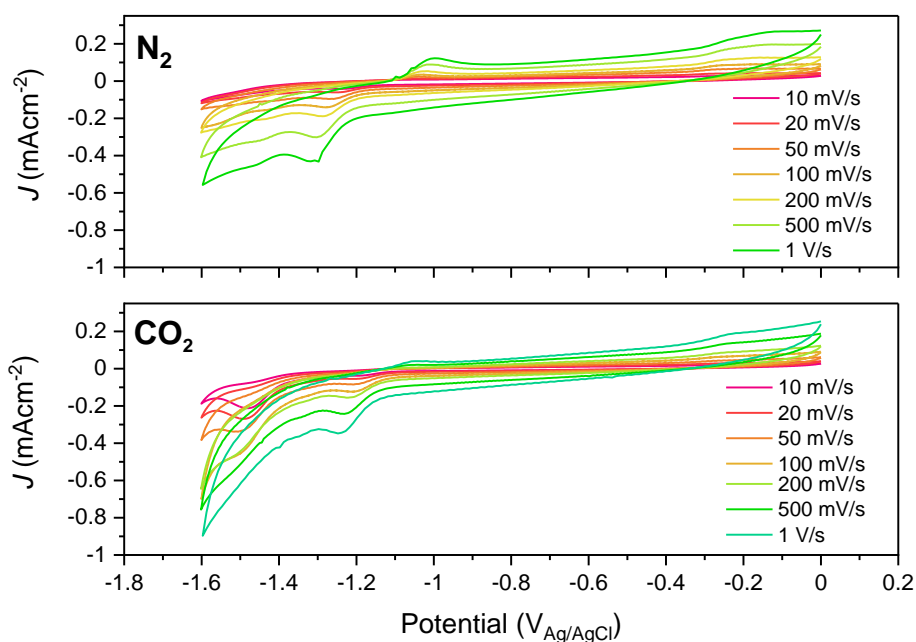


Figure 95 CVs at a range of scan rates in 30 wt% MEA under N₂ (pH 12.0) (top) and CO₂ (pH 10.5) (bottom)

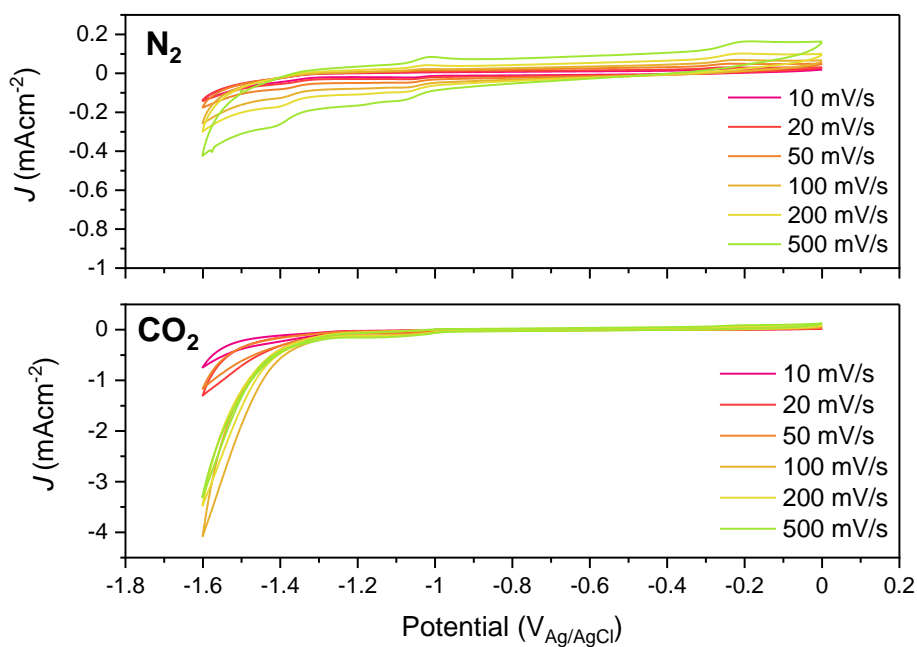


Figure 96 CVs at a range of scan rates in 30 wt% DEA under N₂ (pH 11.8) (top) and CO₂ (pH 8.9) (bottom)

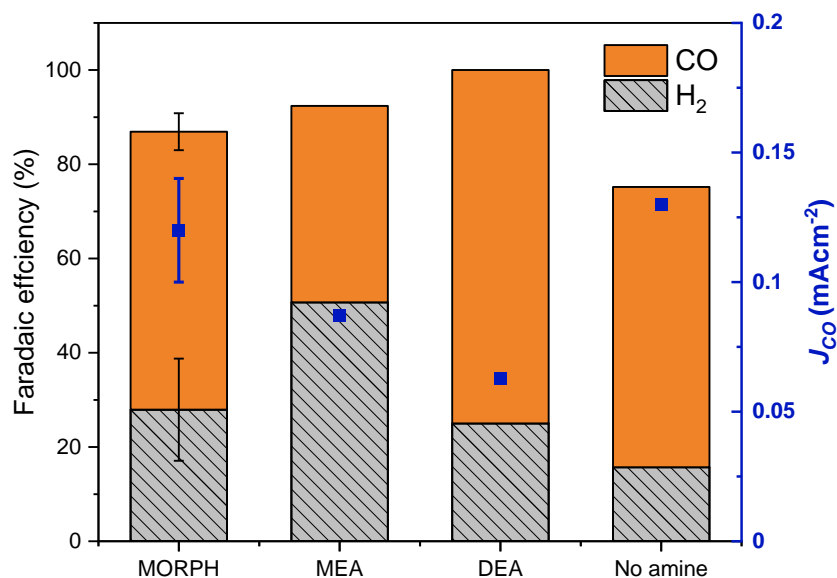


Figure 97 FEs and J_{CO} of 0.5 mM Mn(bpy-COOH) in 30 wt% of MORPH-CO₂, MEA-CO₂, DEA-CO₂ and 0.5 M NaHCO₃ (no amine) after 2 h electrolysis at $-1.3 V_{Ag/AgCl}$

Bulk electrolysis was also carried out in 0.5 mM Mn(bpy-COOH) in 30 wt % of either MEA (pH 10.5) or DEA (pH 8.9) purged with CO₂, where $-1.3 V_{Ag/AgCl}$ was applied for 2 h. The results of which are compared with MORPH-CO₂ and NaHCO₃ (denoted as no amine) in **Figure 97**. CO is produced in each case, though with varying selectivity, with DEA giving the highest selectivity of CO/H₂ = 3.0 and MEA the lowest CO/H₂ = 0.8. **Figure 97** shows indications that while Mn(bpy-COOH) can produce significant quantities of CO in a variety of amines, the CO partial current density for morpholine is the highest. The J_{CO} is the lowest in DEA despite the higher selectivity due lower total currents, suggesting HER is suppressed in DEA. This initial data suggests the catalytic activity of Mn(bpy-COOH) is not just limited to morpholine and may be of interest for integrated capture and conversion in a range of amine mixtures.

4.6 Conclusions and future work

Here spectroscopic evidence is provided of an interaction between water soluble complex, Mn(bpy-COOH), and aqueous solutions CO₂ capture amine, MORPH and its corresponding carbamate. This interaction demonstrated a point of interest for CV analysis and electrolysis of Mn(bpy-COOH) in 30wt% MORPH where impressive initial FE_{CO} values of 59% was produced after 2h at -1.3 V_{Ag/AgCl}, with the only other product being hydrogen. The selectivity was found to be increased even further with addition of 2 M KCl, though the reason for this is unclear. Experiments minimising the availability of free, dissolved CO₂, show a decrease in selectivity, however even in these conditions, CO production was still notable, thus the carbon source used by Mn(bpy-COOH) is unclear. Significant activity was also shown in DEA and MEA, which are the most commonly used amines for CO₂ capture industrially, showing this effect is not limited to morpholine.

While these initial results appear promising, issues with reproducibility need to be resolved, with increased control over pH and CO₂ loading, operation at higher currents and further insight into optimisation of detecting gas products to lower the error in these amine mixtures. More in-depth analysis of catalyst behaviour in these capture mixes compared with traditional electrolytes, as most classic CO₂ reduction catalysts show significantly lower selectivity in amine mixtures, even when the amounts of dissolved CO₂ are shown to be comparable.

There is also significant scope for further catalyst development, possibly focussing on hydrogenation catalysts which are able to interact and catalytically convert the carbamate species directly, potentially accessing higher value products than CO. Spectroelectrochemistry could also be very powerful in identifying interactions not just with the starting complex, as shown here, but the active complex formed under electrolysis.

4.7 References

- 1 I. Sullivan, A. Goryachev, I. A. Digdaya, X. Li, H. A. Atwater, D. A. Vermaas and C. Xiang, *Nat Catal*, 2021, **4**, 952–958.
- 2 F. Vega, M. Cano, S. Camino, L. M. G. Fernández, E. Portillo and B. Navarrete, in *Carbon Dioxide Chemistry, Capture and Oil Recovery*, InTechOpen, 2018, pp. 141–163.
- 3 M. Li, K. Yang, M. Abdinejad, C. Zhao and T. Burdyny, *Nanoscale*, 2022, **14**, 11892–11908.
- 4 B. Lv, B. Guo, Z. Zhou and G. Jing, *Environ Sci Technol*, 2015, **49**, 10728–10735.
- 5 S. E. Jerng and B. M. Gallant, *iScience*, 2022, **25**, 104558.
- 6 A. Khurram, L. Yan, Y. Yin, L. Zhao and B. M. Gallant, *J Phys Chem C*, 2019, **123**, 18222–18231.
- 7 A. Kohl and R. Nielsen, *Gas purification*, Gulf Publishing Company, Houston, Texas, 5th ed., 1997.
- 8 Y. E. Kim, J. A. Lim, S. K. Jeong, Y. Il Yoon, S. T. Bae and S. C. Nam, *Bull Korean Chem Soc*, 2013, **34**, 783–787.
- 9 S. A. Mazari, R. Abro, A. W. Bhutto, I. M. Saeed, B. S. Ali, B. M. Jan, L. Ghalib, M. Ahmed and N. M. Mubarak, *J Environ Chem Eng*, 2020, **8**, 103814.
- 10 G. T. Rochelle, *Curr Opin Chem Eng*, 2012, **1**, 183–190.
- 11 M. Narimani, S. Amjad-Iranagh and H. Modarress, *J Nat Gas Sci Eng*, 2017, **47**, 154–166.
- 12 B. Rezaei and S. Riahi, *J Nat Gas Sci Eng*, 2016, **33**, 388–396.
- 13 J. D. Davis, *PhD Thesis*, University of Texas, 2009.
- 14 H. Lepaumier, D. Picq and P. L. Carrette, *Ind Eng Chem Res*, 2009, **48**, 9061–9067.
- 15 S. D. Petty and B. S. Ho, *J Pet Technol*, 1984, **36**, 1603–1612.

- 16 L. Chen, F. Li, Y. Zhang, C. L. Bentley, M. Horne, A. M. Bond and J. Zhang, *ChemSusChem*, 2017, **10**, 4109–4118.
- 17 K. Shen, D. Cheng, E. Reyes-Lopez, J. Jang, P. Sautet and C. G. Morales-Guio, *Joule*, 2023, **7**, 1260–1276.
- 18 T. Li, E. W. Lees, M. Goldman, D. A. Salvatore, D. M. Weekes and C. P. Berlinguette, *Joule*, 2019, **3**, 1487–1497.
- 19 L. A. Diaz, N. Gao, B. Adhikari, T. E. Lister, E. J. Dufek and A. D. Wilson, *Green Chem*, 2018, **20**, 620–626.
- 20 G. Lee, Y. C. Li, J. Kim, T. Peng, D. Nam, A. S. Rasouli, F. Li, M. Luo, A. H. Ip, Y. Joo and E. H. Sargent, *Nat Energy*, 2021, **6**, 46–53.
- 21 J. H. Kim, H. Jang, G. Bak, W. Choi, H. Yun, E. Lee, D. Kim, J. Kim, S. Y. Lee and Y. J. Hwang, *Energy Environ Sci*, 2022, **15**, 4301–4312.
- 22 E. Pérez-Gallent, C. Vankani, C. Sánchez-Martínez, A. Anastasopol and E. Goetheer, *Ind Eng Chem Res*, 2021, **60**, 4269–4278.
- 23 M. M. Waegele, C. M. Gunathunge, J. Li and X. Li, *J Chem Phys*, 2019, **151**, 160902.
- 24 G. Marcandalli, M. C. O. Monteiro, A. Goyal and M. T. M. Koper, *Acc Chem Res*, 2022, **55**, 1900–1911.
- 25 M. C. O. Monteiro, F. Dattila, B. Hagedoorn, R. García-Muelas, N. López and M. T. M. Koper, *Nat Catal*, 2021, **4**, 654–662.
- 26 J. Bi, P. Hou, F. W. Liu and P. Kang, *ChemSusChem*, 2019, **12**, 2195–2201.
- 27 H. Kumagai, T. Nishikawa, H. Koizumi, T. Yatsu, G. Sahara, Y. Yamazaki, Y. Tamaki and O. Ishitani, *Chem Sci*, 2019, **10**, 1597–1606.
- 28 H. Koizumi, H. Chiba, A. Sugihara, M. Iwamura, K. Nozaki and O. Ishitani, *Chem Sci*, 2019, **10**, 3080–3088.
- 29 M. Bhattacharya, S. Sebghati, R. T. VanderLinden and C. T. Saouma, *J Am Chem Soc*, 2020, **142**, 17589–17597.
- 30 M. Bhattacharya, S. Sebghati, Y. M. Vercella and C. T. Saouma, *J Electrochem Soc*, 2020, **167**, 086507.

- 31 F. M. Stuardi, A. Tiozzo, L. Rotundo, J. Leclaire, R. Gobetto and C. Nervi, *Chem A Euro J*, 2022, **28**, 1–9.
- 32 S. Kar, M. Rahaman, V. Andrei, S. Bhattacharjee and S. Roy, *Joule*, 2023, **2**, 1–20.
- 33 J. J. Walsh, C. L. Smith, G. Neri, G. F. S. Whitehead, C. M. Robertson and A. J. Cowan, *Faraday Discuss*, 2015, **183**, 147–160.
- 34 J. J. Walsh, G. Neri, C. L. Smith and A. J. Cowan, *Organometallics*, 2019, **38**, 1224–1229.
- 35 G. J. Fan, A. G. H. Wee, R. Idem and P. Tontiwachwuthikul, *Ind Eng Chem Res*, 2009, **48**, 2717–2720.
- 36 M. M. Webster, M. Lugo-Pimentel, I. Kretzschmar and M. J. Castaldi, *Ind Eng Chem Res*, 2020, **59**, 8562–8570.
- 37 B. S. Ault, T. M. Becker, G. Q. Li and M. Orchin, *Spectrochim Acta A Mol Biomol Spectrosc*, 2004, **60**, 2567–2572.
- 38 H. K. Hall, *J Am Chem Soc*, 1964, **86**, 5709.
- 39 N. S. Matin, J. E. Remias, J. K. Neathery and K. Liu, *Ind Eng Chem Res*, 2013, **52**, 5221–5229.
- 40 B. Siritanaratkul, C. Eagle and A. J. Cowan, *Acc Chem Res*, 2022, **55**, 955–965.
- 41 G. Neri, J. J. Walsh, G. Teobaldi, P. M. Donaldson and A. J. Cowan, *Nat Catal*, 2018, **1**, 952–959.
- 42 M. Bourrez, M. Orio, F. Molton, H. Vezin, C. Duboc, A. Deronzier and S. Chardon-Noblat, *Angew Chem, Int Ed*, 2014, **53**, 240–243.
- 43 T. E. Rosser, C. D. Windle and E. Reisner, *Angew Chem, Int Ed*, 2016, **55**, 7388–7392.
- 44 G. Neri, P. M. Donaldson and A. J. Cowan, *Phys Chem Chem Phys*, 2019, **21**, 7389–7397.
- 45 J. J. Walsh, M. Forster, C. L. Smith, G. Neri, R. J. Potter and A. J. Cowan, *Phys Chem Chem Phys*, 2018, **20**, 6811–6816.
- 46 S. Weisenberger and A. Schumpe, *AIChE J*, 1996, **42**, 298–300.

Chapter 4 Integrating CO₂ capture and electrocatalytic conversion

- 47 G. J. Browning and R. H. Weiland, *J Chem Eng Data*, 1994, **39**, 817–822.
- 48 B. Siritanaratkul, P. K. Sharma, E. H. Yu and A. J. Cowan, *Adv Mater Interfaces*, 2023, **10**, 1–10.
- 49 Y. Q. Wang, X. H. Dan, X. Wang, Z. Y. Yi, J. Fu, Y. C. Feng, J. S. Hu, D. Wang and L. J. Wan, *J Am Chem Soc*, 2022, **144**, 20126–20133.
- 50 I. Bhugun, D. Lexa and J.-M. Savéant, *J Phys Chem*, 1996, **100**, 19981–19985.
- 51 S. Sato, K. Saita, K. Sekizawa, S. Maeda and T. Morikawa, *ACS Catal*, 2018, **8**, 4452–4458.

Chapter 5 Conclusions and future work

In this thesis, novel approaches towards electrochemical CO₂ reduction with molecular complexes have been explored, including the modification of catalyst, electrolysis technique and substrates.

As the CO₂ reduction community looks to scaling up, removing diffusion limitations of both catalyst and substrate are of significant interest. Considering this, a pyrene modified Ni(cyclam) complex was synthesised with hopes of harnessing the selectivity of Ni(cyclam) in aqueous electrolyte while immobilising and improving the electron transfer from the electrode to catalyst. The catalyst was synthesised successfully and retained some activity towards CO₂ reduction, though this was diminished compared to the parent due to alkylating a nitrogen atom on the cyclam ring. The catalyst was immobilised to various carbon supports successfully and easily, where shifts in the reduction couple and binding energy of the Ni centre were observed suggesting electroactive interaction between the catalyst and electrode. However, it was quickly identified that the water solubility of the complex was an issue, as immobilised catalyst would be lost from the electrode surface into solution. This highlights the desirability for immobilised molecular catalysts to be insoluble however remain active for CO₂ reduction in aqueous electrolyte.

The catalyst was investigated on a GDE setup, first used in a flow cell where PTFE was added to catalyst ink in attempts to minimise catalyst wetting and dissolution. The Ni(CycPy) modified GDE gave good initial CO production (FE_{CO} 61% at 0.9 mAcm⁻²) however, this declined as even with PTFE addition, catalyst was still lost from the surface of the electrode throughout the reaction. Finally the GDE/Ni(CycPy) was tested in a zero-gap cell with no liquid catholyte to prevent dissolution losses. The zero-gap cell was used with a reverse-bias BPM configuration, resulting in a much lower pH at the cathode, recently shown to mitigate CO₂ losses to the bicarbonate equilibrium. Initial experiments of Ni(CycPy) in the zero-gap showed higher CO selectivity than both Ag and the parent complex, Ni(cyclam), at low current densities (2.5 mAcm⁻²), suggesting high selectivity for CO₂ reduction even at higher proton concentrations.¹ However as the current density increased, this activity dropped off quickly,

attributed to a decrease in the stability of Ni(CycPy) as a result of N-alkylation to CO poisoning, a common degradation pathway in Ni(cyclam) catalysts.²⁻⁴

Recently, the stability of CO₂ reduction with metal catalysts have been greatly improved using pulsed electrolysis techniques by inhibiting catalyst poisoning.⁵⁻⁹ This concept was applied to Ni(cyclam) in Chapter 3, where ms asymmetric pulses were shown to significantly improve the selectivity and stability of the catalyst, increasing the selectivity by over four times compared to potentiostatic electrolysis without compromising the total cell energy efficiency. Investigation through varying the anodic potential, electrochemical and XPS analysis, identified that regular oxidation of reversibly poisoned [Ni(cyclam)CO]⁺ prevented the build-up of hydrogen evolving Ni(0) species on the electrode surface.

Most pulsed electrolysis studies show symmetric pulses, meaning the maximum duty cycle achievable is 50%.¹⁰ By investigating the durations of the anodic pulse, it was observed that anodic pulses as short as 40 ms showed improved CO selectivity, achieving duty cycle of over 99%. Anodic pulses of up to 1.0 s showed further improvements in CO selectivity, but at the cost of the duty cycle, highlighting the large scope for optimisation of these parameters. Unfortunately, pulsed electrolysis was less successful when used in the zero-gap electrolyser, only showing improved selectivity under 30 min at these higher currents. Pulse parameters require optimisation, not only for the catalyst and reaction, but also for the specific electrochemical cell set-up which was limited due to the time constraints of the project.

In Chapter 4, the various speciation in an aqueous amine capture mixture was identified spectroscopically. Amine-catalyst interaction of a water-soluble Mn(bpy) catalyst was then observed with FTIR. This was followed by a preliminary electrochemical investigation where competitive FE_{CO} of 59% was observed in industrially relevant amine mixtures at low over potentials. Following literature, CO selectivity was improved further with cation addition, though the mechanism of this is unclear. Electrolysis was done after a second N₂ purge to attempt to lower the dissolved CO₂ present in solution, while a drop-in selectivity suggests that the dissolved CO₂ was acting as a substrate for the catalyst, significant CO is still produced, convoluting whether or not Mn(bpy-COOH) is able to reduce to carbamate directly, a concept of significant interest for future work. Lastly, initial experiments show the selectivity of Mn(bpy-COOH) is not limited to morpholine but is also observed with common capture amines: MEA and DEA, with the latter showing an impressive FE_{CO} of 70%.

Unfortunately, despite very interesting initial results, reproducibility was proven to be difficult with large discrepancies between measurements taken in 2021 compared to 2023 which were unable to be resolved in the time frame of this PhD. The complexity of capture solutions arising from the variety of species present at varying concentrations, depending on CO₂ loading, temperature and pH, significant control over these parameters is required in future studies on these mixtures.

More generally, mechanistic insight into CO₂ capture mixes during electrolysis is required on both metal and molecular catalysts, possibly obtainable through in situ spectroelectrochemistry. Those interested in molecular complexes for integrated CO₂ capture and conversion could move away from common CO₂ reduction catalysts, instead looking at developing new electrocatalysts designed to catalyse the reduction of the carbamate source directly. Possibly inspired by complexes used in thermal hydrogenation of similar functional groups such as amides, particularly focussing on phosphine complexes which are prevalent in hydrogenation field and largely unexplored in electrochemical conversion of CO₂ capture mixtures.

References

- 1 B. Siritanaratkul, M. Forster, F. Greenwell, P. K. Sharma, E. H. Yu and A. J. Cowan, *J Am Chem Soc*, 2022, **144**, 7551–7556.
- 2 S. Pugliese, N. T. Huan, A. Solé-Daura, Y. Li, J.-G. Rivera de la Cruz, J. Forte, S. Zanna, A. Krief, B.-L. Su and M. Fontecave, *Inorg Chem*, 2022, **61**, 15841–15852.
- 3 K. Bujno, R. Bilewicz, L. Siegfried and T. A. Kaden, *J Electroanal Chem*, 1998, **445**, 47–53.
- 4 J. D. Froehlich and C. P. Kubiak, *J Am Chem Soc*, 2015, **137**, 3565–3573.
- 5 R. Shiratsuchi, Y. Aikoh and G. Nogami, *J Electrochem Soc*, 1993, **140**, 3479–3482.
- 6 J. Lee and Y. Tak, *Electrochim Acta*, 2001, **46**, 3015–3022.
- 7 J. Yano and S. Yamasaki, *J Appl Electrochem*, 2008, **38**, 1721–1726.
- 8 P. Friebe, P. Bogdanoff, N. Alonso-Vante and H. Tributsch, *J Catal*, 1997, **168**, 374–385.
- 9 C. W. Lee, N. H. Cho, K. T. Nam, Y. J. Hwang and B. K. Min, *Nat Commun*, 2019, **10**, 1–8.
- 10 R. Casebolt, K. Levine, J. Suntivich and T. Hanrath, *Joule*, 2021, **5**, 1987–2026.

Chapter 6 Experimental Methods

6.1 Catalyst Synthesis

The cyclam-pyrene ligand (CycPy) was developed by and synthesised in collaboration with Dr Gaia Neri while the Ni(cyclam) was synthesised from literature by Dr Bhavin Siritanaratkul at the Stephenson Institute for Renewable Energy at the University of Liverpool.

6.1.1 NiCycPy (Chapter 2)

Synthesis of 4-(pyren-1-yl)butanal (**1**): To a solution of 1-pyrenebutanol (1.2 g, 4.3 mmol) in dry DCM (15 ml) under an inert atmosphere, a suspension of pyridinium dichromate (2.5 mg, 6.65 mmol) in dry DCM (15 ml) was added rapidly. The resulting suspension was stirred under argon overnight. The suspension is then diluted with 600 ml of diethyl ether and washed with water first then brine twice. The organic phase was dried over MgSO₄, then filtered and the solvent was evaporated. The resulting orange oil was purified using a silica plug eluted with chloroform. Yellow oil, obtained: 900 mg, yield : 75%. ¹H NMR (400 MHz, CDCl₃): δ 9.75 (s, 1H), 8.25 (d, J = 9.3 Hz, 1H), 8.18 (dd, J = 7.6, 2.0 Hz, 2H), 8.10 (dd, J = 8.5, 4.4 Hz, 2H), 8.03 (s, 2H), 8.02 – 7.99 (m, 1H), 7.80 (d, J = 7.8 Hz, 1H), 3.35 – 3.27 (m, 2H), 2.49 (td, J = 7.2, 1.6 Hz, 2H), 2.15 (p, J = 7.3 Hz, 2H). ¹³C NMR (101 MHz, CDCl₃): δ 200.99, 130.25, 129.71, 128.84, 127.53, 126.32, 126.28, 126.07, 125.60, 124.72, 123.92, 123.82, 123.81, 123.67, 123.65, 122.03, 42.20, 31.33, 22.71.

Synthesis of tri-tert-butyl-11-(4-(pyren-1-yl)butyl)-1,4,8,11-tetraazacyclotetradecane-1,4,8-tricarboxylate (**2**): 976 mg of Boc₃cyclam^{1,2} (1.95 mmol) and 800 mg of **1** (2.9 mmol) were added to a round bottom flask containing 4 Å activated molecular sieves under argon and dissolved in dry DCE (20 ml). The solution is stirred for 2 hours under argon at room temperature. Sodium triacetoxyborohydride (827 mg, 3.9 mmol) was added under an Ar blanket and the solution is stirred for 24 hours. The crude solution was washed with three aliquots of 2 M NaHCO₃ then the organic fraction was dried over MgSO₄, filtered and the solvent was evaporated to yield a yellow oil. The product was isolated by flash column

chromatography, eluting first with DCM then with DCM:EtOAc 50:50. Yellow foam, obtained: 1.16 g, yield: 83%. ^1H NMR (400 MHz, CDCl_3): δ 8.25 (d, $J = 9.3$ Hz, 1H), 8.15 (ddd, $J = 7.9, 3.8, 1.3$ Hz, 2H), 8.10 (dd, $J = 8.5, 3.2$ Hz, 2H), 8.01 (d, $J = 2.2$ Hz, 2H), 7.98 (d, $J = 7.6$ Hz, 1H), 7.84 (d, $J = 7.8$ Hz, 1H), 3.33 (t, $J = 7.8$ Hz, 7H), 3.26 (s, 7H), 2.55 (s, 2H), 2.41 (t, $J = 7.6$ Hz, 4H), 1.81 (q, $J = 7.6$ Hz, 4H), 1.72 (p, $J = 7.3$ Hz, 2H), 1.61 (s, 4H), 1.45 (d, $J = 4.5$ Hz, 27H). ^{13}C NMR (101 MHz, CDCl_3): δ , 155.65, 136.76, 131.40, 130.88, 129.76, 128.54, 127.50, 127.22, 127.17, 126.54, 125.79, 125.06, 125.00, 124.83, 124.79, 124.65, 123.37, 79.47, 79.30, 55.38, 53.47, 51.46, 46.87, 45.70, 33.49, 29.80, 28.53, 28.48, 26.75.

Synthesis of 1-(4-(pyren-1-yl)butyl)-1,4,8,11-tetraazacyclotetradecane (CycPy **3**): 1.16 g of 2 (1.53 mmol) was dissolved in 15 ml of DCM, then 7.5 ml of TFA are added dropwise at room temperature. The solution is stirred at room temperature until no change is detected in the TLC (DCM:EtOAc 50:50), ca. 6 hours. The solvent is rotary evaporated (MeOH is continually added to aid with complete TFA removal). The crude is purified by passing through an Amberlite IRN-78 twice, eluting with MeOH. Yellow oil, obtained: 620 mg, yield 83%. ^1H NMR (400 MHz, CDCl_3): δ 8.24 (d, $J = 9.3$ Hz, 1H), 8.13 – 8.02 (m, 4H), 7.98 – 7.89 (m, 3H), 3.30 (t, $J = 7.7$ Hz, 2H), 2.69 – 2.65 (m, 2H), 2.53 – 2.46 (m, 4H), 2.46 – 2.41 (m, 2H), 2.38 (t, $J = 5.7$ Hz, 4H), 2.30 (q, $J = 6.1, 5.7$ Hz, 4H), 2.16 (d, $J = 5.3$ Hz, 2H), 1.64 – 1.53 (m, 2H), 1.49 (t, $J = 6.2$ Hz, 2H), 1.80 (p, $J = 7.7$ Hz, 2H), 1.65 (d, $J = 7.1$ Hz, 2H). ^{13}C NMR (101 MHz, CDCl_3): δ 137.19, 131.40, 130.87, 129.67, 128.55, 127.45, 127.31, 127.22, 126.50, 125.76, 124.97, 124.79, 124.77, 124.59, 123.55, 54.69, 54.37, 52.73, 51.32, 49.87, 49.34, 48.57, 47.75, 47.67, 33.50, 30.07, 28.67, 26.49, 26.21. MS (ESI+): m/z calcd. for $\text{C}_{30}\text{H}_{40}\text{N}_4$: 456, found: 457 $[\text{M}+\text{H}^+]$. CHN microanalysis: anal. calcd. for $\text{C}_{30}\text{H}_{40}\text{N}_4$: C, 78.90, H, 8.83, N, 12.27; found: C, 74.5, H, 9.28, N, 13.54 ($\text{C}_{30}\text{H}_{40}\text{N}_4 \cdot 0.6 \text{NH}_4\text{OH} \cdot \text{H}_2\text{O}$)

Synthesis of Ni(1-(4-(pyren-1-yl)butyl)-1,4,8,11-tetraazacyclotetradecane)dichloride ($\text{Ni}(\text{cycPy})\text{Cl}_2$), a solution of CycPy (47 mg, 0.1 mmol) in ethanol (5 ml) at room temperature and a solution of $\text{NiCl}_2 \cdot 6\text{H}_2\text{O}$ (24 mg, 0.1 mmol) in ethanol (5ml) were added. The mixture turned bright orange upon contact. The solution was left at room temperature for 48h. After which, purple crystals had formed, and the intensity of the colour of the solution had dropped significantly. The purple crystals were filtered and washed three times with ethanol and left to dry in air. Obtained: 38.20 mg, yield: 54%. UV-vis (MeOH): $\lambda_{\text{max}} = 463$ nm. MS (ESI+): m/z calcd. For $\text{C}_{30}\text{H}_{40}\text{Cl}_2\text{N}_4\text{Ni}$: 586.27, found: 549.2 $[\text{M}-\text{Cl}]^+$ CHN microanalysis: anal. calcd. for $\text{C}_{30}\text{H}_{40}\text{Cl}_2\text{N}_4\text{Ni}$: C, 61.46, H, 6.88, N, 9.56; found: C, 61.65, H, 6.73, N, 9.41.

6.1.2 NiCyc (Chapter 3)

Synthesised in house from literature.³

Cyclam ligand (1,4,8,11-tetraazacyclotetradecane) (607 mg, 3.01 mmol) was added to EtOH (100 mL) and stirred until completely dissolved. NiCl₂•6H₂O (720 mg, 3.03 mmol) was added to the solution, and left stirring overnight at room temperature. Diethyl ether was added to precipitate the [Ni(Cyc)]Cl₂, and the precipitates were filtered, collected and dried in air. Obtained: 817 mg, yield: 82%. MS (ESI+) 257 [M+ -2Cl]; CHN microanalysis: Calculated for C₁₀H₂₄Cl₂N₄Ni: C, 36.40; H, 7.33; N, 16.98. Found: C, 36.39; H, 7.31; N, 16.92.

6.1.3 Mn(bpy-COOH) (Chapter 4)

Synthesised in house modified from literature.⁴

A solution of 4,4'-dicarboxy-2,2'-bipyridine (180 mg, 0.74 mmol) in 8 ml of methanol was added to a solution of Mn(CO)₅Br (200 mg, 0.72 mmol) in toluene (20 ml). The mixture was refluxed for 180 minutes at 40 °C, then kept in the fridge overnight. The orange-red precipitate that formed was filtered off, and the resulting red solution was rotary evaporated to dryness to yield a bright red powder. Yield = 26.4%; ¹H NMR (400 MHz, D₂O): δ ppm 9.27 (s, 2H), δ 8.62 (s, 2H), δ 7.89 (s, 2H). FTIR (H₂O): 2044, 1951, 1942 cm⁻¹; anal. calcd for C₁₅H₈BrMnN₂O₇•0.05C₇H₈: C, 39.42; H, 1.81; N, 5.99. Found: C, 39.73; H, 2.03; N, 6.37.

6.2 Catalyst immobilisation/ electrode fabrication

Immobilisation and electrochemical measurements of NiCycPy in the flow cell (chapter 2) were done by Dr Verity Piercy while immobilisation and electrochemical measurements of NiCycPy (Chapter 2) and NiCyc (Chapter 3) in the zero-gap configuration were done by Dr Bhavin Siritanaratkul at the Stephenson Institute for Renewable Energy and University of Liverpool.

6.2.1 Immobilisation to GCE and CNT

Carbon nanotube (CNT) or glassy carbon electrodes (GCE) were prepared by soaking either carbon nanotubes or glassy carbon plates in solutions of 1 mM Ni(CycPy) in methanol. The

CNT or GCE plates were then washed in triplicate with methanol followed by distilled water. For the CNT electrode, a solution of 1 mg CNTs and 50 μL 5 wt% Nafion in 1 mL MeCN was made up before 10 μL was drop casted onto a clean GCE.

6.2.2 Immobilisation to GDE in flow cell

Gas diffusion electrodes (GDE) for use in the flow cell were prepared by spray coating down a catalyst ink onto a 10.5 cm^2 area of ELAT LT1400, the back of the GDL had been pre-treated by spraying down 1 mL 5 wt% PTFE solution. The catalyst ink consisted of 10.5 mg of [Ni(cycPy)] electrocatalyst was dissolved in 8 mL methanol, 8 μL Nafion 117 (5 wt%) and 8 μL PTFE (60 wt%). The addition of 10.5mg Ensaco 350G carbon support was also added as part of the GDE optimisation. The catalyst ink was sprayed down onto the GDL, over a hot plate at 50 $^{\circ}\text{C}$, using a Harder and Steinbeck Evolution air brush at a N_2 pressure of 0.5 bar. The anode was prepared by spray coating a catalyst ink onto a 10.5 cm^2 area on a Ti plate. The catalyst ink consisted of 32 mg RuO_2 dispersed in 1 mL water and 1 mL propan-2-ol and 160 μL of Nafion 117 (5 wt%) sonicated for 30 seconds and was then spray coated down onto the Ti plate, over a hot plate at 100 $^{\circ}\text{C}$, at a N_2 pressure of 0.5 bar.

6.2.3 Immobilisation to GDE in zero-gap cell

Electrode fabrication for use in the zero-gap cell (NiCycPy, Chapter 2 & NiCyc, Chapter 3) is as reported elsewhere but summarised here.⁵ The GDE was made by spray coating a catalyst ink onto 5 cm^2 Sigracet 39 BB carbon paper. The catalyst ink was made up of 5 mg of Ni(Cyc) or Ni(CycPy) to 1 mL H_2O , 1 mL isopropyl alcohol and 80 μL of 5% Nafion solution before being sonicated for 5 min and spray coated onto the carbon paper substrate at 30 $^{\circ}\text{C}$. For the RuO_2 anode 9 mg of RuO_2 nanoparticles were added to 1 mL H_2O , 1 mL isopropyl alcohol 80 μL of 5% Nafion solution before sonicating for 30 min and spray coated onto carbon paper substrate at 95 $^{\circ}\text{C}$.

6.3 Electrochemistry

Electrochemical measurements were carried out using Biologic SP-200, Biologic VSP and Ivium Vertex potentiostats.

Most electrochemistry was run in a standard glass half-cell using a glassy carbon electrode ($A = 0.071 \text{ cm}^2$) (IJ Cambria Scientific Ltd) as the working electrode, a platinum mesh as the counter electrode, separated by a glass sleeve with a Vycor frit and a Ag/AgCl reference electrode (see picture below).

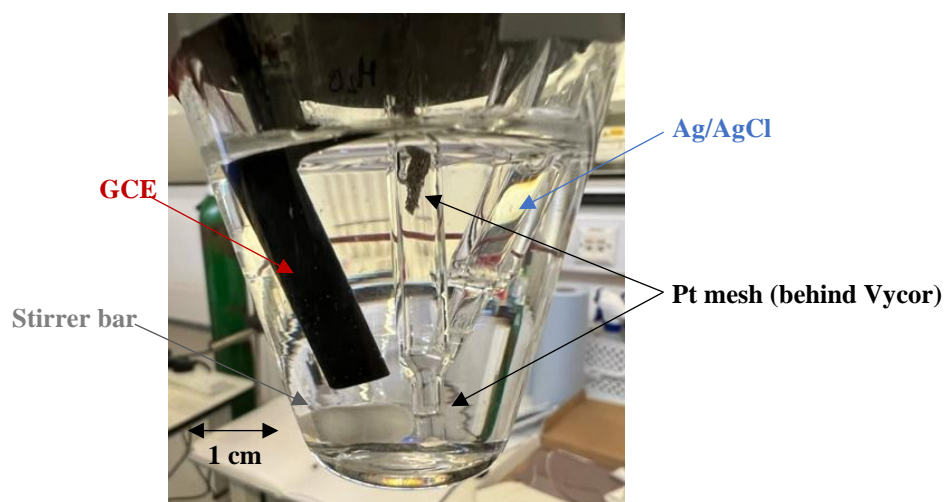


Figure 98 Photograph of cell set-up used in electrolysis

The GC working electrode was polished with $1.0 \mu\text{m}$ and $0.05 \mu\text{m}$ MicropolishTM Alumina on 8" microcloth (Buehler) for 4 minutes before sonicating with Milli-Q.

Aqueous electrolytes were made up in Milli-Q water ($18.2 \text{ M}\Omega$). Electrolytes used in Chapter 3 were pre-electrolysed (-0.1 mA) overnight with a titanium plate (working) and carbon counter. The cell was purged with either Ar, N_2 , CO_2 (for cyclic voltammetry and impedance spectroscopy) or CO_2 with 1% CH_4 (BOC) (for chronoamperometry) for ~ 30 minutes prior to experiments. All electrochemistry was run at room temperature and pressure. Electrolysis experiments used the same cell and electrode configuration as the CV studies with the addition of a magnetic stirrer bar.

Electrochemical measurements done with the flow cell (Chapter 2) were conducted in a commercial 4-compartment 10.5 cm^2 GDE flow cell (Electrocell Micro Flow cell). The cell was set-up as a 3-electrode measurement in a gas push through configuration, with gas products sampled from the headspace of the catholyte. The 0.5 M KHCO_3 electrolyte solutions were circulated by Verderflex peristaltic pumps, the anolyte and catholyte were circulated at a rate

of 22 mL min⁻¹ and 12 mL min⁻¹, respectively. The catholyte was pre-saturated with CO₂ for 30 minutes to remove dissolved oxygen. A leak-free Ag/AgCl reference electrode (Alvatek) was inserted close to the surface of the GDE cathode and separated from the RuO/Ti plate anode by a Selemion AMV-N membrane (Bellex). The flow of CO₂ was controlled by a Bürkert Type 8741 mass flow controller and was provided to the cell at a flow of 20 mL min⁻¹. The flow of CO₂ post cell was monitored by a manual bubble flowmeter (Merck).

Electrochemical measurements done with zero-gap cell (Chapter 2 & 3) were constructed by ‘cold pressing’ the bipolar membrane between the anode and cathode layers (with the cation exchange layer towards the cathode and the anion exchange layer towards the anode) between the bipolar plates of the electrolyser cell. The membrane-electrode assembly was assembled in a 5 cm² electrolyser from Dioxide Materials. The electrolyser consists of a titanium anode plate with an active area of 9 cm² and a stainless-steel cathode plate with an active area of 5 cm², separated by Teflon spacers. The membrane electrode assembly is sandwiched between these plates to provide a zero-gap assembly to which gas is flowed to the cathode and electrolyte is flowed to the anode. The cell was assembled with a torque of 3 Nm. CO₂ was flowed at 20 sccm, first passing through an H₂O bubbler at room temperature to humidify the gas before entering the electrolyser. Anolyte (milli-Q H₂O) was flowed across the anode at 15 ml/min. Electrochemistry was performed in a 2-electrode configuration under constant current conditions. Before measurement, the cell was pre-conditioned at open circuit, with CO₂ and anolyte flowing, for at least 30 min until the cell resistance was stabilized. For comparison of activity at different current densities, the measurement was conducted in order of increasing currents on the same cell setup, 10 min at each current with a 30 min pause in between each segment with CO₂ and anolyte kept flowing.

6.4 Product detection

6.4.1 GC

Gaseous products were measured by gas chromatography, by taking manual injections (100-500 µL) directly from the cell headspace using a 500 µL gas tight syringe (Hamilton, 1750 SL) and analysed using an Agilent 6890N with a 5 A molecular sieve column (ValcoPLOT, 30 m length, 0.53 mm ID) with He carrier gas and a pulsed discharge detector (D-3-I-HP, Valco Vici). Moles of product were quantified using a calibration curve from known concentrations

of H₂, CO and CH₄. A CH₄ internal calibrant of known concentration (1%) was also used in the cell to confirm the accuracy of the calibration

$$\text{Faradaic efficiency(\%)} = \frac{\text{moles(products)} \times \text{no. (electrons for reaction)}}{\text{moles(electrons)}} \times 100$$

The faradaic efficiency was calculated using the equation above where the number of electrons for the reaction is 2. Moles of electrons are obtained from charge passed during electrolysis.

Gaseous products from zero-gap cell were measured by gas chromatography using a Varian CP-4900 MicoGC with a 5 A molecular sieve column (Molsieve, 10 m) with Ar carrier gas and a thermal conductivity detector (TCD). The measurement was carried out at constant column temperature 100°C, constant pressure 21.7 psi, backflush time 5 s and injection time 50-500 ms.

6.4.2 GC-MS

Liquid products were checked for by GC-MS with an auto sampler taking injections of electrolyte before and after electrolysis and analysed with an Agilent 7890B GC with a DB-5ms column (Molsieve, 20 m) with He carrier gas and TCD. Coupled with a Agilent 5977B EI High Efficiency Source (HES) Mass Selective Detector (MSD) and an auto-ranging Flame Ionisation Detector (FID).

6.4.3 IC

Liquid products were checked for by injecting 2 mL of electrolyte before and after electrolysis into an Eco IC setup for anion detection with a metrosep A sup 5-150/4 column and a metrosep A sup 5 guard/4.0 with a pump rate of 0.7 mL/min, pressure of 7.3 MPa and conductivity of ca. 16.17 $\mu\text{S}\cdot\text{cm}^{-1}$. An eluent of 3.8 mM potassium carbonate and 1.2 mM potassium bicarbonate and a regen solution of 350 mM sulphuric acid and 100 mM oxalic acid and 5% acetone was used. The system was calibrated using a calibration curve of known concentrations of formate.

6.4.4 ¹H NMR

^1H NMR spectra were recorded using a Bruker 400 MHz spectrometer. Samples for Chapter 4 were made up with DMSO for quantification and D_2O as the deuterium lock. The coupling constants, J , are given in Hz and the multiplicity of the peaks are denoted as: s, singlet; d, doublet, and t, triplet.

6.5 Catalyst Analysis

6.5.1 ^1H NMR

^1H NMR spectra were recorded using a Bruker 400 MHz spectrometer. The samples containing Mn(bpy-COOH) catalyst (chapter 4) were prepared in amber tubes due to the light sensitivity of the catalyst. The coupling constants, J , are given in Hz and the multiplicity of the peaks are denoted as: s, singlet; d, doublet; dd, doublet of doublets; t, triplet; q, quartet and m, multiplet.

6.5.2 UV/Vis

UV/Vis spectra of known catalyst concentrations in various solvents were recorded using a 10 mm pathlength quartz cuvette on a Shimadzu UV-2550 UV-VisNIR spectrophotometer.

6.5.3 FT-IR

FT-IR analysis of Mn(bpy-COOH) in various aqueous solvents (Chapter 4) was done using a Vertex 70 FT-IR Spectrometer with a Deuterated Triglycine Sulfate (DTGS) detector in transmission mode. Samples were mounted in a Harrick cell with a 50 μm spacer and recorded with a resolution of 2 cm^{-1} over 124 scans.

6.5.4 XPS

XPS measurements for NiCycPy (Chapter 2) were performed by external service Harwell XPS and fitted by Dr Verity Piercy at the Stephenson Institute for Renewable Energy and University of Liverpool. XPS measurements for Chapter 3 were done at Harwell XPS by Dr Preetam Sharma from Department of Engineering at Loughborough University.

XPS measurements for Chapter 2 using a Thermo NEXSA XPS fitted with a monochromated Al $K\alpha$ X-ray source (1486.7 eV), a spherical sector analyser and 3 multichannel resistive plate, 128 channel delay line detectors. All data was recorded at 19.2 W and an X-ray beam size of 200 x 100 μm . Survey scans were recorded at a pass energy of 160 eV, and high-resolution scans recorded at a pass energy of 20 eV. Electronic charge neutralization was achieved using a Dual-beam low-energy electron/ion source (Thermo Scientific FG-03). Ion gun current = 150 μA . Ion gun voltage = 45 V. All sample data was recorded at a pressure below 10^{-8} Torr and a room temperature of 294 K. Data was analysed using CasaXPS v2.3.19PR1.0. Peaks were fit with a Shirley background prior to component analysis. Lineshapes of LA(1.53,243) were used to fit components.

XPS measurements for Chapter 3 were performed using a Kratos Axis Supra instrument using Al $K\alpha$ X-ray source (1486.7 eV), spherical mirror analyser and 128 channel delay-line detector. With an X-ray beam size of 400 x 400 μm . The survey scans were performed at 80 eV pass energy and high-resolution scans were performed at 20 eV pass energy. The energy calibration was performed using O 1s peak at 530.9 eV. All sample data was recorded at a pressure below 10^{-6} Torr and a room temperature of 294 K.

6.6 References

- 1 L. Fabbrizzi, F. Foti, M. Licchelli, P. M. Maccarini, D. Sacchi and M. Zema, *Chem. Eur. J.*, 2002, **8**, 4965–4972.
- 2 A. Zhanaidarova, C. E. Moore, M. Gembicky and C. P. Kubiak, *Chemical Communications*, 2018, **54**, 4116–4119.
- 3 J. D. Froehlich and C. P. Kubiak, *Inorg Chem*, 2012, **51**, 3932–3934.
- 4 J. J. Walsh, C. L. Smith, G. Neri, G. F. S. Whitehead, C. M. Robertson and A. J. Cowan, *Faraday Discuss*, 2015, **183**, 147–160.
- 5 B. Siritanaratkul, M. Forster, F. Greenwell, P. K. Sharma, E. H. Yu and A. J. Cowan, *J Am Chem Soc*, 2022, **144**, 7551–7556.

Appendix

Mn(bpy-COOH) in CO₂ capture amines

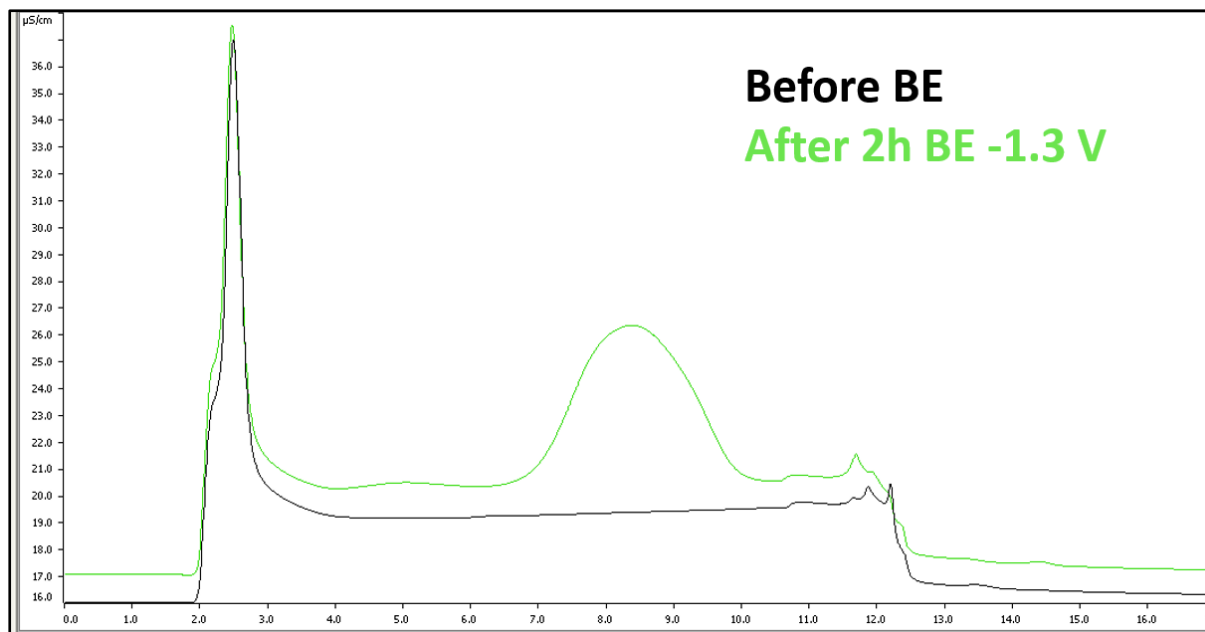


Figure 99 0.5 mM Mn(bpy-COOH) in 30 wt% MORPH-CO₂ before and after electrolysis for 2 h at -1.3 V_{Ag/AgCl}

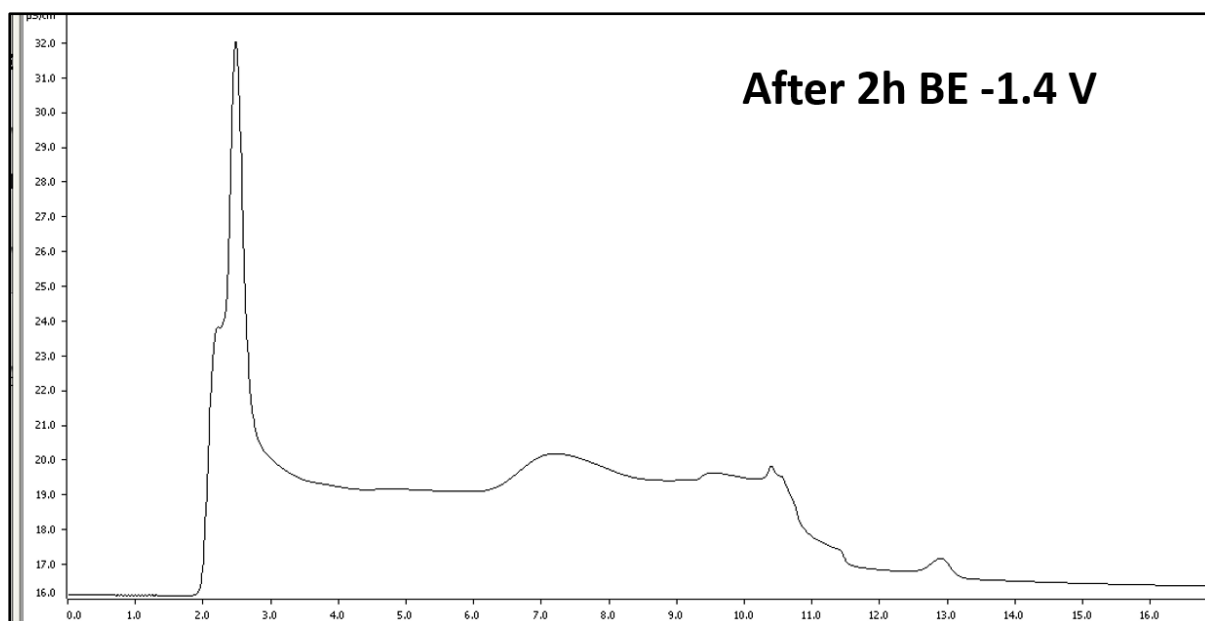


Figure 100 0.5 mM Mn(bpy-COOH) in 30 wt% MORPH-CO₂ after electrolysis for 2 h at -1.3V_{Ag/AgCl}

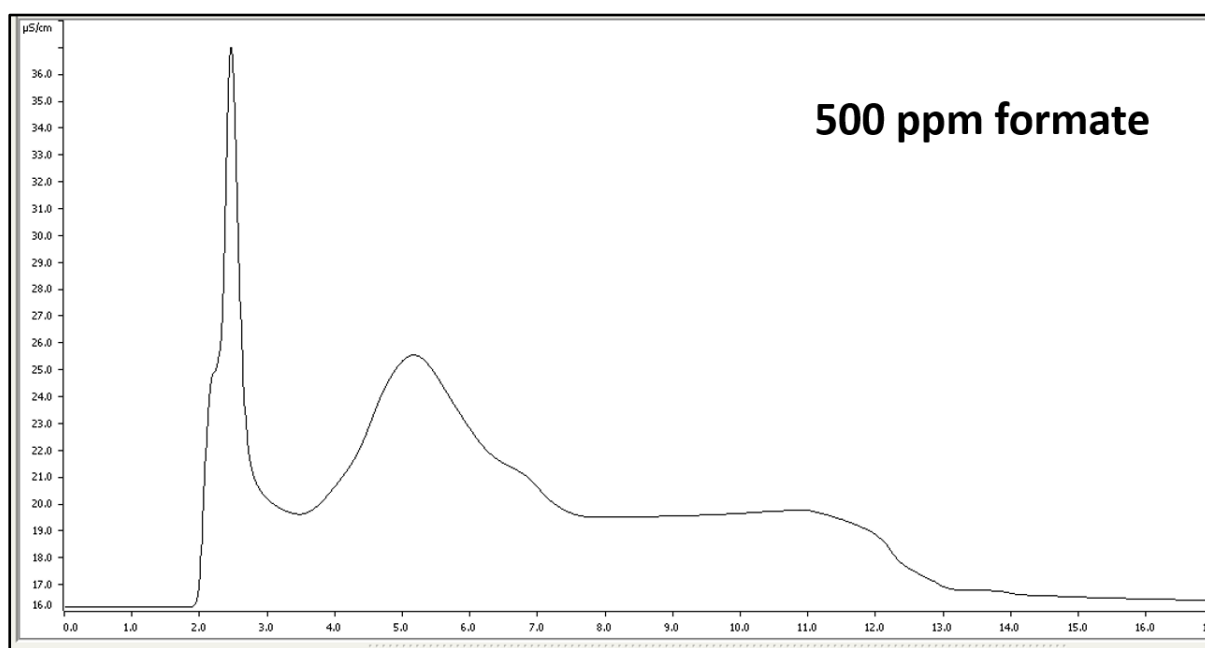


Figure 101 30 wt% MORPH-CO₂ 500ppm formic acid (peak at 5.2 min)

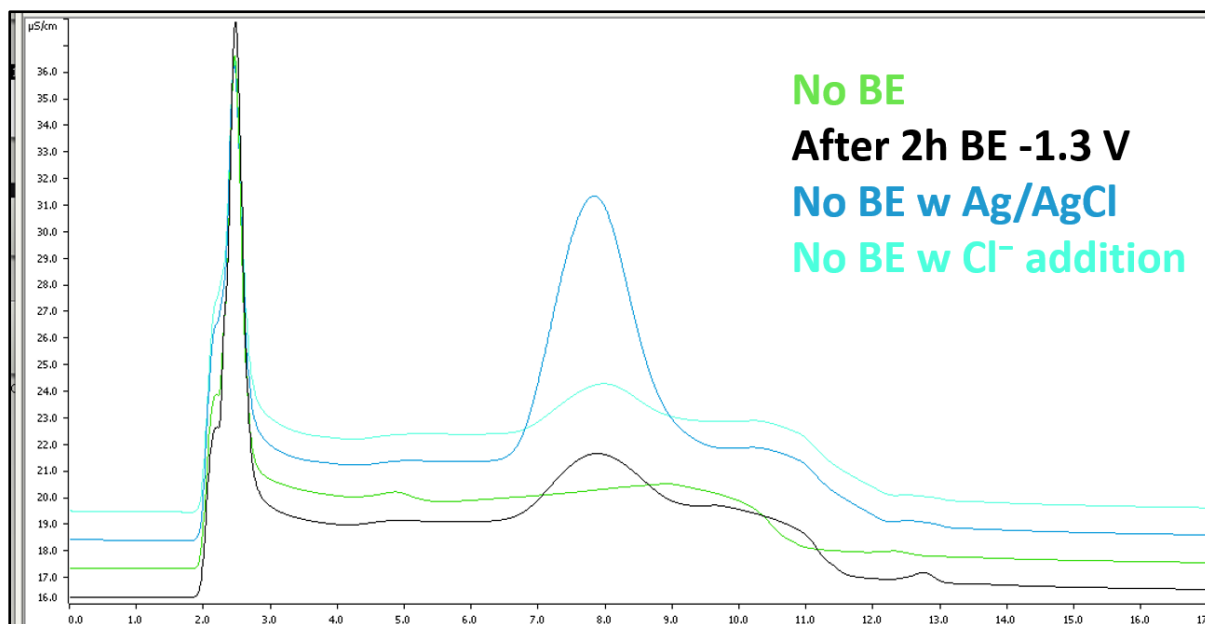


Figure 102 Solutions of 30 wt% MORPH- CO_2 with and without electrolysis for 2 h at $-1.3 V_{\text{Ag}/\text{AgCl}}$. Ag/AgCl reference was added to a solution of 30 wt% MORPH- CO_2 for 3 hours to identify peak at 8 min as chloride ions

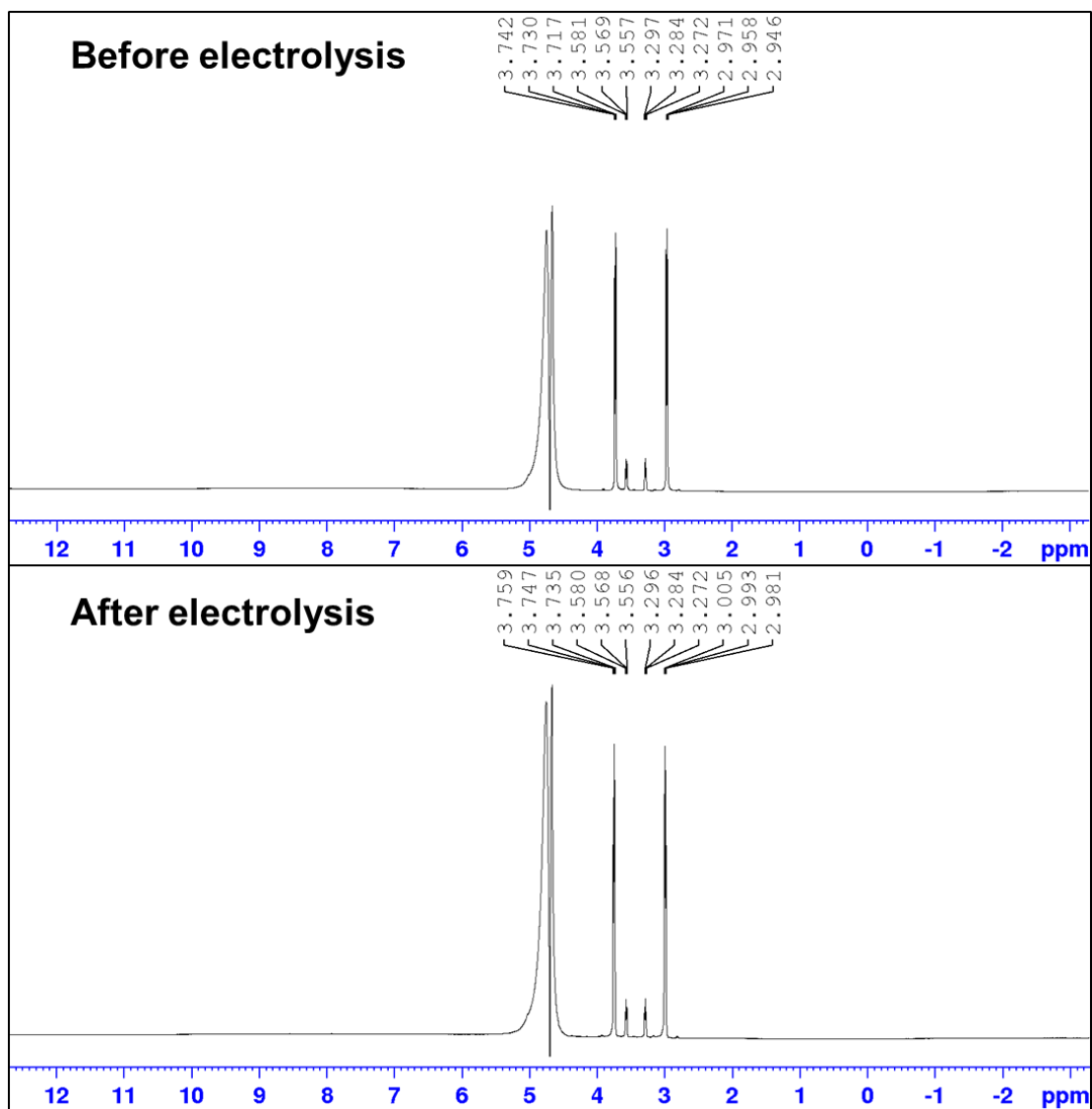


Figure 103 ^1H NMR of 30 wt% MORPH- CO_2 before and after 2 h electrolysis at $-1.3 V_{\text{Ag}/\text{AgCl}}$

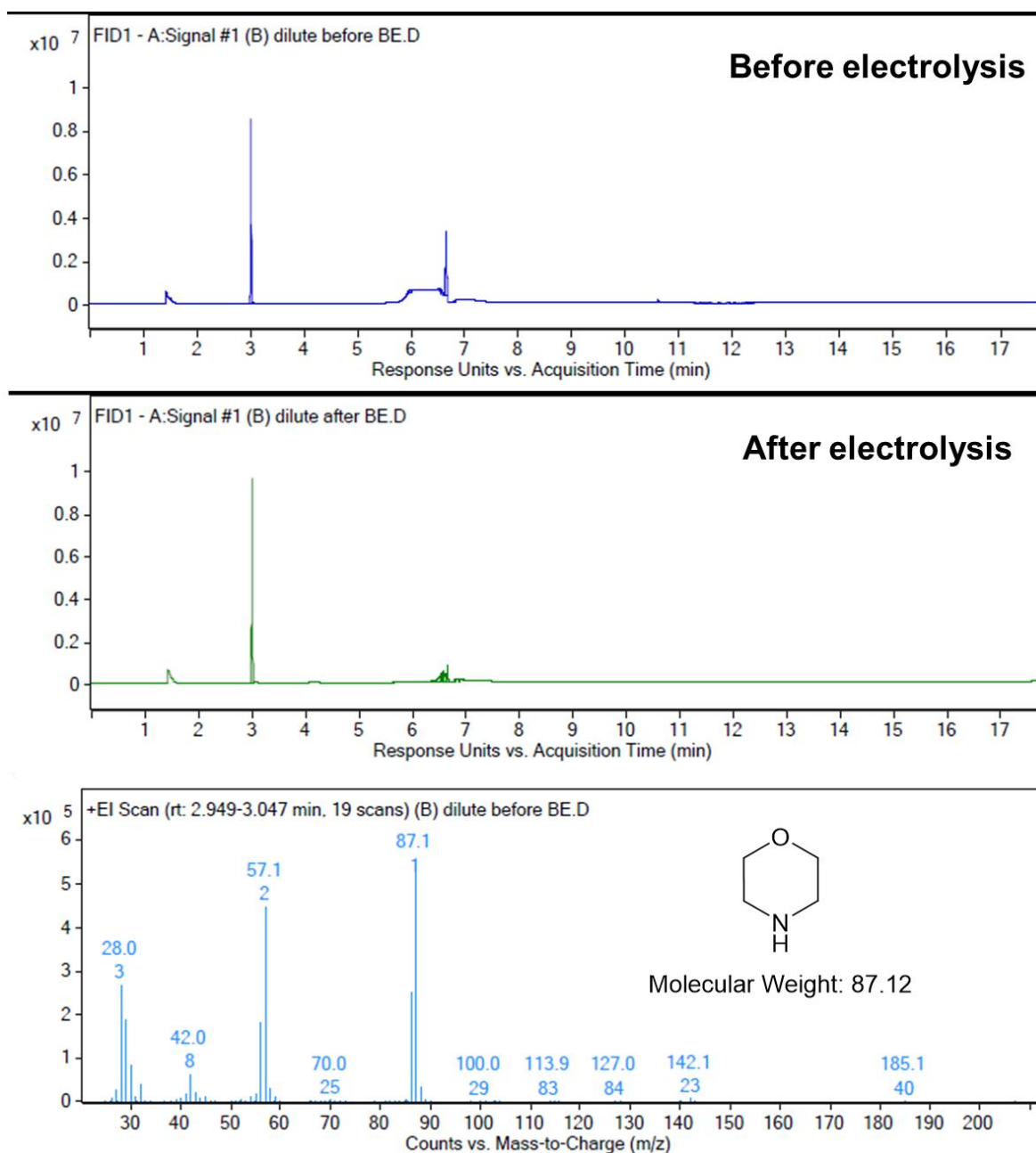


Figure 104 GC-MS data of 0.5 mM Mn(bpy-COOH) in 30 wt% MORPH-CO₂ before (top) and after (middle) 2 h electrolysis at -1.3 V_{Ag/AgCl}. With mass spec of peak at 3 min corresponding to morpholine (bottom)